

# Modelling and characterisation of a 3D printed peristaltic pump

**MP McIntyre**

 [Orcid.org/0000-0002-3393-3937](https://orcid.org/0000-0002-3393-3937)

Dissertation accepted in fulfilment of the requirements for the degree *Master of Engineering in Mechanical Engineering* at the North-West University

Supervisor: Prof G van Schoor

Co-supervisor: Prof KR Uren

Co-supervisor: Mr CP Kloppers

Graduation: October 2020

Student Number: 24211303

---

## Abstract

---

Peristaltic pumps are positive displacement pumps that mechanically imitate the peristaltic process. The unique design and operation of the pumps allows it to have a wide range of applications, from blood pumps in heart-lung machines to industrial cement pumps. Another possible application might be as an electro-hydrostatic actuator (EHA), provided that the pump completely occludes the process tube. In order for the pump to be utilised as an EHA, the pump must have known flow characteristics for accurate actuation capabilities. This study aims to create a model-assisted design approach to calculate the required pump geometry needed to adhere to required design specifications as an EHA.

A first principles modelling approach is followed with the flow characteristics derived from the geometric relations pertaining to roller-type peristaltic pumps. Novel methods of approximating the volume displacement caused by a roller engaging the tube are presented within this model. A generalised lumped parameter model is created in an attempt to model the pressure response of the hydraulic circuit that the pump is integrated with.

A three-roller peristaltic pump is designed using the model-assisted approach in Solidworks. Manufacturing commences using polyethylene terephthalate (PETG) material on a Prusa MK2.5 and Prusa MK3 printer. A test bench is constructed for model validation purposes regarding the roller volume displacement, pump flow rate, and pressure pulsations of the pump over varying motor speeds. A two-roller configuration of the same pump is also tested to validate some of the premises of selecting a three-roller pump as an EHA and further model validation.

The simulation of the three-roller pump shows an average correlation coefficient of 0.83 for the inlet pressure and 0.74 for the outlet pressure when compared to experimental results. The modelled flow of the three-roller pump had an average error of 2.37 % and a maximum deviation of 9.02 %, where the two-

---

roller pump had an average error of 1.97 % and a maximum deviation of 4.03 % over all tested motor speeds. The flow rate of the pump was found to have a non-linear relationship to the motor speed, where the model represents an idealistic linear relationship. The non-linear flow was found to correlate strongly to the peak inlet pressures of the pump.

The pump managed to achieve vacuums under 5 kPa (absolute) and generate pressures above 140 kPa (gauge) for both the two-roller and three-roller configurations. The three-roller configuration had a more stable hydrostatic capability for high-pressure, tests as expected. Due to the friction of the rollers the two-roller configuration had a maximum operational speed of 400 r/min compared to 150 r/min for the three-roller configuration. This is associated with a maximum flow rate of 9.35 L/min for the two-roller configuration and 3.28 L/min for the three-roller configuration.

**Keywords: Peristaltic, pump, model, design, EHA**

---

## Acknowledgements

---

**“If I have seen further it is by standing on the  
shoulders of Giants.”**

**– Isaac Newton**

I would like to thank the following persons and institutions, in no specific order, for the contribution they made to the completion of this dissertation:

- The North-West University, Potchefstroom Campus for the opportunity and financial support to learn more about this magnificent world, and providing me with an exceptional education.
- To my study leaders, Prof. George van Schoor, Prof. Kenny Uren, and Mr. C.P. Kloppers for their patience, understanding, and support throughout my studies. Had it not been for you, I may not have had the opportunity to find my appreciation for math and science.
- To my mother and father for their hard work, love and support. Thank you for being both my rock and motivation through hard times and good times.
- Ms. Adri Benade and the MakerSpace students for their help and suggestions with regards to additive manufacturing.
- To Gert Kruger, who developed the dSPACE interface board and assisted with the electronics aspect of the project.
- To the members of the McTronX research group for their feedback and interesting discussions.
- To Lemmer Vermooten and Pieter Oberholzer for your humour and supporting roles throughout this study.
- To the unmentioned friends and family that supported me over the years.

---

# Contents

---

<b>List of Figures</b>	<b>vii</b>
<b>List of Tables</b>	<b>xiii</b>
<b>List of Abbreviations</b>	<b>xv</b>
<b>Nomenclature</b>	<b>xvii</b>
<b>1 Introduction</b>	<b>1</b>
1.1 Background . . . . .	1
1.2 Motivation . . . . .	3
1.3 Problem statement . . . . .	4
1.4 Objectives and methodology . . . . .	4
1.5 Outline of the dissertation . . . . .	7
<b>2 Literature study</b>	<b>8</b>
2.1 Introduction . . . . .	8
2.2 Literature survey . . . . .	9
2.3 Industry 4.0 . . . . .	10
2.4 Peristaltic pumps . . . . .	12
2.5 Modelling theory . . . . .	16
2.6 Additive manufacturing . . . . .	24
2.7 Critical literature review . . . . .	27
<b>3 Peristaltic pump modelling</b>	<b>29</b>
3.1 Introduction . . . . .	29
3.2 Modelling methodology . . . . .	30
3.2.1 Reference geometry and positions . . . . .	31
3.2.2 Assumptions . . . . .	34
3.3 Degree of occlusion . . . . .	35
3.4 Roller volume approximation . . . . .	39

3.5	Lumped parameter model . . . . .	50
3.6	Peristaltic pump model . . . . .	55
3.6.1	Numerical modelling . . . . .	55
3.6.2	Simulink/Simscape . . . . .	56
3.7	Model verification . . . . .	58
3.7.1	Roller volume displacement approximation . . . . .	58
3.7.2	Peristaltic pump lumped parameter model . . . . .	60
3.8	Conclusion . . . . .	65
<b>4</b>	<b>Peristaltic pump design</b>	<b>66</b>
4.1	Introduction . . . . .	66
4.2	Material and printer selection . . . . .	67
4.3	Design considerations . . . . .	68
4.3.1	Software . . . . .	68
4.3.2	Slicing: infill, orientation, and support . . . . .	68
4.3.3	Topology optimisation . . . . .	71
4.4	Physical constraints . . . . .	72
4.5	Design specifications . . . . .	73
4.6	Concept designs . . . . .	78
4.6.1	Concept A - Multiple circular raceways design . . . . .	80
4.6.2	Concept B - One circular raceway design . . . . .	81
4.6.3	Concept design discussion . . . . .	81
4.7	Iterative design improvements . . . . .	83
4.8	Final design . . . . .	86
4.9	Pump manufacturing . . . . .	88
4.10	Conclusion . . . . .	92
<b>5</b>	<b>Test bench design</b>	<b>93</b>
5.1	Introduction . . . . .	93
5.2	Test objectives . . . . .	94
5.3	Resistance test bench . . . . .	98
5.4	Compliance test bench . . . . .	100
5.5	Roller volume displacement test bench . . . . .	101
5.6	Peristaltic pump test bench . . . . .	105
5.6.1	Instrumentation . . . . .	107
5.6.2	Calibration . . . . .	113
5.7	Data comparison and validation methods . . . . .	115
5.7.1	Roller volume displacement tests . . . . .	115
5.7.2	Peristaltic pump tests . . . . .	115
5.8	Conclusion . . . . .	118

---

<b>6 Results</b>	<b>119</b>
6.1 Introduction . . . . .	119
6.2 Model validation . . . . .	120
6.2.1 Roller volume displacement . . . . .	120
6.2.2 Flow characteristics . . . . .	122
6.2.3 Pressure pulsations . . . . .	130
6.3 Pump characteristics . . . . .	141
6.4 Conclusion . . . . .	145
<b>7 Conclusion</b>	<b>148</b>
7.1 Introduction . . . . .	148
7.2 Reflection on research objectives . . . . .	149
7.3 Research findings . . . . .	150
7.4 Recommendations . . . . .	152
7.5 Further research . . . . .	153
7.6 Final remarks . . . . .	154
<b>Bibliography</b>	<b>156</b>
<b>Appendices</b>	<b>164</b>
<b>A Peristaltic pump patents</b>	<b>165</b>
<b>B Simulink model and MATLAB code</b>	<b>169</b>
<b>C Design drawings</b>	<b>170</b>
<b>D Additional test bench information</b>	<b>201</b>
<b>E Additional experiment information</b>	<b>204</b>

---

## List of Figures

---

1.1	Illustration of the operation of a two-roller peristaltic tube pump	2
1.2	Conceptual overview of the research methodology followed in this study . . . . .	5
2.1	Design illustration of Kling's peristaltic pump design without a backplate . . . . .	14
2.2	Symmetry similarity found on rotary peristaltic pump patents . .	16
2.3	A lumped parameter model diagram of a two-roller peristaltic pump proposed by Moscato et al. . . . .	18
2.4	Measured values of a roller's volume displacement during engagement with a process tube for a roller type peristaltic pump . . . . .	19
3.1	Illustration of the modelling methodology used to model the peristaltic pump characteristics . . . . .	30
3.2	Roller positions of a two-roller peristaltic pump pertaining to pulsatile flow characteristics . . . . .	32
3.3	Schematic diagram illustrating the pump dimensional parameters and flow variables . . . . .	33
3.4	Illustration of the geometric distances and angles used to define the pump's angle of engagement . . . . .	35
3.5	Diagram illustrating the occlusion value with regards to the roller position and compression occurrence . . . . .	38
3.6	Verification of distance $\delta$ by means of comparison to Pythagorean distance between central distance and leading edge . . . . .	38
3.7	Illustrative diagram of a straight cylindrical section of the process tube collapsed by the roller for volume displacement indication .	39
3.8	Illustration of the roller angle $\lambda$ used to determine $X$ . . . . .	40
3.9	Illustration of the two dimensional surfaces of the roller and the tube used to approximate the volume displacement of the roller .	41



3.10	Illustration of the side view of a roller collapsing the process tube to indicate the integration area . . . . .	42
3.11	Illustration of the radii of an ellipse used to calculate the ellipse area	42
3.12	Illustration of the inflating angle and $\delta$ for varying roller positions	43
3.13	Example illustration of the midpoint rule used for discrete integration . . . . .	44
3.14	Illustration indicating the angles of $\gamma$ relating to incremental step size $dx$ in $X_{max}$ . . . . .	45
3.15	Length value $l$ across the roller angle $\{-\lambda : \lambda\}$ as the roller disengages the tube for $\theta = \{0 : \phi\}$ . . . . .	46
3.16	Illustration indicating effect of the backplate curvature on the roller angle $\lambda$ . . . . .	48
3.17	Illustration of the effects of different polynomial orders of the volume function on the flow values over time for perfect occlusion and compression . . . . .	49
3.18	Indication of fluid segment between two rollers in a rotary peristaltic pump for average flow calculations . . . . .	50
3.19	The lumped parameter model diagram of a two-roller peristaltic pump for reference purposes . . . . .	51
3.20	Illustration of the nominal flow variables used in relevant literature	52
3.21	Illustration of an equivalent circuit model of a roller-type peristaltic pump integrated within a hydraulic system . . . . .	54
3.22	Simulink/Simscape model used to simulate the pressure pulsations of a peristaltic pump . . . . .	57
3.23	Volume approximation values plotted for varying roller sizes . . . . .	59
3.24	Roller induced flow value plots for varying roller sizes, adjusted for comparison . . . . .	60
3.25	Pressure waveform plot of the simulation response indicating waveform characteristics . . . . .	62
3.26	Verification of the lumped parameter model with respect to the pressure response with approximated flow parameters . . . . .	64
4.1	Renderings of different infill patterns of a cube on Ultimaker Cura with 25 % infill . . . . .	69
4.2	Renderings of different infill percentages of a cube on Ultimaker Cura with grid infill pattern . . . . .	70
4.3	Rendering of a sliced preview of an off-balance block on a build plate to simulate an orientation induced overhang and support structure . . . . .	70
4.4	Rendering of a wall bracket before and after a topology optimisation design study in Solidworks . . . . .	71

4.5	Illustration of maximum coupler size with respect to the backplate radius, offset radius, and coupler radius . . . . .	76
4.6	Length value across the roller angle $\{-\lambda : \lambda\}$ as the roller engages the tube over the angle $\theta$ for the specified design . . . . .	76
4.7	Integration roller volume displacement values over the rotational motor angle for the designed pump . . . . .	77
4.8	Roller induced flow values over time for a disengaging roller with the specified design parameters for various volume function polynomial orders . . . . .	77
4.9	Illustration of the area of intersecting circles used for circular raceway modelling . . . . .	79
4.10	3D printed peristaltic pump design process flow chart . . . . .	80
4.11	Photo-realistic rendering of the concept A Solidworks design . . . . .	80
4.12	Photo-realistic rendering of the concept B Solidworks design . . . . .	82
4.13	Photo-realistic rendering of the roller housing assembly for concept designs A and B . . . . .	82
4.14	Illustration indicating normal forces that create resistance on the concave roller from the concave raceway design . . . . .	83
4.15	Photo-realistic rendering of the first iteration and design improvement of the peristaltic pump design . . . . .	84
4.16	Illustration of the process tube raceway design improvement from a circular form to a square/flat form . . . . .	84
4.17	Photo-realistic rendering of the revised roller housing assembly associated with the first revision . . . . .	85
4.18	Rendering image of the required support structures for the roller design before and after revision . . . . .	85
4.19	Partial design drawing indicating of the reduction in occlusion range in pump design drawings between various design revisions . . . . .	86
4.20	Photo-realistic rendering of the second iteration of the peristaltic pump design . . . . .	86
4.21	Photo-realistic rendering of the final design of the peristaltic pump . . . . .	87
4.22	Rendering of the sectional view of the final design of the peristaltic pump . . . . .	88
4.23	Photo showing the close-up view of the clearances of the top part of the roller housing for the shaft coupler and roller housing screws . . . . .	89
4.24	Photo showing the manufactured roller housing assemblies for two-roller and three-roller pump configuration . . . . .	90
4.25	Photo showing the fully assembled pump integrated with test bench for testing and validation . . . . .	91
5.1	High level functional block diagram of the resistance test bench . . . . .	95

5.2	High level functional block diagram of the compliance test bench	96
5.3	High level functional block diagram of the roller volume displacement test bench . . . . .	97
5.4	High level functional block diagram of the peristaltic pump test bench . . . . .	97
5.5	Component level functional block diagram of the resistance test bench . . . . .	98
5.6	Resistance test results indicating a non-linear mass flow and pressure gradient characteristic of the restricting gate valve . . . . .	99
5.7	Photo of the isolated inlet section of the peristaltic pump test bench used for the compliance test . . . . .	100
5.8	Compliance test results of the isolated inlet line . . . . .	101
5.9	Illustration of the volume displacement test set-up as seen from above . . . . .	102
5.10	Photos showing the roller volume displacement test bench . . . . .	102
5.11	Photo of the internal pump components indicating the total angle of rotation for the volumetric displacement tests . . . . .	104
5.12	Photo of the internal pump components with demarcations for the incremental steps . . . . .	104
5.13	Experimental results of the rotation angles for the volumetric displacement tests . . . . .	105
5.14	PPTB pressure and flow testing piping and instrument diagrams .	106
5.15	Photo of the top-down view of the PPTB configured for the flow tests indicating the P& ID components . . . . .	107
5.16	Photo of the peristaltic pump test bench indicating the various components of the test bench . . . . .	108
5.17	Component level functional block diagram of the peristaltic pump test bench . . . . .	109
5.18	Photo of the dSPACE interface board for circuit isolation and protection developed by the North-West University . . . . .	110
5.19	Photo of the Kern ABS 220-4N and generic digital weight scales side-by-side . . . . .	112
5.20	Pressure sensor calibration test values of the two Honeywell pressure sensors and the testo 622 barometer as the reference . . . . .	113
5.21	Accuracy test comparisons for the connected thermocouple and the generic scale . . . . .	114
5.22	Indication of correlation between variables on the x-axis and y-axis	116
6.1	Volume displacement results of a peristaltic pump roller during engagement . . . . .	120

6.2	Adjusted roller volume test results compared to the volume displacement approximation model, RMSE = 0.1218 mL . . . . .	122
6.3	Experiment 2: Control volume test results indicating the priming effect . . . . .	125
6.4	Experiment 1: Volume displacement results . . . . .	125
6.5	Experiment 1–4: Pump volume displacement test results compared to the modelled values . . . . .	126
6.6	Experiment 5: Pump volume displacement test results compared to the modelled values . . . . .	127
6.7	Experiment 1 and 5: Volume displacement compared to the inlet peak maximum pressures . . . . .	129
6.8	Experiments 1–4: Flow compared to the modelled flow using the approximated roller volume . . . . .	129
6.9	Experiment B: Ambient pressure reading indicating the sensor values, the noise bands, and the mean pressure values . . . . .	130
6.10	Savitzky-Golay filter applied to the outlet pressure sensor data for 20 r/min and 50 r/min of Experiment B . . . . .	131
6.11	Experiments A, B, and C: System response pressure at the pump outlet at 100 r/min . . . . .	132
6.12	Experiments A, B, and C: Adjusted system pressure response at the pump outlet at 100 r/min . . . . .	133
6.13	Experiments A, B, and C: Adjusted system pressure response at the pump inlet at 100 r/min . . . . .	133
6.14	Experiment A: Averaged peak maximum and peak minimum pressure values for the inlet and outlet . . . . .	134
6.15	Experiment A, B, and C: Comparison of peak maximum and minimum pressure values . . . . .	135
6.16	Experiment A and C: Root mean square error of the pressure values with regards to Experiment B . . . . .	136
6.17	Experiment B: Comparison to Simulation A pressure results . . . . .	138
6.18	Experiment B: Comparison to Simulation A pressure values for a motor speed of 20 r/min . . . . .	139
6.19	Experiment B and D: Pearson correlation coefficient of the simulated inlet and outlet pressures . . . . .	139
6.20	Experiment B: Comparison of peak maximum and minimum pressure values of Simulation A . . . . .	140
6.21	RMSE values over varying r/mins for simulations with both the measured roller volume and approximated roller volume . . . . .	141
6.22	Maximum and minimum working pressure test results for the three-roller pump configuration . . . . .	141

---

6.23	Maximum and minimum working pressure test results for the two-roller pump configuration . . . . .	142
6.24	Hydrostatic test: Roller positions for the positive and negative pressure gradients . . . . .	143
6.25	Hydrostatic test: Positive pressure gradient results . . . . .	144
6.26	Hydrostatic test: Negative pressure gradient results . . . . .	144
B.1	Modelling and simulation block diagram . . . . .	169
D.1	Peristaltic pump test bench inlet line dimensions . . . . .	202
D.2	dSPACE 1104 Simulink block diagram . . . . .	203
E.1	Experiment B: Surface plot of the inlet pressure sensor (P1) data at 150 r/min . . . . .	205
E.2	Experiment B: Surface plot indicating the processed pressure sensor data for 150 r/min . . . . .	205
E.3	Experiment B: Processed pressure waveforms of P1 sensor data . . . . .	209
E.4	Experiment B: Processed pressure waveforms of P2 sensor data . . . . .	210
E.5	Experiment D: Processed pressure waveforms of P1 sensor data . . . . .	211
E.6	Experiment D: Processed pressure waveforms of P2 sensor data . . . . .	212

---

## List of Tables

---

2.1	Additive manufacturing core technologies and manufacturing methods adopted from Bikas et al. . . . .	26
2.2	Processing errors pertaining to part tolerance regarding additive manufacturing . . . . .	26
3.1	Simscape/Simulink component list used for the peristaltic pump simulation inside the Simulink environment . . . . .	57
3.2	Indication of maximum volume displacements and angles of engagement relational to the roller size . . . . .	60
3.3	Simulation parameters used to verify the lumped parameter model	61
3.4	Simulation results and comparison to theoretical and reference values, with adjusted parameter results indicated in brackets . . .	63
4.1	Table of peristaltic pump design specifications . . . . .	78
5.1	Test objectives and data acquisition techniques . . . . .	94
5.2	Test bench sensor drift/uncertainty table . . . . .	112
5.3	Additional calibration sensor drift/uncertainty table . . . . .	114
5.4	Table of tests conducted on the peristaltic pump and how they are referred to . . . . .	117
6.1	Indication of part tolerances caused by printing inaccuracies . . .	121
6.2	Accuracy comparison of the roller volume approximation methods for the maximum volume displaced . . . . .	122
6.3	Experiments 1–5: Accuracies of the modelled pump volume displacement for the flow test volumes . . . . .	127
6.4	Comparison of the Pearson correlation coefficients of the peak pressure values of each flow experiment compared to the volume displacement of each test . . . . .	128
6.5	Simulation parameters used to validate the lumped parameter model . . . . .	137

---

6.6	Pump characteristics for three-roller and two-roller configuration	145
A.1	Various patents filed for peristaltic pump designs and operations from 1957 to 2011 . . . . .	166
C.1	Table indicating design drawing numbers and their descriptions .	171
C.2	Peristaltic pump bill of materials: three-roller configuration . . . .	172
C.3	Peristaltic pump bill of materials: two-roller configuration . . . .	173
E.1	Calculated motor speeds for the pressure tests and simulations of three-roller pump configuration . . . . .	206
E.2	Calculated motor speeds for the flow tests of three-roller pump configuration . . . . .	207
E.3	Calculated motor speeds for the two-roller pump configuration experiments . . . . .	208

---

## List of Abbreviations

---

<b>Abbreviation</b>	<b>Description</b>	<b>Page List</b>
3D	three dimensional	ix, 3–6, 10, 12, 15, 24, 25, 27, 28, 50, 66, 80, 92, 146, 147, 150–152
ADC	analog to digital converter	109–112
ADC	digital to analog converter	111
AI	artificial intelligence	12
CAD	computer aided design	6, 27, 68, 92
CFD	computational fluid dynamics	24
CNC	computer numerical control	24, 72
CPB	cardiopulmonary bypass	13
CPS	cyber-physical systems	11
CPU	central processing unit	109
CTB	compliance test bench	94, 96
D2F	digital to frequency	113
EHA	electro-hydrostatic actuator	i, 2, 4, 5, 7, 12, 27, 30, 66, 92, 147, 151, 152
FFF	fused filament fabrication	25, 26, 28
FSS	full-scale span	109–111
IoT	internet of things	12



---

<b>Abbreviation</b>	<b>Description</b>	<b>Page List</b>
NPSH	net positive suction head	139
NRMSE	normalised root mean square error	115, 121, 126, 148
PETG	polyethylene terephthalate	i, 67, 88, 147
PLA	polylactic acid or polylactide	67
PPTB	peristaltic pump test bench	94–96
PwC	PricewaterhouseCoopers	9, 10
R & D	research and development	108, 109, 111
RMS	root mean square	113
RMSE	root-mean square error	115, 121, 126, 134, 137, 143, 148, 149
RTB	resistance test bench	94, 95
RVTB	roller volume test bench	94
USB	universal serial bus	94

---

## Nomenclature

---

The next list describes several symbols and subscripts that will be later used within the body of the document. If the units are not specified in the body of the document the SI units provided can be assumed.

### Number sets

$\mathbb{R}$  Real numbers

### Symbol set A: Physics variables

$\rho$	Material density	[kg/m <sup>3</sup> ]
$\tau$	Torque	[Nm]
$l$	Length	[m]
$P$	Pressure	[Pa]
$Q$	Volumetric flow rate	[m <sup>3</sup> /s]
$t$	Time	[s]
$V$	Volume	[m <sup>3</sup> ]

### Symbol set B: System and pump variables

$\epsilon$	Surface roughness	[mm]
$\omega$	Rotational speed of the motor	[rad/s]
$B$	Bulk modulus	[Pa]
$C$	Compliance / Capacitance	[m <sup>3</sup> /Pa]
$I$	Fluid inertia	[Pa · s <sup>2</sup> /m <sup>3</sup> ]

---

$L$	Inductance	[H]
$N$	Rotational speed of the motor	[r/min]
$NU$	Number of rollers on the specified pump	[-]
$R$	Head loss / Resistance	[Pa/m <sup>3</sup> ]
$r$	Radial distance	[m]
$Re$	Reynolds number	[-]
$w$	Tube wall thickness	[m]

**Symbol set C: Angles**

$\beta$	Contact angle of the pump	[°]
$\phi$	Angle of engagement of the pump	[°]
$\theta$	Rotational angle of the motor	[°]

**Subscripts**

$avg$	The average value of the specified characteristic
$b$	Pertaining to the backplate
$ed$	Pertaining to the roller induced characteristic
$eff$	Pertaining to the total or effective value of a characteristic
$f$	Pertaining to the fluid characteristics
$g$	Pertaining to the gas characteristics
$in$	Pertaining to the inlet of the pump
$i$	Inner value in reference to radius or initial value
$m$	Middle in reference to distance, or mechanical in reference to compliance
$nom$	The nominal value of the specified characteristic
$offset$	Pertaining to the offset distance of the roller
$out$	Pertaining to the outlet of the pump
$o$	Outer value in reference to radius

*res* Denoting a characteristic of the reservoir tank

*roller* Pertaining to the roller

*rot* Pertaining to one rotation of the motor

---

**“The companies - and nations - that act now to seize its promise  
will thrive in the 21st century. Those who are devoted to  
incremental change and fail to engage in smart manufacturing  
will rapidly fall behind.”**

**– Sujeet Chand**

Chief Technology Officer – Rockwell Automation

**– Jim Davis**

Vice Provost - Information Technology – University of California, Los Angeles

---

# CHAPTER 1

---

## Introduction

---

### 1.1 Background

Peristaltic pumps are positive displacement pumps that mechanically imitate the peristaltic process. Peristalsis is a naturally occurring fluid transport mechanism found in living creatures, humans included. It works by partial or total radial contraction of an organ and translation of this contraction across the length of the organ. The contraction reduces the available volume in the lumen at the site of contraction and induces forces on the internal material normal to that of the organ wall in the direction of movement. According to literature most peristaltic pumps currently found operate on the discussed principle.

A peristaltic pump induces flow in a tube by collapsing a selected process tube and translating the occlusion in a manner that resembles peristalsis. This can be done by various methods, the most common being that of a rotary peristaltic pump illustrated in Fig. 1.1. Rotary peristaltic pumps (also referred to as roller pumps, tube pumps, or hose pumps) use a roller to collapse the process tube by squeezing the tube between an outer casing (also referred to as a backplate or backing plate in relevant literature [1, 2]) and the roller. The roller moves over the tube in the direction of transportation, inducing a flow inside the process tube.

The peristaltic pump's ability to move slurries and sensitive material has allowed the peristaltic pump to have a wide range of applications other than medical. These applications include: concrete pumps, micro-dosing pumps, abrasive material pumps, as well as a range of fluid and slurry transport pumps in

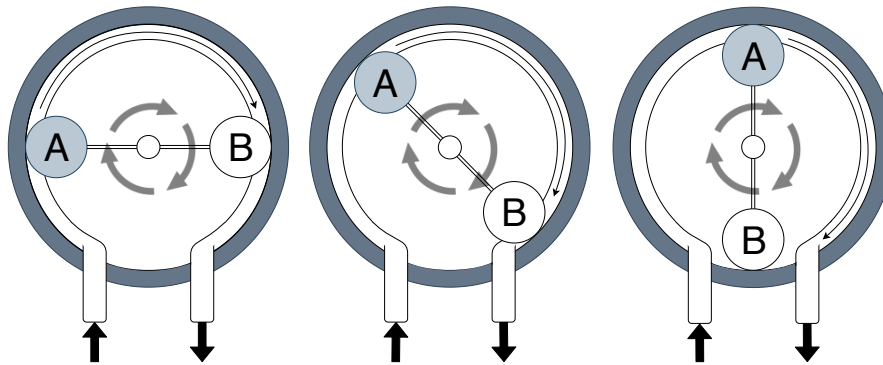


Figure 1.1: Illustration of the operation of a two-roller peristaltic tube pump

the food and beverage industry [3–6]. The wide range of use is due to the unique fact that the tube pump isolates the fluid/slurry being transported from the mechanical components of the pump with the use of a process tube. This allows sensitive materials (such as blood) to be transported without contamination from the mechanical parts, or abrasive materials corroding the mechanical parts. In this case contamination encompasses solid particulates due to mechanical wear, oil and grease for lubrication, or possible chemical reactions with pump components, to name a few.

With full occlusion of the process tube, the inlet and outlet can be completely sealed off from one another. Compression of the process tube could increase the degree to which the inlet and outlet are sealed from each other. This can allow the pump to maintain a static pressure differential between the inlet and outlet while the rollers remain in place. This, in theory, could allow the peristaltic pump to behave similarly to an electro-hydrostatic actuator (EHA).

An EHA is a hydrostatic actuator that does not require an oil reservoir or electro-hydraulic servo valves, as required by conventional hydraulic actuators. The term hydrostatic refers to the capability of maintaining a static pressure during operation, usually by limiting flow, in order to produce a constant displacement on the actuating end of the system. This is achieved by means of closed circuit hydrostatic transmissions, implying that the intake and outlet of the pump are directly connected to the hydraulic cylinder [7].

If the peristaltic pump is to be used as an EHA, the pump must have known characteristics for accurate actuation of a piston. The pump can be characterised to some degree by modelling the pump's input and output, and the response

of the system in which the pump is implemented. Various literature sources provide information of the modelling of pulsatile flow associated with specific types of peristaltic pumps. These sources however fall short when providing a generalised model for roller pumps with varying amounts of rollers. The applicability of a generalised model allows for the peristaltic pump to be designed with a target flow rate, which is an important factor for actuation.

## 1.2 Motivation

The physical foundations which Industry 4.0 and smart manufacturing are built on are: robotics, computers/data centres, logic controllers, and sensors, without even mentioning electricity generation. According to the Information Technology & Innovation Foundation, some of the key technologies enabling smart manufacturing are [8]: sensor technologies, wireless connectivity, data analytics, generative design, computer-aided design, and advanced robotics.

It can be argued that improving certain micro-aspects of Industry 4.0, such as robotic actuators or wireless connectivity, also improves Industry 4.0 and it's future implementation. As an example: Improving the actuator of a robotic manipulator may lead to improved characteristics such as increased accuracy. This in turn may lead to less manufacturing faults and/or faster production times.

Research on these fields lead to an investigation on how to produce inexpensive robotics that are reliable and accurate for use in small businesses and educational institutions. The investigations included comparing robotic actuators, sensors, and materials. Having stated this, it can be concluded that actuators and sensors would make up the majority of the cost. However, materials have a unique problems of their own, as manufacturing techniques could vary for the same part [9].

Hobbyists and educational institutions give valuable insight into some of the cheapest produced robotic manipulators available with the use of additive manufacturing and inexpensive actuators. In this study additive manufacturing is commonly referred to as three dimensional (3D) printing, and is not to be confused with the material jetting process with the same name. 3D printing also implies that the manufacturing technique remains rather constant. The reduced cost is, however, offset by a lack of control and accuracy. A common problem mentioned in the 3D printed robotics literature is backlash and wear on the gears associated with the power transfer method. This leads to an investigation



of other methods of transferring power across the manipulator, as improving the power transmission could lead to improved accuracy and reduced backlash.

The most common power transfer methods include: gears, belts, chains, pulleys, hydraulics, and pneumatics. This study found that hydraulics and pneumatics were severely underrepresented in 3D printed robotics. This is due to complexities that arise for parts that require either a large strength or a high quality finish. Such parts would include impellers found in kinetic pumps and compressors, or the gears, lobes, and other mechanical parts required for positive displacement pumps. However, one positive displacement design stood out from the rest. The unique design of a rotary peristaltic pump makes it a suitable candidate for additive manufacturing.

3D printed hydraulics and pneumatic actuators could advance 3D printed robotics. The introduction of hydraulics and pneumatics for 3D printed robotics will allow for the comparison of a larger variety of power transmissions in 3D printed robotics, increasing the possible uses of inexpensive robotics. The peristaltic pump has desirable characteristics that could allow it to be used as a 3D printed EHA.

With the ability to 3D print a peristaltic pump comes the ability to customise the peristaltic pump to the user's needs. For this reason, it is desirable to model the pump based on the pump's design, allowing users to model their individual pumps. This requires a first-principle approach to create a design-based model of the rotary peristaltic pump.

### **1.3 Problem statement**

There is a need for a model-assisted design procedure for a 3D printed peristaltic pump. The design procedure should not only accurately account for the effects that the choice of system components have on the pump's performance, but the effects of the 3D printing process. The material choice should thus also be accounted for.

### **1.4 Objectives and methodology**

The main objective of this study is to develop a model-assisted design approach for a 3D printed peristaltic pump. The model should allow for the characterisa-

tion of a peristaltic pump prior to its construction in order to design a pump with desired characteristics (such as flow rate).

This is done as an attempt to ultimately provide an alternative actuation method for 3D printed robotics. The model-assisted design approach is to be used for further studies of 3D printed peristaltic pumps applied as EHAs. The following objectives need to be addressed by this study:

1. Modelling the dynamics of a roller-type peristaltic pump.
2. Designing and manufacturing a peristaltic pump with desired characteristics with the use of the model, capable of being 3D printed.
3. Designing and constructing a test bench for characterising the performance of the peristaltic pump and for model validation purposes.
4. Testing the pump for model validation and further recommendations.

Fig. 1.2 portrays a conceptual overview of the research methodology to be followed in the study.

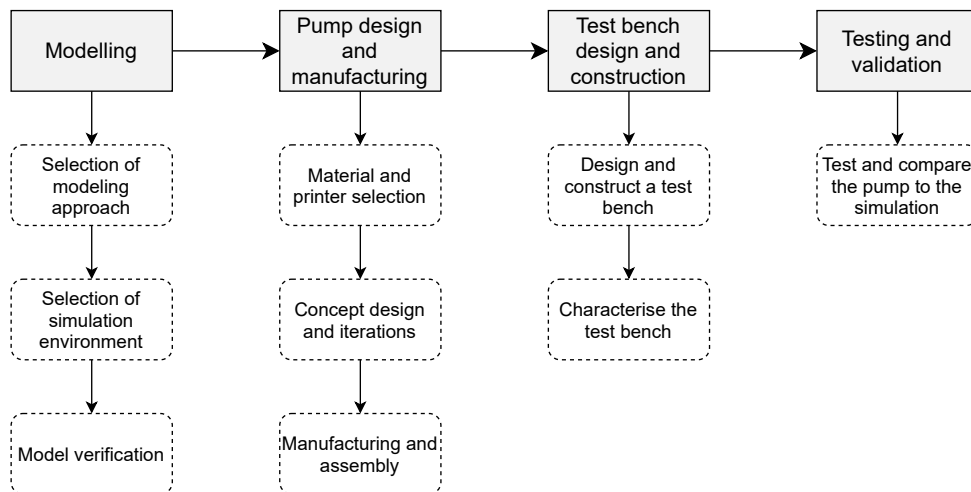


Figure 1.2: Conceptual overview of the research methodology followed in this study summarising the objectives (solid-line) and methodology (dashed-line)

In order to complete the objectives listed for this study, the following methodology will be followed:

1. Creating a model to describe the pump characteristics:
  - (a) Create a numerical analysis of the geometric relations pertaining to current peristaltic pump designs in a computational software environment.
  - (b) Design a lumped parameter model of the system, with the model parameters derived from the numerical analysis of the flow, independent of motor characteristics.
  - (c) Verify the model in order to ensure that it behaves as expected and depicts realistic values.
2. Designing and manufacturing of a peristaltic pump based on desired values derived from the model:
  - (a) Select appropriate thermoplastic materials and printing method for 3D printing.
  - (b) Create conceptual designs using a computer aided design (CAD) program and iteratively improve the designs until the design meets all required criteria.
  - (c) Manufacture pump parts using 3D printing and assemble the peristaltic pump.
3. Designing and construction of a test bench to validate the model:
  - (a) Design and construct a test bench capable of testing the pressure pulsations, volume displacement, and maximum working pressures of the peristaltic pump.
  - (b) Test and characterise the test bench variables (such as resistance and compliance) to minimise possible deviation of the simulation.
4. Testing and validation of the model and simulation:
  - (a) Test the pressure characteristics and flow characteristics of the pump under varying operational conditions, such as motor speed.
  - (b) Compare the simulation and model values to the experimental values via data analysis.

## 1.5 Outline of the dissertation

Chapter 2 discusses the relevant literature used to make design and modelling decisions. It includes a brief overview of the literature in the literature review section, followed by in-depth discussions of the relevant literature sources before concluding with a critical review of the literature.

Chapter 3 discusses the modelling of the peristaltic pump. An in-depth investigation into the pulsatile flow attributes of the peristaltic pump is given with accompanying volume displacement approximation methods. The lumped parameter model, which describes the pump's behaviour to external inputs and operational circumstances, is then described. The models are then used to simulate the pump's pressure pulsations with given parameters as inputs for validation.

Chapter 4 discusses the relevant design aspects of the peristaltic pump in conjunction with additive manufacturing techniques. Using a hypothetical design requirement, the design specifications in this chapter are derived from the modelling in Chapter 3, which is used to validate the model in Chapter 6. The chapter ends with the manufacturing of the pump. The CAD drawings of the design are included in Appendix C.

Chapter 5 discusses the test bench design and testing methods used for validation. This chapter includes measuring physical aspects of the test bench pertaining to the simulation. The sensors, tolerances, and limitations are mentioned prior to the discussion on the validation method.

Chapter 6 discusses the experimental test results and the comparison thereof to the simulation results. The volume approximation is discussed first with comparison to the roller volume displacement tests. The modelled flow rate is then compared to the experimental flow rate over varying motor speeds. Similarly, the simulation's pressure response of the inlet and outlet line are compared across varying motor speeds to the experimental results. Lastly, the pump's maximum and minimum working pressures, along with the hydrostatic pressure tests, are discussed.

Chapter 7 discusses the findings of this study with recommendations on improvements for future studies into the topic. The characteristics of the peristaltic pump that enable it to be used as an EHA, as well as the use of the model-assisted design approach, are discussed in this section.

## CHAPTER 2

---

### Literature study

---

#### 2.1 Introduction

This chapter begins with a literature survey in which relevant literature is discussed. Following the literature survey is a more in-depth discussion of research related to this study.

The in-depth discussions begin with additional information pertaining to Industry 4.0 and its relevance to this study. Thereafter the discussion shifts with the focus on peristaltic pumps and their designs. This is to gather additional information pertaining to the pumps and their working principles, prior to reviewing modelling methodologies. The modelling techniques used in relevant literature are discussed with a focus on models that use first principle approaches, realistic assumptions, and achieved accurate results. Aspects pertaining to additive manufacturing and relevant research fields are discussed thereafter.

The chapter concludes with a critical review of the literature presented. Literature that will be focussed on are briefly discussed along with the motivation for the focus.

## 2.2 Literature survey

The information regarding Industry 4.0 was gathered from auditing and assurance companies as well as management consultancies that specialise in consulting, risk and financial advisory, and innovation management. These companies include: PricewaterhouseCoopers (PwC), Deloitte, and the Boston Consulting Group. The technical reports and white papers published from these companies indicate problems that limit the implementation, or the speed of implementation, of Industry 4.0.

A good source of information regarding pumps and their applications is M. Volk's handbook: "Pump Characteristics and Applications" [10]. The references made to pumps and their applications will be sourced from this book. This includes the working principles and definitions. Volk gives a good classification of hydraulic pumps (courtesy of the New Jersey Hydraulics Institute) which simplifies pump selection based on pump characteristics.

Descriptions of different types of rotary peristaltic pumps, as well as their applications, are given by J. Klespitz et al. [11]. However, no mention is made of adopting the peristaltic pump as an electro hydrostatic or hydraulic actuator.

A. Loth and R. Förster [12] describe a micro roller pump for micro dosing. Reference is also made to some of the common design aspects of the tube/hose type peristaltic pump. These design aspects are still proven useful when designing a peristaltic pump, however, E. N. Aitavade et al. [3] give a better and more in-depth indication of these aspects. Focus will thus be placed on Aitavade.

Reference is made to available patents of peristaltic pumps regarding the geometry of the pumps, as literature regarding the design facets of peristaltic pumps tend to be scarce.

The first principles methods used to describe systems and their response is outlined by D. C. Karnopp et al. [13], and E.O. Deobelin [14]. Information specific to the modelling of peristaltic pumps is outlined by the works of G. Wright [15] and F. Moscato et al. [16].

The first principles methods are outlined with specific reference to the modelling of hydraulic systems and their electrical analogues. This includes the modelling theory for calculating the resistance incurred from moving fluids, inertia caused by the rate of change of the flow rate's acceleration, and the effective

compliance of the fluid and system in which it is contained.

B. Redwood et al. [17] describe the technologies and materials used in additive manufacturing. Redwood indicates the unique attributes and the design limitations of each of the additive manufacturing technologies. Due to the rapid rate at which these technologies are improving some technologies may not be present. H. Bikas et al. [18] reduces these technologies into brief summaries with some additional technologies with merit. Due to the higher relevance, focus is placed on the work of Bikas et al. The implications that additive manufacturing techniques have on designing, manufacturing, and even social aspects are reviewed by H. Lipson et al. [19] but are not discussed in detail in this study.

P.A. Kobryn et al. [20] shortly describes the past progress that has led to additive manufacturing technologies today, with emphasis placed on the aerospace industry. The manufacturing accuracy regarding three dimensional (3D) printing, specifically part tolerance, is taken into consideration with the work of U. Berger [21]. The wear of thermoplastics is described by the work of W. Brostow et al [22].

The following in-depth discussions focus on the most important aspects from the aforementioned literature. Other literature sources are also included, where applicable, in order to acquire a broader knowledge on the topic being discussed.

## 2.3 Industry 4.0

The German national strategic initiative 'Industry 4.0', first implemented in 2011, aims to increase the economic output of Germany. This is done by means of digitisation and the interconnection of products, value chains and business models with the use of smart factories [23]. The possible effects on the design, manufacturing, operation, and service of production systems could have a large impact on economic productivity. Estimates suggest productivity gains of 5 to 8 % totalling € 90 billion to € 150 billion over a span of ten years for the German economy [24].

A global survey conducted by PwC in the year 2016 suggests that lack of digital culture and training, insufficient talent, and high financial investment requirements are the biggest challenges facing the adoption of Industry 4.0 practices [25]. The possible effects of this could imply that smaller companies, or even countries with emerging markets, might fall behind on the implementation

of industry 4.0 practices and lose competitiveness. Addressing the high financial requirements of Industry 4.0 practice implementation may cause a wider adoption of Industry 4.0. This in turn increases the likelihood of a larger population becoming familiar with Industry 4.0 practice, effectively increasing the size of available talent pools.

Industry 4.0 is a response to the rise of international competition with production of parts with marginally less quality at better costs. The initiative takes advantage of technologies associated with the fourth industrial revolution as a means of preparation. A large focus of this initiative is to supply highly customised products with minimal lead time. This incorporates smart manufacturing, in which intelligent and customised products autonomously lead their way through the supply chain [26].

Deloitte defines the previous and current industrial revolutions based on the large scale impact that the advancement of a specific technology has on manufacturing sectors. As a result the current and previous industrial revolutions can be identified as four main revolutions. The first two revolutions were introduced with technologies that allowed for utilisation of steam power, and the creation of assembly lines powered by electricity later on. The third and most recent revolution, indicated by the first programmable logic control system in the year 1969, further increased production output by automating simple tasks in sequence [27, 28].

The revolutionary stages may differ depending on what is considered significant change or advancement in manufacturing methodology and technologies. This outlook however describes and defines the technologies underlying Industry 4.0. The first industrial revolution, indicated by the first mechanical weaving loom in the year 1784, was brought about with the ability of harnessing steam and water power. The second industrial revolution is indicated by the first assembly line in the year 1870. Assembly lines made use of electrical energy and the division of labour, allowing for mass production of parts and products.

The third industrial revolution, along with the computing advancements made with Moore's law, laid the foundation for the fourth and current industrial revolution with the aid of sensor technology. Industry 4.0 encapsulates the integration of cyber-physical systems (CPS) with the manufacturing floor. The term 'Cyber-Physical System' is used for a system comprising both physical components (such as robotics and sensors) and generative information. The information retrieved from the system is used for statistical analysis and optimisation, with focus on autonomy. Currently, Industry 4.0 and smart manufacturing are the



latest areas of development and research in the global industrial sector. This comes with the introduction of developing technologies, such as advanced analytics with the use of ‘Big Data’ and artificial intelligence (AI), interconnectivity with the use of the internet, and the internet of things (IoT) [27, 29, 30].

At present the use of robotics to automate is unprecedented and new technologies are being developed on a regular basis. With robotics and sensors centred at the heart of current global industrial endeavours, such as Industry 4.0 and smart manufacturing, improvements made to robotics in general can indirectly impact these endeavours favourably. Reducing the cost of robotics could lead to a wider adoption of these technologies, influencing both the industrial and educational sectors.

## 2.4 Peristaltic pumps

M. Volk [10] indicates that positive displacement pumps, such as the peristaltic pump, have some useful application criteria, including: high pressure, high efficiency, fragile solids handling, seal-less pumping, accurate and repeatable flow measurement, and constant flow/variable system pressure to name a few. These characteristics of positive displacement pumps make them ideal for use as an electro-hydrostatic actuator (EHA). Volk also states that engineers tend to have a preference for centrifugal pumps over their positive displacement counterparts. This is due to less pulsations and lower maintenance with fewer moving parts, such as check valves and loaded bearings. Positive displacement pumps do, however, have practical uses, and pump selection remains dependent on the application.

The restrictions caused by additive manufacturing shortfalls allow for the peristaltic pump and the diaphragm pump to be considered for 3D printed pumps. This is due to the use of other external parts which mitigate the shortfalls of additive manufacturing. These parts include the collapsible tube of the peristaltic pump, and the diaphragm membrane and check valves for the diaphragm pump. Volk compares the characteristics of these pumps, and shows that the diaphragm pump has a larger pulsation quality (which is not a desirable quality for actuation). Due to the pulsation quality, minimisation of the use of external parts, and the possibility of being used as an EHA with reversible flow, the focus is placed on the peristaltic pump.

The first occurring patent for a peristaltic pump was a hand operated single-roller tube pump produced in 1855 by Rufus Porter and J. D. Bradley in the

United States and named "The elastic-tube pump" [31, 32]. Subsequent patents were filed in later years but the peristaltic pump only gained fame when introduced into the operating room as a blood pump with the work of J. Gibbon that started in 1937. Gibbon devoted his life to designing a heart-lung machine, capable of oxygenating and circulating the blood of a patient. His work along with the vast amount of preluding work which lead to his achievements would in turn save many lives [33].

Although described as having been the most commonly used pump for cardiopulmonary bypass (CPB), its popularity has been declining due to improvements in its competitors, such as the centrifugal pump [32]. A study conducted by B.L. Mejak indicated that roller pumps were used as the main blood pump by 44 % of correspondents (chief perfusionists in USA cardiac surgical centres) compared to 49 % using centrifugal pumps in the year 2000 [34]. Due to its versatility however, the peristaltic pump has also gained more uses, and continues to do so in non-medical fields as new technologies develop.

The use of a flexible membrane to transport the fluids through the pump allows for changes of the membrane to impact the uses of the pump, while maintaining the same pump design. This allows the same pump to accompany a wide variety of materials by simply replacing the membrane.

The patent of I.J. Phallen [35] states that peristaltic pumps can be classified into two main categories, namely; linear peristaltic pumps and rotary peristaltic pumps. Phallen goes on to state that rotary peristaltic pumps tend to have shorter service times due to the harsher deformation of the tubes.

The linear peristaltic pumps referred to in Table A.1, Appendix A, make use of more complex mechanics to collapse a process tube in a straight manner. The trade off in complexities is a reduction in wear of the process tube. The rotary pumps all make use of similar mechanics: Rollers, driven by an electric motor, collapsing a process tube. The rotary pumps can be classified into two groups based on their design. Those with a backplate and those without. The backplate allows for a forced occlusion, meaning that the tube is forced shut between the roller and backplate. Those without a backplate have the process tube stretched across the rollers indicated in N.G. Kling's [2] patent and shown in Fig. 2.1 (patent expired).

The design with a backplate allows for higher pressures and less leakage from the high pressure side to the low pressure side. This method could harm sensitive materials as a larger shear force is applied to the fluid. The forces applied

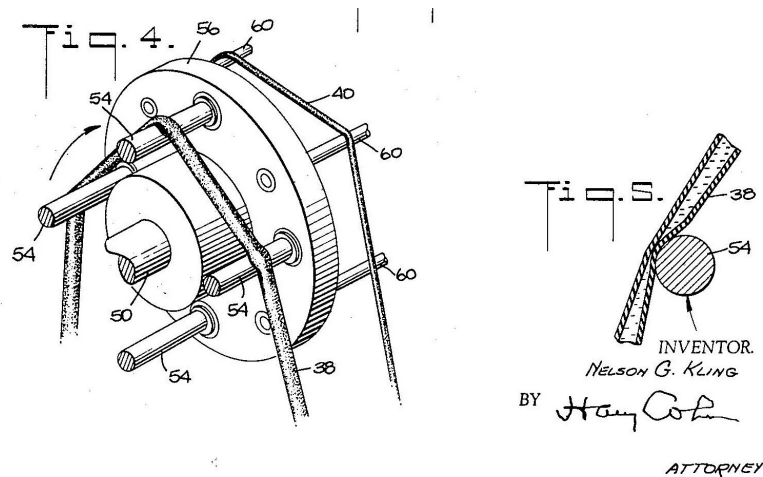


Figure 2.1: Design illustration of Kling's peristaltic pump design without a backplate [2]

to the tube will also shorten the process tube's life span as larger deformations of the tube occur under larger forces. The design without the backplate has a passive safety as a result of the reduced pressure capabilities. As the process tube is not forced shut, if a large enough pressure occurs at the inlet or outlet, it can overcome the collapsing force of the rollers.

Since this study focusses on the use of a peristaltic pump for hydraulic actuation, higher pressures are needed from the pump. For this reason, focus will be placed on the rotary peristaltic pump with a backplate. Rotary peristaltic pumps (specifically those with backplates) have different designs based on their operational requirements. Although similar in design, the tube type pump varies from the hose pump.

The hose pump is designed to handle higher pressures. This implies the casing and process tube have to be stronger than that of the tube pump. The differences the hose pump exhibits from a tube pump can be listed as: thicker tubes (often called hoses), lubricant filled casings, larger pump size, and slower rotational speeds. To accommodate the larger forces, hose pumps tend to be larger than tube pumps and are made out of stronger materials. The single roller design with a 360 degree casing is more popular among hose pumps. Tube pumps often have a minimum of two rollers and can have as many as 12 rollers [3].

Some of the tube types available are [3]: Silicon, Autoprene, Viton, Tygon,

Prothane II, Vinyl- and Fluor polymer. These tube types alone allow a pump to handle various foods, beverages, concentrated acids, and inorganic materials with working temperatures ranging up to 220 °C, depending on the tube material selection.

One of the most common aspects associated with peristaltic pumps is their pulsatile flow. The pulsatile flow is caused by the roller engaging and disengaging the tube repeatedly. In some scenarios this is advantageous, such as with blood pumps as it imitates the pulsation of a heartbeat to a small degree [15]. In other cases where consistent flow is required, pulsation dampers are available.

When a roller comes into contact with the process tube a force is applied to the tube causing its collapse. The collapse of the tube results in a diminishing volume. The fluid within the tube needs to be displaced in order to accommodate this reduction in volume. This displacement of fluid induces flow within the process tube, opposing normal flow.

The same mechanics are present at the pump outlet but in reverse as the volume displaced by the roller is now removed and the volume needs to be replaced with surrounding fluid as the pipe returns to its original shape. The induced flow at the outlet also opposes normal flow but decreases pressure instead of increasing it. An account of these mechanics are discussed in more detail in the Modelling theory section of this chapter with the work of Moscato et al. [16].

Most of the rotary peristaltic pumps show similarity regarding symmetrical design around one axis (described as the  $y$ -axis for demonstration purposes). This usually implies that the inlet of the pump is angled at the same angle as that of the outlet. This also implies reversing the motor would result in identical flow to that of normal operation but in reverse. This symmetry is indicated by Fig. 2.2.

Peristaltic pumps can be powered by a variety of motors. Most commonly the pumps are powered by motors with a high degree of control, such as servo and stepper motors. Servo motors have a more constant torque to motor speed curve, and are commonly found in robotics. Stepper motors have the advantage of being cheaper than their servo counter-parts (both the motor and the motor driver) and have a high torque at low motor speeds. For this reason stepper motors are more prevalent in low cost 3D printed robotics.

A number of recent articles indicate a newer use of piezoelectric peristaltic micro-pumps such as on-chip cooling and micro dosing. The literature sources

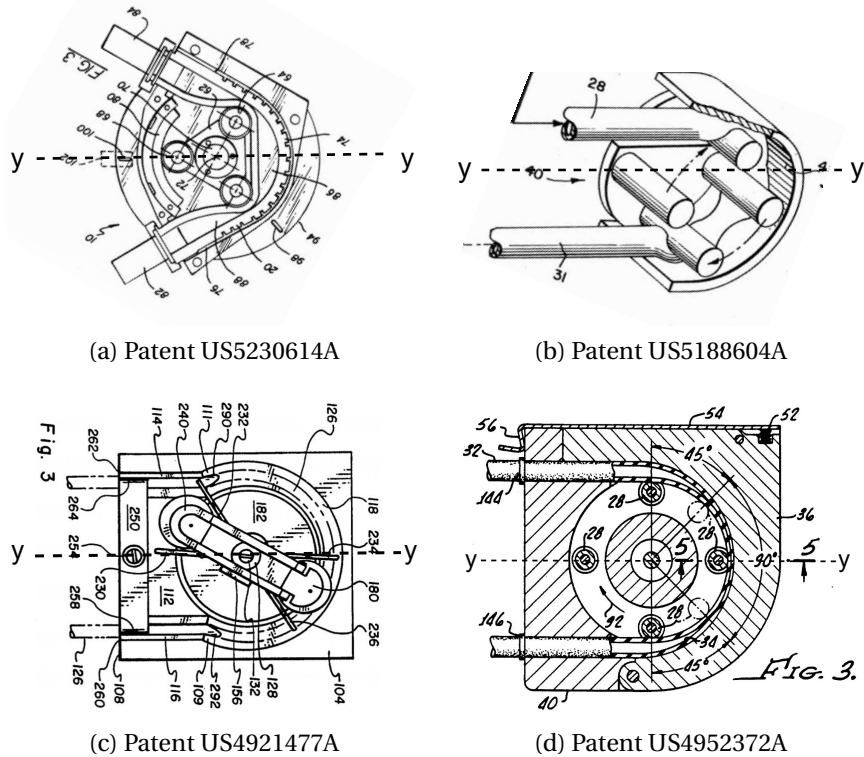


Figure 2.2: Symmetry similarity found on rotary peristaltic pumps referencing designs of (a) B. Huber [36], (b) R.P. Davis [37], (c) J.L. Orth [38], (d) Zanger et al. [39]

regarding these micro-pumps are not applicable to this study, as they are linear peristaltic pump types, however, they are worth mentioning for future researchers. A. Geipel [40] and F. Thoma et al. [41] describe peristaltic micro-pumps for optimized and automated drug delivery. G. Beckers et al. [42] describe a modelled design of a quasi-static peristaltic piezoelectric micro-pump. Qiao Lin et al. [43] simulate a peristaltic micro-pump and K. Tatsumi et al. [44] develop a numerical study on the fluid-flow characteristics of a micro-pump.

## 2.5 Modelling theory

Karnopp et al. define models of systems as "...simplified, abstracted constructs used to predict their [the systems'] behaviour" [13]. Models of systems can be derived from the system's response to certain external inputs, also referred to as data-driven models. An alternative which is advantageous when data of the

system is limited is the first-principles approach, where the system is modelled based on the underlying physics [45].

Data-driven models are cheaper to produce in terms of labour and are reliably created, meaning that the model, which is based on the actual system's response, is relatively accurate in terms of the specific system. The problem with data driven models is that they are specific to the system on which they are modelled. This implies that if certain variables in the system were to change, the model might no longer remain accurate. This method of modelling also requires data from the system, which implies that the system is constructed before the model.

First-principle modelling requires in-depth knowledge of the system and the physics that describe it. These models can be time consuming to create as the formulation of the models are mathematical in nature. The advantage of first-principle models are that they can be adapted to different systems by changing known parameters in the model. They also offer a preview of how the system will react to inputs prior to the system being built. The drawbacks, however, are that accuracy is not always guaranteed, and can only be measured by comparing the model to the actual response of the system.

The modelling approach can be influenced by the amount of information that is known of the system. Further classification can be given by the knowledge of what is done to the information in order to acquire a mathematical model. P. Czop et al. [45] classify modelling into three distinct groups, namely: a black-box approach, a grey-box approach, and a white/transparent-box approach. These classifications are made based on the information pertaining to the structure and parameters of the model. The white-box approach indicates that a good grasp of the processing of information is known and indicates first-principle modelling. The black-box approach indicates that it is not very clear on how the information is processed and indicates a data-driven model.

The black-box approach is based on regression techniques, and is commonly found in machine learning. The white-box approach, also referred to as analytical modelling, commonly utilises lumped parameter models to define the working system. The grey-box approach is a mixture of the first principles and data driven modelling [45].

S.L. Weinberg et al. [46] review methods of modelling peristaltic pumping in both inertia-free flow and inertial flow. This is done by varying the densities of the working fluid, with the inertia-free flow having a Reynolds value less than

1 ( $\therefore R_e < 1$ ). Weinberg et al. model an infinite periodic wave train transporting fluid from one reservoir to another with the following conditions: (i) the peristaltic wave must be progressive and periodic; (ii) there must be an integral number of wavelengths between reservoirs; (iii) the pressure difference between the reservoirs must be constant. Similarly, T.W. Latham [1] models a two dimensional sinusoidal wave propagation pertaining to that of a peristaltic pump with a low Reynolds number.

F. Moscato et al. [16] explicitly models a two-roller tube type roller pump with the use of first principles. The modelling includes a lumped parameter model as shown in Fig. 2.3 and is tested at flow rates with inherently larger Reynolds numbers than that of Weinberg et al. The first principle methods Moscato uses align with those of D.C. Karnopp [13] and E.O. Doebelin [14].

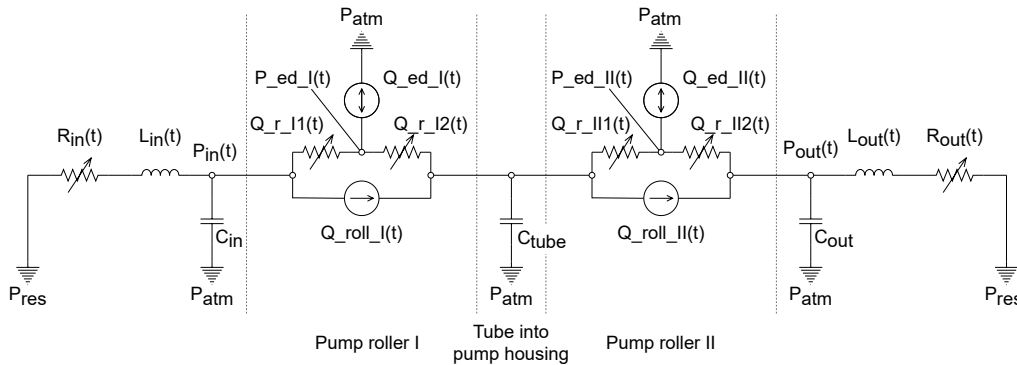


Figure 2.3: A lumped parameter model diagram of a two-roller peristaltic pump proposed by Moscato et al. [16]

Moscato indicates that the pressure pulsation caused by the roller coming in and out of contact with the tube is due to the pump's roller displacing a volume as it occludes the process tube. To mitigate confusion, occlusion refers to the partial or total collapse of the process tube. This volume is measured as the roller comes into contact with the tube ( $\theta = 0$ ) to where the tube is fully collapsed ( $\theta = \alpha$ ). These values of the volume of the roller ( $V_r$ ) are then cubically interpolated over the angle of the motor ( $\theta$ ) to give a polynomial. The polynomial, indicated in Fig. 2.4, thus describes the volume displacement of the roller in terms of the angle of the motor. It is used to give indication of the flow produced as  $\int_0^\alpha Q_{ed}(\theta) d\theta = V_r(\theta)$ . Here  $\theta = \omega t$  where  $\omega$  is the rotational speed of the motor and  $t$  represents the time variable. The flow can thus be found by differentiating the volume over time as indicated in (2.1).

$$Q_{ed}(\theta) = \frac{dV_r(\theta)}{dt} \quad (2.1)$$

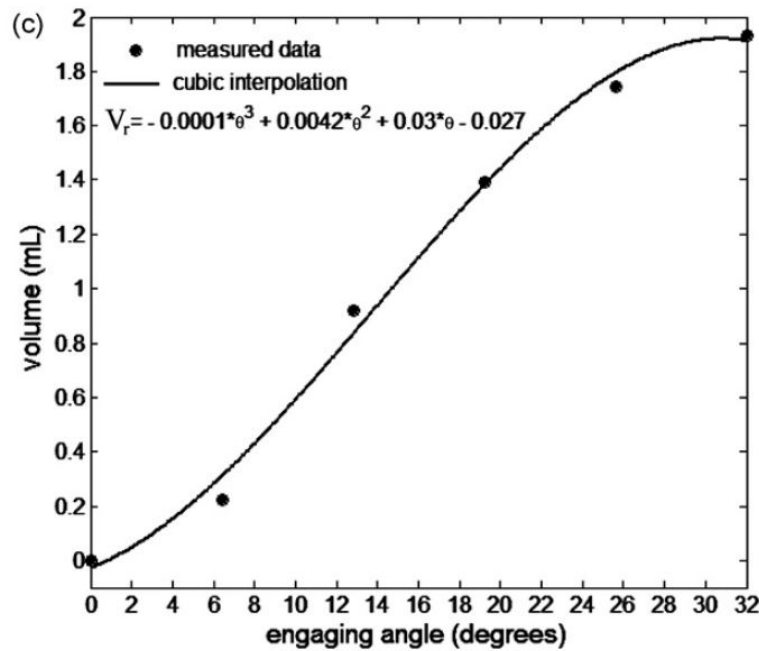


Figure 2.4: Measured values of a roller's volume displacement during engagement with a process tube for a roller type peristaltic pump (reprinted with permission)<sup>1</sup>

Moscato does not however model the volume displaced by the roller. Instead, a model is created based on experimental data and polynomial fitting. This implies a grey-box modelling approach as the model is a combination of both analytical and data-driven modelling. Moscato uses a third degree polynomial to sufficiently define an equation for the roller volume displacement specific to the pump he used with the volume equation  $V_r(\theta) = 0.0001\theta^3 + 0.0042\theta^2 + 0.03\theta - 0.027$  for clarification. The third degree polynomial, however, suggests a negative volume displacement of 0.027 mL at  $\theta = 0^\circ$ . This could imply a higher polynomial order might provide better results. However, Moscato may have been limited by the small amount of sample points, or found the polynomial to be sufficient enough for their purposes.

<sup>1</sup>Reprinted from Medical Engineering & Physics, Vol. 30, F. Moscato et al. [16], Pressure Pulsations in Roller Pumps: A Validated Lumped Parameter Model, Pages 1149–1158, Copyright (2008), with permission from Elsevier.



G. Wright [15] confirms many of the modelling decisions made by Moscato in reference to the pulsations of a heart beat. Wright states that the pulsatile power (which is determined from pulsatile flow) is directly dependent on the blood inertia and arterial resistance, and indirectly dependent to arterial compliance and peripheral vascular resistance. Wright goes on to state that these relationships are time dependent. These characteristics can be modelled mathematically, as Moscato had done, by utilising variables pertaining to the effective fluid resistance, fluid inertia, and compliance of the system.

These hydraulic characteristics can be modelled as an electrical analogue, for simplicity, regarding the lumped parameter model. This is also present in Moscato's model with pressure relating to potential, and flow to current. This would imply that the viscous friction is equivalent to resistance, the fluid inertia to inductance, and the compliance to the capacitance. According to D. C. Karnopp et al. [13], pressure changes due to the inertia, compliance, and friction of a fluid can be modelled respectfully as:

$$\Delta P_I = I\dot{Q}, \quad (2.2)$$

$$\Delta P_C = \frac{1}{C_f}\Delta V, \quad (2.3)$$

and

$$\Delta P_{R_f} = R_f Q. \quad (2.4)$$

$\Delta P_I$  refers to the pressure change caused by the fluid inertia  $I$  and is directly proportional to the change in flow rate of the fluid  $\dot{Q}$ .  $\Delta P_C$  refers to the pressure change caused by the compliance of the fluid in relation to the change in volume  $V$ . The compliance of the fluid is, in this case, referring to the compressibility of the fluid.  $\Delta P_C$  is thus directly proportional to the change in volume with regards to the fluid.  $\Delta P_{R_f}$  indicates the change in pressure caused by the viscous friction  $R_f$  and is directly correlated to flow of the fluid  $Q$ .

The symbols  $R$  and  $C$  are used here as they refer to the same phenomena in both fluid and electrical circuits, that is:  $R$  represents the resistance to the flow/current, and  $C$  the storage of potential energy. To mitigate confusion between the fluid symbols and their electrical counterparts, the symbols specific to the fluid variables are discussed in this section and are subscripted with  $f$  (fluid) and  $_{eff}$  (effective). The symbols specific to the electrical analogue of the fluid variables are only applied in Chapter 3, with the difference reiterated there.

Karnopp goes on to indicate that the compliance, inertia, and viscous friction (assuming laminar flow) of a fluid in a rigid pipe segment can be calculated respectively using (2.5), (2.6), and (2.7).

$$C_f = \frac{V_0}{B} \quad (2.5)$$

$$I = \frac{\rho_f l}{A} \quad (2.6)$$

$$R_f = \frac{128\mu l}{\pi d_i^4} \quad (2.7)$$

The compliance of the fluid  $C_f$  is inversely proportional to the bulk modulus of the fluid  $B$  and directly proportional to the initial volume  $V_0$ . The fluid inertia is directly proportional to the density  $\rho_f$  and the length of the tube segment  $l$ , and inversely proportional to the area of the tube's cross section  $A$ . The friction is directly proportional to the fluid's viscosity  $\mu$ , the length of the tube segment  $l$ , and inversely proportional to the inner diameter of the tube  $d_i$ . The compliance value  $C_f$ , however, is only sufficient for fluid contained in rigid tubes. This is problematic as the peristaltic pump has a section of compliant tubes. Fortunately, Karnopp also indicates that the compliance of tubes can be calculated as:

$$C_m = \frac{2r_0 V_0}{wE}. \quad (2.8)$$

Here the mechanical compliance value  $C_m$  of the tube can be calculated with the initial radius of the tube  $r_0$ , the initial volume of the tube segment  $V_0$ , the thickness of the tube wall  $w$ , and the modulus of elasticity of the tube material  $E$ . The total compliance (or effective compliance)  $C_{eff}$  pertaining to the fluid and its container can then be determined by summing the fluid and mechanical compliances as in (2.9). As the peristaltic pump should be able to pump a large variety of fluids, including gasses it may be worth noting the compliance (compressibility) for gasses. The compliance of a gas can be calculated with the density of the gas  $\rho_g$ , the speed of sound in the gas  $c$ , and the initial volume of the gas indicated in equation 2.10.

$$C_{eff} = V_0 \left( \frac{1}{B} + \frac{2r_0}{wE} \right) \quad (2.9)$$

$$C_g = \frac{V_0}{\rho_g c^2} \quad (2.10)$$

The pressure caused by elevation difference (such as that in the reservoir) with regards to fluids can be calculated with the fluid density  $\rho_f$ , gravitational acceleration  $g$ , and difference in elevation  $h$  as:

$$P_h = \rho_f g h. \quad (2.11)$$

These equations supplied by Karnopp are for idealistic fluids and tube sections, usually associated with infinite lengths. Due to the idealistic assumptions made with these equations, better approximations can often be made. The speed of the fluid should also be taken into account as the calculation for viscous friction supplied by Karnopp in (2.7) only hold true for laminar flow.

The flow of a viscous fluid in a tube can be characterised by the unitless Reynolds number associated with the velocity  $v$ , viscosity  $\mu$ , and hydraulic diameter  $d_i$  of the tube as in (2.12). The Reynolds number can define the flow of the fluid to be laminar ( $Re \leq 2100$ ), transient ( $2100 < Re \leq 4000$ ), or turbulent ( $4000 < Re$ ) [47].

$$Re = \frac{\rho_f d_i v}{\mu} \quad (2.12)$$

E.O. Doebelin [14] states that the end affects of real capillary tubes for laminar flow can be taken into account by adjusting the laminar resistance equation supplied by Karnopp with association of the Reynolds number as:

$$R_f = \frac{128\mu l}{\pi d_i^4} \left( 1 + 0.0434 \frac{d_i}{l} Re \right). \quad (2.13)$$

It is worth noting that oscillating flow changes the fluid inertia significantly. This occurs as the velocity profile for steady flow has a parabolic shape, where the volume of fluid with respect to oscillating flow is treated more like a rigid body. This results in the effective mass being 4/3 of the actual mass [14] and implies that the fluid inertia for oscillating flows can be calculated as:

$$I = \frac{4\rho l}{3A}. \quad (2.14)$$

The head loss associated with the skin friction in the tube can also be calculated by means of the Darcy–Weisbach equation (2.15) with the SI unit as metres. The Darcy friction factor  $f$  can be found with the associated relative surface roughness of the tube and the Reynolds number of the fluid on Moody's diagram.

$$h_f = f \frac{l}{d_i} \frac{v^2}{2g} \quad (2.15)$$

For laminar flows this factor can be calculated in (2.16). The Colebrook-White equation calculates this factor for turbulent flows by iteratively solving for  $f$  in (2.17) and takes into account the surface roughness  $\epsilon$  of the tube. Other equations such as the Hazen-Williams equation and the Manning equation can also be used to estimate the head loss, however, Menon mentions that they encompass larger uncertainties than that of the Colebrook-White equation, but are easier to solve [47].

$$f = \frac{64}{Re} \quad (2.16)$$

$$\frac{1}{\sqrt{f}} = -2 \log_{10} \left( \frac{\epsilon/d_i}{3.7} + \frac{2.51}{Re\sqrt{f}} \right) \quad (2.17)$$

The effective fluid resistance is characterised by the pressure drop over the system divided by the flow rate as in (2.18) with  $\Delta P$  as the difference in pressure and  $Q$  as the flow rate. This equation is especially useful when determining the resistance of a system experimentally.

$$R_{eff} = \frac{\Delta P}{Q} \quad (2.18)$$

Other than skin friction (friction caused by the fluid layer closest to the tube wall) in straight pipes, it is likely that the system in which the pump is used will contain valves or fittings (such as tees and elbows). Minor head losses are associated with valves, fittings, and orifices which should be taken into account when modelling hydraulic systems. Both S. Menon [47] and M. Volk [10] indicate that minor head losses associated with bends and reductions can be calculated with the formula:

$$Hf = K \times \frac{v^2}{2g}, \quad (2.19)$$

where  $Hf$  indicates the minor head loss,  $K$  the resistance coefficient, and  $v$  the velocity of the fluid. The effective friction is then summing the minor head losses associated

associated with the skin friction ( $R_{eff} = h_f + Hf$ ). These values can be inserted into an electrical analogue lumped parameter model with  $I \equiv L$ ,  $C_{eff} \equiv C$ , and  $R_{eff} \equiv R$  for each tube segment.

It should be noted that experimental tests that characterise a systems resistance, inertia, and compliance are favoured over theoretical values. This is due to large inaccuracies that may occur due to non-ideal conditions. One such example is the effect of entrained air on the compliance of the system, which

has the potential to create a value with an order of magnitude difference to the theoretical value, with roughly 1% of the volume as entrained air.

A noteworthy mention on the modelling of peristaltic pump is the work of G. Formato et al. [48]. Formato et al. model a single roller hose pump with the use of computational fluid dynamics (CFD) software with acceptable accuracy which give an indication to the high pressure pulsations associated with a single roller pump. The modelling in this paper is, however, not applicable, as this study focusses on the first principles approach without reliance on CFD software.

## 2.6 Additive manufacturing

Additive manufacturing allows for constructing highly complex structures at relatively low cost and short lead time when compared to current manufacturing techniques. This allows for more frequent innovations and higher customization of products [49]. The degree to which additive manufacturing can optimise a part is unique as additive manufacturing generates the part. This is in contrast to subtractive manufacturing techniques, such as computer numerical control (CNC) machining, that remove material from the raw material block in order to give the desired form.

Additive manufacturing is said to have evolved from rapid prototyping technologies, which allows users to print non-functional or semi-functional prototypes. Currently, additive manufacturing is described as a form of direct manufacturing, with the goal of building fully functional components. This is especially useful in the aerospace industry as less material implies less material cost and better fuel efficiency for an aircraft with less weight. Not only does additive manufacturing show potential in the production and/or repair of components, but delivers parts with both sufficient and repeatable mechanical performance [20].

Lipson et al. [19] indicate that the complexity and variety of designs on a 3D printer is "free". This implies that there is no cost associated to the complexity or the variety of designs other than material and operating time. Another benefit Lipson lists is zero lead time, as the printer can print on demand as needed. The fact that 3D printers offer highly customisable and complex geometries of parts with minimal removal of material reduces the waste associated with conventional manufacturing processes. This in turn makes additive manufacturing more desirable with respect to waste optimisation.

3D printed robotic manipulators are cost efficient and easy to produce when external items such as motors, drivers, bearings, and fasteners are easily accessible. This along with the ease of operability and attainability of 3D printers allow users to print their own, or other open source robotic arms and manipulators. This allows for the construction of low cost robotic arms/manipulators in small businesses, education institutions, and among robotic enthusiasts. Collaborative web sites such as [Hackaday.io](http://Hackaday.io), [Poppy-project.org](http://Poppy-project.org), and [ThingyVerse](http://ThingyVerse) share open source information and designs, including robotic manipulator designs, among their users. Some open source robotic manipulator designs include: the UFactory uArm, Thor, EEZYbotARM MK2, LittleArm, Roboteurs RBX1 Remix, 3D Printable Robot Arm, Zortrax Robotic Arm, and BCN3D Moveo to name a few [50–57].

Low cost 3D printers however tend to create parts that have relatively large tolerances due to inaccuracies and tolerances of the physical printer. This can result in backlash and non-linearities of an actuated system dependent on these parts, such as a robotic manipulator or arm [21, 58]. Furthermore, W. Brostow et al. [22] describe polymers as viscoelastic, meaning their properties change over time. By modelling and testing polymers with scratch tests Brostow et al. concluded the same result with polymers as D.R. Askeland [59] had with metals. That is material brittleness increases wear by reducing plastic recovery.

Bikas et al. [18] define the current additive manufacturing technologies based on their core working principles shown in Table 2.1. The laser polymerisation technique listed can further be subdivided into more commonly found manufacturing processes such as: Stereolithography (SLA), Solid Ground Curing (SGC), Liquid Thermal Polymerisation (LTP), Beam Interface Solidification (BIS), and Holographic Interference Solidification (HIS).

Similarly the laser melting technique listed can be subdivided into: Selective Laser Sintering (SLA), Selective Laser Melting (SLM), Direct Metal Laser Sintering (DMLS), Laser Engineered Net Shaping (LENS), Direct Metal Deposition (DMD), Laser Powder Deposition (LPD), and Selective Laser Cladding (SLC).

Different materials require different manufacturing processes, mostly due to required melting temperatures. For this reason steel cannot commonly be additively manufactured using fused filament fabrication (FFF) technology. Higher strength materials (such as steel) typically require more complex manufacturing technologies, such as laser processing, material jetting, or electron beam processes.

Higher precision of the additive manufacturing technology is closely corre-

Table 2.1: Additive manufacturing core technologies and manufacturing methods adopted from Bikas et al. [18]

<b>Core technology</b>	<b>Manufacturing techniques</b>
1. Laser-based processes	a) Laser polymerization b) Laser melting
2. Extrusion processes	a) Fused Filament Fabrication (FFF) / Fused Deposition Modelling (FDM) b) Robocasting
3. Material jetting processes	a) Three-dimensional printing (3DP) b) Inkjet printing (IJP) c) Multijet Modelling (MJM) d) Ballistic Particle Manufacturing (BPM) e) Thermojetting
4. Adhesive processes	a) Laminated Object Manufacturing (LOM) b) Solid Foil Polymerisation (SFP)
5. Electron beam processes	a) Electron Beam Manufacturing (EBM)

lated to a higher cost. This is mainly due to higher accuracies being available on state-of-the-art technologies [17, 21]. U. Berger [21] lists the processing errors of additive manufacturing machines that affect accuracy and repeatability of printed parts and are indicated in Table 2.2.

Table 2.2: Processing errors pertaining to part tolerance regarding additive manufacturing adopted from U. Berger [21]

<b>Systematic errors</b>	<b>Accidental errors</b>
Stiffness	Vibrations
Machine geometry	Temperature
Positioning error	Atmospheric humidity
Backlash	Positioning variation

FFF printers are focussed on in this study as they are the most widely available printer type and incur the least amount of costs associated with manufacturing. FFF printers mainly consist out of: a build plate, a printing head, and a frame for motor positioning. The printer head contains an extruding stepper motor and a hot end (heating element, thermocouple, and nozzle attached to a heating block). The thermoplastic is fed from a spool into the printer head

and heated at the hot end to melting temperatures. The viscous plastic is then extruded onto the build plate. As the plastic is extruded, the print head moves around the build plate in the pattern of the designs first layer. After the initial layer is complete, the printer head adjusts height and prints a second layer on top of the first layer according to the instruction on the controller. The instructions are derived from the computer aided design (CAD) file with the use of slicing software. This process is repeated layer upon layer until the final part is complete [17].

To assist with adhesion, the build plate is normally heated to roughly 50 – 70 °C . The printer head and build plate combined have three degrees of freedom around the X, Y, and Z axis. These degrees of freedom are actuated by motors (most commonly stepper motors) and timing belts.

The printer obtains design information from GCODE created by a slicer from the CAD drawing. The slicer allows a list of options to control the 3D printer as the part is printed. These options vary widely from the translational speed of the motors, retraction as well as the extrusion speed of the extruder, and part properties such as: shell thickness, infill density and pattern, and support generation.

## 2.7 Critical literature review

Information pertaining to rotary peristaltic pump design and modelling is rather scarce in contrast to the large amount of available patent information. This is likely due to private companies withholding information from the public domain in order to keep a competitive advantage. Design information and references are thus obtained from relevant patents.

The majority of rotary peristaltic pump designs referred to in the patent list were symmetrical around one axis ( $y$ -axis), allowing identical reverse flow during reverse actuation. This is ideal for this study as it simplifies the modelling of the peristaltic pump. The best suited pump type for the application as an EHA is that of a roller pump with a backplate. A hose pump would be ideal in this case however limitations due to the manufacturing process must be taken into consideration. These considerations include material strength, and build size. With these limitations in mind, the tube-type roller pump seems best suited for low to medium pressures, and is an ideal candidate for the focus of this study.

The low Reynolds number and sinusoidal waveforms of S.L. Weinberg et



al. [46] suggest that the intention of their study was to model naturally occurring peristalsis, limiting its use for roller pump modelling. The modelling theory that T.W. Latham [1] provides also pertains to sinusoidal peristaltic waveforms, which can be used for pump designs with a large number of rollers. However, this model can be problematic with pump designs containing fewer than four rollers, as the peristaltic waveform no longer represents that of a sinusoidal wave.

The most relevant literature is that of F. Moscato et al. [16]. Moscato et al. describe the flow pulsations of the roller pump by attributing the pulses to each individual roller, rather than a sinusoidal waveform. This allows the model to be more generally applicable, where quick repetitive pulsations may automatically start to form the sinusoidal waveform from the aforementioned studies.

The lack of a model for the volume displacement of the roller occluding the process tube also allows for further investigation into modelling the peristaltic pump. A model describing the volume displacement may prove extremely useful in modelling the dynamic characteristics of a peristaltic pump. Focus will thus be placed on the modelling approach of Moscato et al. with the first principles described by E.O. Doebelin [14] and D. C. Karnopp et al. [13]. The lumped parameter model of F. Moscato et al. will have to be adjusted to make the model generally applicable to pumps with more than two rollers.

In order to manufacture an affordable and easy to create pump, the pump will be constructed on a standard desktop FFF printer. The design will thus be orientated around the available printers for the project, namely the Prusa MK2.5 and Prusa MK3. This selection is justified as the FFF technology is seen as the least complicated technology. This implies that the material strength is not as great and the associated tolerances are quite large. Thus, if a pump can be manufactured and tested with this technology, it should theoretically be possible to create the pump with almost all available technologies, with materials having similar or greater mechanical properties.

The manufacturing accuracy regarding 3D printing, specifically part tolerance, is taken into consideration with the work of U. Berger [21]. The accuracy of the printer affects the tolerance of the printed parts and should be taken into consideration by means of larger clearances on the designed parts. The wear of thermoplastics described by Brostow [22] motivate a gear-less pump design to mitigate wear of the printed parts. A gear-less design is further motivated as it could possibly increase the accuracy of the validation tests by mitigating backlash and physical disconnect.

### Peristaltic pump modelling

---

#### 3.1 Introduction

This chapter discusses the modelling of the peristaltic pump and its response to the hydraulic circuit integration. With regards to this study, the term ‘system’ refers to the hydraulic circuit connected to the pump’s inlet and outlet.

This chapter first discusses the modelling methodology, which includes the reference geometry and assumptions used to describe the pump and its dynamics. Once the assumptions have been declared in the modelling methodology section, the discussion goes into depth regarding the degree of occlusion of the pump. Thereafter the modelling of the volume that the roller displaces is discussed. Following the numerical modelling section of the roller volume displacement, the development of the lumped parameter model is discussed.

This chapter is concluded with a brief discussion on the software environment and simulation approach, before verifying the model. Model verification is done by using the pump and system variables found in [16], which describes the modelling of a two-roller peristaltic pump. The theoretical model pertaining to the peristaltic pump can then be used to design a peristaltic pump with a desirable flow rate for a specific rotational speed in Chapter 4.

## 3.2 Modelling methodology

A similar approach to that of Moscato et al. [16] will be used to create a generalised roller-type peristaltic pump model. Without explicitly stating so, Moscato first characterised the flow associated with the pump and thereafter obtained the pressure response caused by the pulsatile flow of the peristaltic pump. Similarly the initial numerical study of this chapter describes the flow of the peristaltic pump based on the designed geometry. The flow is then utilised within a lumped parameter model, as seen in [16], to simulate the peristaltic pump operating within a known system. This approach is followed in order to obtain the pressure response of the system the pump is integrated with, and is outlined in Fig. 3.1. It is important to note that the flow is not derived from the simulation, but from the model that describes the parameters of the simulation. The intended purpose for the lumped parameter model is to describe the system variables for simulation purposes. This is to allow for simulation of the pressure response of the system to the flow pulsations from the pump.

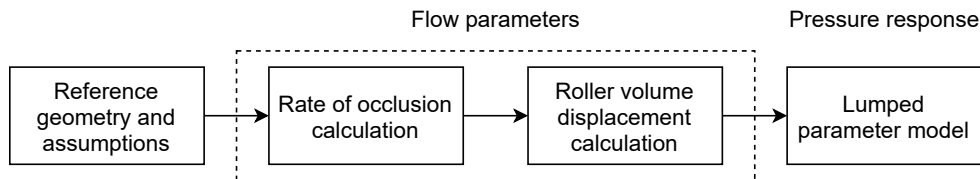


Figure 3.1: Illustration of the modelling methodology used to model the peristaltic pump characteristics

The modelling methodology of this study differs from that in [16], as the article describes a model specific to a two-roller peristaltic pump. This study attempts to create a generalised model for multi-roller peristaltic pumps. The general model should allow for varying amounts of rollers utilised on the pump, different pump sizes, and different tube sizes. The majority of the modelling focus is placed on the geometric relations of the pump to model the flow of the pump, and specifically the roller induced flows. This is to add congruent information on the modelling of peristaltic pumps, as [16] uses a data driven approach for the roller induced flow. Additionally, the application of the pump as an electro-hydrostatic actuator (EHA) would rely on the flow of the pump, as positive displacement pumps can sustain linear flow under varying pressure differentials across the pump assuming non-compressible fluids are used. Thus the flow takes precedence over the pressure when modelling a positive displacement pump for actuation with incompressible fluids.

### 3.2.1 Reference geometry and positions

A combination of the pump design, the system which the pump is connected to, and pump operation give rise to the unique pressure pulsation characteristics commonly associated with peristaltic pumps. Pump design aspects that influence the pressure pulsations are: roller size, tube size, inlet and outlet angle, number of rollers, and backplate diameter. The system aspects that influence the pressure pulsations are located on the inlet and outlet lines of the pump to the system. These aspects of the inlet and outlet lines are dependent on: line length, line diameter, material strength of the line, line wall thickness, head loss, and ambient pressure. Operational aspects that influence the pressure pulsations are operational speed (rotational speed of the motor) and angular acceleration of the motor.

The flow that correlates to the pressure pulsation originates from the volume that the roller displaces as it comes into or out of contact with the process tube [16]. The movement of a roller coming into contact with the tube is denoted as engagement, while the movement of a roller coming out of contact with a tube is denoted as disengagement. These movements can also be used to describe certain periods for modelling purposes, and can be specified as the range of motion where a roller is in contact with the tube, but is not at its maximum occlusion/compression value. These values are described in detail later in this chapter. This induced flow is thus dependent on the degree of occlusion of the tube, as a larger occlusion implies a larger change in volume.

Using a two-roller pump as an example, indicated by Figs. 3.2a, 3.2b, and 3.2c, the reference positions can be better described. With a clockwise rotation this example indicates that roller A comes into contact with the tube (denoted as the engaging position) while roller B keeps the tube shut. This is indicated in Fig. 3.2a as the starting position and Fig. 3.2b as the end position for the angle of engagement. Fig. 3.2b indicates roller A in the engaged position as the tube is fully occluded, and roller B in the disengaging position, where occlusion starts to decrease. Roller B then moves away from the backplate until it no longer occludes the tube at the disengaged position indicated in Fig. 3.2c. These positions apply to every roller on the peristaltic pump during a full rotation and are reliant on the direction of rotation.

In order to maintain a hydrostatic pressure with a pressure differential between the inlet and outlet, at least one roller needs to occlude the tube completely. The minimum requirement of one roller occluding the tube during rotation implies that a minimum span of occlusion per roller is required, and is

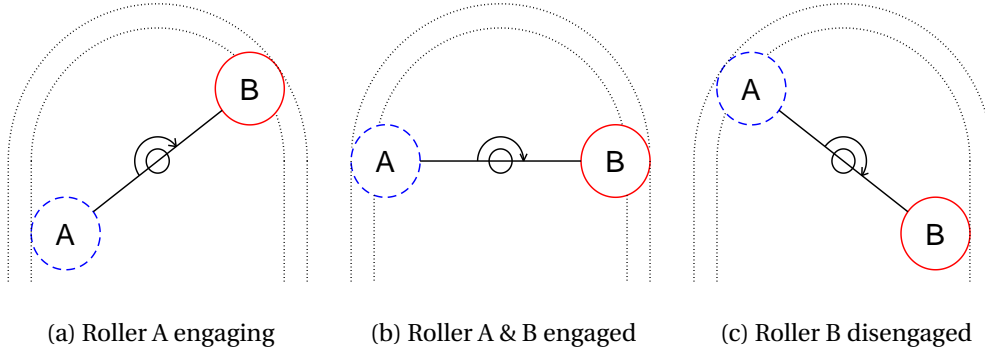


Figure 3.2: Roller positions of a two-roller peristaltic pump pertaining to pulsatile flow characteristics

dependent on the number of rollers on the pump. The minimum span is defined as the arc length between two rollers on the pump. Constant occlusion implies that during the process of the roller engaging or disengaging the tube, another roller will be in full contact with the tube. This is with exception of a single roller design as it acts as its own opposing roller. This would also imply that the flow at the inlet and the outlet of the pump is not affected by the flow on the opposing side of the pump.

When referring to the flows created by the pump, rotational flow  $Q_{nom}$  is used to denote the nominal flow of the fluid through the tube without the additional roller induced flow  $Q_{ed}$ . This nominal flow can also be thought of as an ideal flow of a pump with a negligible volume displacement of its rollers.  $Q_{avg}$  denotes the average flow through the pump which takes the displaced volume of the roller into account. This is calculated with the average value of the induced flow subtracted from the nominal flow over a certain period of time. The nominal flow and the roller induced flow are indicated in Fig 3.3 along with other system variables. The inner radius of the process tube is denoted as  $r_i$  and the outer radius as  $r_o$ .

The nominal flow will be defined as the flow in the tube caused by a single roller with a negligible displaced volume with full occlusion rotating around the central axis of rotation of the motor at a radial distance  $r_m$  (3.1).  $r_m$  is equal to the radial distance from the center of rotation to the center of the process tube (3.2). The distance to the centre of the roller can be found by subtracting the outer radius of the tube  $r_o$  from the radius of the backplate  $r_b$ .  $Q_{nom}$  is thus directly proportional to the rotational speed of the motor  $\omega$  (in rad/s), the

radius of the outer casing of the pump, and the outer radius of the process tube. The  $x$ -axis and  $y$ -axis are also depicted in Fig. 3.3, which pertain to the  $y$ -axis described with the pump designs of the literature study, and will be used again for the design of the pump in Chapter 4.

$$Q_{nom} = r_m \times \omega \times \pi r_i^2 \quad (3.1)$$

$$r_m = r_b - r_o \quad (3.2)$$

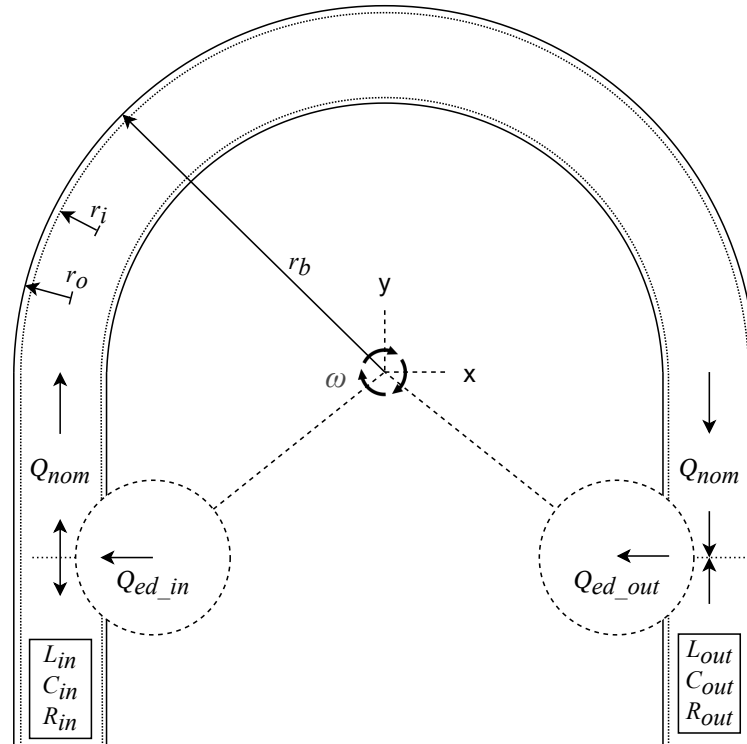


Figure 3.3: Schematic diagram illustrating the pump dimensional parameters and flow variables

The system variables are comprised of the fluid inertia ( $I$ ), the effective head loss ( $R_{eff}$ ), and the effective compliance ( $C_{eff}$ ) for the inlet and the outlet of the pump. For this section, in order to better describe the lumped parameter model, these variables will be described as their electrical analogues, inductance ( $L$ ), resistance ( $R$ ), and capacitance ( $C$ ) respectively. The values of these variables are calculated up to the engaged position for the inlet line, and up to the disengaging position for the outlet line of the pump shown in Fig 3.2.

### 3.2.2 Assumptions

In order to ensure accuracy and simplicity in the modelling process, assumptions are made regarding the pump design. The symmetry around the  $y$ -axis of the peristaltic pump allows for the inlet and outlet to be identically reversible. This implies that should the pump operate in reverse, assuming the inlet and outlet have similar system variable values, the pulsations associated with both the inlet and outlet are applicable to the revised operation. The symmetry also allows the roller induced flow from the inlet to be equal to the inverse and reversed roller induced flow of the outlet. Thus, it is assumed that the pump is symmetrical around the  $y$ -axis, as seen with the reviewed patents. The rollers are assumed to be symmetrically placed around the central shaft of the motor, allowing for uniform pulsations.

The inlet and outlet are assumed to be straight and enter/exit the pump tangentially to the backplate (or outer casing). This simplifies the calculation of the degree of occlusion. It is also assumed that there is no leakage between rollers, and that there is always one roller fully occluding the tube. This implies that there is no flow between occlusions and between the inlet and outlet of the pump, other than the nominal flow, and roller induced flow.

The rollers, in reality, roll over the process tube with minimal friction. In order to mitigate confusion between the rotation of the roller and the rotation of the pump, the roller motion will be described as a frictionless contact without rotation. This implies that reference made to the central axis of rotation pertains to the shaft of the motor/pump. The connection between the rollers and the shaft of the motor, the backplate, and the rollers themselves are considered to be rigid. The tube is also assumed to comply perfectly around the roller's surface, without additional bending associated from shear stress near the roller. These assumptions can be summarised as:

1. The pump is symmetrical around the  $y$ -axis
2. The rollers are placed symmetrically around the axis of rotation
3. The inlet and outlet are tangent to the backplate during roller engagement/disengagement
4. No leakage occurs over the occlusion of a roller while it is fully engaging the tube
5. There is always at least one roller fully occluding the tube
6. The rollers and pump components are completely rigid
7. The roller slide over the process tube with no friction
8. The process tube is completely compliant specifically to the form of the roller

9. The ratio of the roller length to the backplate length is sufficiently small
10. The motor performs ideally and continuously

With the reference geometry and assumptions declared, the modelling can be undertaken starting with the degree of occlusion.

### 3.3 Degree of occlusion

The degree of occlusion describes how the roller collapses the process tube and to what extent. This degree of occlusion can be mathematically determined by calculating the distance between the roller's leading edge and the backplate. The leading edge of the roller is a descriptive term used to describe the closest point of a roller to the backplate. This leading edge is indicated on the disengaging and disengaged roller positions in Fig. 3.4.

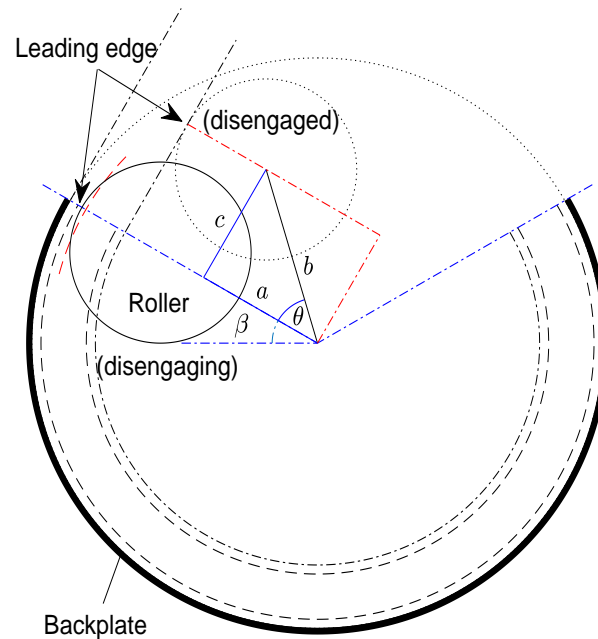


Figure 3.4: Illustration of the geometric distances and angles used to define the pump's angle of engagement ( $\theta = \phi$ )

In Fig. 3.4,  $\theta$  indicates the angle rotation of the motor with its value equal to the angle of engagement  $\phi$ . As stated previously, the angle of engagement refers to the angle the motor must rotate to bring the roller from a fully occluded tube to a non-occluded tube (from the disengaging position to the disengaged



position) and vice versa. The angle of engagement at the outlet is equal to that of inlet for a pump with symmetry around the  $y$ -axis.

The contact angle  $\beta$  describes the engaged/disengaging positions with respect to the  $x$ -axis of the pump and defines the total span of total occlusion for a roller. The angle characterises a phase offset between the inlet pulsation and the outlet pulsation but does not affect the amplitude of the pulsation. For the pump representation in Fig. 3.3  $\beta$  is equal to  $0^\circ$  at the inlet and outlet implying that the rollers fully occlude the tube for a span of  $180^\circ$ . Fig. 3.4 indicates  $\beta$  as  $30^\circ$  for the symmetrical pump implying the rollers fully occlude the pump for a span of  $240^\circ$ .

With the assumption of a straight inlet and outlet to the pump, the inlet and outlet must be tangent to the backplate at an angle perpendicular to the contact angle  $\beta$ . Knowing this,  $\phi$  can be calculated in (3.3) using lengths  $a$  and  $b$  with the contact angle as the reference.  $b$  is the designed length from the centre of rotation of the pump to the centre of rotation of the roller (referred to as the roller offset radius  $r_{offset}$ ).  $a$  is perpendicular to the contact angle and parallel to the inlet/outlet.  $a$  has a length from the centre of the roller to the centre of the axis of rotation of the pump when the roller makes initial/final contact with the tube.  $a$  can be calculated in (3.4) as the difference between the radius of the backplate  $r_b$ , the outer diameter of the process tube, and the radius of the roller  $r_{roller}$ .

$$\phi = \cos^{-1}\left(\frac{a}{b}\right) \quad (3.3)$$

$$a = r_b - 2r_o - r_{roller} \quad (3.4)$$

$$b = r_{offset} \quad (3.5)$$

Using Fig. 3.4 as a reference with the roller's initial position at the disengaging position, the dynamic distance between the backplate and the leading edge can be formulated. A clockwise rotation will bring the roller out of contact, implying that theta ranges from  $\beta$  to  $\beta + \phi$ . To simplify the trigonometric equations the angle's rotation will be calculated with reference to  $\beta$ , thus the rotation ranges from 0 to  $\phi$ . The distance between the backplate and the leading edge is denoted by  $\delta$ .

For pumps that do not fully occlude the tube, the maximum occlusion  $Occ$  (which is a unitless number between 0 and 1) can be calculated as:

$$Occ = 1 - \frac{r_b - r_{roller} - r_{offset} - 2w}{2r_i}, \quad (3.6)$$

with the tube wall thickness as:

$$w = r_o - r_i. \quad (3.7)$$

The dynamic occlusion  $Occ_d$  can be calculated using  $\delta$  as the roller comes into or out of contact as:

$$Occ_d = 1 - \frac{2r_o - \delta}{2r_i}. \quad (3.8)$$

With the angle  $\theta$  equal to zero as the initial condition, it can be deduced that the initial value for  $\delta$  is equal to the difference of the backplate radius and the sum of the offset and roller radius. This value defines the amount of compression that might occur with the pump design. If the initial  $\delta$  value is equal to twice the value of the process tube wall thickness, no compression occurs. If the value is larger, complete occlusion does not occur. If the value is smaller than twice the wall thickness compression occurs.

Compression occurs when maximum occlusion is exceeded, indicated by Fig. 3.5. This can be done intentionally in order to deter leakage, or can accidentally occur due to mechanical tolerances of the parts. The maximum compression of the tube when fully occluded can be calculated with:

$$Comp = 2w - (r_b - r_{offset} - r_{roller}). \quad (3.9)$$

As the motor rotates clockwise, the leading edge of the disengaging position of the roller in Fig. 3.4 moves away from the backplate. The distance between the leading edge of the roller and the outer casing is denoted as the length  $\delta$  and is calculated with  $\theta \in \mathbb{R} : 0 \leq \theta \leq \phi$  as:

$$\delta(\theta) = r_b - (r_{roller} + r_{offset} \cdot \cos(\theta)). \quad (3.10)$$

It can be helpful to use the trigonometric identity  $\cos(\theta) = \sin(90^\circ - \theta)$  as it aids in visualising the angle being used. The  $\delta$  value can be compared to the dynamic radius of the roller  $r_d$ , which is the distance from the centre of rotation to the leading edge of the roller. This distance can be calculated with the Pythagorean theorem as:

$$r_d(\theta) = \sqrt{(r_{roller} + r_{offset} \cdot \cos(\theta))^2 + (r_{offset} \cdot \sin(\theta))^2}. \quad (3.11)$$

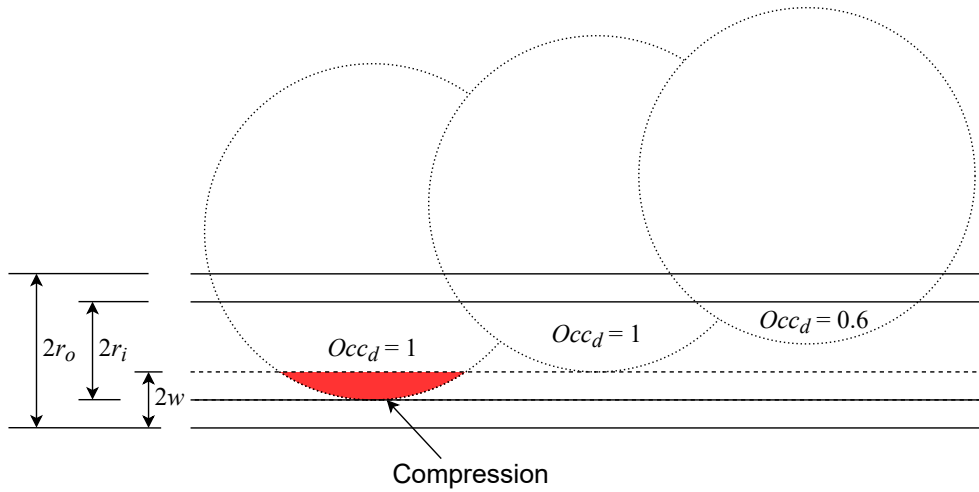


Figure 3.5: Diagram illustrating the occlusion value with regards to the roller position and compression occurrence

The change in this distance should be inversely proportional over the working angle as the pump rotates. This should indicate the dynamic radius decreasing in size while the leading edge distance increases in size as the roller disengages. To verify this, theoretical fractional values can be given to  $r_b$ ,  $r_{roller}$ , and  $r_{offset}$ . If  $r_b$  is set equal to 1 (total distance),  $r_{roller}$  equal to 0.3, and  $r_{offset}$  equal to 0.7 so that  $r_{roller} + r_{offset} \leq r_b$ ,  $\delta$  and  $r_d$  can be compared over various angles of  $\theta$  as in Fig. 3.6. The dynamic radius should have an initial value equal to  $r_b$  and  $\delta$  equal to zero. At an angle of  $90^\circ$  the dynamic radius should have a value of 0.76 and  $\delta$  equal to the difference between  $r_b$  and  $r_{roller}$ .

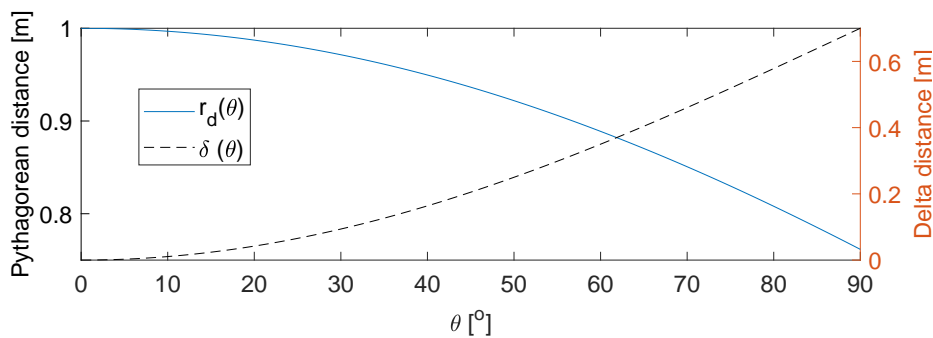


Figure 3.6: Verification of distance  $\delta$  by means of comparison to Pythagorean distance between central distance and leading edge

### 3.4 Roller volume approximation

In order to characterise the flow pulsation of the pump, the volume that the roller displaces must be obtained. There are various methods to approximate the maximum volume displaced by the roller. The initial two methods of approximation offer a discrete approach where only the maximum volume that the roller displaces can be calculated. The third method using discrete integration offers a continuous volume displacement approximation during contact with the tube. Each of these methods may vary by degree in accuracy and will be discussed in order. The first approximation of the volume can be done by calculating the cylindrical volume with a length equal to the length that the roller occupies indicated in Fig. 3.7 as:

$$V_{cylinder} = \pi r_i^2 \cdot 2X. \quad (3.12)$$

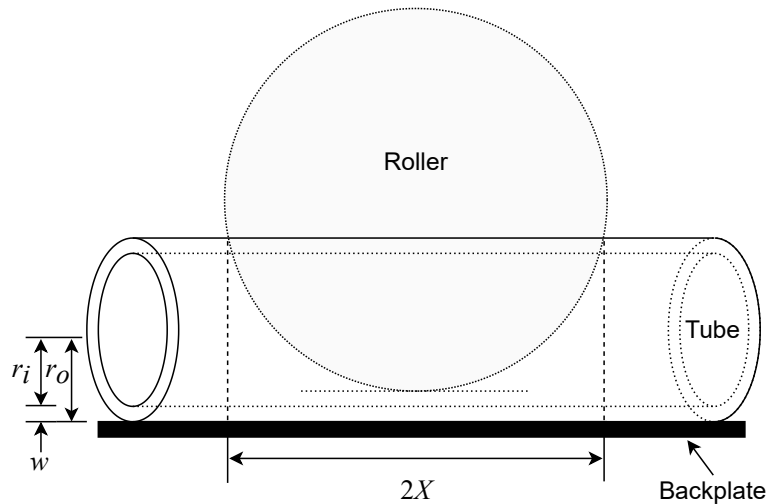


Figure 3.7: Illustrative diagram of a straight cylindrical section of the process tube collapsed by the roller for volume displacement indication

If it is assumed that the roller perfectly occludes the tube as in Fig. 3.7, the length of  $X$  can be calculated with the radius of the roller and the inner radius of the tube. It should be noted that an additional height is present when the tube collapses. The top wall is transposed towards the bottom until the top wall connects with the bottom wall. For a perfect occlusion of 1 this implies that the roller does not come into contact with the backplate, but has a distance equal to  $2w$  from the backplate (not to be confused with motor speed  $\omega$ ). The area remains the same but is simply transposed a distance of the additional height.

The width of the wall thickness as indicated by Fig. 3.8. This initial approximation method is very inaccurate and can only give a very rough indication of the volume.

$$\lambda = \cos^{-1} \left( \frac{r_{roller} - 2r_i}{r_{roller}} \right) \quad (3.13)$$

$$X = r_{roller} \cdot \sin(\lambda) \quad (3.14)$$

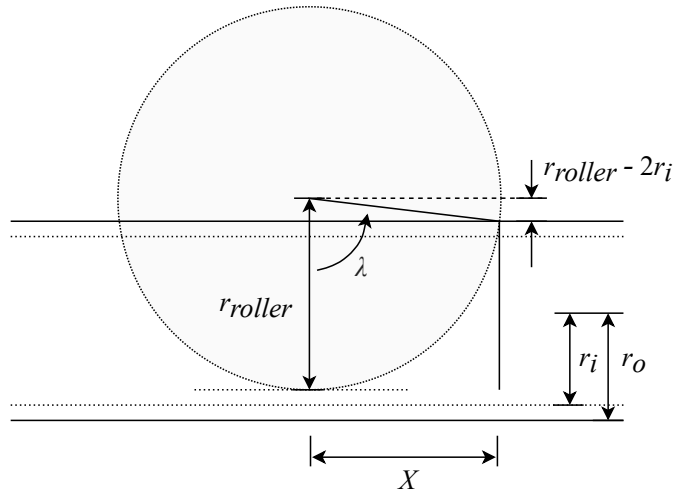


Figure 3.8: Illustration of the roller angle  $\lambda$  used to determine  $X$

The approximation can be improved with a two dimensional fractional value of the roller surface area over that of the cylindrical surface area illustrated in Fig. 3.9. If we let the roller and the tube occupy a rectangular section, we can see that the circle of the roller occupies the larger surface, however, it does not occupy the full rectangle as with the previous cylindrical approximation.

The two dimensional surface occupied by the cylindrical surface can be calculated as:

$$A_{cylinder} = X \cdot 2r_i. \quad (3.15)$$

The surface of the roller can be deduced by calculating roller surface area for the angle  $\lambda$  by subtracting the surface of the triangle located above the tube's outer radius as:

$$A_{roller} = \frac{\lambda}{360} \pi r_{roller}^2 - \frac{1}{2} X \cdot (r_{roller} - 2r_i). \quad (3.16)$$

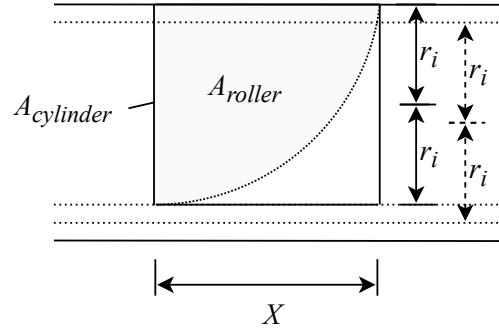


Figure 3.9: Illustration of the two dimensional surfaces of the roller and the tube used to approximate the volume displacement of the roller

The fractional value of the roller surface to that of the cylinder surface can then be multiplied by the volume of the full cylindrical volume calculated in the first approximation attempt. The approximated volume by this method can thus be calculated as:

$$V_{roller} = \frac{A_{roller}}{A_{cylinder}} \cdot \pi r_i^2 \cdot 2X. \quad (3.17)$$

The final method of approximation, however, can be done by means of integration as the roller engages/disengages the tube. Due to the assumption that the roller is cylindrical in shape, it can also be assumed that the outer casing against which the tube is collapsed is a flat surface. As the roller comes into contact with the tube, the tube is deformed from a circle to an elliptical shape. For simplicity, we can assume that a perfect ellipse is formed by the tube as it collapses. Fig. 3.10 illustrates these areas as  $A_1$  and  $A_2$  for the circle and ellipse respectively. The area of an ellipse can be calculated with the radius of the short side  $r_s$  and the larger radius of the long side  $r_l$  in (3.18), and is illustrated in Fig. 3.11.

$$A_{ellipse} = \pi \times r_l \times r_s \quad (3.18)$$

Assuming that the inner perimeter of the tube stays constant as the tube collapses,  $r_l$  can be calculated with the equation for an approximate perimeter of an ellipse (3.20). The initial and constant perimeter of the ellipse can be calculated with the formula for the circular circumference of the uncompressed tube as:

$$S = \pi \cdot 2r_i, \quad (3.19)$$

where the perimeter of an ellipse is approximately equal to:

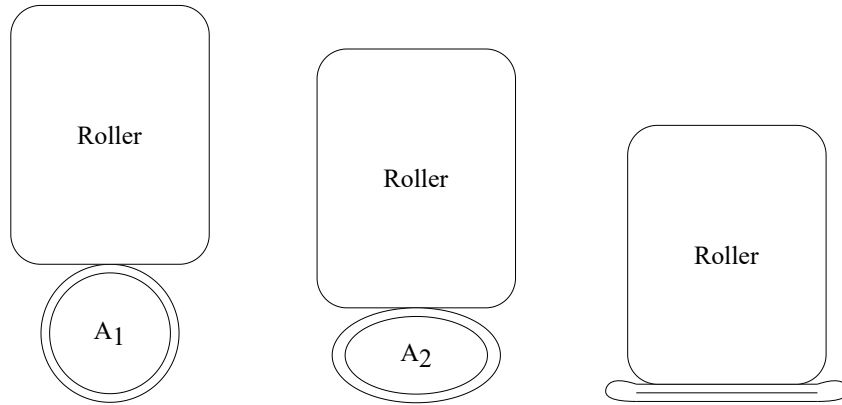


Figure 3.10: Illustration of the side view of a roller collapsing the process tube to indicate the integration area

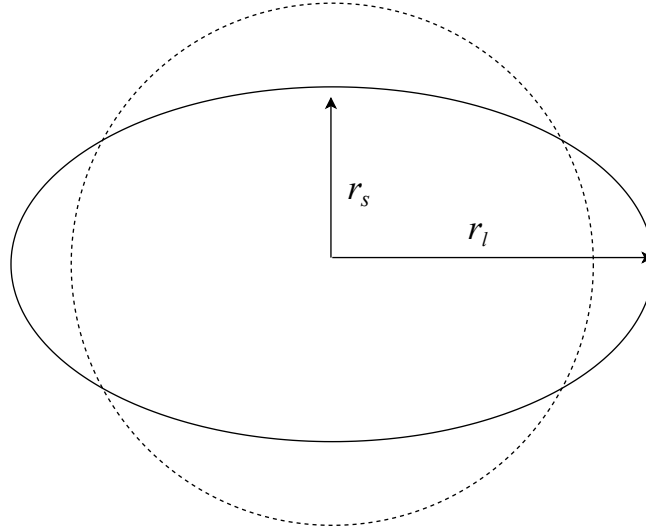


Figure 3.11: Illustration of the radii of an ellipse used to calculate the ellipse area

$$p = 2 \cdot \pi \sqrt{\frac{r_l^2 + r_s^2}{2}}. \quad (3.20)$$

With  $p$  as a constant equal to  $S$ ,  $r_l$  can be calculated as a dependent variable of  $r_s$  as:

$$r_l = \sqrt{\frac{S^2}{2 \cdot \pi^2} - r_s^2}. \quad (3.21)$$

In order to find the volume, the distance that the roller indents into the roller, with respect to a non-collapsed tube, needs to be calculated across the entire

surface of the roller that is in contact with the tube. To assist with determining the indentation length across the surface of the roller, the inflating angle  $\lambda$  (also referred to as the roller angle) is calculated. This angle ranges from the leading edge of the roller (the central bottom point of the roller in Fig. 3.12) to the point where the roller no longer makes contact with the tube for that specific angle of  $\theta$ . Fig. 3.12 illustrates how the inflating angle decreases as the roller comes out of contact with the tube, with the horizontal distance  $X$  decreasing along with it, where  $Y(\theta) = 2r_o - \delta(\theta)$ . Using trigonometric functions  $\lambda$  can be calculated as:

$$\lambda(\theta) = \cos^{-1} \left( \frac{r_{roller} - (2r_o - \delta(\theta))}{r_{roller}} \right), \quad (3.22)$$

and  $X$  can be calculated with:

$$X(\theta) = r_{roller} \cdot \sin(\lambda(\theta)). \quad (3.23)$$

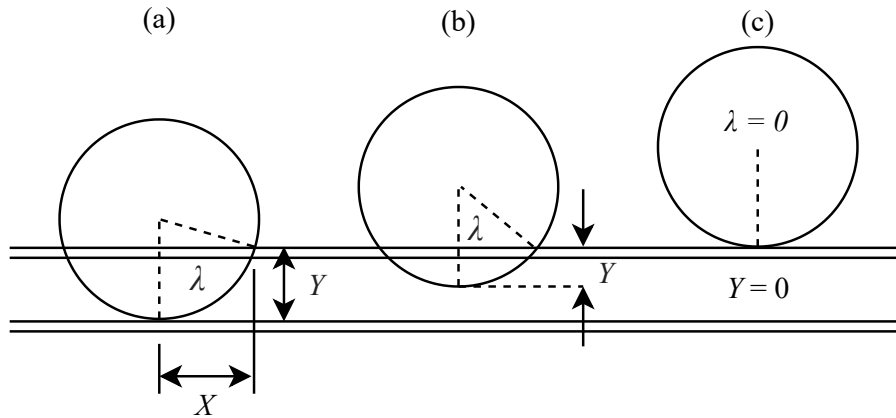


Figure 3.12: Illustration of the inflating angle and  $\delta$  for (a) full occlusion, (b) intermediate occlusion, and (c) no occlusion

Let  $\theta$  be divided into  $n$  equal increments from 0 to  $\phi$ . The volume that the roller displaces for each  $\theta$  value as the roller engages/disengages can be calculated using the midpoint rule integration technique. This is accomplished by finding the corresponding area  $A$  at each point in  $X$  in steps of the segmentation length  $dx$ . These areas are then multiplied by  $dx$  to create sectional volumes  $V_s$  at each point in  $X$  indicated in Fig. 3.13.

This method is advantageous over the continuous integration method as physical limits can be placed on the radii when they have reached their maximum values. This allows volume calculation even when the roller collapses the



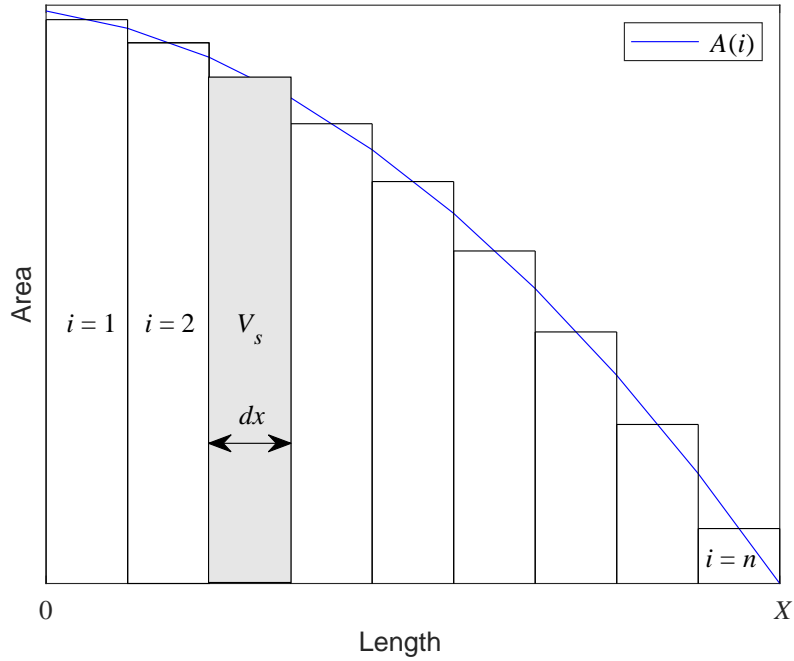


Figure 3.13: Example illustration of the midpoint rule used for discrete integration

tube further than the occlusion limit of 1, as in the case of compression. This method is, however, only accurate for a small segmentation length  $dx$ , as the error increases as  $n$  decreases and  $dx$  increases.

The segmentation length  $dx$  can be calculated by dividing the maximum total horizontal length  $X_{max}$  (which occurs at  $\theta = 0$ ) by  $n$  as indicated in Fig. 3.14.

$$dx = \frac{X_{max}}{n} \quad (3.24)$$

With a constant value for  $dx$ , the  $X(\theta)$  value is incremented from  $X(\theta)$  to zero with a step value equal to  $dx$ , with  $i$  the corresponding positional element of each increment for every point in  $\theta$ , thus:

$$x(i) = X(\lambda) - i dx. \quad (3.25)$$

The values of the area used to determine  $V_s$  (denoted as  $A_{V_s}$ ) are the averages between two corresponding area values for the  $dx$  values (3.30). These values indicate the midpoint between the two determined area values. It should be stated, however, that the right-hand Riemann's sum should give a better approximation for large increment sizes. This is due to the idealistic assumption

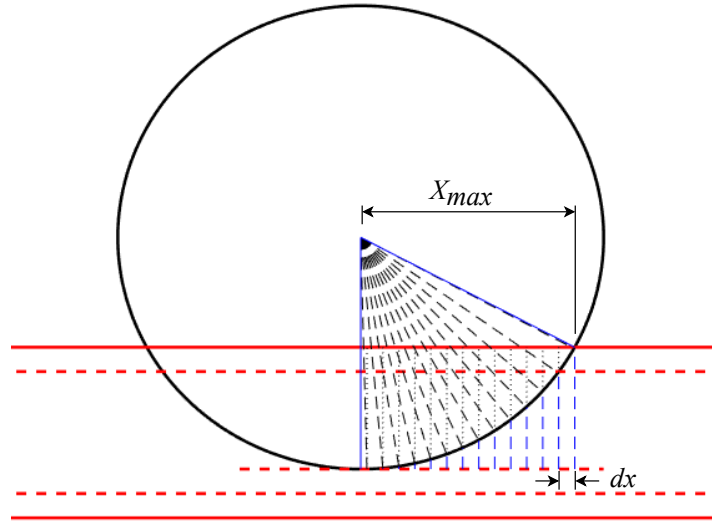


Figure 3.14: Illustration indicating the angles of  $\gamma$  relating to incremental step size  $dx$  in  $X_{max}$

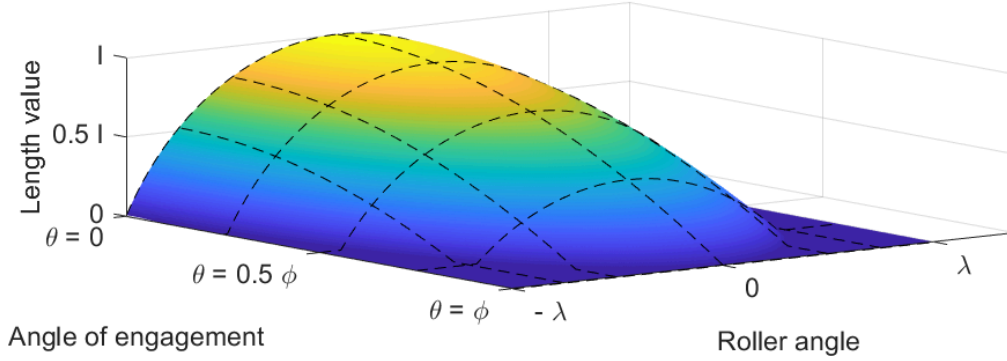
that the tube perfectly conforming to the roller's form will produce a smaller volume than that in reality. The right-handed Riemann's sum might balance this inaccuracy to a degree by over estimating the volume by a small amount. This effect, however, becomes negligible with smaller increment sizes, implying more increments and a better integration approximation.

The total volume displaced by the roller  $V_d$  for each angle of  $\theta$  can then be determined by summing the sectional volumes over the horizontal length  $X$  and thus over the span of the roller surface. The angle of each  $x$  value in  $X(\theta)$  can then be calculated with (3.26) where  $\gamma \in \mathbb{R} : 0 \leq \gamma \leq \lambda(\theta)$ .

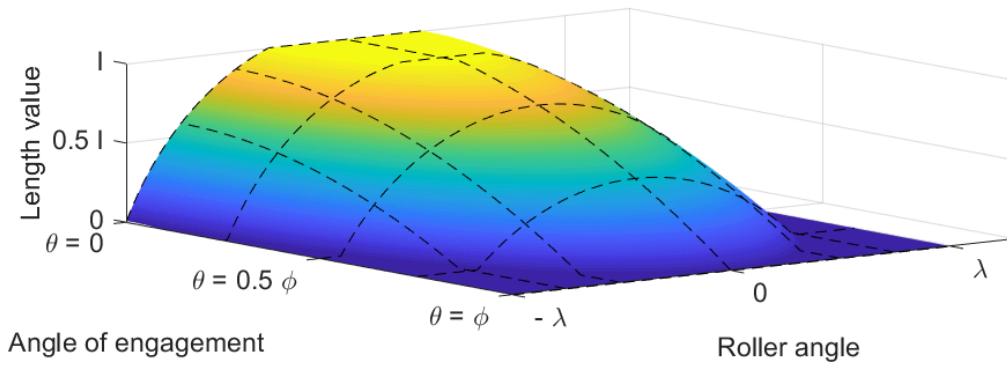
$$\gamma(i) = \sin^{-1} \left( \frac{x(i)}{r_{roller}} \right) \quad (3.26)$$

The vertical length between the roller and the tube  $l$ , which is used to determine  $r_s$ , can then be calculated for each point in  $X(\theta)$  to determine  $A_{V_s}$  and  $V_s$ . The values span half of the tube, and should thus be calculated across the roller angle range of  $\{-\lambda : \lambda\}$ , as indicated in Fig. 3.15a. If compression should occur, a limit can be set on the value of  $l$  as  $0 \leq l \leq \delta(0)$  indicated in Fig. 3.15b. The calculation can be simplified, however, by calculating the volume over half of the roller angle from  $\{0 : \lambda\}$  and multiplying it by two as the roller is symmetrical. This simplification results in:

$$l(i) = (2r_o - \delta(\theta)) - r_{roller} (1 - \cos(\gamma(i))). \quad (3.27)$$



(a) Uncompressed occlusion



(b) Compressed occlusion

 Figure 3.15: Length value  $l$  across the roller angle  $\{-\lambda : \lambda\}$  as the roller disengages the tube for  $\theta = \{0 : \phi\}$ 

The short radius of the ellipse  $r_s$  used for the volume integration can be calculated as:

$$r_s(i) = \frac{l(i)}{2}. \quad (3.28)$$

Thus the area can now be calculated with  $r_l$  as a dependent variable of  $r_s$  and thus of  $i$  as:

$$A(i) = \pi r_s(i) \sqrt{\frac{S^2}{2 \cdot \pi^2} - r_s(i)^2}. \quad (3.29)$$

The area at each point in  $X$  can then be determined, and the average between each two values found to complete the midpoint rule as:

$$A_{V_s}(\theta, i) = \frac{A(i) + A(i+1)}{2}. \quad (3.30)$$

It is important to note that the area underneath the roller has been determined with these equations. It is clear that the area at the centre of the roller during full occlusion is equal to zero. The area where the tube no longer makes contact with the roller is equal to  $\pi r_i^2$ . The volume that is displaced is thus the inverse of the area determined and can easily be accounted for. Because the tube is cylindrical, the required area to determine the sectional volume is equal to the difference between the uncompressed tube area and the determined area. Thus the sectional volume can be determined as:

$$V_s(\theta, i) = (\pi r_i^2 - A_{V_s}(i)) \cdot dx. \quad (3.31)$$

The total volume that the roller displaces for the specific angle of rotation of the motor  $\theta$  is then calculated as:

$$V_d(\theta) = \sum_{i=1}^n 2 \cdot V_s(i). \quad (3.32)$$

As the calculations are based on a roller moving from the disengaging position to the disengaged position the maximum volume displaced by the roller occurs at  $\theta = 0$  and thus  $V_d(\phi) = 0$ . The maximum volume approximated by the integration method is thus:

$$V_{roller} = V_d(0). \quad (3.33)$$

The angle of the pump can be calculated as a variable of time with the revolving speed  $\omega$  values as  $\theta = \omega \cdot t$  with  $t$  as the time variable. The induced flow of the rollers  $Q_{ed}$  can thus be calculated as:

$$Q_{ed} = \frac{dV_d(\omega \cdot t)}{dt}. \quad (3.34)$$

The crux of these approximation methods is that the accuracy is dependant on the ratio of the roller radius to that of the offset radius. Since the tube segment evaluated in these approximation methods is straight, it resembles a roller to backplate radius ratio  $\Psi$  of near zero. As the radial length of the backplate approaches that of the roller's, or vice versa, the linear tube segment approximation will no longer yield accurate results. It can be said that as the ratio approaches a value of one, the volume that the roller displaces approaches the total volume in the tube segment inside the pump  $V_{tube}$ . That is to say:

$$\lim_{\Psi \rightarrow 1} V_d(0) = V_{tube}, \quad (3.35)$$

where the volume of the tube inside the pump can be calculated as:

$$V_{tube} = \pi r_i^2 \cdot \left( 2\pi \frac{180 + 2\beta}{360} (r_b - r_o) \right), \quad (3.36)$$

and the roller to backplate ratio as:

$$\Psi = \frac{r_{roller}}{r_b}. \quad (3.37)$$

This effect is indicated in Fig. 3.16, where a large roller to backplate radius ratio, commonly seen on single-roller pump designs, is used to emphasise the impact of the curved backplate. The assumption of a straight inlet/outlet tangent to the backplate, however, should ensure that the rate that the volume is displaced during engagement/disengagement remains quite accurate. This implies that this inaccuracy of the volume approximation should have a minor impact on the flow caused by the roller coming into contact with the tube, provided the roller to backplate radius ratio remains low enough.

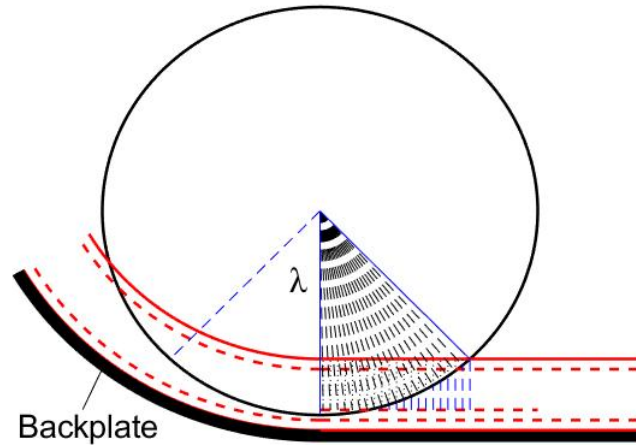


Figure 3.16: Illustration indicating effect of the backplate curvature on the roller angle  $\lambda$

For numerical data it is necessary to find the polynomial of the modelled volume in order to calculate the expected flow. The flow induced by the roller is affected by the polynomial order selected for the curve of the volume displacement over the motor's rotational angle. For this study polynomial orders of the 3rd, 4th, and 5th degree were compared (shown in Fig. 3.17) in order to select the best suited polynomial for the flow simulations. The 5th order polynomial is selected in this case as it has the best boundary values, where the boundary

values of the flow are expected to be zero. The 4th degree polynomial would also suffice for instances where perfect occlusion occurs (no compression of the tube). Because the pump is symmetrical around the  $y$ -axis, the value of  $Q_{ed}$  at the inlet is equal to the reversed inverse value of  $Q_{ed}$  at the outlet.

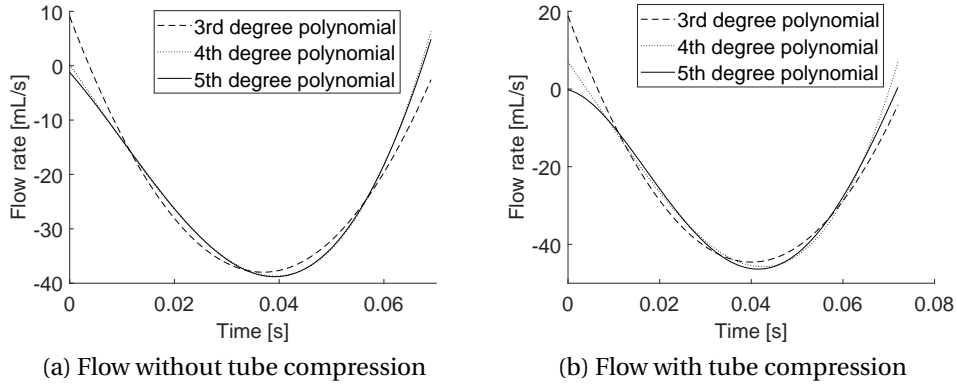


Figure 3.17: Illustration of the effects of different polynomial orders of the volume function on the flow values over time for perfect occlusion and compression

The average flow can be calculated by subtracting the flow induced by the rollers from the maximum flow and calculating the average flow over a period of time in (3.38). This can be verified by calculating the volume that the pump displaces (3.39) and multiplying it with the rotational speed of the pump as in (3.41). The volume that the pump displaces per revolution can be calculated by multiplying the sectional volume  $V_{sec}$  with the amount of sections, which is equal to the amount of rollers  $NU$ . The sectional volume indicates the volume of the fluid in the tube between two rollers and is calculated by subtracting the volume of one roller from the total volume of tube between two rollers as in (3.40). This sectional volume is indicated by the shaded area in Fig. 3.18. The volume displaced by one roller is subtracted, as half of a roller is present at each end of the tube section.

$$Q_{avg} = \frac{1}{t} \int_0^t (Q_{nom} - Q_{ed}) dt \quad (3.38)$$

The volume displaced by the pump for one rotation as:

$$V_{rot} = V_{section} \cdot NU, \quad (3.39)$$

with the sectional volume as:

$$V_{section} = \pi r_i^2 \cdot \left( \frac{2\pi}{NU} (r_b - r_o) \right) - V_{roller}. \quad (3.40)$$

The average flow per second can be calculated numerically by multiplying the volume displaced per revolution ( $V_{rot}$ ) with the speed  $N$  in r/min as:

$$Q_{avg} = \frac{V_{rot} \cdot N}{60}. \quad (3.41)$$

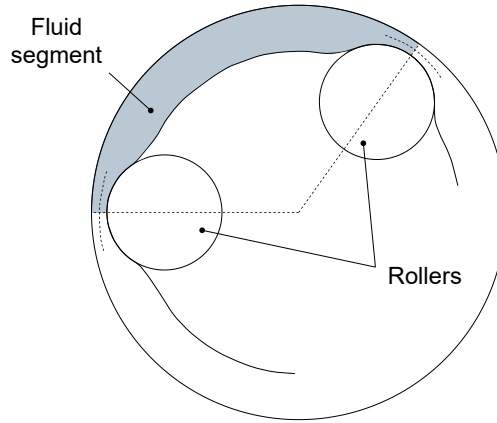


Figure 3.18: Indication of fluid segment between two rollers in a rotary peristaltic pump for average flow calculations

### 3.5 Lumped parameter model

The lumped parameter model of Moscato et al. [16] was studied in detail, with attempts made at recreating the simulation with the values and variables given in the paper. This proved difficult, and several discrepancies arose to the proposed model. For reference, the lumped parameter model proposed in [16] (found in the literature study) is shown again in this section in Fig. 3.19. This is done as a detailed discussion is undertaken in order to give insight into the derivation of a generalised lumped parameter model. This general lumped parameter model is used for the simulation of the pressure response of the system in which the three dimensional (3D) printed peristaltic pump is integrated with.

For clarification, a line in this section refers to the hydraulic segment of fluid connected to the pump. These usually consist of tubes connected in series or

parallel to the inlet and outlet of the pump, and are hence referred to as inlet and outlet lines.

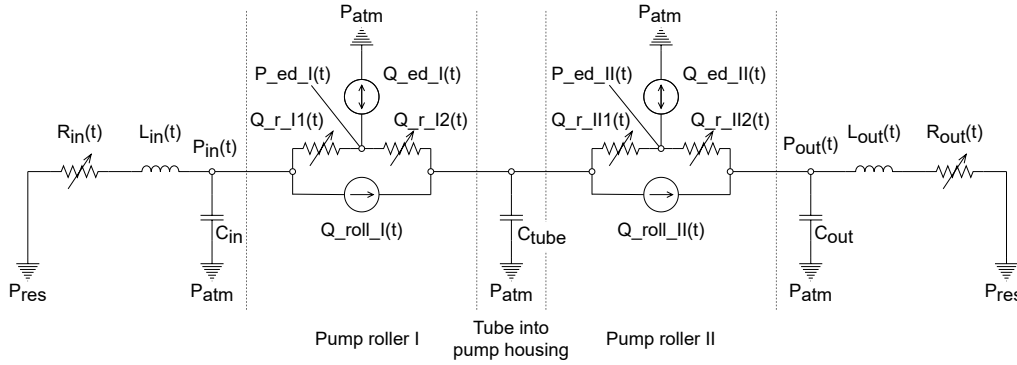


Figure 3.19: The lumped parameter model diagram of a two-roller peristaltic pump proposed in [16]

$P_{in}$  and  $P_{out}$  in Fig. 3.19 indicate the inlet and outlet pressures, where the inlet line and outlet line connect to the pump. The inlet and outlet line are seen connected to identical subsystems, which represent the properties of the rollers in the pump. Between the two rollers is an additional capacitance variable, representing the compliance of the tube segment between the two rollers.

The roller induced flow sources ( $Q_{ed_I}$  and  $Q_{ed_{II}}$ ) are variable flow sources with the values derived from the motor speed and the differentiation of the roller volume across the engage angle. The nominal flow variables (denoted as  $Q_{roll_I}$  and  $Q_{roll_{II}}$ ) are also variable flow sources with their maximum value equal to that of the nominal flow described earlier in this chapter. These flows are based on whether or not the roller is in contact with the tube in [16], hence creating a flow during movement. These nominal flow variables range from 0 to  $Q_{nom}$  in a linear fashion across the angle of engagement seen in Fig. 3.20. For clarification, the pump modelled here is a two-roller pump symmetrical around the  $y$ -axis with a contact angle of  $180^\circ$ .

This brings about the first discrepancy, namely unaccounted flow. The sum of these two flow variables results in a spike in flow through the system during roller engagement/disengagement. This spike is unaccounted for, with a magnitude near that of the roller induced flow, which is problematic.

The second discrepancy is attributed to the roller induced flows  $Q_{ed}$ , as the induced flow values contain both the positive displacement flow and negative displacement flow. This is strange as the input should be attributed with a posi-



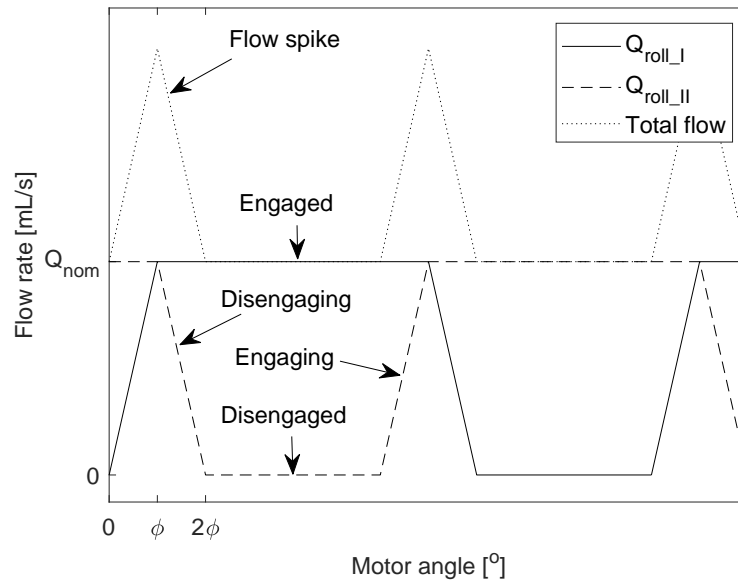


Figure 3.20: Illustration of the nominal flow variables used with the model in [16] with indication of the accounted flow spike

tive displacement, as it opposes the direction of the flow. For the same reason the outlet should be attributed with a negative flow only. This discrepancy resulted in the simulation having a pulsation period double than that expected, with the wavelike pressure pulsations not resembling the results from the article. To be fair, the discrepancies of the model might be due to a lack of understanding of the simulation procedure.

Furthermore, it is not described whether or not the model is applicable to pumps with more or less than two-rollers. The model, however, does not appear to accommodate pumps with different numbers of rollers, as an additional  $Q_{roll}$  variable would be required for a third roller. This would also increase the total flow of the model above that which is physically possible of the pump, as the unaccounted flow spikes would increase in length as the flows overlay each other.

These discrepancies motivate an alternative approach for modelling a generalised lumped parameter model for roller-type peristaltic pumps. The model proposed in [16] can be simplified by removing the subsystems of the rollers in the lumped parameter model. The  $Q_{roll}$  variables that describe the volumetric flow rate of the pump should also be revised. The assumption of complete occlusion of the tube implies isolation of the pressure response between the

inlet and the outlet. This implies that the inlet and outlet can be modelled as two separate subsets connected to one another by a flow source. It is common for positive displacement pumps to be modelled as flow sources, rather than pressure sources (as with kinetic pumps), as the pressure differential over the pump does not deter flow idealistically [60].

The reservoir pressure of the inlet and outlet lines can be modelled as voltage sources leading towards the pump. The additional flows created by the rollers  $Q_{ed}$  can be modelled as variable flow sources at the pump inlet and outlet as in [16]. The DC flow source of the lumped parameter model has a value equal to that of the nominal flow of the pump. The additional flow source at the inlet of the pump denoted as  $Q_{ed\_in}$  is expected to be a positive flow source, while the additional flow source at the outlet of the pump  $Q_{ed\_out}$  is expected to be a negative flow source.

The total resistance for a single line with multiple tube sections can be calculated as the sum of all resistive values in series (3.42). For multiple inlet/outlet lines the total resistance value for each line would need to be added as resistance values in parallel to get the total resistance value for the line (3.43).

$$R_{series} = R_1 + R_2 + \dots + R_n \quad (3.42)$$

$$\frac{1}{R_{parallel}} = \frac{1}{R_1} + \frac{1}{R_2} + \dots + \frac{1}{R_n} \quad (3.43)$$

The total capacitance for a single line with multiple tube sections can be calculated by summing the compliance values of each section of the inlet/outlet line as capacitors in parallel (3.44). If multiple inlet/outlet lines are present, the total capacitance of each additional line can be added together as capacitors in parallel as well. This is due to the compliance of each section of the line acting as a capacitor in series, where each section adds an individual capacitance value directly to the inlet/outlet line.

$$C_{total} = C_1 + C_2 + \dots + C_n \quad (3.44)$$

The total inductance value for a single line with multiple tube sections can be calculated as multiple inductance values in series (3.46). For multiple inlet/outlet lines the total inductance value for each line would need to be added as inductance values in parallel to get the total inductance value for the line (3.45).

The total resistance and inductance values can be placed in series on the inlet and the outlet lines with the nominal flow rate as the central source. Thus the inlet and outlet are coupled to the nominal flow rate in series. The total capacitance value can be placed in parallel to the inlet and outlet line between the flow source and the resistance and inductance values with a common ground as the reference. The variable flow sources of the  $Q_{ed}$  values can be placed between the central flow source and the capacitor values as indicated in Fig. 3.21.

$$\frac{1}{L_{parallel}} = \frac{1}{L_1} + \frac{1}{L_2} + \dots + \frac{1}{L_n} \quad (3.45)$$

$$L_{series} = L_1 + L_2 + \dots + L_n \quad (3.46)$$

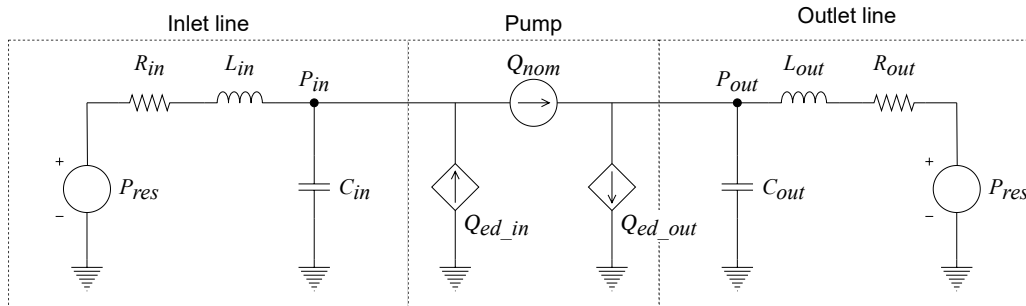


Figure 3.21: Illustration of an equivalent circuit model of a roller-type peristaltic pump integrated within a hydraulic system

Since the variable flow sources are based on the volume displacement of a roller, a pump with any amount of rollers should theoretically be able to be modelled with the following limitation: The number of rollers on the pump model should not exceed that which the pump is physically capable of handling. This is because the rollers physically occupy the available space inside the pump, which implies that there is a physical limitation on the number of rollers on a certain pump design. Generally, larger roller sizes reduce the number of rollers that the pump can be designed with, whereas smaller rollers increase the number of rollers that the pump can be designed with.

This model is not, however, perfect and does not account for the capacitance of the tube between the inlet and the outlet, as seen in [16]. This could alter the values slightly as the capacitance between the two rollers should theoretically transport fluid from the inlet to the outlet under larger pressures. For this reason the lumped parameter model should not be used to determine the flow through the pump. Thankfully the lumped parameter model is dependant on the modelled flow, and so it is not necessary to obtain further flow values.

## 3.6 Peristaltic pump model

The modelled flow values presented in this section were calculated in MATLAB. The results are then used in a Simulink simulation environment that solves the lumped parameter model. The model consists of elements of both the Simulink and Simscape libraries/toolboxes. The multi-domain simulation environment of Simulink allows the Simulink components to receive values from the MATLAB workspace, and pass the values on to the Simscape objects as desired. In other words, the Simulink environment is used to control and evaluate the Simscape toolbox components.

### 3.6.1 Numerical modelling

The discrete integration approximation method is used to determine the roller induced flow based on the geometry of the pump. For this reason the pump geometry is first defined. The variables required to determine the flow are determined in the same order as they are presented in this chapter.

The trigonometric functions are first solved to determine engaging angle  $\phi$ , after which the leading edge distance can be calculated. The inflating roller angle which is based on the leading edge distance can then be calculated over the engaging angle. The maximum angle that can be used to determine the maximum horizontal length  $X$  is thus also solved and  $X$  can be calculated. The maximum volume displacement approximations can thus be calculated with these values.

A reference vector is created by defining  $dx$  by dividing  $X$  by the number of elements in  $\theta$  and incrementally increasing the vector's value from 0 to  $X$  in increments of  $dx$ . The complimentary roller angle for each incremental distance in this vector is then determined. The complimentary length can be determined based on the leading edge distance and the complimentary roller angle. This complimentary length is in the form of a matrix and is where the aforementioned hard limits are applied.

With the complimentary length determined, the radii of the collapsing ellipse can be determined and thus the area. The area is subtracted from the area of the uncompressed tube for each value in the reference vector ranging from 0 to  $X$ . Each area is then multiplied by the distance  $dx$  and summed.

A polynomial is fit to the approximated volume to be differentiated in or-

der to calculate the flow generated by the volume being displaced. Using the rotational speed of the pump, the time attributed to the angle vector can be calculated and used to determine the flow value over the time span of the engage angle. The  $Q_{ed\_in}$  and  $Q_{ed\_out}$  flow vectors are generated as a vector of zeroes with a length equal to the simulation time divided by the simulation step time  $h$ .

Based on the rotational speed and the pump geometry, the engaging and disengaging times are calculated. The roller induced flow is then added to  $Q_{ed\_in}$  and subtracted from  $Q_{ed\_out}$  with regards to when the roller engages or disengages the tube.

### 3.6.2 Simulink/Simscape

The  $Q_{ed\_in}$  and  $Q_{ed\_out}$  vectors are imported into the Simulink environment by using a repeating sequence block.<sup>1</sup> The time vector used for the sequence is equal to the simulation time span with increments of  $h = 0.001$  s. The variable-step solver `ode15s` (stiff) was selected to solve the model with a maximum step size of 0.001 s. The current sources, resistors, capacitors, and inductors are given their values in the MATLAB environment. The variables within the MATLAB workspace can be called within the Simulink/Simscape environment to derive values of certain components.

The voltage sources located on the inlet and outlet lines normalise the pressure displayed on the scopes to that of the ambient pressure in the reservoir.<sup>2</sup> The current sources have the same values of the modelled flow in mL/s. It is important to note the units used within the simulation, as the resistors, capacitors, and inductors, will have their units based on the flow. This implies that the resistance, capacitance, and inductance units are kPa·s/mL, mL/kPa, and kPa·s<sup>2</sup>/mL respectively. The pressure variables are exported to the MATLAB workspace via sinks once the simulation is completed to be saved and processed.

The simulating model is indicated in Fig. 3.22, with blue components indicating Simscape blocks and black components indicating Simulink blocks. The blocks used within the simulation are numbered from 1 to 13, indicating the thirteen different types of blocks used. Indication is made in Fig. 3.22 of the component numbers next to their corresponding components for reference. The components of the simulation are listed in Table 3.1 along with an indication of the containing library/toolbox of the component.

<sup>1</sup>Blocks refer to the library component programmed with a specific function.

<sup>2</sup>The reservoir pressure is the taken as the absolute pressure reading at the bottom of the

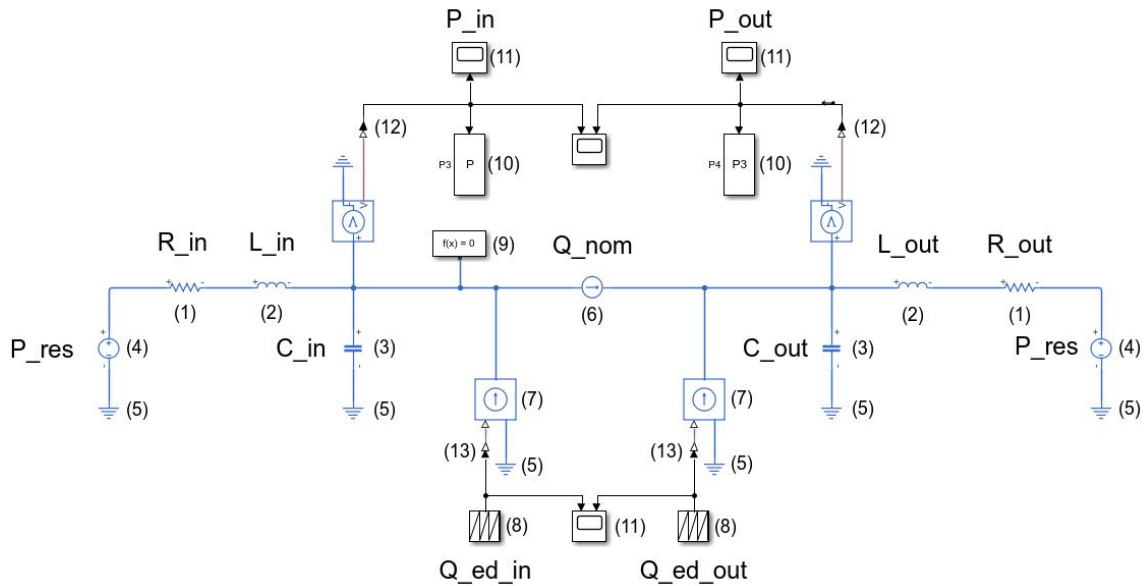


Figure 3.22: Simulink/Simscape model used to simulate the pressure pulsations of a peristaltic pump

Table 3.1: Simscape/Simulink component list used for the peristaltic pump simulation inside the Simulink environment

Item number:	Component library:	Description:
1	Simscape	Resistor
2	Simscape	Inductor
3	Simscape	Capacitor
4	Simscape	Voltage source
5	Simscape	Electrical reference
6	Simscape	DC current source
7	Simscape	Controlled current source
8	Simulink	Repeating sequence
9	Simulink	Solver configuration
10	Simulink	Sink (to workspace)
11	Simulink	Scope
12	Simulink	PS-Simulink converter
13	Simulink	Simulink-PS converter

reservoir.

### 3.7 Model verification

Information pertaining to the experimental tests and the corresponding simulations of a two-roller pump are given in [16]. Unfortunately some of the geometries of the pump are not included in the paper, such as the radial sizes of the roller and backplate. This can be attributed to a different modelling approach that focusses on the pressure dynamics of the pump, where the importance of these geometries were mitigated by data-driven modelling of the flow. Indication is however made of the roller offset radius, tube diameters, and system variables. These variables, geometry sizes, and results can be used to verify the modelling and simulation described in Chapter 3 to some degree.

The roller volume and flow rate can be validated by comparing the form of the volume displacement per unit of rotation to that of the curve outlined in [16]. The exact values will not be obtainable, as the needed geometry is not provided, however, an iterative approach can be undertaken to further study the volume and induced flow rate curves.

The peristaltic pump lumped parameter model can be evaluated with regards to the following aspects: The interval between peak to peak values of a pressure signal (period of the wavelength), periods between the variable inputs of the inlet and outlet line, and maxima and minima values of the pressure signals. These aspects are chosen to be verified as their theoretical value can be calculated, or they can be compared to the test results in [16].

#### 3.7.1 Roller volume displacement approximation

The discrete integration method for the roller displacement volume approximation can be compared to the values of the data driven model given in [16]. Because the radial sizes of the backplate and roller are not given, the volume was iteratively solved using a fixed roller offset length. The size of the backplate was set to be equal to the sum of the roller radius, roller offset radius, and twice the wall thickness of the tube as in (3.47). This assumption of the backplate length can be made, as it is indicated in [16] that perfect or near perfect occlusion of the pump achieved.

$$r_b = r_{roller} + r_{offset} + 2w \quad (3.47)$$

With the offset radius and the tube dimensions known, the roller radius was adjusted until the maximum volume resembled that of the value in [16]. The function of the volume over the angle of rotation provided in [16] is referred

to as the reference volume, and can be determined as  $V_{ref}(\theta) = -0.0001(\theta)^3 + 0.0042(\theta)^2 + 0.03(\theta) - 0.027$ . Fig. 3.23 indicates the volume approximation using discrete integration compared to the polynomial volume function of [16] as a reference. The angle of engagement of the reference volume was given as  $32.00^\circ$ , whereas the modelled approximation volume had an angle of  $29.16^\circ$ . The difference in the engaging angle can be attributed to the assumption that the tube conforms perfectly to the form of the roller. Another possibility for the discrepancy can be attributed to imperfect testing, as the tube might bend inconsistently during testing.

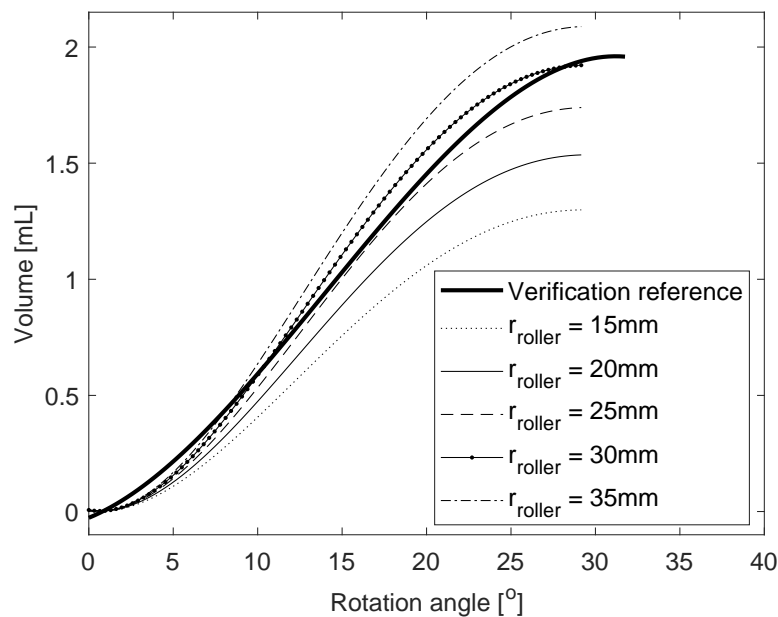


Figure 3.23: Volume approximation values plotted for varying roller sizes ( $r_{roller}$ ) over the angle of rotation of the motor with a comparison to the reference value

The roller radius size with the closest volume to that of the reference is 30 mm, however, the size is likely smaller than this due the assumptions of the modelling mentioned previously. Table 3.2 indicates the varying roller sizes with their corresponding maximum volume values and engagement angles. It is clear that if the backplate radius is dependant on the roller radius, as in 3.47, that the angle of engagement stays constant. Fig. 3.24 indicates that the more realistic roller sizes of 20 mm and 25 mm have the closest resemblance to the reference roller induced flow in terms of magnitude.



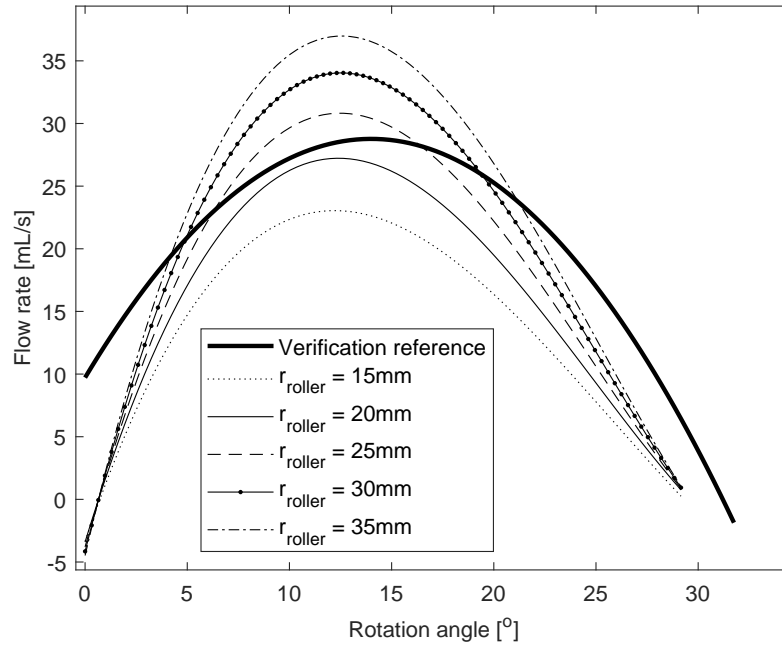


Figure 3.24: Roller induced flow value plots for varying roller sizes, adjusted for comparison

Table 3.2: Indication of maximum volume displacements and angles of engagement relational to the roller size

<b>Roller size [mm]:</b>	<b>Maximum displaced volume [mL]:</b>	<b>Angle of engagement [°]:</b>
15	1.30	29.16
20	1.53	29.16
25	1.74	29.16
30	1.92	29.16
35	2.09	29.16

### 3.7.2 Peristaltic pump lumped parameter model

In order to separately verify the values of the simulation, the reference volume shown in Fig. 3.23 was used as an input parameter to the generalised lumped parameter model. The variables of the simulation were set equal to that of the control test found in [16]. Another discrepancy regarding the resistance of the inlet and outlet arose, as the magnitude of the resistance was described as

being dependant on the flow, implying a second order relationship to the flow ( $\text{kPa}\cdot\text{s}^2/\text{mL}^2$ ). This discrepancy was solved by obtaining the average resistance value relational to the average flow of the pump, and using the average value as the resistance value. The parameters used for the verification are provided in Table 3.3, with the volume displacement of the roller defined by the function provided in [16]. The volume function is used initially in order to verify the lumped parameter model separately from the roller volume approximation.

Table 3.3: Simulation parameters used to verify the lumped parameter model

<b>Parameter:</b>	<b>Symbol:</b>	<b>Value:</b>	<b>Units:</b>
Operational speed	$N$	54	r/min
Number of rollers	$NU$	2	-
Pump contact angle	$\beta$	0	$^\circ$
Angle of engagement	$\phi$	32	$^\circ$
Reservoir pressure	$P_{res}$	1.867	kPa
Nominal flow	$Q_{nom}$	30.167	mL/s
Inner tube radius	$r_i$	4.765	mm
Tube wall thickness	$w$	1.590	mm
Inlet resistance	$R_{in}$	0.278	$\text{kPa}\cdot\text{s}/\text{mL}$
Outlet resistance	$R_{out}$	0.165	$\text{kPa}\cdot\text{s}/\text{mL}$
Inlet capacitance	$C_{in}$	0.060	$\text{mL}/\text{kPa}$
Outlet capacitance	$C_{out}$	0.060	$\text{mL}/\text{kPa}$
Inlet inductance	$L_{in}$	0.016	$\text{kPa}\cdot\text{s}^2/\text{mL}$
Outlet inductance	$L_{out}$	0.014	$\text{kPa}\cdot\text{s}^2/\text{mL}$

The relevant periods from peak to peak of the outlet and inlet pressures ( $P_{out}$  and  $P_{in}$ ) are indicated in Fig. 3.25 as  $T_1$  and  $T_2$  respectively. The period between two peak maxima values can be calculated with reference to the rotational speed and number of rollers on the pump, as in (3.48), and should be the same for the inlet and outlet.

$$T_1 = T_2 = \frac{2\pi}{NU \cdot \omega} \quad (3.48)$$

The input offset period  $T_3$ , also indicated in Fig. 3.25, defines the period of time between the peak values caused by the roller induced flow input variables for the inlet and outlet line. This period is defined by the contact angle of the pump  $\beta$ , the angle of engagement  $\phi$ , and the motor speed  $\omega$  as:

$$T_3 = \frac{\pi(2\phi + \beta)}{360\omega}. \quad (3.49)$$

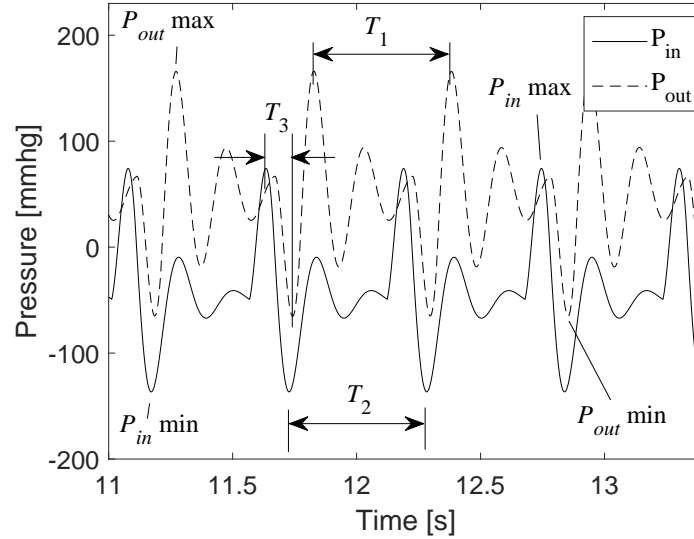


Figure 3.25: Pressure waveform plot of the simulation response indicating the outlet pulsation period ( $T_1$ ), inlet pulsation period ( $T_2$ ), input offset period ( $T_3$ ), and inlet and outlet minima and maxima

Table 3.4 indicates the values obtained from the simulation with provided flow inputs, as well as the theoretical values determined numerically. Additionally, the experimental values provided in [16] are also listed for further comparison. By increasing the outlet capacitance  $C_{out}$  by 0.0120 mL/kPa (20 %) and reducing the outlet resistance by 0.041 kPa·s/mL (25 %) the outlet pressure better resembled the experimental values of [16] as  $P_{out} \max = 144.0$  kPa and  $P_{out} \min = -51.6$  kPa.

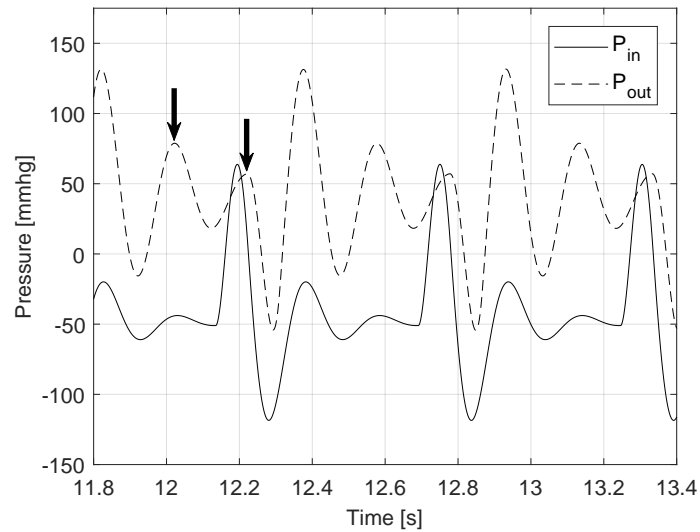
Lastly, a roller size of 22.5 mm was specified for the displacement approximation, as the correlating roller induced flow has the exact same magnitude as that of the reference, and used for a final simulation comparison. Fig. 3.26 indicates the pressure response of the simulation to the approximated flow inputs with adjusted outlet capacitance and resistance values.  $P_{out} \max$  and  $P_{out} \min$  are equal to 133.6370 kPa and  $-54.69$  kPa respectively, with  $P_{in} \max$  and  $P_{in} \min$  equal to 63.90 kPa and  $-119.69$  respectively. The experimental values of the control experiment of [16] are also provided for comparison. The values are not identical but show the very close correlation in the pressure waveform over time. The largest differences between the reference (control test) values and

Table 3.4: Simulation results and comparison to theoretical and reference values, with adjusted parameter results indicated in brackets

<b>Variable:</b>	<b>Theoretical value:</b>	<b>Simulation value:</b>	<b>Experimental reference from [16]</b>	<b>Units:</b>
$T_1$	0.5556	0.5565	$\approx 0.55$	s
$T_2$	0.5556	0.5558	$\approx 0.55$	s
$T_3$	0.0989	0.1076	$\approx 0.1$	s
$P_{out}$ max	-	165.8 (144.0)	$\approx 140$	kPa
$P_{out}$ min	-	-65.3 (-51.6)	$\approx -55$	kPa
$P_{in}$ max	-	74.2	$\approx 70$	kPa
$P_{in}$ min	-	-136.6	$\approx -135$	kPa

simulation values are found on the outlet pressure. The wave is seen to oscillate with larger pressure values than that of the reference. These oscillations, which refer to the second and third peaks, are indicated by the arrows in Fig. 3.26a.

This discrepancy could possibly be due to the loss of the intermediate capacitor, which resembled the tube segment between the rollers transporting fluid. This possibility is further motivated due to the fact that increasing the outlet capacitance increases model accuracy in this case.



(a) Simulated control test with approximated induced flow input

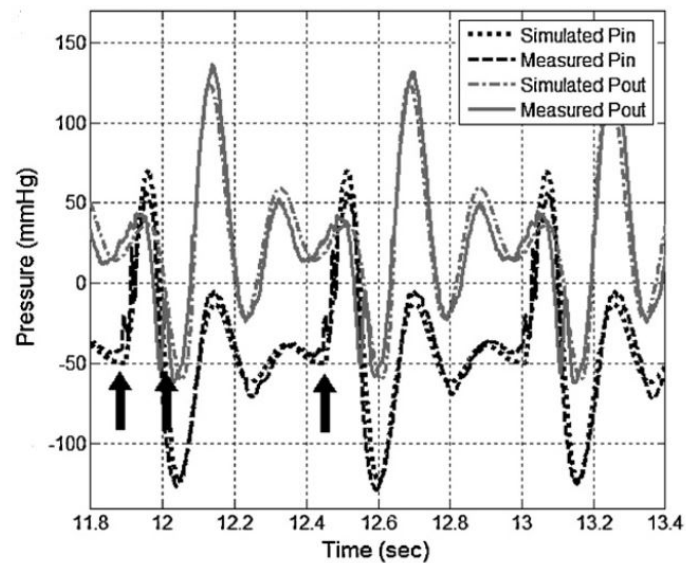
(b) Moscato et al. control test (reprinted with permission)<sup>3</sup>

Figure 3.26: Verification of (a) the generalised lumped parameter model with modelled inputs with respect to (b) the pressure response of Moscato et al. [16]

<sup>3</sup>Reprinted from Medical Engineering & Physics, Vol. 30, F. Moscato et al. [16], Pressure Pulsations in Roller Pumps: A Validated Lumped Parameter Model, Pages 1149–1158, Copyright (2008), with permission from Elsevier.

## 3.8 Conclusion

This chapter provides insight on the modelling of a roller-type peristaltic pump using the geometry of the pump to obtain flow variables. The flow variables are used to attempt to model the pressure response of the system the pump is integrated with in continuous rotation.

Three roller volume approximation techniques are described for modelling the total volume displaced of the roller during complete occlusion. The discrete integration approximation offers a continuous volume displacement value during the engaging/disengaging phase of the roller, whereas the other approximations are not suitable for this. The accuracy of the approximation methods are reliant on the roller radius to backplate radius ratio, where smaller ratios imply better accuracy. This may imply that the approximation methods and modelled flow rates are not suitable for the single-roller peristaltic pump designs, commonly associated with larger roller sizes. A straight inlet/outlet tangent to the backplate should be considered a vital parameter to the approximations, and should ensure accuracy for pumps with smaller roller to backplate ratios.

A generalised lumped parameter model is derived with the work of Moscato et al. [16] and is a reduced form of this model. The generalised model is motivated by certain discrepancies found regarding flow characteristics and inputs of the model it was derived from. Additionally, the new model allows for modelling pumps with varying numbers of rollers, provided the parameters are realistic with respect to the physical limitations of the pump.

The peristaltic pump model was simulated in Simulink/Simscape with the parameters and input variables calculated in MATLAB. The results are verified by comparison to the experimental results provided in [16] with varying geometrical parameters i.e. roller radius size and backplate radius size. The simulation results show strong correlation with the provided experimental values, and exhibit predictable behaviour with regards to the input variables.

As the peristaltic pump is considered to be a positive displacement pump, a pump design can be specified using the modelled flow rates  $Q_{avg}$  and  $Q_{nom}$ , and pump volume displacement per rotation  $V_{rot}$ .

### Peristaltic pump design

---

#### 4.1 Introduction

This chapter discusses the design of the peristaltic pump to be manufactured using three dimensional (3D) printing assisted by the model developed in Chapter 3.

The material and printer selection, as well as the design considerations are discussed first to ascertain the design constraints and specifications discussed thereafter. The design considerations focus on the aspects that may influence the method of designing and developing the pump's parts. The section includes a look at software selection, infill style and percentage, and topology optimisation.

The physical constraints following the design specifications section are mostly derived from the assumptions made in the modelling section. The model is then used to provide design specifications of the pump for the hypothetical application as an electro-hydrostatic actuator (EHA) with certain required characteristics.

After the design specifications have been reviewed, the two concept designs generated are detailed and discussed. The concept design with the most desirable characteristics is selected and iteratively improved upon until the pump has met all the desired characteristics. The chapter is concluded with a discussion on the final design and the manufacturing method of the pump.

## 4.2 Material and printer selection

Polyethylene terephthalate (PETG) has adequate properties for mechanical parts in polymer products and is readily available at the manufacturing facility. Another option for the Prusa printer would be polylactic acid or polylactide (PLA), however it does not have better material characteristics for this purpose. In addition, PLA tends to be more brittle and has less mechanical strength.

The Prusa MK2.5 and Prusa MK3 have substrate bed dimensions of 210 mm by 210 mm and a maximum print height of 250 mm. These dimensions limit the parts to be printed with regards to maximum size. Both of these printers do not offer dissolvable support and the part must therefore be optimised for minimum support.

Hoses used in higher pressure hose type peristaltic pumps require a larger force to occlude the tube. This implies that there will be a stronger material required for the backplate and connection of the roller. The printer is limited by the strength of the material selected for manufacturing, and thus tube-type roller pumps would be better suited for this application.

Of the tube types available, silicon and Autoprene polymer tubes have the best characteristics for the use of hydraulic actuation with regards to additive manufacturing. Autoprene is more resistant to wear but requires a larger force to collapse than silicon. Silicon is the most common material for peristaltic pump process tubes [3] and is one of the softer tube materials.

In order to negate the pump being limited by the strength of printed components, silicone is selected for the tube material. This is due to the availability of the tube, the lower price of the tube, and the low force required to collapse the tube. The selected tube material is a high strength silicon polymer available with the Versilon SPX-60 FB tube manufactured by Saint-Gobain.

Compliant tubes, such as those used in peristaltic pumps, are associated with a minimum bend radius. This radius defines the radius that the tube can be bent at a constant radius before the stress between the inner and outer radii causes the tube to collapse. This is an undesired collapse as it can obstruct flow and cause inaccuracies regarding the modelling. The bend radius is correlated to the inner and outer radius of the tube and should be taken into consideration when designing the backplate with dimensional restrictions.



Since the material used for the pump is relatively soft and is manufactured in a method that offers flexibility, it should be considered designing the parts to allow for external strength and support. This external strength and support can be applied with common construction items such as nuts and bolts.

## 4.3 Design considerations

### 4.3.1 Software

Various vendors offer slicing software and licenses. CAD software is usually used in professional settings and licenses can vary in price. Some CAD programs are open source and free to use, and offer similar functionality when designing parts. Professional CAD programs, however, offer simulation packages that allow for design studies on pre-designed parts. Some of the professional computer aided design (CAD) programs include AutoCAD, SOLIDWORKS, Autodesk Inventor, CATIA, Siemens NX, and TurboCAD. Slicer programs also offer similar functionality with each other, and paid versions usually add some degree of complexity or customisation. Open source slicer software is common and usually meet all the requirements needed to successfully additively manufacture a part. Common slicer programs include: Cura, Slic3r, OctoPrint, Simplify3D, Repetier-Host, and IdeaMaker.

Some programs offer built in CAD and slicing functionality, such as Siemens NX, while others allow for slicing software to be add-in applications. CAD and slicer vendors offer similar results in terms of additive manufacturing. Thus focus will not be placed on the specifics of the software. There are, however, design considerations to be taken into account with regards to slicing. For simplification of the study the designs will be made on Solidworks and sliced in Cura. The slicing considerations discussed are thus created on Cura with the simplistic part used for demonstration purposes (a block) made in Solidworks.

### 4.3.2 Slicing: infill, orientation, and support

The two largest factors to take into account when slicing are time and design. Depending on the settings on the slicing program the print time can easily be halved. The slicing of the component should also not neglect the design quality regarding strength, appearance, and functionality. Time and material (and therefore cost) can be reduced by removing internal material from the part. This can be done by housing an infill pattern such as those in Fig. 4.1 inside the external shell. The infill pattern can severely reduce the strength of the part if it is not

selected appropriately.

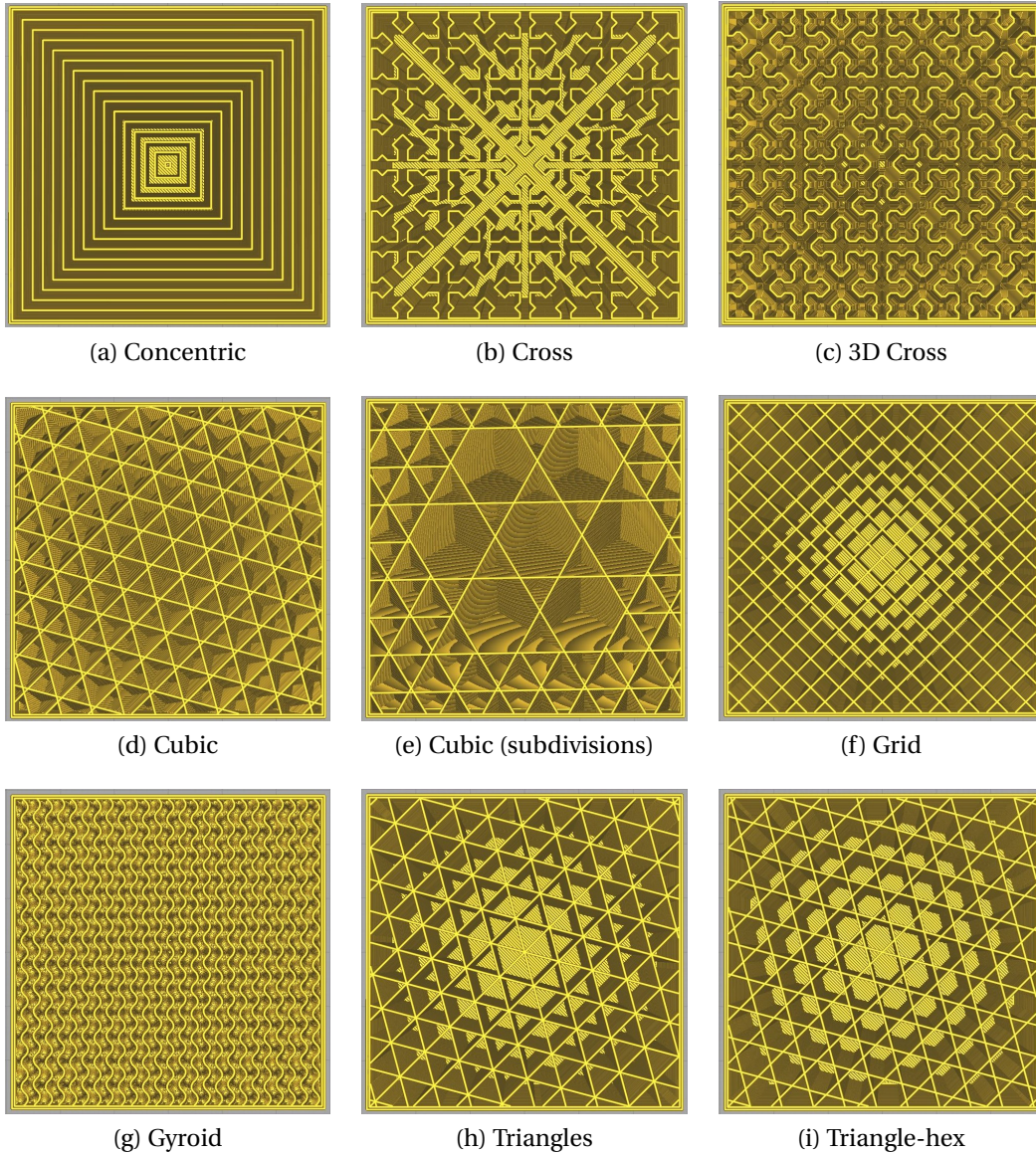


Figure 4.1: Renderings of different infill patterns of a cube on Ultimaker Cura with 25 % infill

The infill density, as indicated in Fig. 4.2, fills the internal volume of the part as a percentage of the total volume. A larger density implies smaller patterns, and a larger mass of the part. The selection of infill pattern and density is design

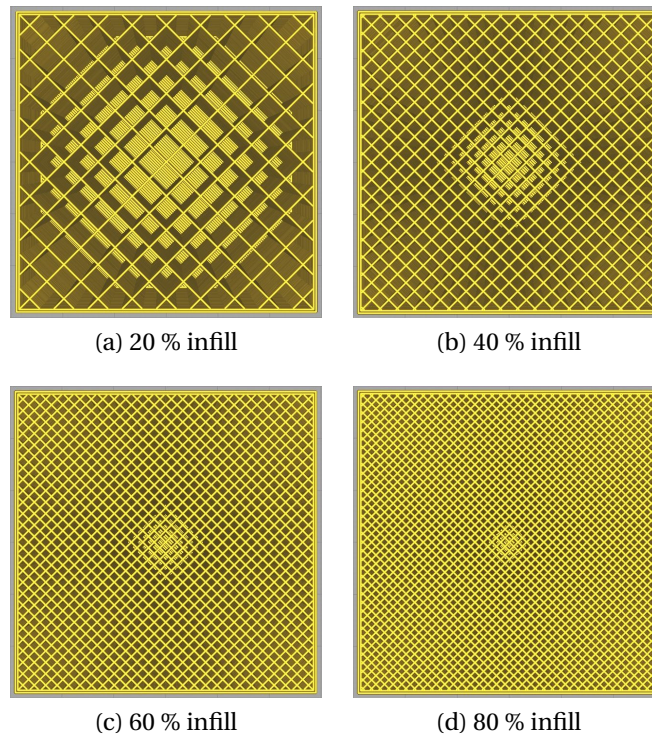


Figure 4.2: Renderings of different infill percentages of a cube on Ultimaker Cura with grid infill pattern

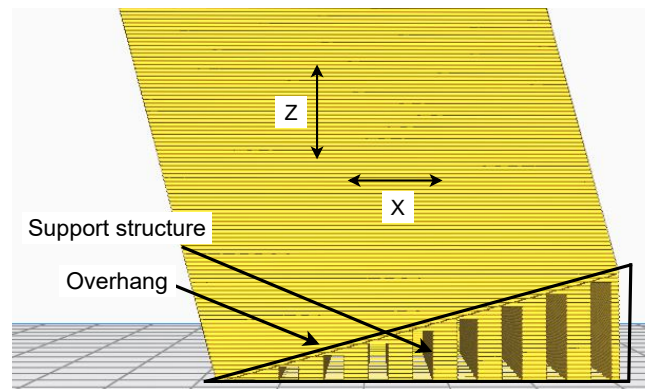


Figure 4.3: Rendering of a sliced preview of an off-balance block on a build plate to simulate an orientation induced overhang and support structure

dependent, as it will vary from part to part.

Some additive manufacturing technologies allow the use of support struc-

tures as a foundation for overhangs. Overhangs are parts of a design that do not have a solid foundation between the layer and the bed or printed material. Fig. 4.3 presents an overhang by purposefully orientating the block with a  $15^\circ$  incline. Support structures were then generated, which would be required in this case for a successful print.

Fig. 4.3 also implies that the orientation of the part must be considered. The design and orientation that require the least amount of support structures is preferable as support structures may leave protrusions on the surface of the part. These protrusions would require surface finishing of the part before it is complete.

### 4.3.3 Topology optimisation

One of the major advantages of additive manufacturing is an additional dimension for topology optimisation. Topology optimisation is the optimisation of a loaded structure (statically determinant) with regards to the amount of material that the structure contains. The effects of removing material from the structure's design impacts its mechanical strength, weight, and dimensions. This optimisation offers design considerations that are considerably lighter while adhering to a standard of structural integrity [61, 62], indicated in Fig 4.4. The change in dimensions also affects flow around the part and is thus also used in optimising thermal conductivity and viscous friction where flow is concerned [63, 64].

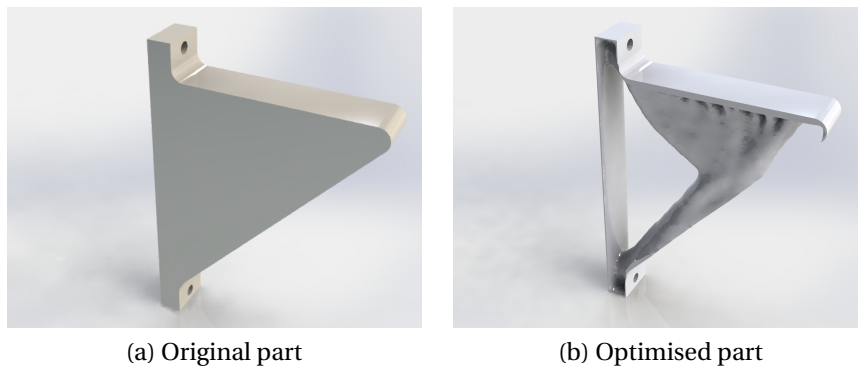


Figure 4.4: Rendering of a wall bracket before and after a topology optimisation design study in Solidworks for a reduction in mass with part strength as the constraint

The degree to which additive manufacturing can optimise a part is unique as

additive manufacturing generates the part, whereas subtractive manufacturing techniques (such as computer numerical control (CNC) machining) remove material from the raw material in order to give the desired form. Additive manufacturing especially useful in the aerospace industry where less material implies less material cost and better fuel efficiency for an aircraft with less weight.

Topology optimisation falls outside of the scope of this study and will therefore be ignored. Topology optimisation however remains a factor to be taken into account in additive manufacturing design, especially in models requiring high strength to mass ratios.

## 4.4 Physical constraints

The physical limitations of the pump require at least one roller to be occluding the process tube during rotation to maintain a static pressure. This requires that the pump's outer casing, which the tube is compressed against, should be designed based on the number of rollers implemented in the pump. For example, a pump with 1 roller (such as a cement pump) needs an outer casing in which the roller is in contact with the outer casing for  $360^\circ$ . For two symmetrically placed rollers the pump requires an outer casing in which the rollers are in contact for at least  $180^\circ$ , for three rollers  $120^\circ$  etc.

In order to remain accurate to the modelling of the pump the pump must be designed to cater to the modelling assumptions. This implies that the pump should be designed to be symmetrical around the  $y$ -axis. The rollers must be symmetrically placed around the central axis of the motor. The inlet and outlet must be straight and enter/exit the pump tangent to the outer casing.

The pump should be designed to fully occlude the tube, which implies that the outer casing radius be no larger than the sum of: The roller radius, the offset radius, and twice the tube wall thickness. The tube pump must exhibit no leakage, and must, therefore, have a minimum of one roller occluding the tube at all times.

The housing of the pump, or the largest parts thereof, cannot exceed the dimensions of the build plate and build height of the Prusa printer. To negate an undesired collapse of the tube the radius of the backplate should not be smaller than the minimum bend radius of the tube specified. Although the sum of the offset radius and the roller radius cannot exceed that of the backplate radius, the tube wall thickness and desired compression thereof should be considered.

The roller size has an impact on both the pulsation size (indicative of the volume displaced), and the resistance of motion encountered by the roller. Larger rollers will create a larger pulsation but will encounter less resistance. This is due to the angle that the normal force of the pressure acts on increases as the roller size increases. The resistance on the roller ultimately affects the maximum working pressure as it results in larger moments around the central shaft and should be taken into account.

The roller size is however limited by the housing which holds the roller. Increasing the rollers size implies that the central diameter of the housing, which connects the rollers to the shaft, must be reduced. A reduction of this diameter reduces the strength, and can ultimately cause failure of the housing and thus of the pump under large moments/torques.

## 4.5 Design specifications

The effects of tolerances and wear can be minimised, or even mitigated, with the use of external parts that are machined. Steel fasteners such as screws, nuts, and bolts can be used to increase part strength as structural members where applicable. Friction between moving parts can be mitigated much in the same way as most manufactured components. This is usually done with the likes of bearings and brushes. Although plastic bearings and brushes do exist, the wear on these parts would require constant maintenance.

The pump design for actuation purposes should negate leakage while minimising pulsations. The possibility of fluid passing one roller is low, but not impossible. This can occur if the tolerance of the pump part occludes the tube weakly and the discharge pressure is high enough. The compliant tube walls can also compress due to the fluid pressure, and will allow fluid to pass the area of occlusion if not sealed properly. This implies that the forced occlusion should compress the tube to some degree. If however there is still leakage due to large pressures, a second roller on the tube could help to negate fluid to pass further.

For this reason the pump design will focus on a three-roller design with the tube always fully occluded by at least two of the three rollers during operation.<sup>1</sup> With three rollers evenly distributed around the roller housing it would imply

---

<sup>1</sup>The pump design is created with the model of three rollers in the pump housing, however, a two-roller housing will also be used within this pump design for experimental purposes.

that the housing must have a contact surface of at least 270 °.

The compression of the tube induces a friction on the roller opposite to the direction of motion. To reduce this, the compression of the tube should be minimised. However, compression will be necessary to compensate for the wide tolerances caused by the printer. Thus a compression of 1 mm is specified for the design.

From the modelling section, the maximum flow rate and average flow rate of the peristaltic pump design can be calculated. The flows of the pump are directly related to the operational speed of the pump and should thus be calculated regarding the operating speeds of the motor.

A stepper motor will drive the pump as it has a much lower cost than a servo motor, as well as offering finer degree of control when compared to a DC motor. This decision is further motivated by the high static holding torque stepper motors can provide, which would allow the pump to be tested for hydrostatic stability.<sup>2</sup> It should be noted that a stepper motor's torque to motor speed ( $\tau/r/\text{min}$ ) curve is not constant with the maximum torque available at lower  $r/\text{min}$  values (usually between 0-500  $r/\text{min}$ ). A 3 Nm Nema 23 stepper motor (model number 57BYGH115-003) can be selected as the driver of the pump as it offers high torque with an adequate proportional size to the pump. However, in order not to damage the pump, the maximum rotational speed of the motor will be capped at 200  $r/\text{min}$ . As the model does not take into account the torque supplied by the motor, any motor can theoretically be used, as long as it can overcome the friction of the rollers occluding the tube.

The flow rate can be specified by taking into account the size of hydraulic cylinders associated with small robotics. Hydraulic cylinders with bore sizes less than 50 mm are commonly referred to as micro-hydraulics or micro-cylinders. C & C Hydraulics offer double acting hydraulic cylinders with bore sizes of 20 and 25 mm. They offer stroke lengths of 25 mm, 50 mm, 80 mm and 100 mm for both cylinders [65]. Bansbach offers hydraulic cylinders with bore sizes between 13 mm and 24 mm with stroke lengths of 20 mm to 200 mm [66]. Hydrokit offers a hydraulic cylinder with a bore size of 25 mm and a stroke length of 150 mm [67].

The hydraulic cylinder from Hydrokit will be used as a hypothetical actuator to specify design criteria of the pump. It would be desirable for the piston to

---

<sup>2</sup>The hydrostatic stability here refers to the degree that a pressure differential can be maintained between the inlet and outlet over time.

move as fast as possible with reference to realistic values. A stroke length of 150 mm can realistically be moved in a span of 1 second. Thus for the design goal, the pump's average flow at the maximum r/min value should displace the volume of a piston with a bore size of 25 mm and a stroke size of 150 mm in roughly 1 second. This would imply an average flow of 73.631 mL per second at 200 r/min.

The sizing of the tube can be arbitrary but should not be too large, as larger tubes have lower working pressures. However, if the tube is too small it cannot adhere to the desired flow rate. For this reason, a comfortable inner diameter of 10 mm can be selected for the tube size. The selected tubing available has a tube with 10 mm inner diameter and 14 mm outer diameter, implying that the specified compression of 1 mm would account for 25% of the wall thickness. This selected tube has a minimum bend radius of 48 mm.

The values of the radius of the backplate, roller, and offset length were iteratively adjusted in the model provided in order to find desired lengths that satisfy the design goals. For the specified maximum average flow rate and maximum motor speed, the radius of the backplate can be specified as 63 mm, with a roller radius of 20 mm, and an offset radius of 40 mm. The distance to the centre of the tube is thus equal to 56 mm. This is larger than the minimum bend radius and adheres to the limitations of the build plate. The backplate radius also allows for additional width for the pump housing and the backplate to be added without exceeding the build plate dimensions.

With the roller radius of 20 mm and the offset length of 40 mm, the central axis that couples to the motor shaft can have a maximum radial limit of 30 mm. This limit is calculated by the difference of the offset diameter and the roller radius in (4.1) as indicated in Fig. 4.5. This is an ideal value however, and tolerances should be accounted for, thus the section cannot be equal or greater to this value.

$$r_{coupler} < \frac{2r_{offset} - r_{roller}}{2} \quad (4.1)$$

The roller size is acceptable with regards to the offset diameter and the tube size. For a roller size of 20 mm, an inner tube diameter of 10 mm, and an outer tube diameter of 14 mm the volume that the roller displaces during full occlusion can be approximated. The flow pulsation characteristics associated with the design are determined with regards to the integration method in the modelling section. The length value used to determine the volume of the roller as the motor rotates over the angle of engagement for the respective roller angle is indicated



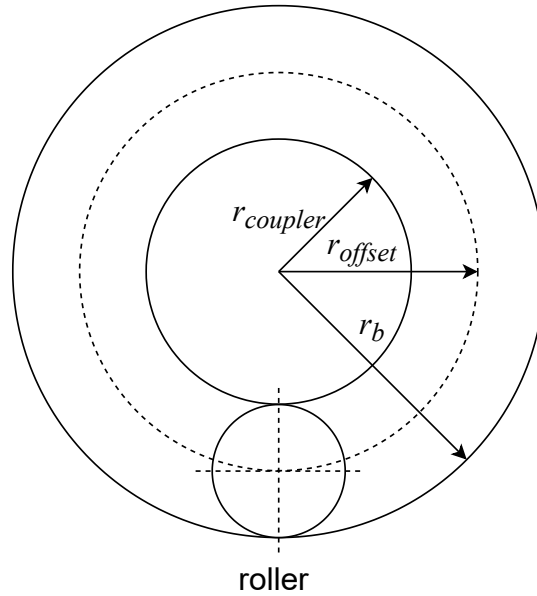


Figure 4.5: Illustration of maximum coupler size with respect to the backplate radius, offset radius, and coupler radius

in Fig. 4.6.

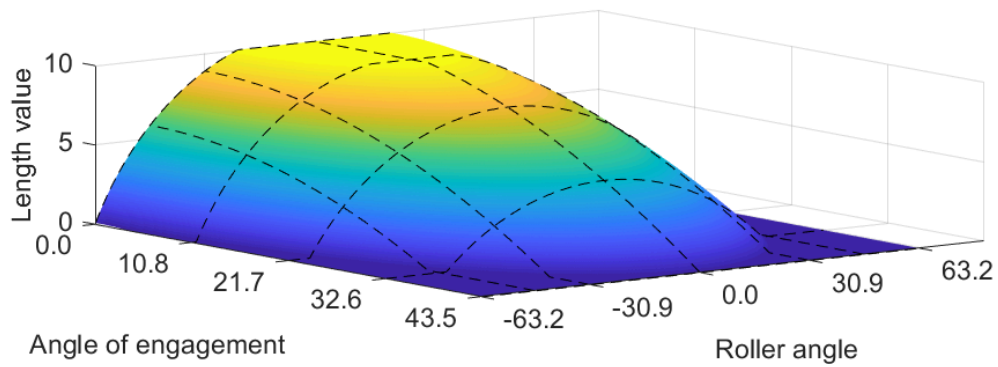


Figure 4.6: Length value across the roller angle  $\{-\lambda : \lambda\}$  as the roller engages the tube over the angle  $\theta$  for the specified design

The cylindrical roller volume displacement approximation of the specified roller and tube is equal to 2.81 mL, the area fraction approximation volume is equal to 2.06 mL, and the integration approximation volume is equal to 1.97 mL

(indicated in Fig. 4.7).

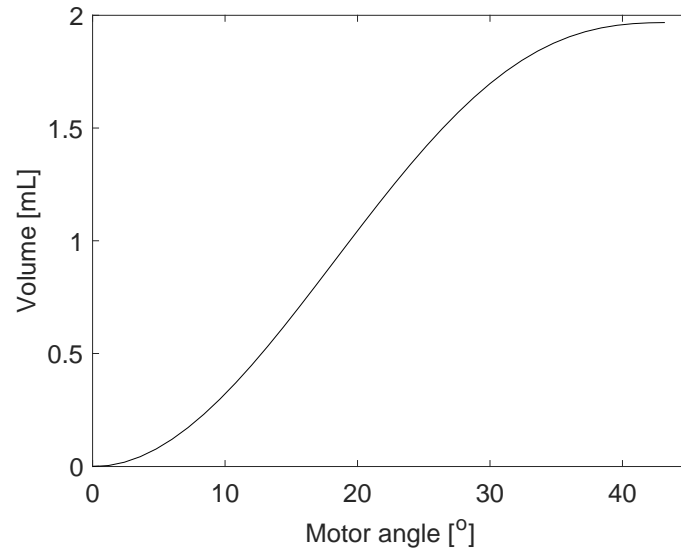


Figure 4.7: Integration roller volume displacement values over the rotational motor angle for the designed pump

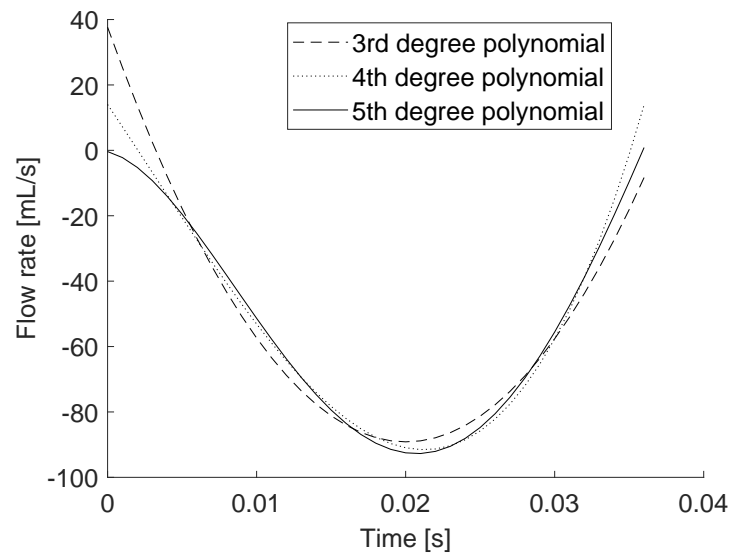


Figure 4.8: Roller induced flow values over time for a disengaging roller with the specified design parameters for various volume function polynomial orders

The maximum roller angle  $\lambda$  for the design is calculated as  $63.2^\circ$  with the

Table 4.1: Table of peristaltic pump design specifications

Parameter:	Symbol:	Value:	Units:
<b>Hydraulic specifications</b>			
Cylinder bore size	-	25	mm
Cylinder stroke size	-	150	mm
Translational time	-	1	s
Maximum operating speed	$N$	200	r/min
<b>Pump specifications</b>			
Roller radius	$r_{roller}$	20	mm
Backplate radius	$r_b$	63	mm
Roller offset radius	$r_{offset}$	40	mm
Number of rollers	$NU$	3	-
Contact angle	$\beta$	$\geq 30$	$^\circ$
Flow rate (at maximum speed)	$Q_{avg}$	73.63	mL

angle of engagement  $\phi$  equal to  $43.5^\circ$ . With a motor speed of 200 r/min it will take 0.0363 seconds for the roller to move from the disengaging position to the disengaged position. The associated flow generated by the roller as it disengages the process tube at 200 r/min is indicated by Fig. 4.8. The theoretical maximum value of the flow pulse generated by the roller is equal to 92.72 mL/s.

Table 4.1 indicates the design specification pertaining to the development of a peristaltic pump from this section in a summarised form. The hydraulic specifications are purely hypothetical and are used to simulate a situation where specific design requirements of a peristaltic pump are needed. The hypothetical situation in this case is to fully translate a hydraulic piston (housed within a hydraulic cylinder) over the stroke length within a specified time at a certain operating speed. The model outlined in Chapter 3 is used to iteratively solve the required offset and roller radial lengths needed to achieve the design criteria, namely average flow.

## 4.6 Concept designs

The initial concept designs had a concave (circular) raceway for the tube, as it was expected to better collapse the tube than a flat raceway. It was noted that the majority of the pumps did not have concave raceways. Testing and iteration later revealed why circular raceways were not present on the designs reviewed in the literature study.

The modelling initially reflected the circular raceway design choice by utilising the area between two intersecting circles  $A_{circ}$  rather than the area of an ellipse as in the previous section. The area was calculated based on the inner radius of the tube and the roller height radius  $r_h$  indicated in Fig. 4.9. Interestingly, the model yielded similar results of that described with an elliptical area, however, it was not included in this study as it was not applicable to the final design.

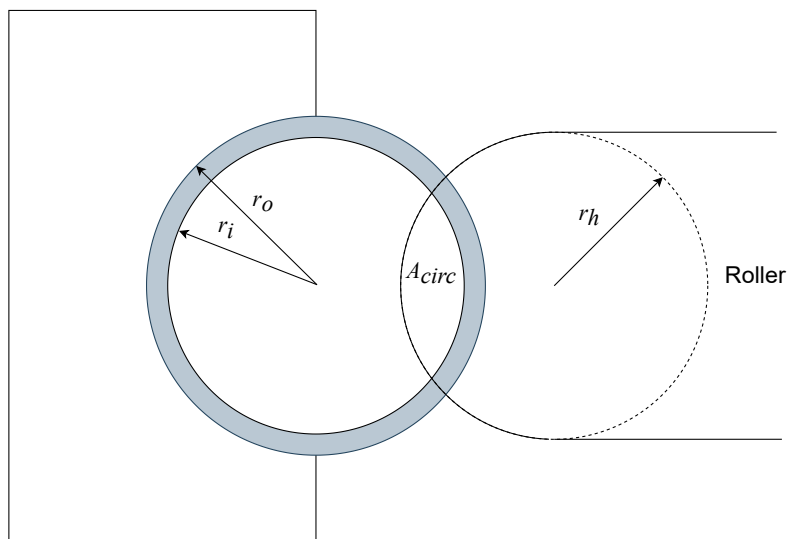


Figure 4.9: Illustration of the area of intersecting circles used for circular raceway modelling

Two concept designs were initially created to form an idea of how the pump should work. The two designs differ mainly by the number of inlets and outlets to the pump. The majority of the designs are similar however as there is a general design type for rotary peristaltic pumps.

The best suited design is selected and iteratively improved by manufacturing, testing, and revision indicated by the flow chart in Fig. 4.10. The iterative design and construction process is made simple with additive manufacturing. Once the design meets all the requirements and its operation is satisfactory, it is then finalised with indication of specific parts used.

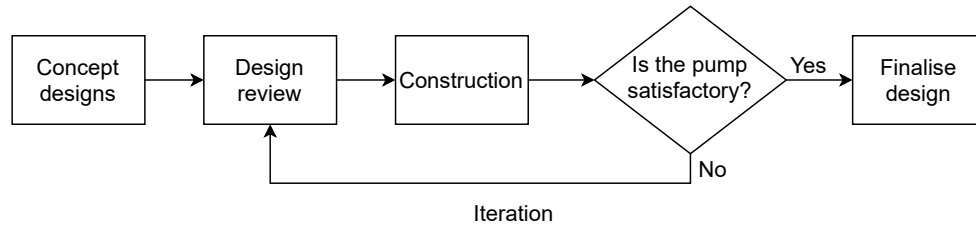


Figure 4.10: 3D printed peristaltic pump design process flow chart

### 4.6.1 Concept A - Multiple circular raceways design

Concept design A (indicated in Fig. 4.11) houses multiple circular raceways in one pump. The idea of this design is that the process tube can be routed in several ways with one pump. This design can allow for up to four tubes to induce flow simultaneously with a parallel configuration. The design can also allow for one tube to be used in a series configuration for all four stages. The series configuration should theoretically minimise leakage and increase the maximum operating pressure. The parallel configuration should theoretically increase flow speed. This would however increase the torque that the pump incurs.

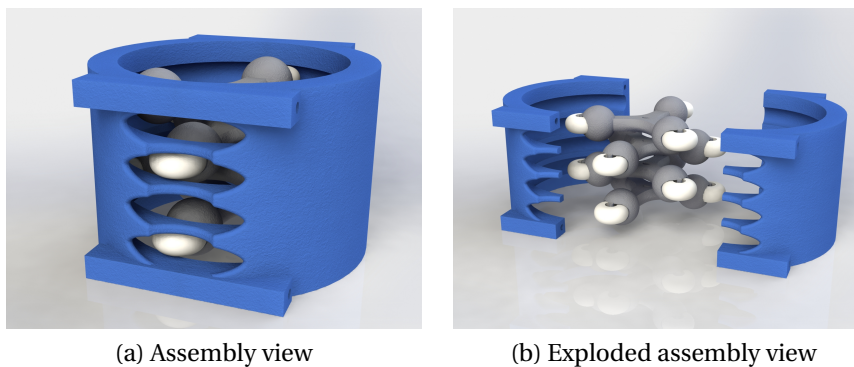


Figure 4.11: Photo-realistic rendering of the concept A Solidworks design

The design uses four roller housing assemblies (structures that hold the rollers); one for each stage and offset  $180^\circ$  from the housing above and below. This offset is to mitigate the large pulsations that might occur with a parallel configuration should all four housings be aligned. Thus, instead of all four compartments simultaneously inducing a pulse, two compartments will induce a pulse at a time.

If a series configuration were to be used, the largest resistive torque imparted on the motor would come from the housing at the pump discharge. The pressure would be reduced across the other rollers from the other housings and thus impart a lower torque over those housings, neglecting the effects of friction.

The pump housing consists of two components that are symmetrically identical to one another. The housing comprising two components is split where the suction/discharge openings are through the entirety of the housing in a straight line as indicated in Fig. 4.11b.

### 4.6.2 Concept B - One circular raceway design

Concept design B only contains one circular raceway and roller housing, but allows for more sections to be stacked on top of one another. This allows for more versatility as many application only require one peristaltic pump section. If needed, more could be stacked with a parallel or series configuration, such as that in concept A. This design is somewhat simplified and does not attach along the suction/discharge openings.

The pump housing consists of two parts that are not symmetrically identical and are named the front and back parts indicated by Figs. 4.12a and 4.12b. The front part of the pump housing contains the openings for the tube to be inserted into the pump. The openings merge into the raceway that travels along the inside of the pump. The back part of the pump housing only contains the raceway for the tube.

The two parts are held together by brackets protruding from the circular housing of the pump. The surface is flat on the top and bottom as to allow more pump housings to be stacked indicated by Figs. 4.12c and 4.12d. The roller housing is similar to that of concept A and indicated in Fig. 4.13.

### 4.6.3 Concept design discussion

Concept design A will be more difficult to manufacture than concept design B as there are more overhangs. This will require more support structures, especially at the openings for the tube. This is especially problematic regarding the overhangs and support structures. Concept design A requires the material separating the openings to be printed on supports, which then requires supports between the current separation and the following separation of the upper stage. This is not advisable, as a structure built on supports can be slightly inaccurate. If supports are further built on this structure in order to uphold another structure the

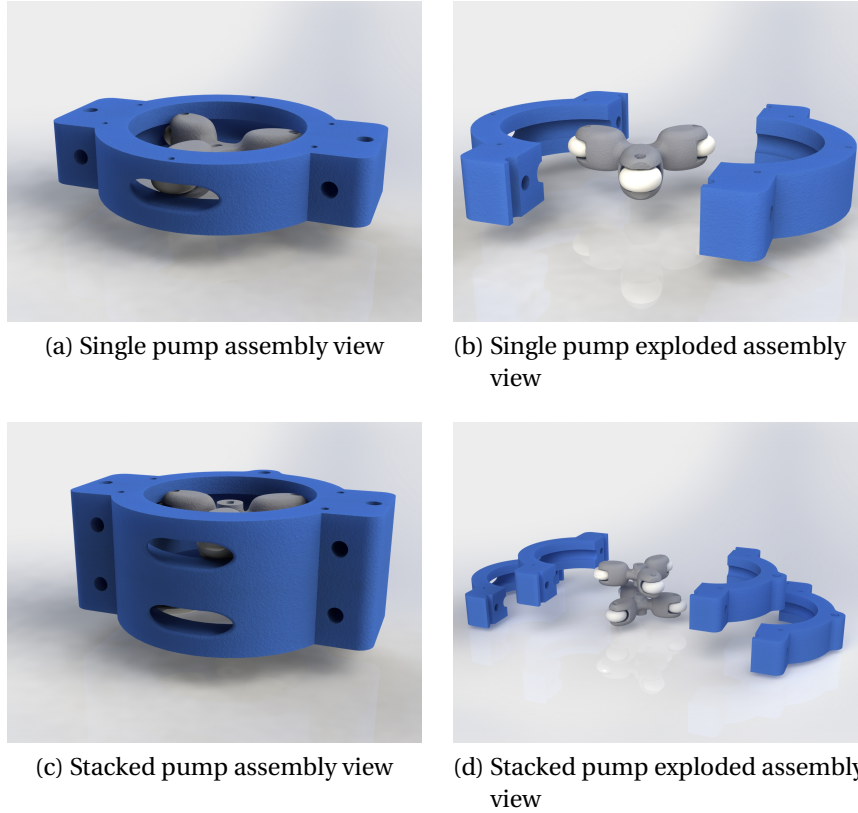


Figure 4.12: Photo-realistic rendering of the concept B Solidworks design

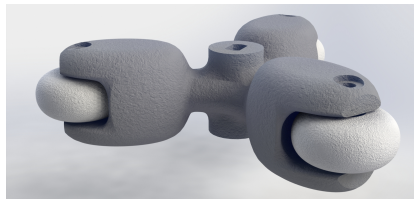


Figure 4.13: Photo-realistic rendering of the roller housing assembly for concept designs A and B

severity of the inaccuracy can increase and print failures can become common.

Concept design B offers more versatility than concept A and has the ability to operate in the same manner as concept A. Concept B would allow for faster construction times as it is a smaller design for one pump. Thus concept B is best suited for the peristaltic pump design.

## 4.7 Iterative design improvements

A major design flaw was recognised with the concept designs upon the first construction. The curved raceway induced an extremely large resistive force on the roller, prior to external pressure being applied. This was due to the tube collapsing around the concave roller. The normal force  $F_n$  in this respect causes a friction  $f$  to occur during rotation of the roller. The forces that induce this friction are indicated in Fig. 4.14.



Figure 4.14: Illustration indicating normal forces that create resistance on the concave roller from the concave raceway design

The first design iteration (indicated in Fig. 4.15) improved upon the roller and the raceway design. The raceway was changed from a circular shape to a flat square shape indicated by Fig. 4.16. The roller was also iterated to accommodate this change. This design is more closely related to the model and gave insight into the modelling of the peristaltic pump.

The revised roller design required a new roller housing to be designed shown in Fig. 4.17. This is due to a larger vertical length required to collapse the full length of the diameter of the tube. The new housing is more simplistic in geometry than the previous iteration and reduces required print supports. The housing consists of a top part and bottom part that are connected by a central protrusion. This protrusion is where the shaft connects to the roller housing. The new design allows this section to be thicker and longer, implying a larger torque can be applied to the housing. The housing is held together by four screws located symmetrically around the central protrusion.

The largest force that the roller housing incurs is the radial normal force from the collapsing of the tubes against the backplate and the torque at the centre of the housing. The revision better accommodates these larger forces. Complexity



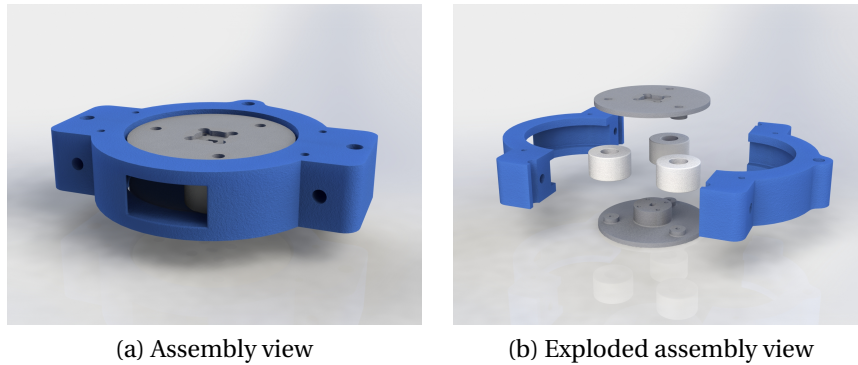


Figure 4.15: Photo-realistic rendering of the first iteration and design improvement of the peristaltic pump design

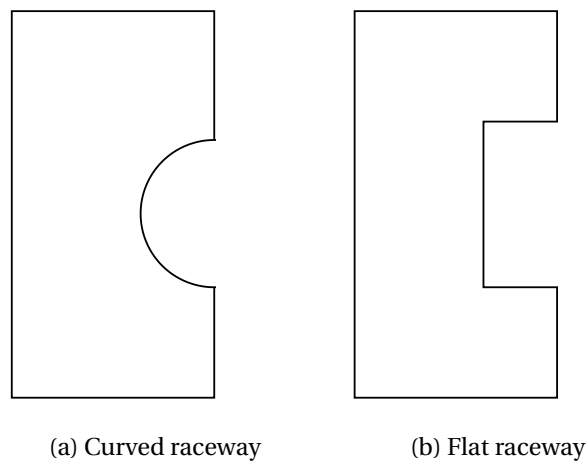


Figure 4.16: Illustration of the process tube raceway design improvement from a circular form to a square/flat form

was added to the roller by allowing the roller housing to protrude slightly where the roller is attached. These protrusions are to strengthen the roller housing and act as a guide for the roller as the pump is assembled. The bearings that the rollers rotate around are held in place by tight tolerances in the centre of the roller. The amount of supports needed for the roller remained roughly the same, but were shifted from the outside of the roller to the inside. The supports required for the rollers before the design review, and after, are indicated by the dotted lines on the cross-section renders in Fig. 4.18.

The initial designs had a total occlusion range of  $260^\circ$ . This would cause

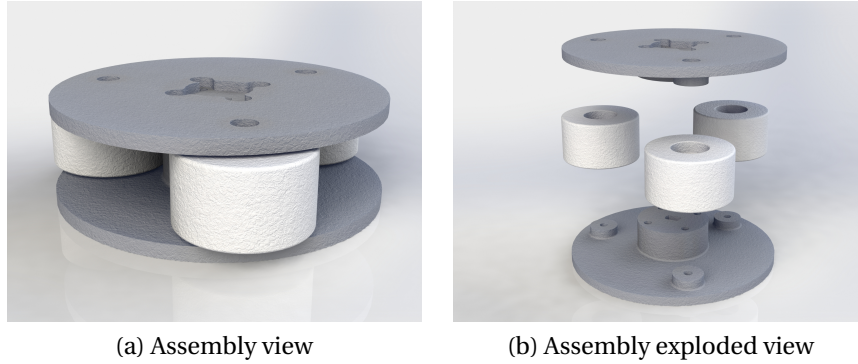


Figure 4.17: Photo-realistic rendering of the revised roller housing assembly associated with the first revision

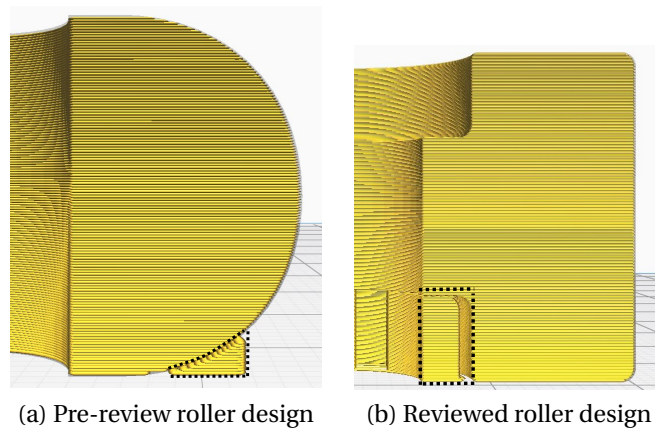


Figure 4.18: Rendering image of the required support structures for the roller design before and after revision

the tubes to bend past the minimum bend radius at the opening of the pump before being connected to the system. To mitigate this bend the occlusion range was reduced to the minimum range specified prior of  $240^\circ$ . This was done by changing the contact angle specified in Chapter 3, which alters the tangent inlet/exit angle. The exit/inlet is perpendicular to this angle, indicated by the construction lines in Fig. 4.19

It was noted that the pump would pull the process tube through the pump in the opposite direction of rotation. To counteract this, an external lip was added where the T-coupling could be held in place. A T-coupling was used in this case, as the pressure sensors would be inserted directly before and after the pump for

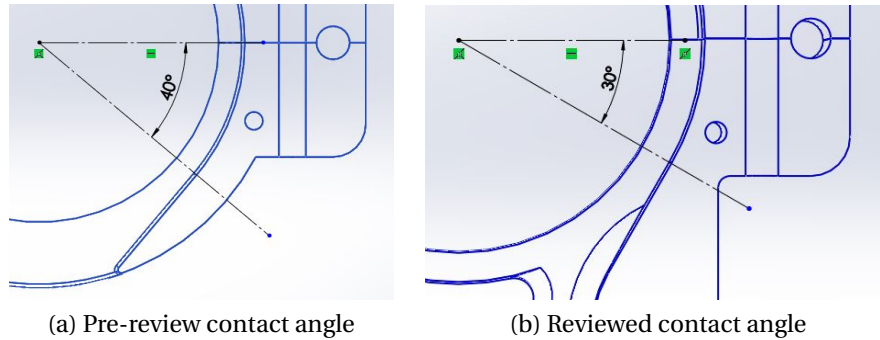


Figure 4.19: Partial design drawing indicating of the reduction in occlusion range in pump design drawings between various design revisions

pressure measurements. This lip can be seen in the second iteration indicated by Fig. 4.20. Additional stand supports were added to the bottom part where the lip occurred. These stand supports are to work with the supports located on the bottom plate of the pump (not present in Figs. 4.11a to 4.20 for emphasis on design changes).

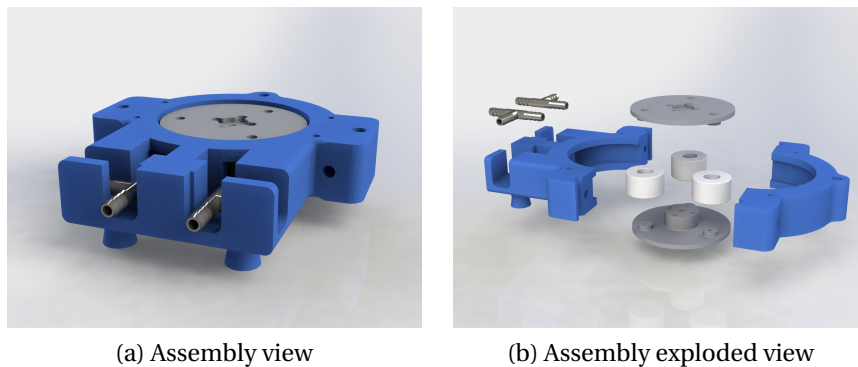


Figure 4.20: Photo-realistic rendering of the second iteration of the peristaltic pump design

## 4.8 Final design

The final design shown in Fig. 4.21 indicates the final assembly. This includes previously hidden parts not shown in the concept section as emphasis is no longer needed. The part colours are changed to reflect the materials available for the construction of the pump (red and white). The design of the second iteration

was sufficient and allowed the pump to work as intended. The pump can still be stacked with an additional design for the front part of the pump (with the lip) without the additional stand supports.

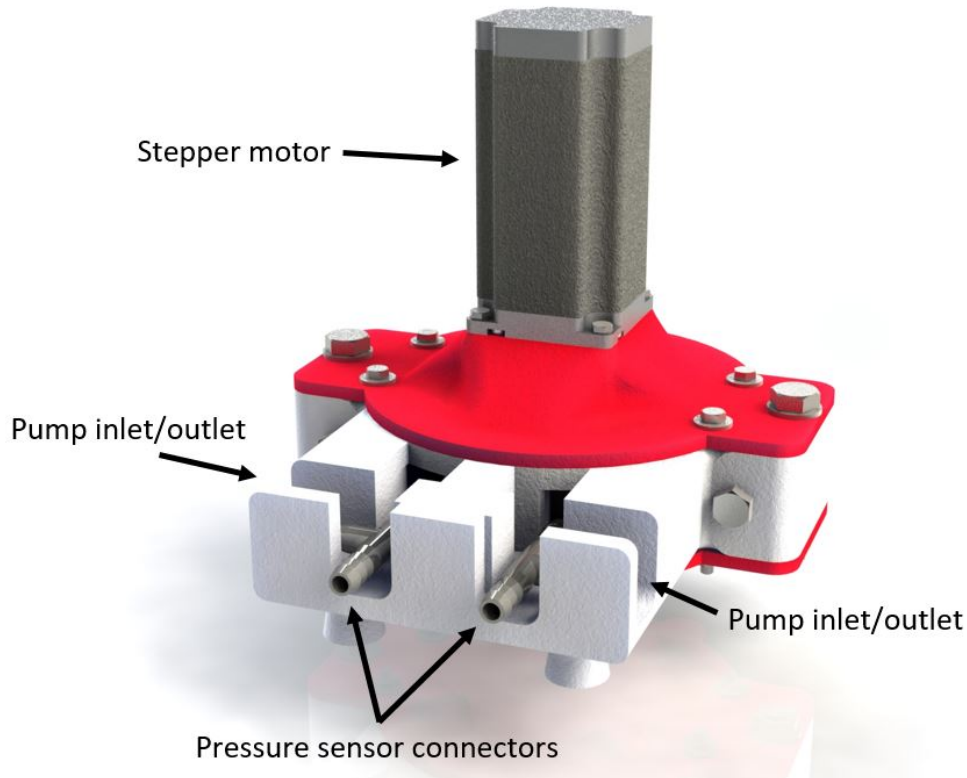


Figure 4.21: Photo-realistic rendering of the final design of the peristaltic pump

The front section and back section of the pump that house the raceway collapse around the roller housing assembly. The pump housing is then connected to the top plate, which houses the Nema 23 stepper motor. The motor is connected to a short shaft by a coupler. The shaft runs through the roller housing assembly to the bottom plate which hold the pump off the ground. The bottom plate holds a bearing in the center where the shaft comes through in order to mitigate radial deflection of the shaft.

The shaft is manufactured with two flat surfaces on opposing sides of the shaft. This acts as a key for the shaft to apply torque without slippage. The length of the screws used were carefully selected in order to mitigate contact, friction, or obstruction within the pump. The most important length selections were for

the roller housing height, roller screws, and motor coupling. The motor coupler is used as a spacer in this design in order to achieve the necessary clearances for the housing to rotate without obstruction. The cross sectional view of the pump in Fig. 4.22 indicates the gaps between components and fasteners. The design drawings of the pump, as well as additional renderings can be found in Appendix C.

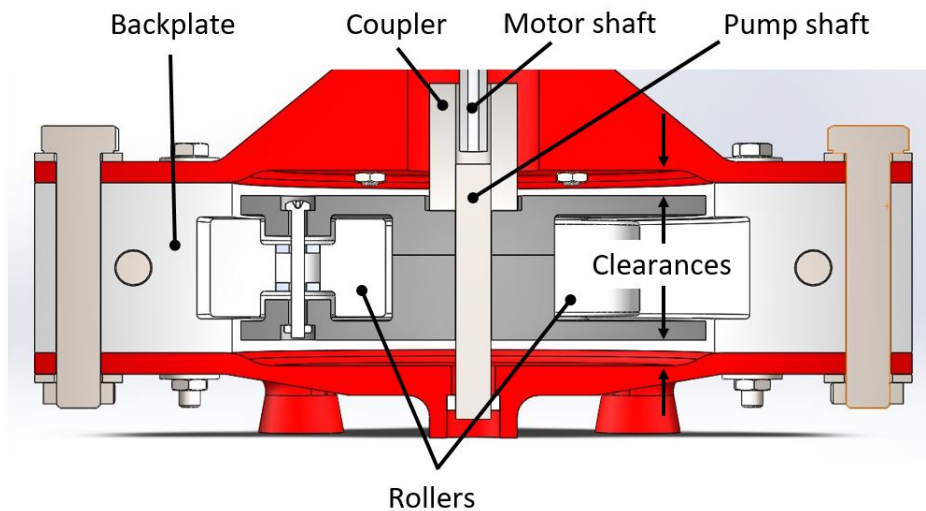


Figure 4.22: Rendering of the sectional view of the final design of the peristaltic pump

## 4.9 Pump manufacturing

The pump was manufactured on the Prusa MK2.5 and MK3 with PETG. The infill pattern was a two-dimensional triangular infill pattern with the alignment along the z-axis (from top to bottom) with a 40 % infill. This provides durability with forces applied radially outwards in the  $x$  and  $y$ -axis directions. Additionally, the wall thickness was set to 2 mm, with a layer height of 0.1 mm. The parts were orientated such that the largest flat surface was the initial build surface for that part. The print bed was heated to 60 °C and the nozzle was heated to 220 °C.

The clearances associated with the through holes on the parts were designed to be large, with the exception of the holes on the roller housing and rollers. The tighter clearances on the housing assembly are necessary, as tighter fits are required to hold certain components in place, such as: the roller bearings inside

the rollers and the shaft into the roller housing. For the smaller clearances of the roller bearings, the hole sizes on the rollers were designed to be as close as to the roller bearing size as possible. The hole surfaces where the roller bearings sit were finished using a drill bit with the same diameter as that of the bearing.

The larger clearances are indicated clearly in Fig. 4.23, where the coupler is required to sit flush with the indented surface for proper spacing. A clamp-type spider coupler (also known as a curved jaw coupler) is used to join the shaft of the motor to the shaft of the pump.

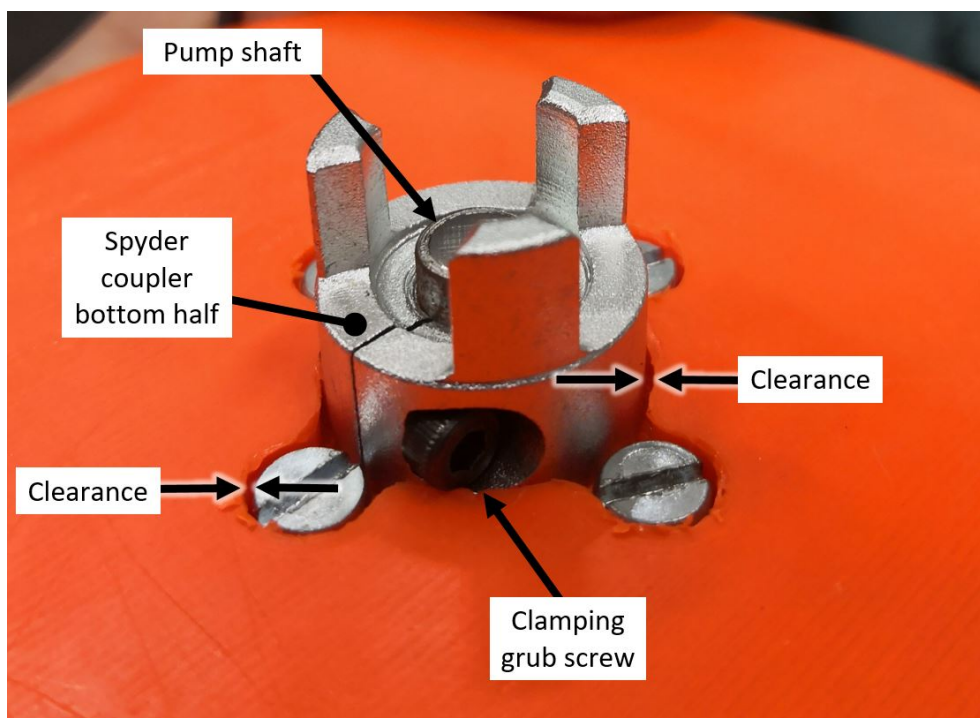
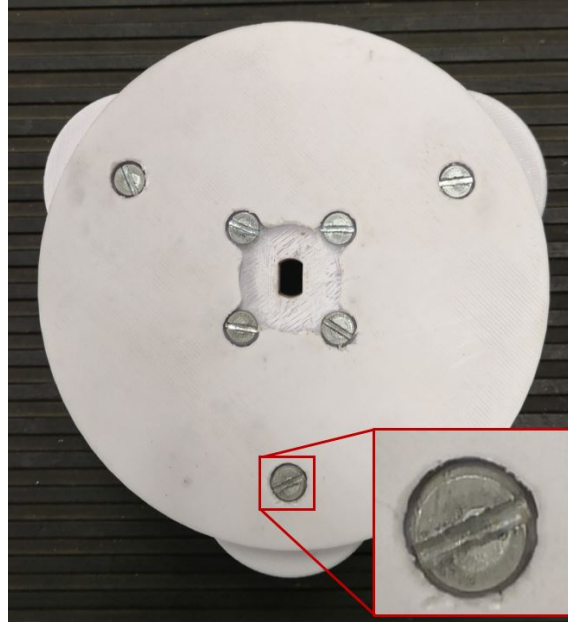
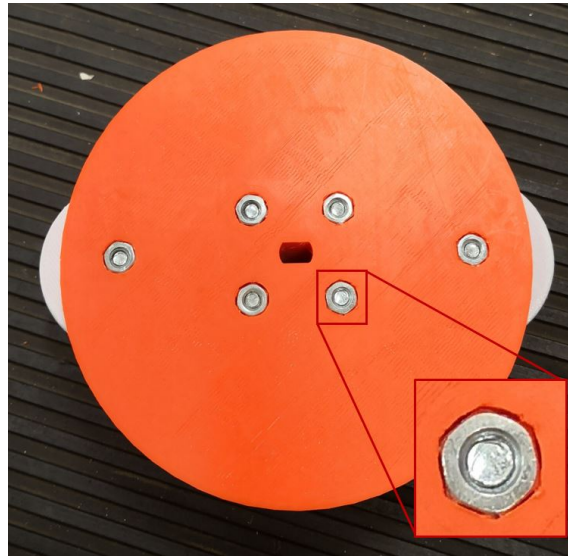


Figure 4.23: Photo showing the close-up view of the clearances of the top part of the roller housing for the shaft coupler and roller housing screws

The flat head M4 screws used for the roller housing have ample clearance, however, the nuts have a closer fit, where the plastic of the part gives way to the shape of the nut (indicated in Fig. 4.24). This allows the nut to sit as if it were a lock-nut, mitigating the possibility of the nut loosening. This is especially important for the rollers, as tightening the screw too much can cause the roller housing to bend/deform under the larger moment. The M4 screws holding the rollers in place are therefore not tightened completely, however, they are flush with the housing. The tight clearance and the ability of the nut to be held in place proved advantageous in this design.



(a) Top view of the manufactured three-roller housing assembly



(b) Bottom view of the manufactured two-roller housing assembly

Figure 4.24: Photo showing the manufactured roller housing assemblies for two-roller and three-roller pump configuration

With the successful manufacturing of the parts, the pump was assembled and integrated with the testing environments outlined in Chapter 5. Fig. 4.25 shows the pump fully assembled and integrated with the designed test bench.

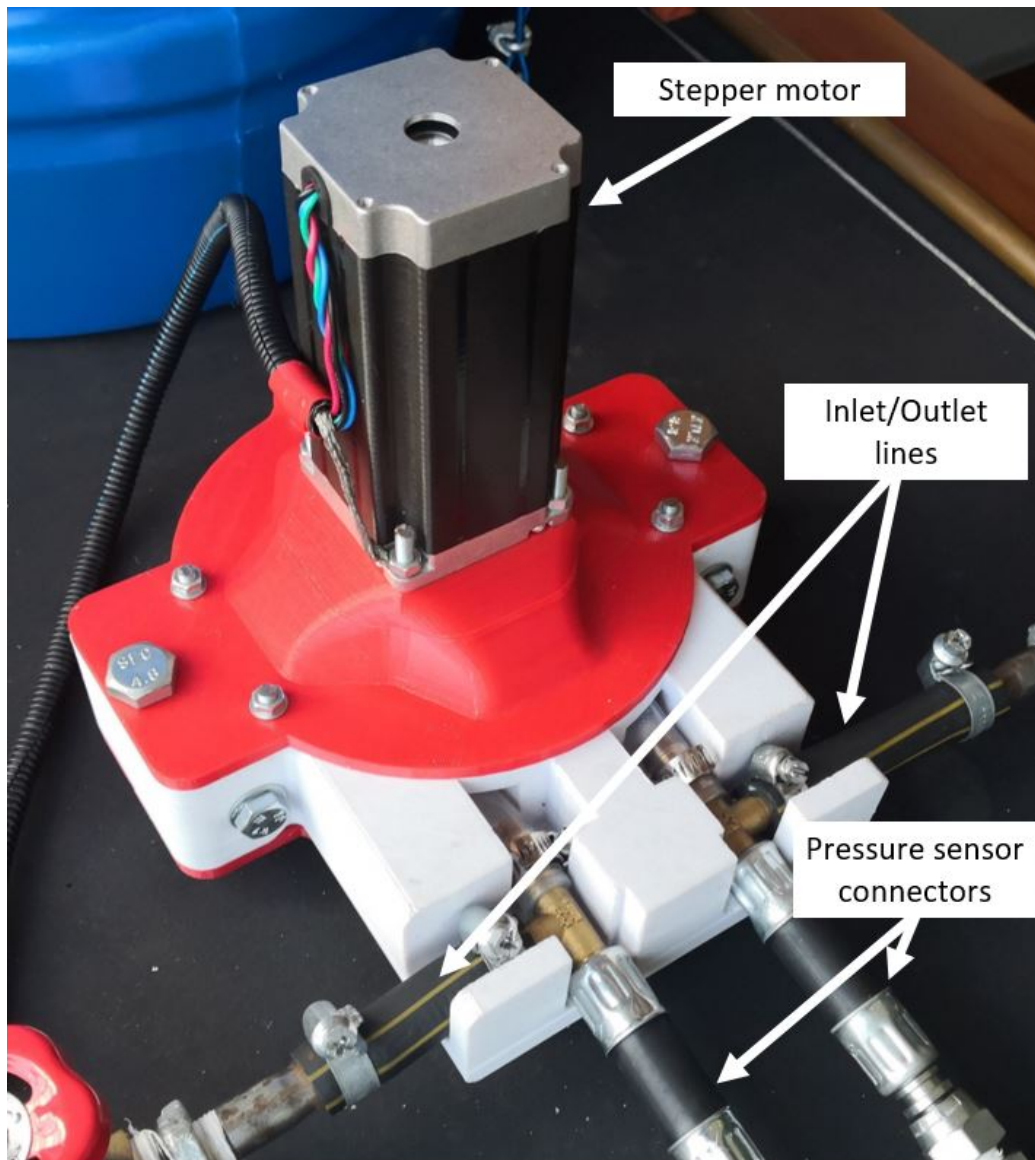


Figure 4.25: Photo showing the fully assembled pump integrated with test bench for testing and validation



## 4.10 Conclusion

This chapter provides a detailed evaluation of the design process of a 3D printed peristaltic pump with required pump specifications. The specifications of the pump are derived from the model provided in Chapter 3 for a hypothetical scenario where the pump is applied as an EHA for the actuation of a micro-hydraulic piston.

The relevant manufacturing constraints of the pump are discussed prior to the design specifications as they are a critical limiting factor in the design process. Design considerations, such as the CAD and slicing software, infill patterns and densities, and topology optimisation are mentioned but are not focussed on in detail, as they are not the main focus of this study.

As previously stated, the modelling in Chapter 3, specifically with regards to the average flow calculation, is used to assist the design process of the pump. This is done by specifying design parameters that relate to the geometry and variables used in the model, namely: Operational speed ( $\omega$ ), tube dimensions ( $r_i$  and  $r_o$ ), compression length ( $Comp$ ), number of rollers ( $NU$ ), contact angle ( $\beta$ ), backplate radial length ( $r_b$ ), and desired flow rate ( $Q_{avg}$ ). The model is then iteratively solved in order to obtain the roller radial length ( $r_{roller}$ ) and roller offset length ( $r_{offset}$ ) required to achieve the desired flow rate.

To ensure accuracy of the validation of the model during testing, the pump is designed based on the assumptions of the modelling section. This includes a straight inlet and outlet that exit the pump tangent to the backplate, utilisation of soft process tubing (silicon polymer), and a small roller radius to backplate radius ( $\approx 1/3$ ). An additional design consideration was made to allow for easy testing of the pump with the front 'lip', which allows for the addition of pressure sensors directly onto the inlet and outlet line using a standard hydraulic tee.

### Test bench design

---

#### 5.1 Introduction

This chapter provides information pertaining to the formulation of the required tests and the associated test bench development to obtain the data for validation purposes. The chapter discusses three main tests conducted, namely: (i) System tests, (ii) Roller volume displacement tests, and (iii) Pump pressure and volume displacement tests.

The chapter starts off with a discussion on the testing objectives, briefly describing requirements of the systems used to conduct the tests. Thereafter the tests are described in more detail individually, starting with the tests required to obtain the resistance and compliance values of the inlet and outlet. Thereafter the roller volume displacement tests are described followed by the description of the pump test bench. The chapter furthermore provides information pertaining to the instrumentation and calibration of the sensors used.

The chapter is then concluded with a breakdown of the pump pressure and volume displacement test structures, as well as the validation method used for all tests.

## 5.2 Test objectives

The goal of the tests described in this chapter is to validate the model of the peristaltic pump described in Chapter 3. This requires the validation of three main aspects, namely: the discrete integration roller volume approximation, the pump volume displacement/flow rate, and the simulated pressure response of the pump with regards to the system it is integrated with. Since the model can only be evaluated with actual system parameters, realistic parameters for the model are only included in the results chapter (Chapter 6), where modelled results are compared with experimental results. The parameters that will be determined empirically include fluid resistance, compliance, and inertia.

In this section, four test benches are described. These test benches are summarised in Table 5.1, along with their designated objectives. These test benches consist of the resistance test bench (RTB), compliance test bench (CTB), roller volume test bench (RVTB), and the peristaltic pump test bench (PPTB)

Table 5.1: Test objectives and data acquisition techniques

<b>Test bench:</b>	<b>Test objective:</b>	<b>Data acquisition method:</b>
RTB	Inlet/outlet resistance	Excel via PLX-DAQ <sup>1</sup> , manual
CTB	Inlet/outlet compliance	Excel via PLX-DAQ
RVTB	Roller volume displacement	Manual acquisition
PPTB	Pump pressure and flow rate	ControlDesk plot export

The system tests and roller volume tests have different test benches to that of the pump tests. This is due to the test requiring mobility regarding some of the locations where water reservoirs could be utilised. Additionally, the variation in test benches is further motivated by the attempt to prevent damage to expensive testing equipment, as water is hazardous to electronic components.

Flow measuring instruments are either inaccurate at low costs or relatively accurate at extremely high costs. For this reason the flow measurements are done using volume displacement over time. The volume of the fluid displaced can be calculated with the use of the density of the fluid  $\rho$  with the unit of  $\text{kg}/\text{m}^3$ . By using scales to weigh the mass of the fluid, the volume can be calculated. By using timers for the flow tests, the volume over a certain period of time can be

<sup>1</sup>Data acquisition in Microsoft Excel in tandem with the PLX-DAQ add-on for communication with the ATmega2056 via a serial communication universal serial bus (USB).

obtained to derive the flow.

The PPTB can be constructed symmetrically with regards to the inlet and outlet. This simplifies testing as the inlet can be assumed to have the same system variables as the outlet and vice versa. The system tests described are conducted to obtain vital system parameters, such as the inlet/outlet resistance (head loss) and compliance of the hydraulic circuit that the pump is integrated with. Due to the difficulty in experimentally determining the fluid inertia, the fluid inertia is adjusted within the simulation to obtain the most satisfactory value. The only system parameters determined are therefore the resistance and compliance.

**RTB:** The inlet or outlet can be isolated (removed from the pump test bench) and implemented into its own test bench to obtain the resistance value of the inlet/outlet. To avoid confusion, the isolated inlet/outlet line is referred to as the isolated line. The resistance value can be obtained by inducing a flow over the isolated line and measuring the pressure difference between the inlet and outlet of the isolated line. Additionally, adjustable resistance values would be ideal to test the simulation under varying conditions. This implies that a flow control valve should be located within the isolated line, and thus on the inlet and outlet lines of the PPTB. A flow control valve is also necessary in order to control the flow speed of the kinetic pump, which is required to produce a steady flow over the isolated line. A timer can be implemented on the control of the pump in tandem with a weight scale in order to obtain the average flow rate over a period of time.

**Requirements:** Computer, I/O board, flow control valve, pressure sensors (x2), isolated PPTB inlet line, kinetic pump, weight scale, reservoirs (x2) – indicated in Fig. 5.1

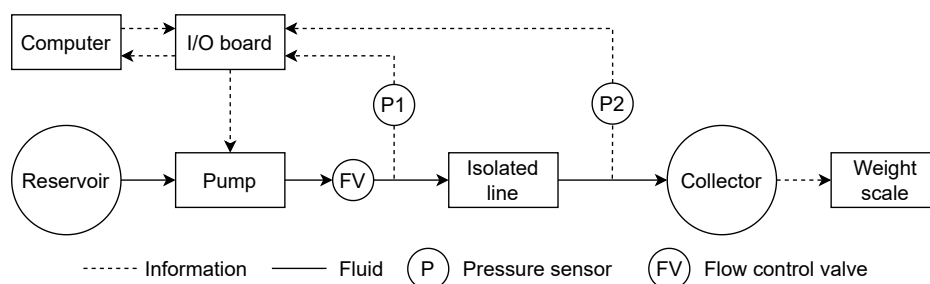


Figure 5.1: High level functional block diagram of the resistance test bench

**CTB:** The compliance of the inlet and outlet of the PPTB can be determined in a similar fashion as in [16]. This implies injecting a known volume of fluid into the isolated line, which is sealed at one end to prevent flow. The change in pressure caused by the change in volume gives an indication of the compliance of the isolated line.

**Requirements:** Pressure sensor, computer, I/O board, syringe, isolated PPTB inlet line, peristaltic pump, process tube, flow control valve – indicated in Fig. 5.2

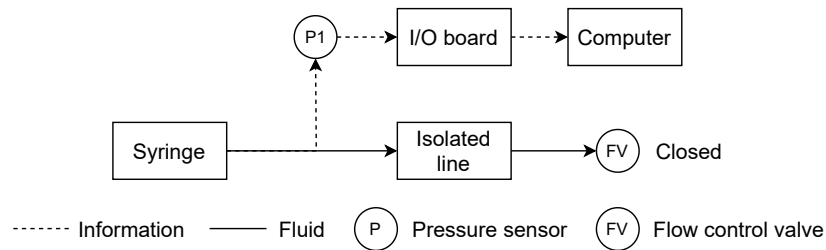


Figure 5.2: High level functional block diagram of the compliance test bench

**RVTB:** In order to validate the discrete integration roller volume approximation method, the volume that a roller displaces as it comes into, or out of, contact with the tube must be experimentally obtained. The values of the test should be obtained at several points across the entire span of the angle of engagement in order to get a good indication of the roller volume displacement.

A similar method can be used for the roller volume displacement test as in [16] as well. The test involves rotating the motor of the pump incrementally with the process tube of the peristaltic pump leading into a volume measuring device. The test can, however, be improved upon by reducing the incremental step size of the samples taken, effectively increasing the amount of data obtained. Additionally, the test can be repeated several times in order to ensure repeatability and accuracy regarding both the measurements and the controller.

As the roller engages the tube it displaces the fluid inside the process tube. If one end of the process tube is clamped while the other side leads into a volume measuring device, the total volume that the roller displaces can be measured. This is true while full occlusion does not occur, as

when full occlusion occurs the fluid inside the tube being displaced no longer represents the roller volume. This effect can, however, be reduced by rotating the pump towards the direction of the clamp, allowing the pressure differential to equalise over time.

**Requirements:** Computer, I/O board, modified peristaltic pump, volume meter, clamp – indicated in Fig. 5.3

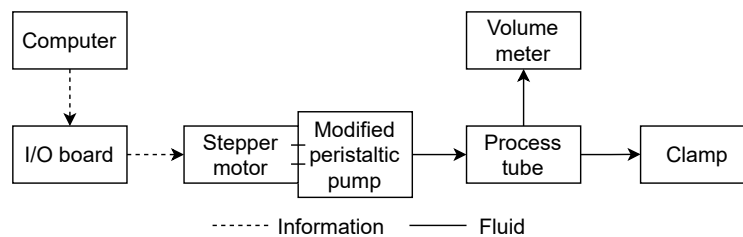


Figure 5.3: High level functional block diagram of the roller volume displacement test bench

**PPTB:** The pressure and volume displacement tests are separate tests for both the pressure pulsation of the pump and volume displacement through the pump. These tests are facilitated by a single test bench that can be altered to accommodate both tests. The pump test bench is the main focus of this chapter and is described in full later in this chapter.

**Requirements:** Computer, I/O board, flow control valve, pressure sensors (x2), peristaltic pump, weight scale, reservoir, beaker – indicated in Fig. 5.4

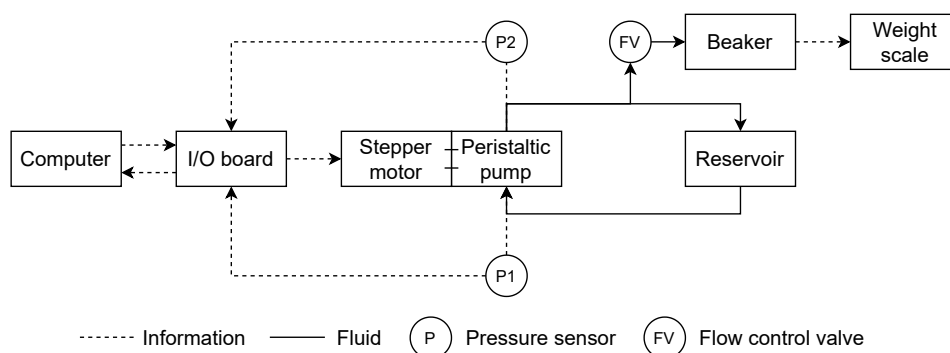


Figure 5.4: High level functional block diagram of the peristaltic pump test bench

### 5.3 Resistance test bench

To determine the resistance of the system, a steady flow was induced over the isolated inlet line of the peristaltic pump test bench. A pressure sensor was placed at the entrance to the isolated line ( $P_1$ ) and the second was placed at the outlet of the isolated line ( $P_2$ ). The resistance of the system was then calculated based on the pressure differential over the isolated line and the flow rate. The flow rate was calculated by measuring the mass of the fluid pumped through the isolated line over a specified period of time. Initially, the purpose of the gate valve was to induce an additional resistance to the inlet or outlet lines.

The resistance test was conducted using a Pedrollo CP 100 (0.25 kW) pump. The pump outlet was connected to the isolated inlet line that connects the peristaltic pump to the reservoir, with the inlet of the pump connected to a large water reservoir. The flow of the pump was controlled using a gate valve located in front of the isolated line of the peristaltic pump test bench. Between the flow controlling gate valve and the isolated test bench line, a pressure sensor was placed. The second pressure sensor was placed at the outlet of the isolated line. The detailed functional block diagram of the resistance test is indicated in Fig. 5.5

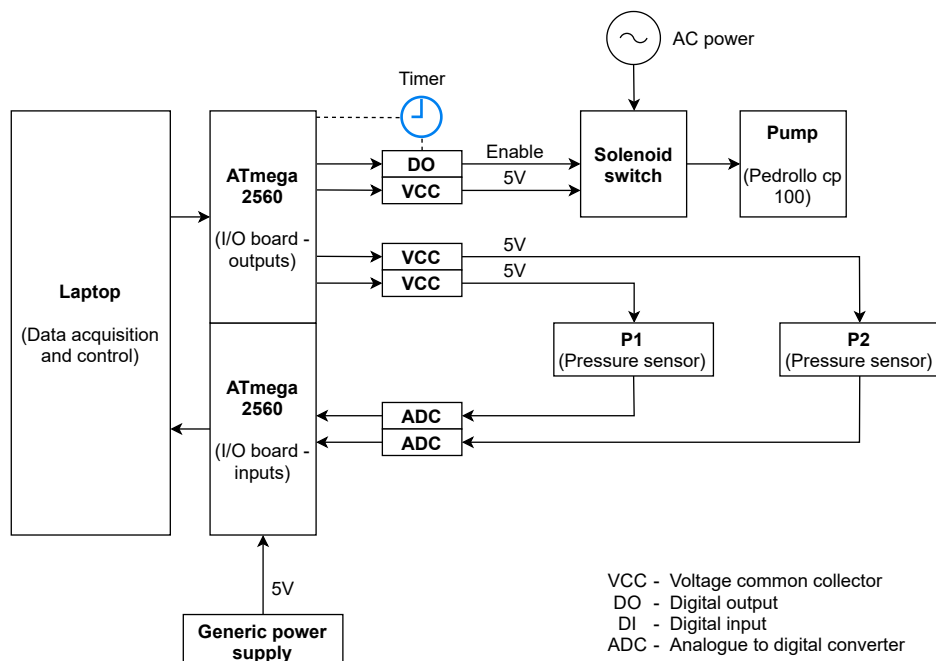


Figure 5.5: Component level functional block diagram of the resistance test bench

The flow control valve located on the isolated line was adjusted in increments of 0.5 turns of the manually adjusted knob. The flow restricting valve located before the isolated line was held constant during testing. The resistance of the isolated line can be calculated using the difference in pressure over the mass flow as:

$$R = \frac{Q}{\Delta P}, \quad (5.1)$$

with

$$\Delta P = P_1 - P_2. \quad (5.2)$$

Testing revealed that the resistances were non-linear in relation to the position of the valve nob and thus the valves were only used for testing the maximum and minimum operating pressures by completely closing the valves. Fig. 5.6 indicates the volumetric flow rate and pressure gradient across the inlet line with reference to the valve nob position (where 0 indicates the valve fully open, and 5 fully closed).

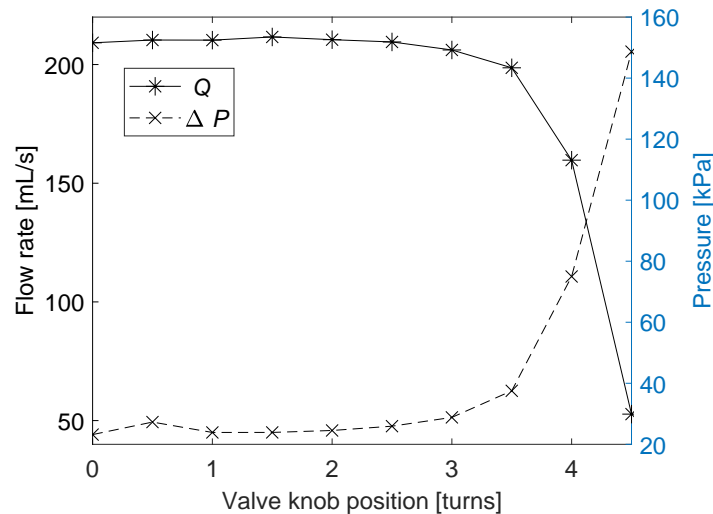


Figure 5.6: Resistance test results indicating a non-linear mass flow and pressure gradient characteristic of the restricting gate valve

The steady state resistance for the inlet line was determined to be 0.1108 kPa/ mL/s with a flow rate of 209.16 mL/s.



## 5.4 Compliance test bench

To test the effective compliance of the inlet line, the inlet is isolated and sealed at one end with a gate valve (referred to as the sealing valve) as indicated in Fig. 5.7. At the opposing end of the flexible process tube, a syringe insert is coupled to allow the insert of a syringe. The system is filled with water and 5 mL of water is taken up into the syringe. The syringe can then be coupled to the system and displace the contained 5 mL of water into the sealed inlet line. The change in pressure relative to the initial pressure can be measured by the pressure sensor. The ATmega 2560 is used for this test to read the pressure sensor values and log the values in Microsoft excel.

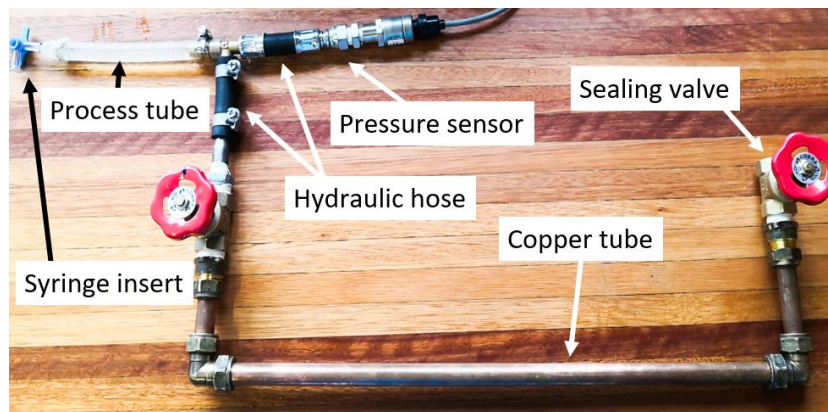


Figure 5.7: Photo of the isolated inlet section of the peristaltic pump test bench used for the compliance test

The test was repeated 10 times to ensure repeatable accuracy and the results are indicated in Fig 5.8.

The effective bulk modulus of the system can then be calculated based on the average pressure difference for all 10 tests in relation to the change in volume as in (5.3). It is important to note that the 5 mL of the syringe needs to be accounted for in the calculation of the total volume as  $V_{total} = V_{inlet} + V_{syringe}$ .

$$B_e = \frac{\Delta P \cdot V_{total}}{\Delta V} \quad (5.3)$$

The effective compliance of the system (or analogous capacitance) is equal to:

$$C_e = \frac{1}{B_e} \quad (5.4)$$

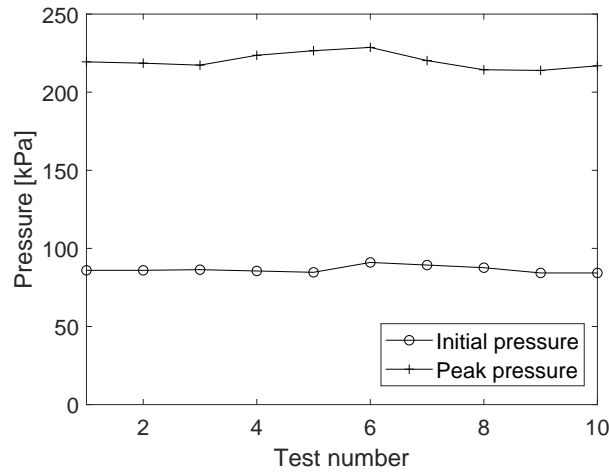


Figure 5.8: Compliance test results of the isolated inlet line indicating the pressure response to the increase in volume

The inlet line volume was mathematically determined to be 119.04 mL. To ensure that the volume is accurate the inlet line regarding the compliance tests was repeatedly filled with water and measured. The test was repeated 10 times to ensure repeatable accuracy. The average experimental volume was found to have a value of 122.77 mL, indicating an error of the theoretical inlet volume of 3.04%. The compliance  $C_e$  of the system was determined to be equal to 0.036 kPa/mL for the measured volume.

The inertia of the fluid (inductance) was left untested and was iteratively fitted using the simulation results with the theoretical value as the initial guess value. The appropriate inertia was determined to be roughly 0.0057 kPa s<sup>2</sup>/mL.

## 5.5 Roller volume displacement test bench

The pump design has 3 rollers rotating at a distance around the central axis of the pump. These rollers are held in place by the roller housing, which is the central disk connected to the motor by a shaft. By removing two of the three rollers, the volume which the roller displaces as it comes into or out of contact with the tube can be tested. This can be done by filling a short segment of process tube with water, clamping the outlet side of the tube, and inserting a measuring device to the inlet side as indicated in Fig. 5.9. The measuring device used is a syringe with its indicator limits ranging from 0 mL to 2 mL in increments of 0.1 mL.

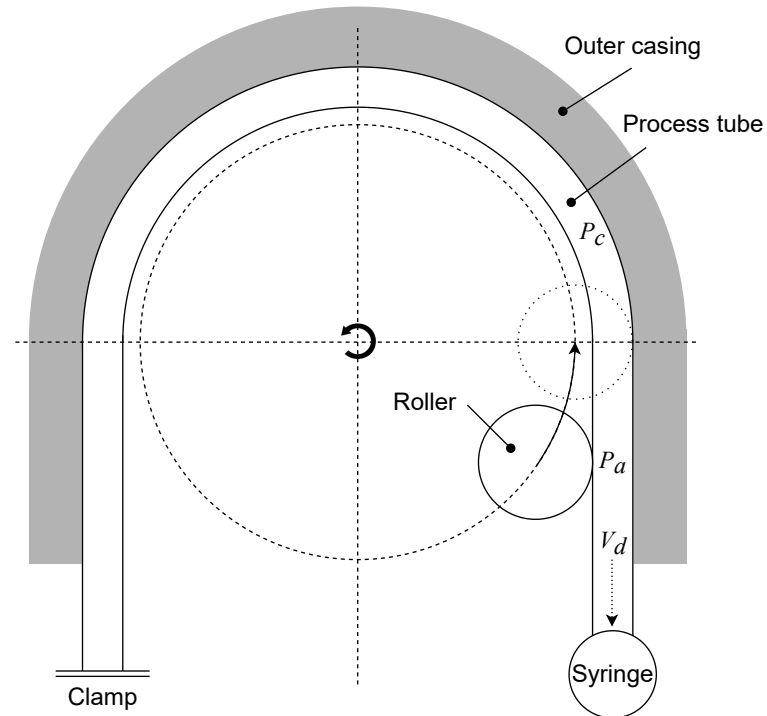
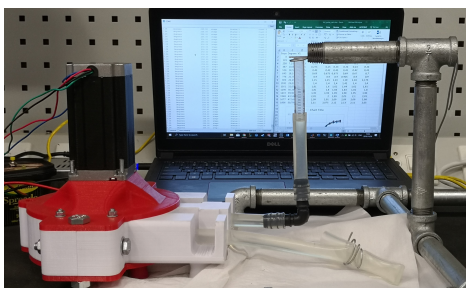
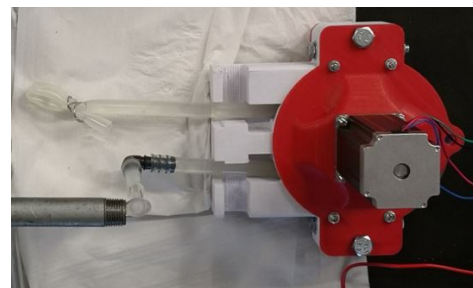


Figure 5.9: Illustration of the volume displacement test set-up as seen from above

The motor is then rotated away from the syringe and towards the clamp. For the angles where the roller does not completely occlude the process tube, the clamp will ensure that the pressure on the clamp's side of the tube ( $P_c$ ) will force the displaced volume ( $V_d$ ) towards the syringe, which is open to the atmosphere ( $P_a$ ).



(a) Side view



(b) Top view

Figure 5.10: Photos showing the roller volume displacement test bench

The ATmega system is used for this purpose to give an exact amount of pulses to the pump, as a complex system is not required to send pulses. The pressure sensors are not used in this test, as the volume displacement measurements are taken by hand.

The angle that the motor rotates is based on the number of pulses sent to the motor driver and the setting of the DQ542MA driver. The theoretical engage angle for the pump was calculated to be  $43.53^\circ$ . For adequate resolution of the volume displacement, without complicating the tests unnecessarily, the total angle was divided into twelve increments, each with a value of  $3.628^\circ$  apart from each other. In order to mitigate loss of data the tests are extended beyond the calculated engage angle and a total of 14 increments are used per test, each with a value of  $3.628^\circ$  apart for a total theoretical rotation of  $50.79^\circ$ . In order to ensure test accuracy, the test, with 14 increments, is repeated seven times for a total of 98 data points.

The stepper motor driver is set to 12800 pulses per revolution to accommodate the closest value to  $3.628^\circ$  per increment. The driver setting of 12800 pulses per revolution implies that it would take 35.56 pulses per degree, and thus 129 pulses, to achieve a value of  $3.63^\circ$ . This allows the theoretical total angle for 12 increments to be  $43.538^\circ$  and the theoretical total angle for 14 increments to be  $50.794^\circ$  (an angle slightly larger than the engaging angle is preferable).

In order to ensure rotational accuracy of both the stepper motor driver and the stepper motor, the 14 increment test was completed prior to the actual test with the bottom of the pump removed to mark incremental positions around the fixed outer casing. This was done by marking the bottom component of the roller housing with the corresponding adjacent initial position on the outer casing. The adjacent outer casing position where the mark stops after each increment was marked thereafter. This allowed the outer casing to become a reference for the rotating roller housing with each increment. The pump was then photographed directly above the pump and the angles calculated in Solidworks using the reference marks on the pumps as indicated in Figs. 5.11 & 5.12.

The initial position is marked by the horizontal line near the bottom with the first increment value thereafter as  $3.37^\circ$ . For the 14 increments of the test the total angle had an error from the theoretical value of  $-0.5441\%$  while Fig. 5.13 indicates the close correlation of the experimental and theoretical rotation angles.

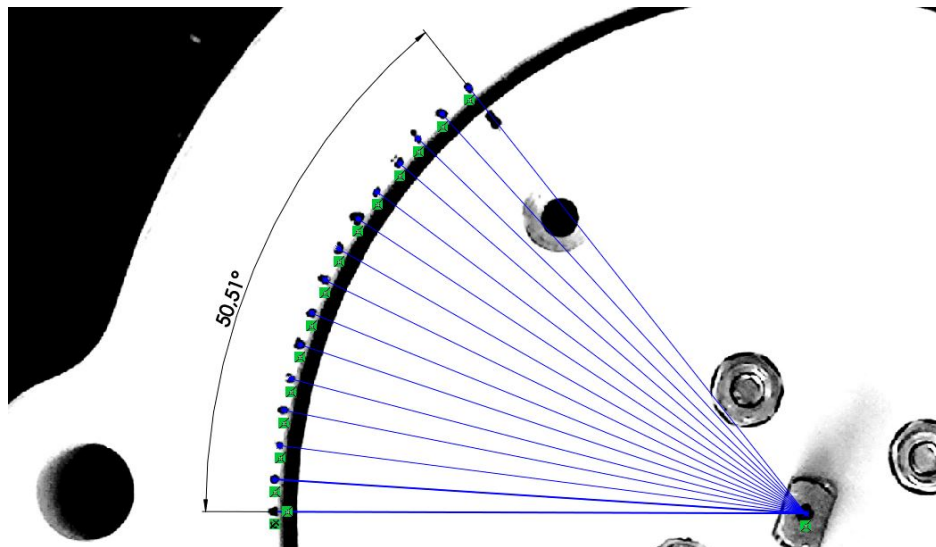


Figure 5.11: Photo of the internal pump components indicating the total angle of rotation for the volumetric displacement tests

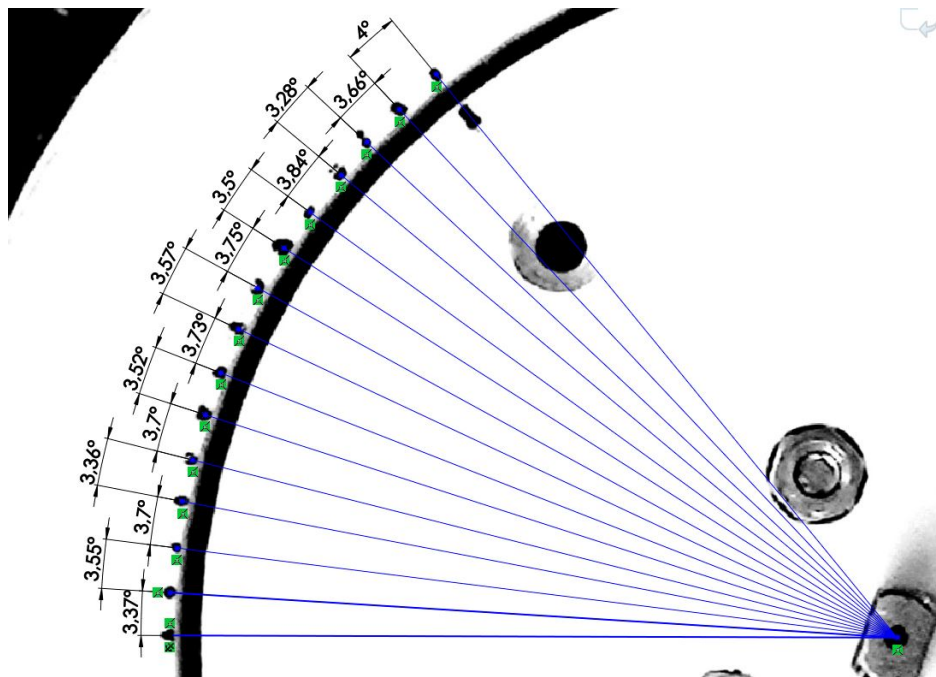


Figure 5.12: Photo of the internal pump components with demarcations indicating the individual angles of rotation per increment for the volumetric displacement tests

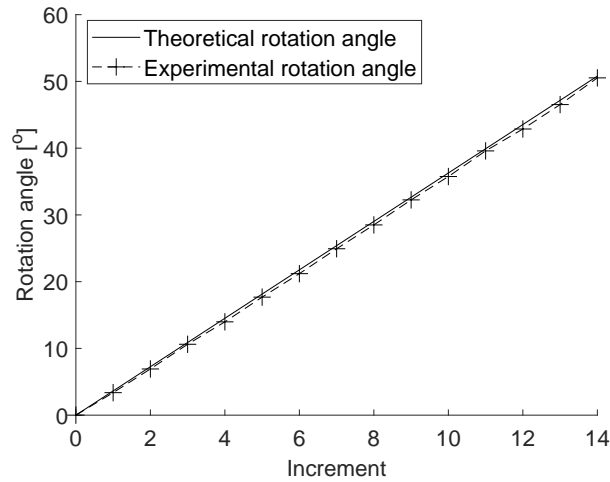


Figure 5.13: Experimental results of the rotation angles for the volumetric displacement test compared to theoretical (ideal) rotation angles

## 5.6 Peristaltic pump test bench

The volume displacement tests are used to determine the flow speed of the pump by measuring the volume that the pump displaces over a finite amount of time. This is done by collecting the fluid pumped in a beaker over a defined period of time, and measuring the weight of the fluid added. The volume can then be calculated using the density of the water. The measured flow of the pump can be tested over varying motor speeds in order to validate the modelled flow. The pressure tests are tests conducted to validate the pressure response of the system to the pulsatile flow input from the pump, with regards to the motor's rotational speed. The pressure is captured using two pressure sensors, one at the inlet of the pump, and one at the outlet of the pump.

A test bench was constructed with desired values regarding the inlet and outlet lines' length and diameter. The inlet and outlet lines are constructed to resemble one another in order to reduce testing needed to characterise the test bench. Thus by finding the resistance and compliance associated with the inlet line the resistance and compliance for the outlet are inherently also tested.

The test bench was constructed in order to deliver two main tests namely: pressure pulsation characterisation and flow characterisation. The piping and instrument diagram of the test bench is indicated in Fig. 5.14. The pressure pulsations were tested in a system where the fluid is pumped from an open reservoir tank (R1) through the inlet line and inlet flow control vale (gate valve) (FV1),

through the pump (PP), and then back to the reservoir via the outlet line (and through flow control valve FV2 and ball valve FV3). The flow of the pump is tested by sealing the outlet line by closing ball valve FV3, and adding an additional outlet line to a beaker E1. The mass of fluid can be measured with the beaker and more accurately give an indication of the flow rate over a period of time.

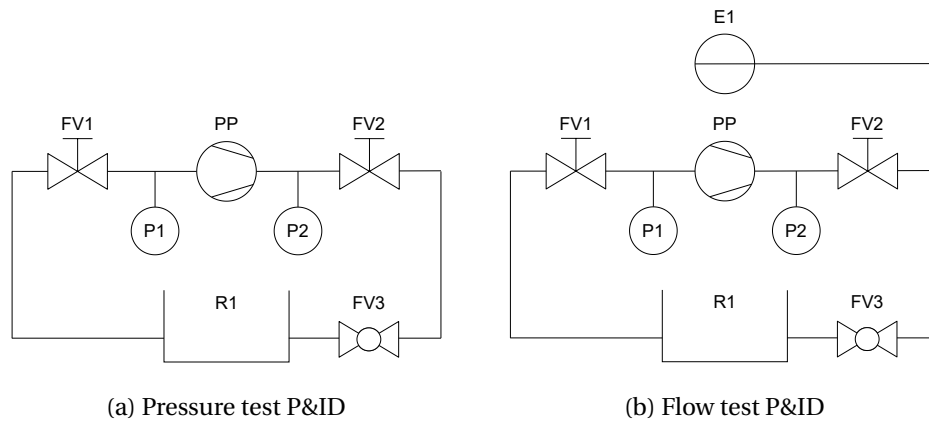


Figure 5.14: PPTB pressure and flow testing piping and instrument diagrams

The pressure associated with the pump is measured directly before and after the pump, indicated by P1 and P2, where P1 indicates inlet pressure and P2 the outlet pressure (indicated in Fig 5.15). FV1 and FV2, being manual gate valves, are used to restrict the flow and increase/decrease the pressure at the inlet and outlet of the pump respectively. The silicone tube used inside the pump has a low modulus of elasticity and as a result has large mechanical compliance. This, along with the bulk modulus of the fluid act as a sort of spring in the fluid system and can have undesirable effects. To negate these effects, the silicon tube segment is made as short as possible and localised to the inside of the pump. However, in order to connect to the rest of the system, a small section of the tube on the inlet and outlet is still present. The rest of the system consists of either high pressure hydraulic hoses or copper tubes in attempt to negate mechanical compliance.

The outlet for the flow test is not characterised, as the pressure pulsations are modelled for a system that moves fluid to and from the same source. The test bench, indicated in Fig. 5.16, has reservoir tank that can hold up to 50 litres of fluid and is open to the atmosphere. The pressure caused by the fluid in the reservoir is denoted as  $P_{res}$  in the lumped parameter model and acts on both the inlet and outlet. The copper tubes have an outer diameter of 15 mm and a wall thickness of  $\sim 0.7$  mm, where the hydraulic hose has an outer diameter of

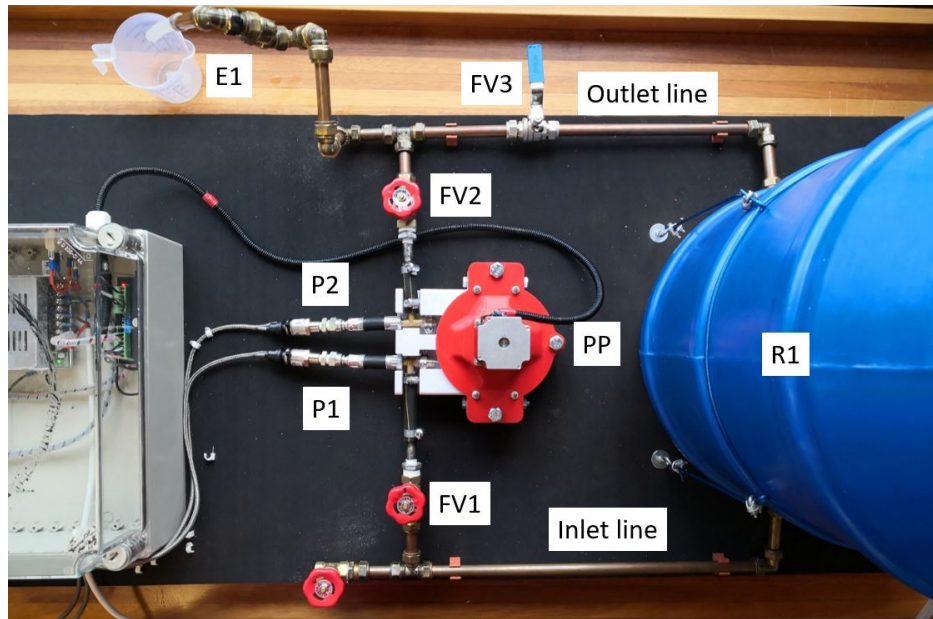


Figure 5.15: Photo of the top-down view of the PPTB configured for the flow tests indicating the P& ID components

17 mm and an inner diameter of 10 mm.

A dSPACE 1104 research and development (R & D) controller board is used in conjunction with a desktop PC to read the sensors, control the system, and log the acquired data. An interface board is used to ease the construction of the electronics box of the test bench as well as protect the dSPACE card. A generic power supply was used to supply power to the dSPACE circuit protection circuit, the stepper motor driver, and the thermocouple for elevated temperature tests. Fig. 5.17 indicates the detailed functional control block diagram of the peristaltic pump test bench.

### 5.6.1 Instrumentation

#### Data acquisition

The dSPACE virtual workspace (ControlDesk) obtains and calculates values based on a pre-constructed Simulink model. The Simulink model essentially indicates to the dSPACE virtual environment what signals to read from the board and how to process said signals with the use of real-time interface blocks. A diagram of the Simulink model used for this test bench can be found in Appendix D.

The dSPACE 1104 R & D controller board utilises a MPC8240 processor with



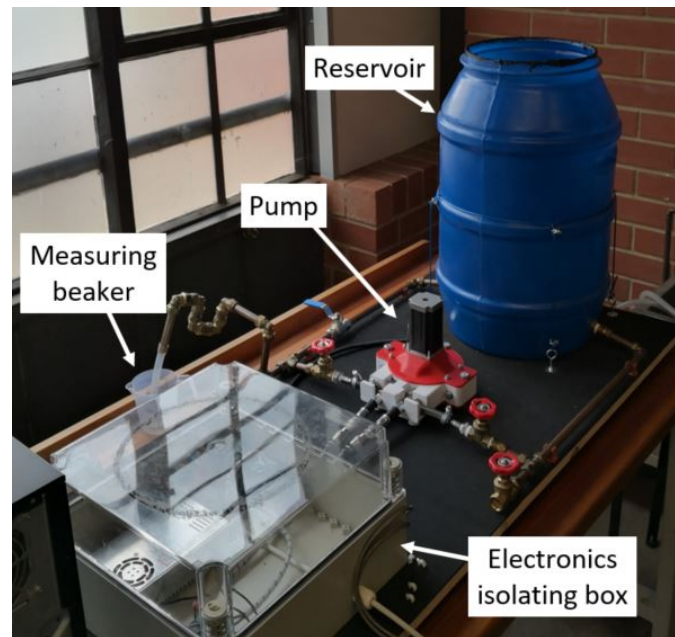


Figure 5.16: Photo of the peristaltic pump test bench indicating the various components of the test bench

PPC603e core and on-chip peripherals. The central processing unit (CPU) has a clock speed of 250 MHz and has two 16 KB on chip caches. The board has a total of five timers, which include: one sample rate timer with a 40 ns resolution (32-bit down counter), four general purpose timers with a 80 ns resolution (32-bit down counter), and one time base counter with a 40 ns resolution (64-bit up counter). The dSPACE board has four muxed channels with one 16-bit analog to digital converter (ADC). The available ADC (4x12-bit, 1x16-bit) are used to read the voltage signals from the pressure sensors during operation and are discussed along with the pressure sensor specifications.

The theoretical time for a roller to move from the engaging to the engaged position (also referred to as the engage time) is roughly 35.8 ms at the maximum operating speed of 200 r/min. If however the tests can be extended past this operating speed, the sample time should accommodate for even shorter engage time intervals. At 300 r/min the engage time can be expected to be 23.9 ms. In order to accurately capture the systems response, without introducing too much noise, roughly one hundred samples can be taken of this interval. This would imply using a fixed sample time in the range of 0.239 ms. For these reasons the sample time is set to 0.2 ms (5 kHz same rate) for all tests conducted on this test bench.

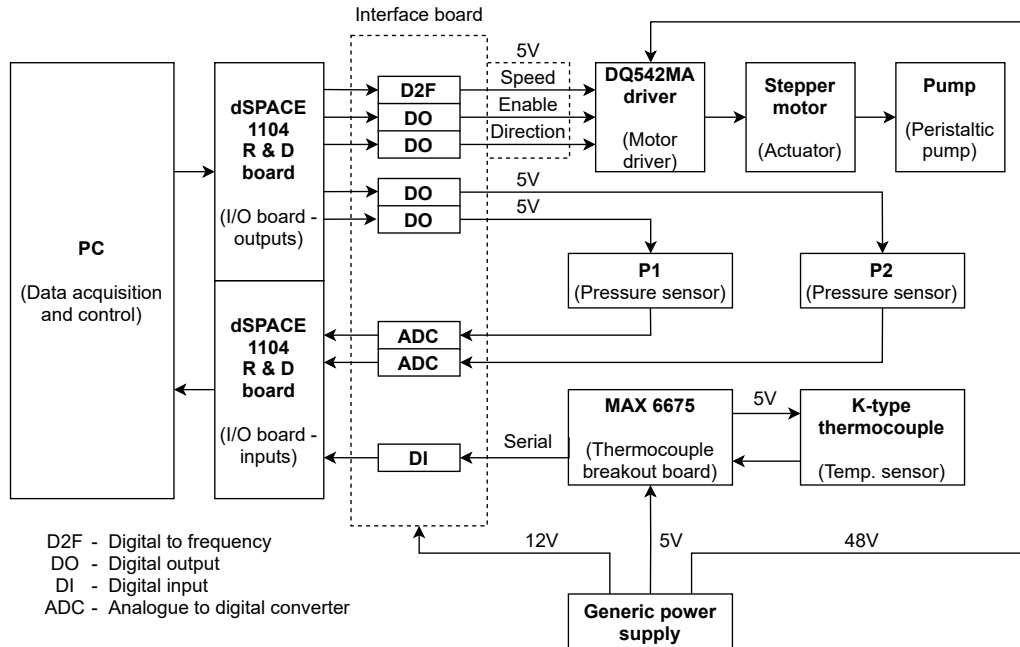


Figure 5.17: Test bench functional block diagram of the PPTB used for the volume model and pressure simulation validation

The North-West University developed general purpose interface boards (indicated in Fig. 5.18) for isolation and circuit protection. The interface board also simplifies connecting to the two 50-pin Sub-D connectors of the dSPACE 1104 card by providing breakout connector pins and spring-operated pins. The specifications and design of the interface board is open-source and can be found at [www.eetips.xyz](http://www.eetips.xyz). The general purpose interface board isolates the dSPACE card, protecting the card from over-voltage by utilising thermal fuses and Zener diodes.

### Sensors

In order to measure the pressure response of the pump and the system two Honeywell PX2EF1XX050PAAAX pressure sensors are used. These pressure sensors are specified to have a 0–344 kPa (0–500 psi) pressure range (0–5 VDC), and a  $\pm 2.000\%$  full-scale span (FSS)<sup>1</sup> total error band (which takes into account all errors). This error value is however not applicable, as mitigation strategies are used to reduce uncertainties. This includes minimising the thermal sensitivity drift of both the sensors and the boards by conducting the experiments in a thermally controlled environment ( $23\text{ }^{\circ}\text{C} \leq T \leq 25\text{ }^{\circ}\text{C}$ ) during testing and

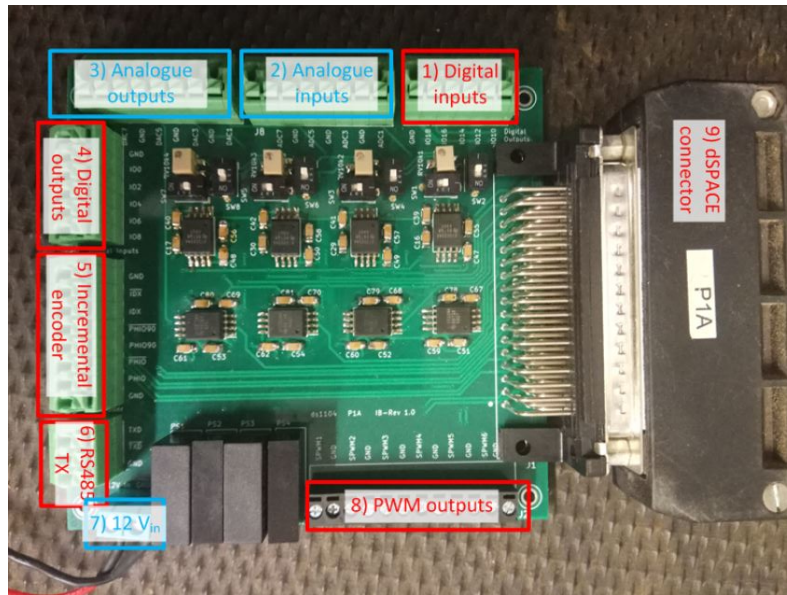


Figure 5.18: Photo of the dSPACE interface board for circuit isolation and protection developed by the North-West University

calibration. Furthermore the tests were conducted in quick succession, mitigating lifetime drift (or simply time drift). The applicable errors specified for the sensors are the accuracy (maximum deviation) with a value of  $\pm 0.250$  % FSS, offset error with a value of  $\pm 1.000$  % FSS.

The sensor is specified as having a 2 ms response time, which is adequate for this study as the shortest observed period is roughly twelve times larger than the response time. The 0.2 ms sample time might seem excessive since the response time of the pressure sensor is roughly ten times larger, however, it is preferable to obtain as much data as possible to mitigate the loss of valuable data.

Additionally, both the 16-bit and 12-bit ADCs have a  $\pm 5$  mV offset error (0.100 % FSS) and a  $\pm 0.250$  % gain error with a 4 ppm/K offset drift and a 25 ppm/K gain drift (the drift error refers to temperature induced errors). Assuming the thermal error drifts are calculated relative to 20 °C this would imply a maximum thermal offset drift of  $\pm 0.002$  % and gain drift of  $\pm 0.013$  % for a 5 °C difference.

The 16-bit ADC has a 2  $\mu$ s conversion time and a > 80 dB signal-to-noise

<sup>1</sup>The full scale span denotes the difference of the output signal measured at the maximum and minimum limits of the pressure sensor (which implies 344 kPa or 5 V in this case).

ratio requirement, whereas the 12-bit has a 800  $\mu\text{s}$  conversion time and a > 65 dB signal-to-noise ratio requirement. The 16-bit channel has an expected resolution of 10.32 Pa (roughly 0.003 % FSS) and the 12-bit channel an expected resolution of 168.56 Pa (roughly 0.049 % FSS). Both of ADCs are adequate for this study, however, to ensure the highest quality data is obtained, the 16-bit ADC will be used. It should be noted that the dSPACE 1104 R & D card is capable of sending and receiving 10 V signals. The FSS in this case is calculated specifically towards the span of the pressure sensor (5 V).

The sensors are coupled to the aforementioned interface board to measure and control the system. The interface board draws power from the power supply to isolate the dSPACE board. In order to reduce noise on the sensors, the sensors are powered by the digital outputs supplied by the dSPACE prototyping board. The accuracy of the digital I/O pins are not specified and it is therefore assumed to have the same accuracy as the board's digital to analog converter (ADC). The expected error of the ADC is specified as having a  $\pm 1$  mV offset error ( $\pm 0.020$  % FSS), a  $\pm 0.100$  % gain error, a 13 ppm/K (0.007 % FSS) offset drift, a 25 ppm/K ( $\pm 0.013$  %) gain drift and a > 80 dB signal-to-noise ratio.

The errors mentioned pertaining to the FSS are offset errors, commonly referred to as zero drift, where as the errors not pertaining to the FSS are commonly referred to as sensitivity drift. These errors are used to calculate the uncertainty of the sensor readings by calculating the combined standard uncertainty in (5.5) where  $u$  denotes the uncertainty factor. In order to minimise the uncertainty of the control boards, the gains and offsets were calibrated prior to experimental testing. The Simulink model diagram reflects this calibration as the analogue calibrations.

$$CU = \sqrt{u_1^2 + u_2^2 + \dots + u_n^2} \quad (5.5)$$

The thermocouple used is a type-K thermocouple connected to a MAX 6675 cold-junction-compensated K-thermocouple-to-digital converter. This converter has an error range of  $\pm 1$   $^{\circ}\text{C}$ , and a 12-bit resolution with a maximum range of 0 to +1024  $^{\circ}\text{C}$ , implying a 0.25  $^{\circ}\text{C}$  resolution.

The weight measuring scales used to determine the volumetric output of the pump were a Kern ABS 220-4N with a resolution of 0.0001 g and a generic digital scale with a resolution of 1 g as indicated in Fig. 5.19. The Kern ABS 220-4N, however, is usually reliable to only 0.01 g without proper calibration, which remains sufficient for this study. The generic scale is needed as the volume for some tests exceeds that of the Kern weight scale.

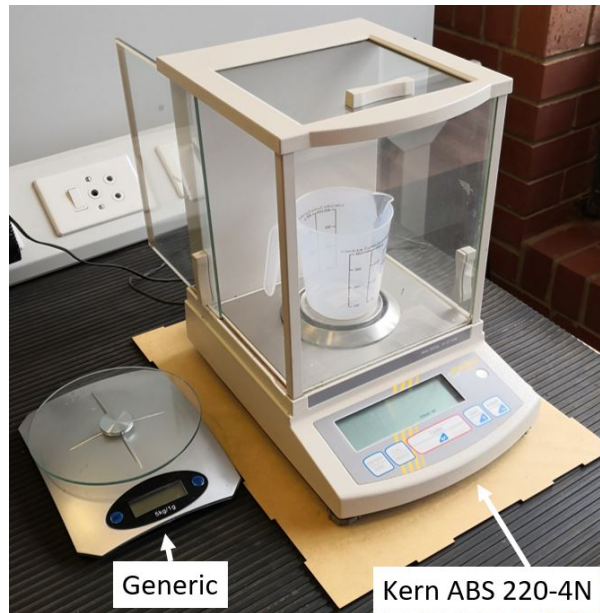


Figure 5.19: Photo of the Kern ABS 220-4N and generic digital weight scales side-by-side

Table 5.2: Test bench sensor drift/uncertainty table

Attribute	Device	Offset drift	Sensitivity drift	Resolution
Pressure	Honeywell PX2	$\pm 1.000\%$	$\pm 0.250\%$	- <sup>2</sup>
	DS1104 inputs	$\pm 0.102\%$	$\pm 0.263\%$	16-bit
	DS1104 outputs	$\pm 0.027\%$	$\pm 0.113\%$	12-bit
	ATmega2560	$\pm 2$ LSB <sup>3</sup>	$\pm 1$ LSB	10-bit
Temperature	Max 6675	$\pm 1.00\text{ }^\circ\text{C}$	-	$0.25\text{ }^\circ\text{C}$
	K-type thermocouple	$\pm 2.2\text{ }^\circ\text{C}$	-	-
Volume	Kern ABS 220-4N	$\pm 0.2\text{ mg}$	-	$10.0\text{ mg}$ <sup>4</sup>
	Generic scale	- <sup>5</sup>	-	1 g
	WeiHeng scale	$\pm 10\text{ g}$	-	5 g

<sup>2</sup>Resolution of the pressure sensor is dependant on ADC, 0.275 kPa (0.08 % FSS) for the 10-bit ATmega ADC, 0.010 kPa (0.003 % FSS) for 16-bit dSPACE ADC.

<sup>3</sup>Least significant bit

<sup>4</sup>The possible resolution of the Kern scale is 0.1 mg, however, the required calibration to achieve this resolution was not conducted.

<sup>5</sup>The offset error of the generic weight scale is negligible in comparison to its resolution.

### Actuators and power supply

The NEMA 23 stepper motor has a step angle of  $1.8^\circ$ . The motor is controlled by a Wantai DQ542MA hybrid stepper motor driver. The stepper motor and driver are controlled by a digital to frequency (D2F) port from the prototyping card. A 1/64 micro-stepping was used to reduce possible noise on the pressures from the stepper motor (12800 pulses per revolution). The stepper motor and driver were found to have an error of roughly 0.2 rotations per 100 rotations (0.2% error) however the data-sheet suggests a maximum error of 1.5 % can be expected. This error does not take motor slip into account. The system is powered by a generic T-350A power supply capable of supplying 8 A at 48 V, 1 A at 12 V, and 0.5 A at 5 V. The motor driver is supplied with 8 A and 48 V, of which a peak current of 2.8 A and a root mean square (RMS) current of 2.03 A was supplied to the motor. This was done to mitigate damage to the motor, as the motor is rated for 3 A.

### 5.6.2 Calibration

The pressure sensors were calibrated using a Testo 622 hygrometer and barometer. The sensors were exposed to various pressures along with the barometer and calibrated using a linear regression technique. The calibration test values which were used to calibrate the pressure sensors are shown in Fig. 5.20.

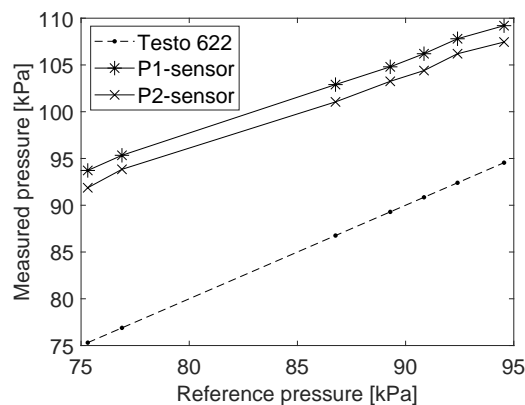
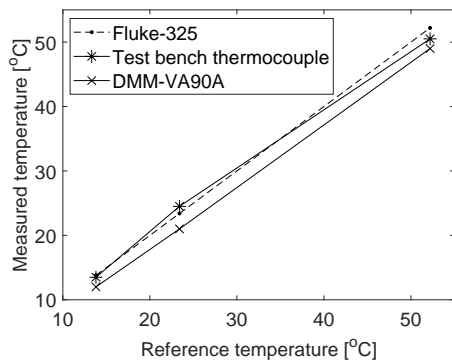


Figure 5.20: Pressure sensor calibration test values of the two Honeywell pressure sensors and the testo 622 barometer as the reference

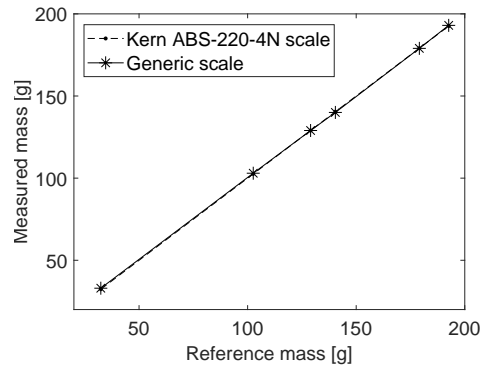
The K-type thermocouple was compared to that of the Fluke 325 multimeter thermocouple and the DMM VA90A multimeter thermocouple to ensure accuracy. Fig. 5.21a indicated the temperature test results compared to one another

with the Fluke 325 as the reference temperature. The temperatures across all three thermocouples had a maximum variance of 3.2 °C and show good correlation. No calibration for the thermocouple was needed as the accuracy was sufficient for the tests, requiring only a steady state temperature.

The weight scales were loaded with different weights and compared to one another in Fig. 5.21b to ensure the accuracy of the generic digital scale. The Kern ABS scale is thus used as the reference value. The digital scale had a maximum error of 0.61 g compared to the Kern ABS weight scale across all calibration tests.



(a) Thermocouple comparative tests



(b) Weight scales comparative tests

Figure 5.21: Accuracy test comparisons for the connected thermocouple and the generic scale

Table 5.3 indicates the sensor drift of the additional sensors utilised for calibration and normalisation not mentioned in the test bench sensor error table (Table 5.2).

Table 5.3: Additional calibration sensor drift/uncertainty table

Attribute	Device	Offset drift	Sensitivity drift	Resolution
Pressure	Testo 622	$\pm 0.30$ kPa	-	0.01 kPa
Temperature	Fluke 325	$\pm 1$ %	-	0.01 °C
	DMM VA90A	$\pm 2$ %	-	0.01 °C
	K-type thermocouple	$\pm 2.2$ °C	-	-

## 5.7 Data comparison and validation methods

### 5.7.1 Roller volume displacement tests

The data obtained from the roller volume displacement tests will indicate the millilitres displaced in reference to the total angle of rotation of the motor. Comparing the data of the modelled/approximated volume displacement to that of the measured roller volume displacement should be quite simple. A root-mean square error (RMSE) and normalised root mean square error (NRMSE) between the average of the tested volumes and the modelled volume should provide a good indication of the model's accuracy.

### 5.7.2 Peristaltic pump tests

The flow rate of the modelled pump can be validated by comparing the average flow of the pump to that of the model. Similar to the roller volume displacement test validation, this validation is simplistic and can be done by calculating the standard deviation and or RMSE. The pressure response is not as simple to validate, as the pressure will have a continuous waveform response.

The similarity of the pressure simulation data compared to the experimental data can be quantified by using the Pearson correlation coefficient (5.6), which is determined using the covariance (5.7) of the data sets  $x$  and  $y$  [68]. However, if the motor speed between the experiment and the simulation have an offset it can render this comparison technique useless. This applies for data where the motor slips as well, and implies that data up to or from the point of where the pump becomes unpredictable should be discarded. The Pearson correlation coefficient  $\rho_{corr}$  used to compare the simulated pressure pulsations and experimental pressure pulsations is calculated as:

$$\rho = \frac{S_{xy}}{\sigma_x \sigma_y}, \quad (5.6)$$

with:

$$S_{xy} = \sum_{i=1}^n (x_i - \bar{x})(y_i - \bar{y}), \quad (5.7)$$

where  $\bar{y}$  and  $\bar{x}$  denote the averages of data sets  $x$  and  $y$  and  $\sigma$  the standard deviation. MATLAB determines the both the correlation coefficient and the test of a null hypotheses, which are values between 0 and 1. The test of a null hypothesis is an indication on how significant the correlation coefficient is, where values below 0.05 are considered significant. Correlation coefficients



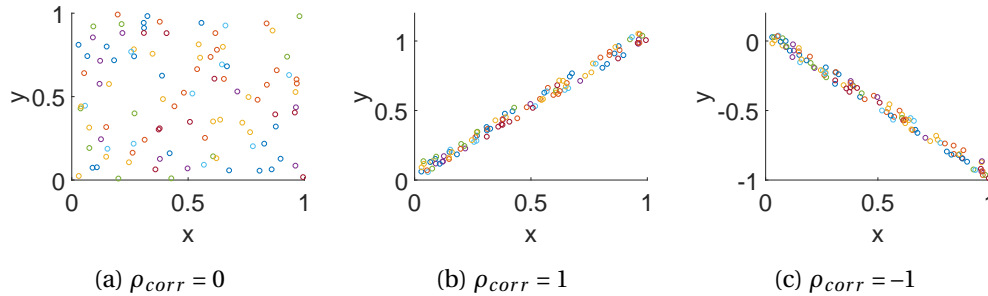


Figure 5.22: Indication of correlation between variables on the x-axis and y-axis

with a null hypothesis value above 0.05 are therefore rejected. A correlation coefficient with a value between 0.7 and 0.89 is considered to be a strong correlation, where a correlation coefficient above 0.9 is considered a very strong correlation between the x and y data entries. Fig. 5.22 gives an indication of different correlation coefficients between an x-axis variable and a y-axis variable.

In order to provide accurate and relevant information, two critical errors of the experiment must be avoided. The first error is incorrect sensor data. This error is mitigated by selecting appropriate sensors, sample times, and proper calibration discussed earlier in this chapter. The second critical error is incorrect motor speeds. Due to the repetitive nature of the rollers coming in and out of contact, a wavelike signal with somewhat predictable behaviour is produced. The motor speed can be calculated by determining the time period between peak values of the wavelike signal to ensure the accuracy of the comparisons. The techniques used to analyse the data as well as the motor speed tables are discussed in Appendix E.

The peak maximum and peak minimum values for both the inlet and outlet pressure sensors offer another method of comparing the experiments with one another as well as with the simulations. This comparison technique uses multiple sample points of each data set across the varying motor speeds and can indicate harmonic effects of the pump and or system components.

Table 5.4 gives an overview of the experiments and their descriptions. The three-roller experiments were tested with motor speeds varying from 10 r/min to 200 r/min in intervals of 10 r/min. When the motor started to slip to the point of no operation (which commonly occurred for the volume tests around 160 r/min) the tests were stopped. While experiment D also ranges from 10 r/min to 200 r/min, Experiment 5 and Simulation C range up to 300 r/min in incre-

ments of 10 r/min. Experiment 2 ranges at intermediate motor speeds from 15 r/min to 165 r/min in intervals of 10 r/min.

Table 5.4: Table of tests conducted on the peristaltic pump and how they are referred to

<b>Name:</b>	<b>Description:</b>
<b>Flow tests:</b>	
Experiment 1	Three-roller pump configuration flow test at room temperature (control)
Experiment 2	Three-roller pump configuration flow test at room temperature at intermediate motor speeds
Experiment 3	Three-roller pump configuration flow test at room temperature (repeated)
Experiment 4	Three-roller pump configuration flow test at elevated temperature
Experiment 5	Two-roller pump configuration flow test at room temperature
<b>Pressure pulsation tests:</b>	
Experiment A	Three-roller pump configuration pressure pulsation test with a reservoir height of 7 cm
Experiment B	Three-roller pump configuration pressure pulsation test with a reservoir height of 30 cm
Experiment C	Three-roller pump configuration pressure pulsation test with a reservoir height of 55 cm
Experiment D	Two-roller pump configuration pressure pulsation test with a reservoir height of 30 cm
<b>Simulations:</b>	
Simulation A	Three-roller pump configuration simulation with measured roller volume
Simulation B	Three-roller pump configuration simulation with approximated roller volume
Simulation C	Two-roller pump configuration simulation with measured roller volume

## 5.8 Conclusion

This chapter provides information on the tests and testing systems required for validating the model of the peristaltic pump. The test systems are catered towards testing the model-based pump design of Chapter 4.

Four test benches are described in this chapter, two of which can be considered subsets of the peristaltic pump test bench, namely: the resistance test bench and compliance test bench. The two test benches are used to obtain the resistance and compliance parameters of the peristaltic pump test bench, and can therefore be considered subsets of the peristaltic pump test bench.

The peristaltic pump test bench and roller volume test bench are used to test three main aspects pertaining to the model and model based pump design, namely: The roller volume displacement approximation, the modelled pump flow rate, and the pressure response of the system the pump is integrated with.

The instruments used to conduct the tests are described with an indication of calibration where necessary. The main sensors used to validate the model are: Pressure sensors, precision weight scales, and a volumetric measuring device (medical syringe). The validation technique is described as well, where the main methods include the root mean square error (RMSE) and the Pearson correlation coefficient.

### Results

---

#### 6.1 Introduction

This chapter discusses the experimental results acquired from the designed test benches. The peristaltic pump model is validated through a range of comparisons between the experimental results and simulated responses of the model.

The chapter begins with the volume displacement approximation of the roller compared to its corresponding experimental data. This is followed by the volume displacement tests of the pump, where the test bench is altered to allow flow from the reservoir out of the system. Next, the pressure pulsations associated with the recirculated flow tests of the peristaltic pump at various motor speeds and its comparison to the simulated values are discussed. The chapter is then concluded with the operational limits of the peristaltic pump, such as the minimum and maximum operating pressures and hydrostatic capabilities of the pump.

Unless specified otherwise, the tests were run at room temperature conditions, implying a temperature of  $\sim 23\text{--}25$  °C and ambient pressure of 86 kPa. When referring to an experiment, reference is being made to the set of tests conducted for a certain aspect e.g. pressure pulsation correlation to reservoir pressure. The tube inside the pump was not replaced in between Experiments A, B, and C (three-roller recirculated flow tests). However, it was replaced in between each experiment pertaining to the pump's volume displacement tests and maximum and minimum pressure tests. This was done to ensure that wear does not affect test results.

## 6.2 Model validation

### 6.2.1 Roller volume displacement

The experimental data indicated in Fig. 6.1 includes the values of all 14 increments for all seven tests completed. The test average shows the close correlation of each test and the individual tests. The general S-shaped curve of the volume displacement as the roller comes into contact with the process tube seen in [16].

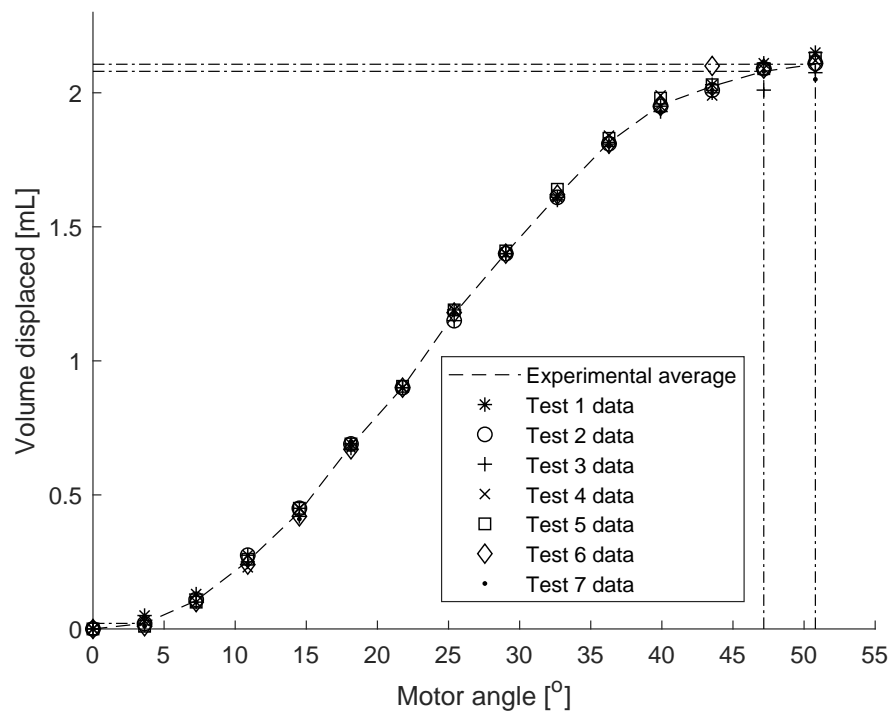


Figure 6.1: Volume displacement results of a peristaltic pump roller during engagement over a rotational span of  $50.79^\circ$

In order to compare the theoretical values to the experimental values the experimental data needs to be fitted to the same  $x$ -axis. This implies that the experimental data with a theoretical total rotation of  $50.794^\circ$  over 14 increments will be reduced to a theoretical total angle of  $43.538^\circ$  and 12 increments. The increments that are neglected during fitting and comparison need to account for the maximum amount of data retrieval, thus it is important to understand which data is negligible.

The two points where data can be lost for this specific test are at the initial

values (at the first increment) and at the final value (last increment). This is due to the uncertainty of the exact point where the roller makes initial contact with the tube, and where the tube is fully occluded. This is also further motivated by the fact that the difference between the initial value and the first incremental value as well as the difference between the final value and the increment directly before the final value have the lowest differences (0.0207 mL and 0.0264 mL respectively).

Additionally, the tolerances of the parts were also taken into consideration with the approximated volumes. The parts were measured with a vernier calliper. The measured distances that affect the approximation are compared to the theoretical sizes in Table 6.1 and give an indication of the printer accuracy.

Table 6.1: Indication of part tolerances caused by printing inaccuracies

	Offset radius	Roller radius	Casing radius
Modelled size:	40 mm	20 mm	63 mm
Measured size:	39.5 mm	19.87 mm	62.76 mm

This results in the modelled engage angle being reduced from  $43.54^\circ$  to  $43.00^\circ$ . This effect is not substantial with regards to fitting the data, but does have an effect on the volume approximated and thus the induced flow rate. These tolerances change the maximum value of the approximated flow induced by the roller by 6.73 %.

The maximum standard deviation over the 12 incremental positions for the seven repeated tests has a value of 0.04 mL indicating that the experimental values do not deviate from each repeated test and that the data is reliable. The root-mean square error (RMSE) (otherwise known as the standard deviation of residuals) between the experimental average and the theoretical data shown in Fig. 6.2 is equal to 0.12 mL (or 5.86 % normalised root mean square error (NRMSE) of 2.08 mL). The roller induced flow, which is derived from the rate of change of the roller's displaced volume, deviates from the expected induced flow derived from the measured roller volume with 3.95 %.

It is understandable that the approximation volume is lower than that of the measured volume as the approximation method does not take the tube walls bending around the area of occlusion into account. Table 6.2 compares the approximation methods mentioned in the modelling chapter and their error from the maximum measured volume displacement.

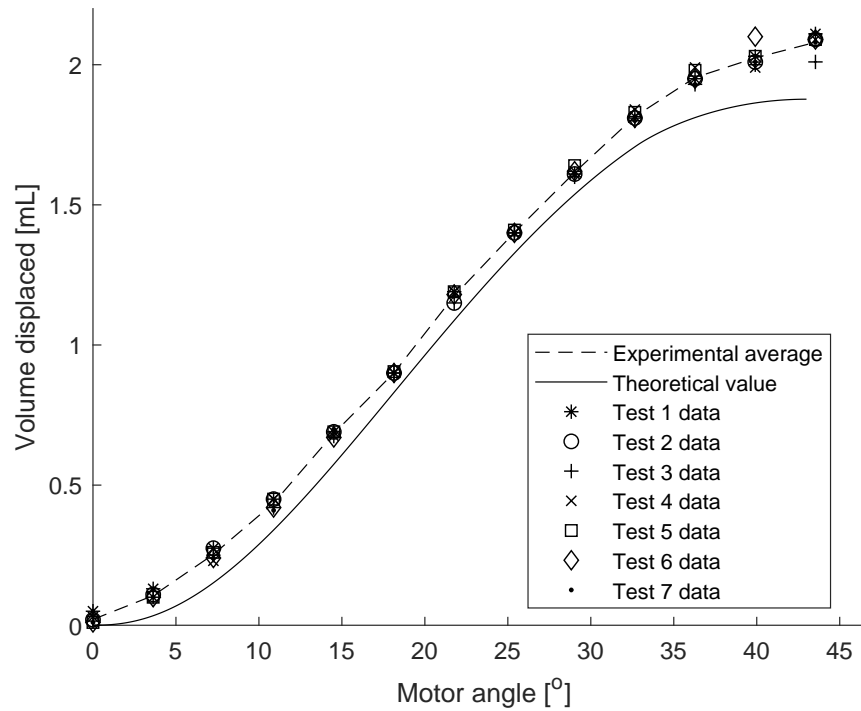


Figure 6.2: Adjusted roller volume test results compared to the volume displacement approximation model, RMSE = 0.1218 mL

Table 6.2: Accuracy comparison of the roller volume approximation methods for the maximum volume displaced

	Cylindrical approximation	Relational area approximation	Integration approximation
Volume:	2.76 mL	2.00 mL	1.88 mL
Percentage error:	32.69 %	3.86 %	9.62 %

## 6.2.2 Flow characteristics

To test the flow of the pump the motor was rotated 10 full rotations with the fluid being displaced into a beaker. The time it takes for the 10 rotations to complete and therefore displace the fluid is dependant on the rotational speed of the pump. The mass of the fluid displaced  $M$  was measured for each test, which was used to calculate the flow speed of the pump in  $\text{m}^3/\text{s}$  as in (6.1).  $K$  denotes the number of rotations and  $N$  the rotational speed in  $\text{r}/\text{min}$ . The motor speed was varied, as with the pressure tests, from 10  $\text{r}/\text{min}$  to 170  $\text{r}/\text{min}$  in intervals of 10  $\text{r}/\text{min}$ . The stepper motor started to slip for the experiments during the

three-roller configuration at roughly 160 r/min. This slippage caused the motor to not turn a full 10 rotations and thus made the test inaccurate. It is for this reason that the three-roller tests are not tested to the full range of 200 r/min.

$$Q = \frac{M}{\rho} \frac{60K}{N} \quad (6.1)$$

The pump was initially tested for one rotation at 2 r/min and 20 r/min to obtain volume displacement values that are not affected by resonance or any possible non-linearity. Each test was repeated 10 times for the assurance of accuracy for both the three-roller pump configuration and the two-roller pump configuration. These tests serve as a control volume for one rotation and also give an indication of the accuracy (or repeatability) of the pump.

For the three-roller pump configuration, the average volume was determined to be 21.01 mL for the 2 r/min tests and 21.02 mL for the 20 r/min tests. The 2 r/min and 20 r/min values had an average standard deviation of 0.13 mL and 0.09 mL respectively for Experiments 1–3. The model suggests a volume displacement of 21.29 mL with the measured roller volume, and 21.88 mL for the approximated roller volume for one rotation of the pump. Using the average of the 2 r/min and 20 r/min tests (21.02 mL) this amounts to an inaccuracy of 1.28 % and 4.03 % respectively.

For the two-roller pump configuration, the 2 r/min and 20 r/min values were experimentally determined to be 22.82 mL and 22.85 mL respectively. The 2 r/min and 20 r/min values had an average standard deviation of 0.17 mL and 0.05 mL respectively for Experiment 5. The model suggests a volume displacement of 23.37 mL with the measured roller volume, and 23.76 mL for the approximated roller volume for one rotation of the pump. Once more, using the average of the 2 r/min and 20 r/min tests (22.84 mL) this amounts to an inaccuracy of 2.32 % and 4.02 % respectively.

These errors are contradictory to what is theoretically expected, as one less roller on the pump should reduce the effect of the approximation error by roughly one third. This discrepancy might be caused by an imprecise tube alignment to the backplate within the pump. This would suggest that the tube does not conform perfectly to the backplate (or raceway), as assumed in the modelling. This would effectively reduce the total volume in the tube inside the pump. In this case, the two-roller pump configuration model can be expected to have a larger deviation than expected from the experimental results, as the two-rollers do not mitigate the deformation of the tube inside the pump, whereas the three-roller configuration does.



To further investigate this discrepancy, the error of the maximum approximated roller displaced volume (0.20 mL) should occur for each roller on the pump. This implies that this error is multiplied for each roller on the pump for a full rotation of the motor. This amounts to an expected error of 2.82 % (0.94 % per roller) for the three-roller configuration, and 1.74 % (0.87 % per roller) for the two-roller configuration, per rotation. The expected accuracy of the modelled volume displacement per rotation using the approximated roller volume can then be calculated by adding this expected error to the modelled volume displacement per rotation using the measured roller volume. This can be considered valid, as the error that occurs on the modelled volume displacement per rotation using the measured roller volume is indicative of the tube alignment errors. Adding these errors yields an expected error of 4.1 % for the three-roller pump configuration values and 4.06 % for the two-roller pump configuration values per rotation, which are within 0.07 % and 0.04 % of the measured errors respectively.

Although insignificant, it should be mentioned that a priming effect was noticed during the initial control volume experiments, which is shown with accompanying linear regression lines in Fig. 6.3. This priming effect can be seen by the increasing volume over each of the tests. The test was initially conducted with the 2 r/min speed, then with the 20 r/min speed. The gradient for the 20 r/min test is thus lower than that for the 2 r/min tests with a larger initial volume. This priming effect can be caused by the new tube being stretched into position when the pump is first run. The effect is no longer present after roughly 20 rotations in a single direction.

Fig. 6.4 indicates the volume obtained from Experiment 1 for the flow rate tests. For each flow experiment (Experiment 1–5) each motor speed was tested 10 times to ensure repeatable accuracy of the tests. For Experiment 1 the average deviance per test is 1.23 mL with a maximum deviation of 4.09 mL. The inaccuracies can be seen to increase at larger motor speeds, specifically at 160 r/min and 170 r/min.

As stated in Chapter 5, multiple flow experiments are conducted in this chapter. This is done in order to determine possible external, or unmodelled, effects on the volume measurement. The flow rate of Experiment 2 is measured at each intermediate interval of Experiment 1 (that is from 15 r/min to 165 r/min in intervals of 10 r/min). Experiment 3 repeats the same tests of Experiment 1 but in a randomised order to deter the possibility of the tube heating with repeated tests or wearing. Experiment 4 follows the same randomisation order of the tests of Experiment 3 but with a water temperature of 40 °C. Experiment 5 pertains to the volume displacement of the dual roller configuration and is

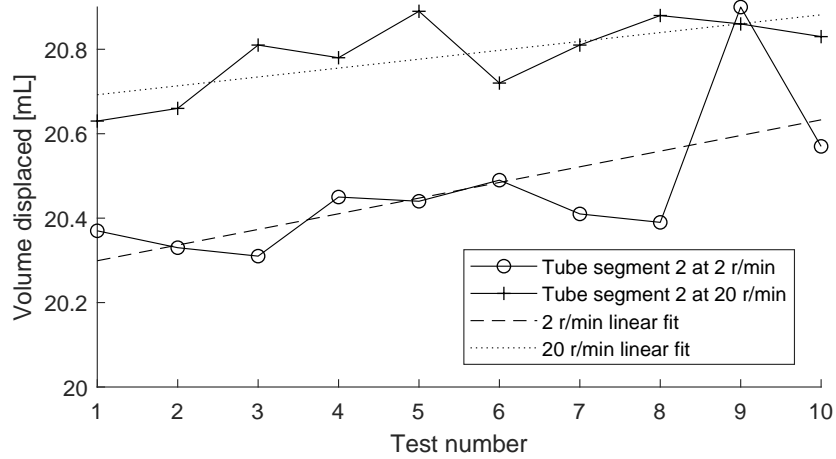


Figure 6.3: Experiment 2: Control volume test results indicating the priming effect

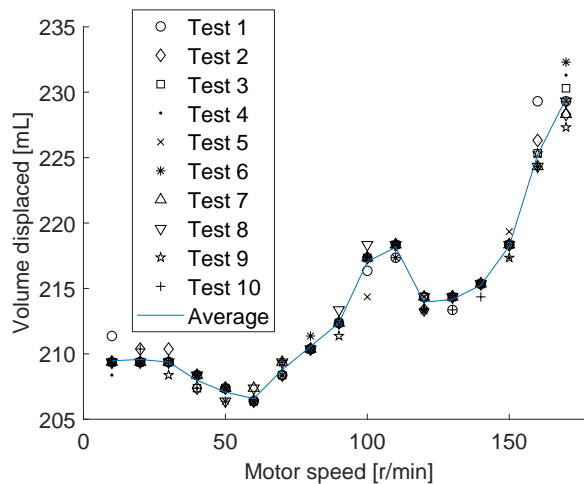


Figure 6.4: Experiment 1: Volume displacement results

compared individually to Simulation C in Fig. 6.6.

Due to the motor slip that occurs on some tests, the volume may inconsistently vary for larger motor speeds. Due to the low probability of measuring more volume than what the pump had displaced, and the high repeatability of the pump, the maximum value of each test is used rather than the average. Experiment 4 which was conducted at 40 °C is seen to have higher initial values, but tends to be more stable compared to the other experiments. This is thought to be caused by the thermal expansion of the process tube under higher temperatures, which would essentially increase the inner diameter of the tube. The resilience

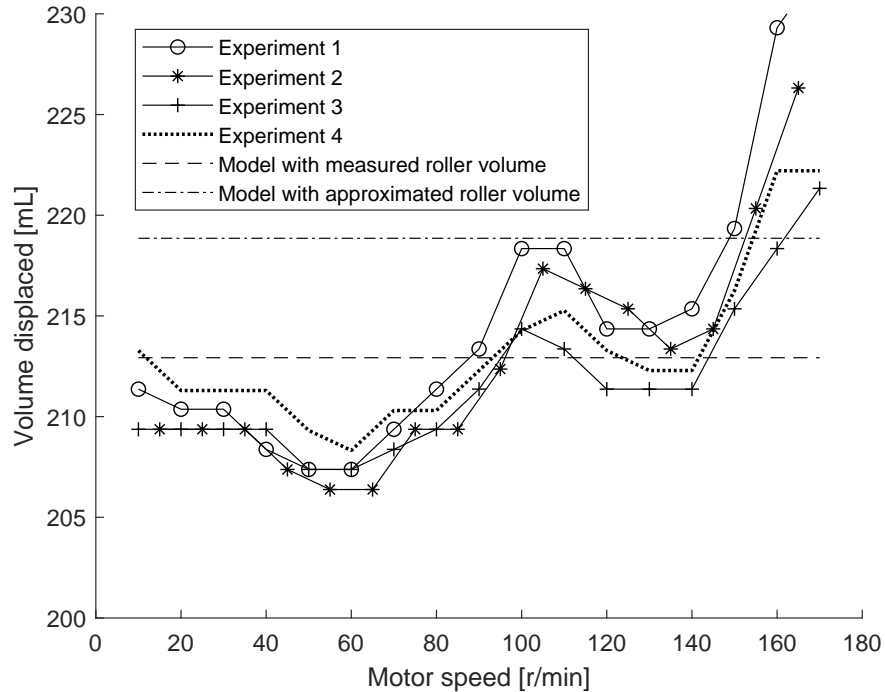


Figure 6.5: Experiment 1-4: Pump volume displacement test results compared to the modelled values using the approximated roller volume and measured roller volume

to the non-linearities is possibly brought about by the thermal change altering the compliance characteristics of the inlet and outlet lines. Under a constant pressure, Menon [47] indicates that the density of water would change from  $997 \text{ kg/m}^3$  at room temperature to  $992 \text{ kg/m}^3$  at  $40 \text{ }^\circ\text{C}$  (0.5%). This is significant in such a way that the inertia and resistance properties of the fluid are altered. A change reduction resistance could correlate to the volume gain, while a reduced inertia can reduce the peak response values.

As the flow of the pump is directly proportional to the volume displacement, the inaccuracies of the volume values reflect directly on the flow. The accuracy of modelled flow can thus be derived from the modelled volume displacement. The RMSE, NRMSE, and maximum deviation of the modelled values compared to all volume displacement tests (used to determine the flow) are indicated in Table 6.3. The NRMSE and maximum deviation percentages are calculated with reference to the average volume displaced for that particular experiment.

It should be noted that the two-roller pump configuration yields more accu-

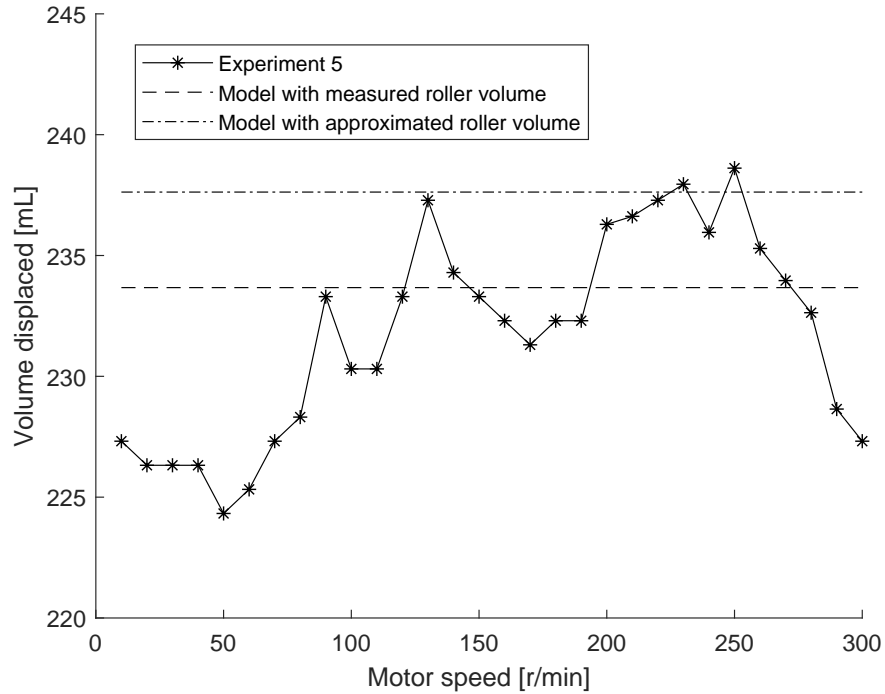


Figure 6.6: Experiment 5: Pump volume displacement test results compared to the modelled values using the approximated roller volume and measured roller volume

Table 6.3: Experiments 1–5: Accuracies of the modelled pump volume displacement using (a) the measured roller volume and (b) the approximated volume

	RMSE [mL]:		NRMSE [%]:		Maximum deviation [%]:	
	(a)	(b)	(a)	(b)	(a)	(b)
Experiment 1	7.14	8.02	3.33	3.74	9.02	6.26
Experiment 2	5.33	8.16	2.50	3.84	6.30	5.87
Experiment 3	3.94	8.11	1.86	3.83	3.97	5.42
Experiment 4	3.82	6.75	1.79	3.16	4.35	4.94
Experiment 5	4.56	7.18	1.97	3.10	4.03	5.74

rate results than that of the three-roller configuration, as theoretically expected. This may be as a result of the larger motor speeds, used for the flow experiments,

providing less time for the tube to deform away from the backplate.

It was noticed that the volume displacement shows a similar form to the peak pressure values of the flow test. The Pearson correlation coefficient for the volume in relation to the peak pressures can be determined with the pressure data from the flow tests. This is done to determine which characteristic of the pump gives rise to this unique attribute. The Pearson correlation coefficients for Experiments 1, 2, and 4 are displayed in Table 6.4. Experiment 3 is neglected as the randomisation of Experiment 3 is present in Experiment 4 and is not seen to have any noticeable effects on the volume displacement. Experiment 5 pertains to the two-roller pump configuration and has correlation coefficients noticeably lower than that of the three-roller configuration, yet is still considered a strong correlation. The best correlation coefficient was found to be that of the inlet peak maximum pressure. The volume of Experiment 1 is as well as Experiment 5 are plotted along with the maximum peak average of the inlet pressures over the varying motor speeds in Fig. 6.7 to give an indication of this correlation.

Table 6.4: Comparison of the Pearson correlation coefficients of the peak pressure values of each flow experiment compared to the volume displacement of each test

	<b>Inlet peak maximum</b>	<b>Inlet peak minimum</b>	<b>Outlet peak maximum</b>	<b>Outlet peak minimum</b>
Experiment 1	0.93	-0.84	0.72	-0.63
Experiment 2	0.90	-0.83	0.80	-0.83
Experiment 3	0.86	-0.75	0.79	-0.49
Experiment 4	0.87	-0.75	0.76	-0.49
Experiment 5	0.70	-0.79	0.49	-0.47

It is hypothesised that the large compliance of the process tube inside the pump is one of the main causes of the non-linear flow characteristics of the pump. This would provide an explanation to the strong correlation of the inlet pressures to the flow rates. It is probable that a large compliance of the process tube allows the tube to expand when exposed to the peak pressures of the system response. With correct timing, these peak pressures can occur right before the roller completely occludes the tube, effectively containing the larger pressure inside the tube segment between two rollers. The volume, contained within the expanded tube segment, would then be transported towards the pump outlet, effectively increasing the amount of volume displaced by the pump. The model does not account for this effect and so this reflected in the error of the modelled

values. The calculated flow rates of Experiments 1–4 are indicated in Fig. 6.8 along with the modelled flow rate using the approximated roller volume.

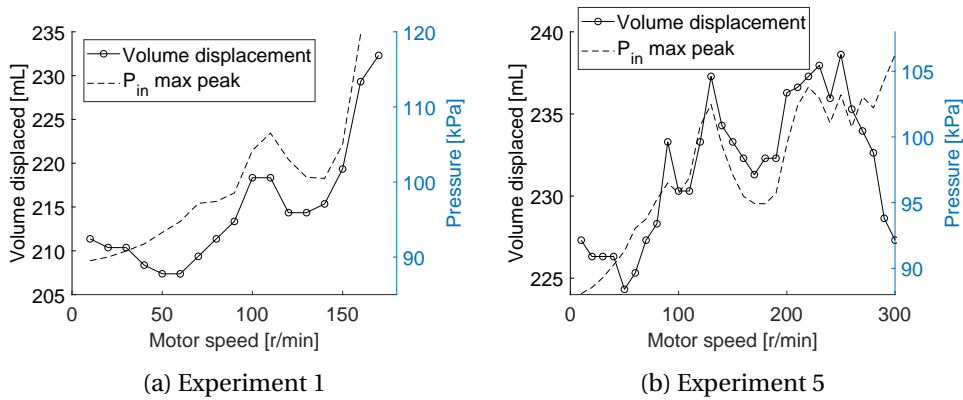


Figure 6.7: Experiment 1 and 5: Volume displacement compared to the inlet peak maximum pressures

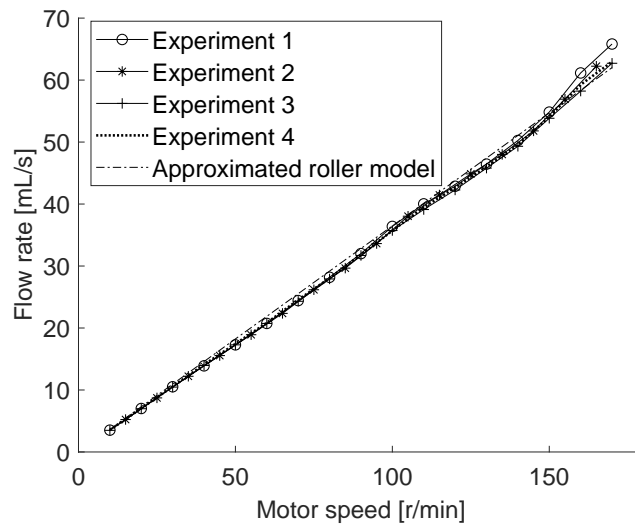


Figure 6.8: Experiments 1–4: Flow compared to the modelled flow using the approximated roller volume

### 6.2.3 Pressure pulsations

The initial pressure tests were conducted with various fluid heights in the reservoir tank. This changes the reservoir pressure slightly and indicates the system response under different reservoir pressures (also referred to as ambient pressures). The responses of the system was tested at 7 cm, 30 cm, and 55 cm and are referred to Experiment A, Experiment B, and Experiment C respectively. The comparisons of all the tests relating to pressure are corrected regarding the offset between the two pressure sensors. The corrected difference in ambient pressure readings between the two pressure sensors for Experiment A, B and C were 0.94 kPa, 0.68 kPa, and 0.84 kPa respectively. These values are within the  $\pm 1.75\%$  sensor uncertainty bracket for each sensor and are acceptable.

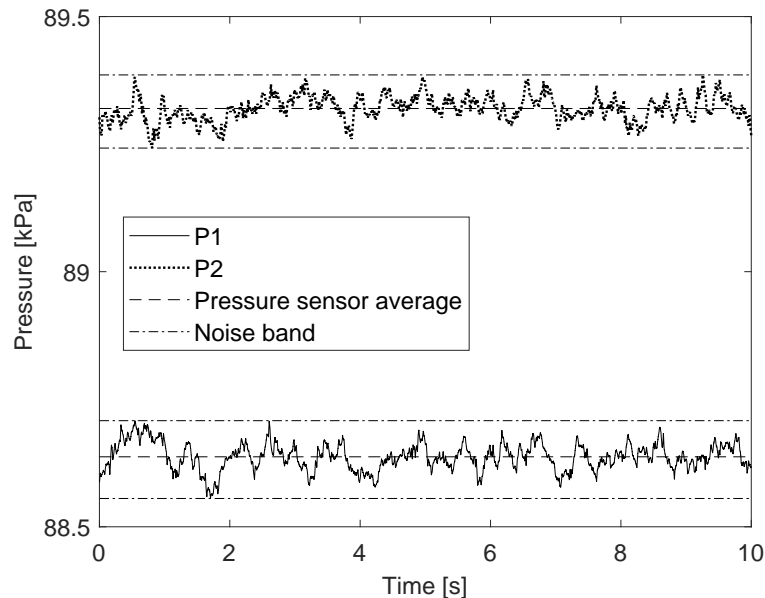


Figure 6.9: Experiment B: Ambient pressure reading indicating the sensor values in the solid (P1) and dotted (P2) lines, the noise bands (dot-dashed lines), and the mean pressure values (dashed lines)

The mean difference in ambient pressure between Experiment A and Experiment C is the largest, and was theoretically determined to be 4.70 kPa, with a measured value of 4.72 kPa. The difference in values can be attributed to a fault in the precise measurement of the actual heights of the fluid in the reservoir. The response is compared for rotational values of 10 r/min to 200 r/min to give an indication of the differences between the system responses at different flow rates of the pump. It was noticed that lower motor speeds had high noise values not caused by environmental noise. This noise changes in relation to the motor

speed and is not prominent at values above 60 r/min. It is hypothesised that this noise is induced by the stepper motor as it changes with motor speed. The additional noise however does not deter the comparisons for validation. The Savitzky-Golay filter [69, 70] was applied to the data for rotational values under 60 r/min and used for comparison as a normal data set. Fig. 6.10 indicates the result of applying the Savitzky-Golay filter to the test data of Experiment B, and also indicates the reduction in what seems to be motor induced noise at higher r/min values.

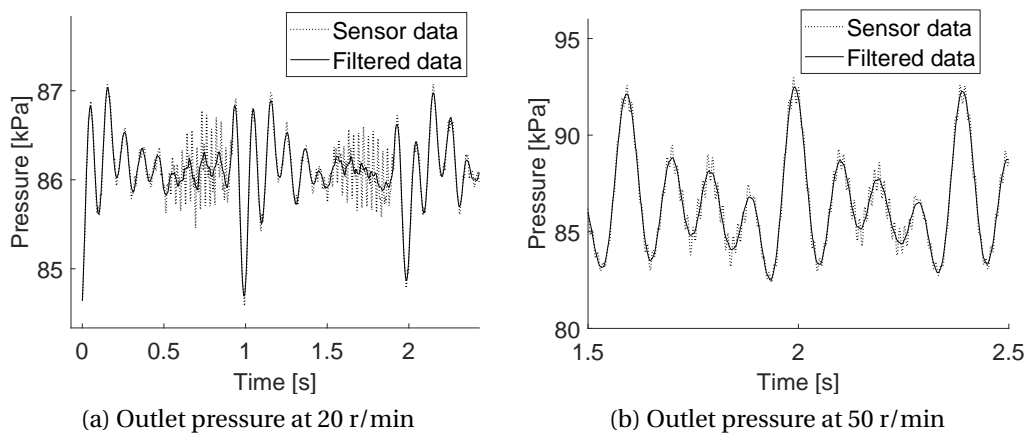


Figure 6.10: Savitzky-Golay filter applied to the outlet pressure sensor data for 20 r/min and 50 r/min of Experiment B

An additional adjustment is made to better gauge the difference in characteristics between the tests. This adjustment was made by measuring the ambient pressure (indicated in Fig. 6.9), calculating the difference between the average pressures over the test time, and adding it to  $P_2$  such that  $P_2 = P_2 + (P_1 - P_2)$ . The mean ambient pressures were used to normalise the data to that of Experiment B. Experiment B is used as a control, as the acquired data was the most consistent and reliable, with minimal motor slipping occurring. This was done in order to discern differences in system response between the tests. Not correcting for the pressure offset in turn makes it difficult to discern differences as indicated by Fig. 6.11.

Fig. 6.12 indicates the same system response of Fig. 6.11 but accounts for the offset in pressures with regards to the ambient pressures taken before each test. The correction allows for differences between the responses to be clearly seen in comparison to one another. The slight increase in pressure is expected to change the response of the system slightly, as adding a steady state pressure changes the compliance characteristics of the system. This can be concluded from the



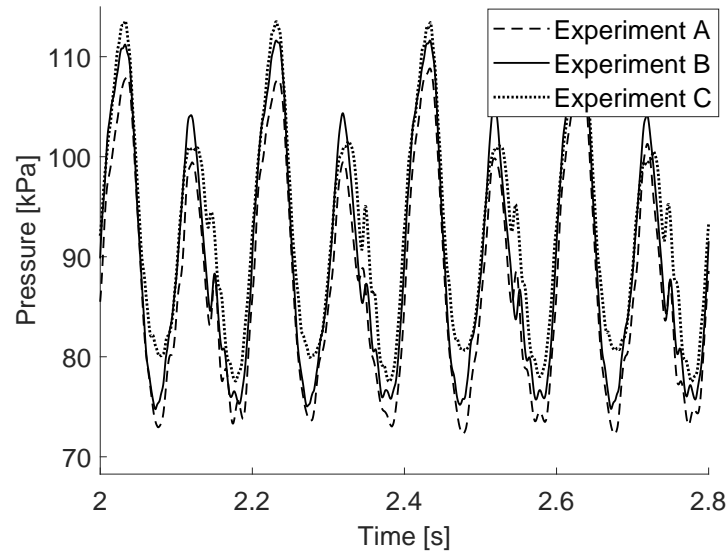


Figure 6.11: Experiments A, B, and C: System response pressure at the pump outlet at 100 r/min

lower secondary peaks and primary troughs, as the response of Experiment C has the lowest secondary peak value as well as the highest primary trough value, indicating that Experiment C has the smallest pressure span. In contrast, Experiment A has the lowest primary trough value, yet Experiment B has the highest secondary peak value. This could indicate a harmonic resonance effect and is why multiple tests are sampled at different motor speeds.

The change in pressures at the pump inlet in Fig. 6.13 seems to have the opposite effect than the effect noticed on the pump outlet. This implies that the peak and trough pressure values for Experiment C are higher than those of Experiment A and Experiment B. This indicates Experiment C has the largest pressure span at the pump inlet in contrast to having the smallest pressure span at the outlet. The effects are more visible by comparing the maximum peak and minimum peak values in relation to the motor speed. In order to do this, the peak minimums and maximums of the pressure waveform of each motor speed test were evaluated and averaged. These averaged peak values are referred to as the peak averages. The peak averages can then be plotted over the varying motor speeds as indicated in Fig. 6.14. This will show the maximum and minimum amplitudes, as well as the span of the pressure pulsations at the inlet and outlet. To avoid confusion, P1 and P2 are often referred to as  $P_{in}$  and  $P_{out}$ , depending on the direction of rotation of the motor.

It should be noted that the motor started to slip at speeds near 160 r/min. This is not an issue with regards to the pressure pulsations as the slippage

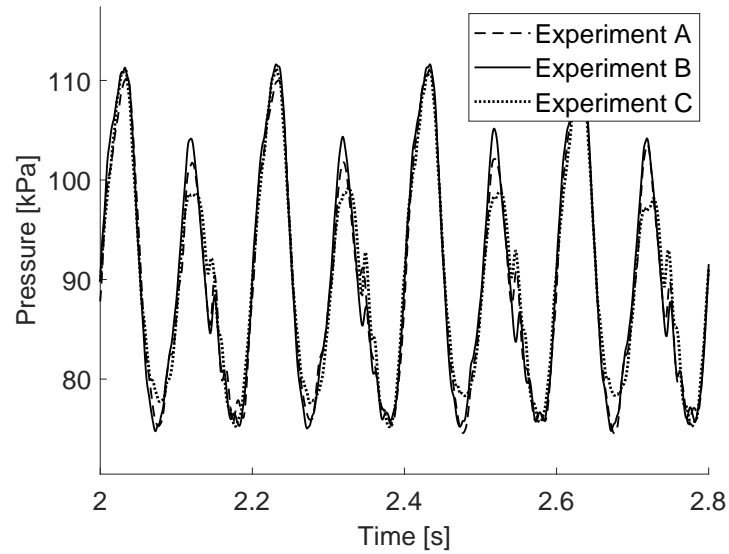


Figure 6.12: Experiments A, B, and C: Adjusted system pressure response at the pump outlet at 100 r/min

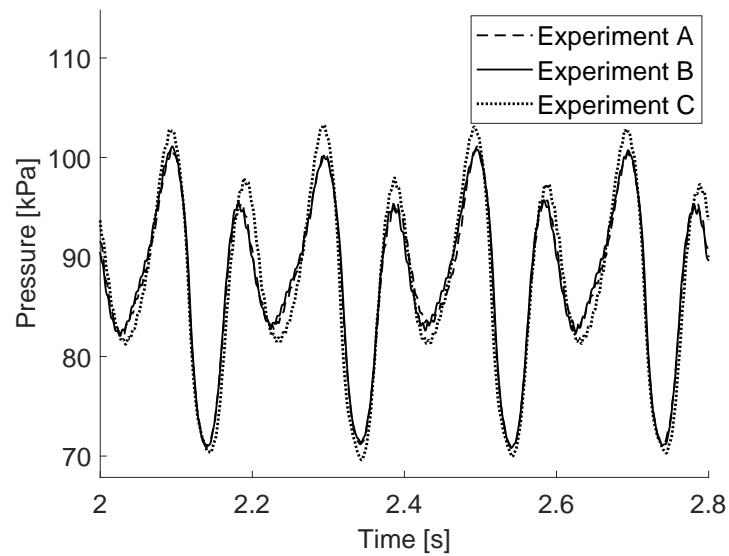


Figure 6.13: Experiments A, B, and C: Adjusted system pressure response at the pump inlet at 100 r/min

occurred infrequently at irregular intervals. This allowed for the pulsation data to be salvaged for rotational speeds up to 200 r/min for the recirculated flow tests. Fig. 6.14 indicates the non-linear relationship of peak maxima and minima pressures to the motor speed. This is made clear by the fact that the flow induced

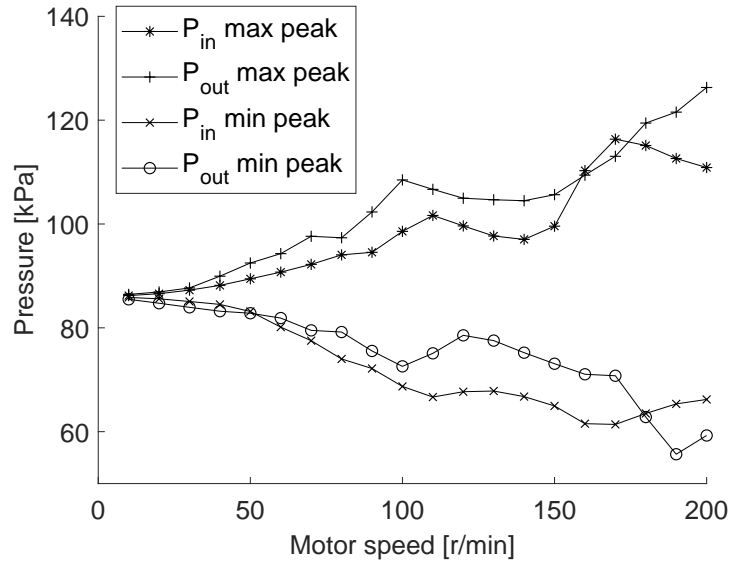


Figure 6.14: Experiment A: Averaged peak maximum and peak minimum pressure values for the inlet and outlet

by the roller linearly increases with the motor speed and should incite a linearly proportional response. The peak of the maximum values at 120 r/min for the inlet and 110 r/min for the outlet might imply a resonant frequency in this range (6 Hz) for the system or pump. The inlet and the outlet have a gradient difference implying a difference in averages across the r/min values which is commonly associated with any element that induces flow. The maximum and minimum peak values at the pump inlet and pump outlet are compared for each height of the reservoir in Fig. 6.15.

Fig. 6.15 indicates that the a larger constant pressure on the system causes the system have a slightly larger reaction over resonant frequencies. This effect seems to be amplified at larger frequencies and is more visible at the pump inlet in Figs. 6.15a and 6.15c between 150 r/min and 200 r/min. This resonant period can also be seen shifting phase at the pump inlet between the varying height values. The phase shifts from a peak resonant value at 170 r/min for the 7 cm height to 180 r/min for the 30 cm height, and finally 190 r/min for the 55 cm reservoir height.

The effects that the additional pressure has on the pump outlet seems insignificant, but this may be due to the low motor speed of the tests. These effects at the inlet can be due to the change in compliance of the inlet and outlet in reaction to the adjusted pressures as stated previously. The compliance is sus-

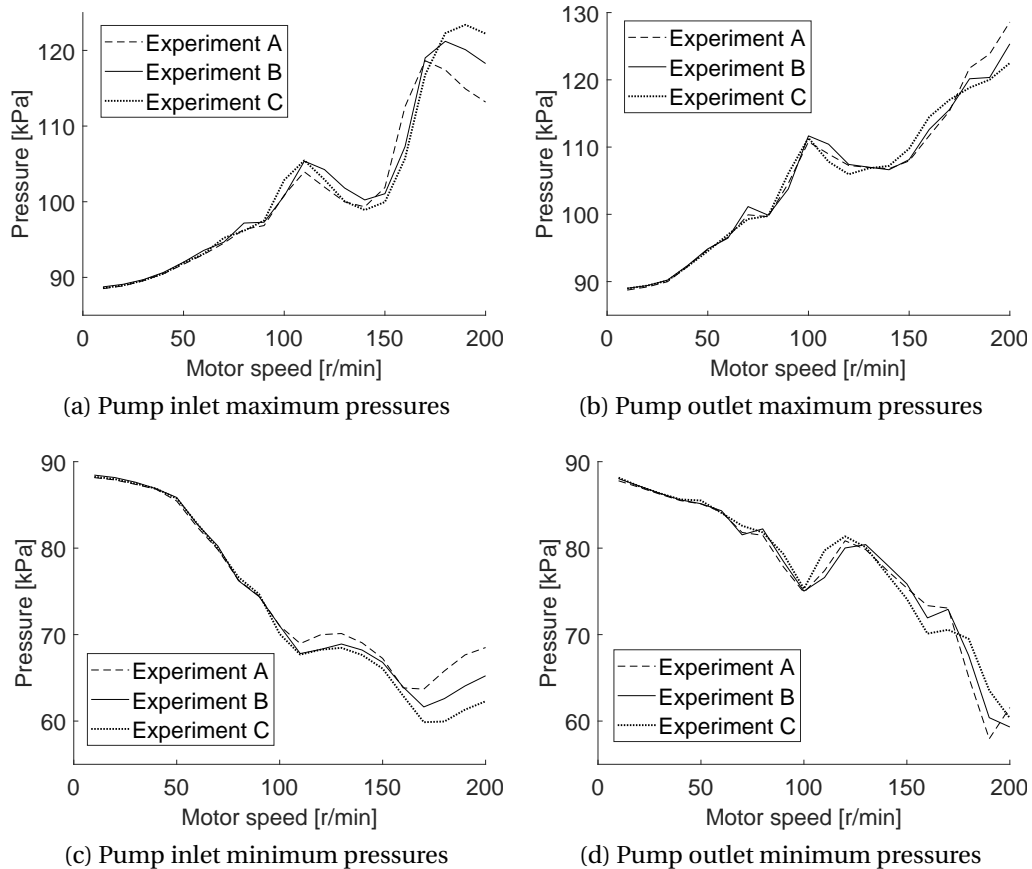


Figure 6.15: Experiment A, B, and C: Comparison of peak maximum and minimum pressure values

pected as the change in reservoir pressure can only impact the fluid resistance and inertia by changing the density of the fluid. The change in density for a constant temperature due to a change in pressure from 86.56 kPa to 91.29 kPa (measured ambient pressures for Experiment A and Experiment C respectively) would be roughly  $0.002 \text{ kg/m}^3$  which is quite insignificant (0.0002% change in density).

The average pressures over the entire test period for each motor speed value were compared but showed no significant deviation between the magnitudes. A better indication of the differences than that of the averages can be made by calculating the RMSE with reference to the Experiment B. Fig. 6.16 indicates the RMSE of Experiment A and Experiment C when calculated with reference to the Experiment B. The values of the RMSE indicate that the aforementioned

characteristics are somewhat correct, in that, the additional pressure increases the peak values for the inlet. The outlet RMSE values indicate a larger response to the 100 r/min value and near the 200 r/min value. This would imply that the resonance of the system is not at 6.5~7 Hz (130~140 r/min).

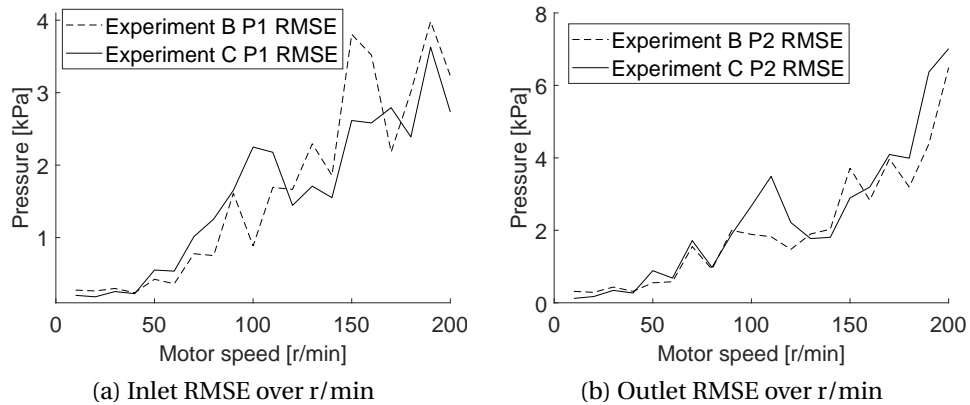


Figure 6.16: Experiment A and C: Root mean square error of the pressure values with regards to Experiment B

Table 6.5 indicates the parameter values used for the simulation of the peristaltic pump in a summarised form. The simulated values of the pressure pulsations for the three-roller and two-roller pump configurations are compared to the pressure control experiments (Experiment B and Experiment D respectively) for validation. The model was simulated using both the flow induced by the measured roller volume displacement as well as the approximated roller volume displacement (Simulation A and B respectively). The simulation pertaining to the approximated volume is, however, only compared to the three-roller pump configuration. The measured volume displacement of the roller is used to give an indication of the accuracy of the simulation, where the approximated volume simulation is used to validate the accuracy of the volume approximation in the simulation environment.

Fig. 6.17 shows the correlation of the form of the pressure pulsations across various r/min values. The simulation and experimental results can be compared with the peak average values in Fig. 6.15 to give an indication of the accuracy of the pressure span of the simulation.

A positive offset is noticed regarding the pump outlet while a negative offset can be seen at the pump inlet. This is more prevalent at lower r/min values such as that of 20 r/min indicated in Fig. 6.18. This can be caused by the constant resistance value used for the simulation value, as E.O. Doebelin suggests that

Table 6.5: Simulation parameters used to validate the lumped parameter model

<b>Parameter:</b>	<b>Symbol:</b>	<b>Value:</b>	<b>Units:</b>
Operational speed	$N$	0–200	r/min
Number of rollers	$NU$	2 and 3	-
Pump contact angle	$\beta$	30	°
Angle of engagement	$\phi$	43.00	°
Reservoir pressure	$P_{res}$	88.637	kPa
Roller radius	$r_{roller}$	19.87	mm
Roller offset radius	$r_{offset}$	39.5	mm
Backplate radius	$r_b$	62.76	mm
Inner tube radius	$r_i$	5	mm
Outer tube radius	$r_o$	7	mm
Inlet resistance	$R_{in}$	0.1108	kPa·s/mL
Outlet resistance	$R_{out}$	0.1108	kPa·s/mL
Inlet capacitance	$C_{in}$	0.036	mL/kPa
Outlet capacitance	$C_{out}$	0.036	mL/kPa
Inlet inductance	$L_{in}$	0.006	kPa·s <sup>2</sup> /mL
Outlet inductance	$L_{out}$	0.006	kPa·s <sup>2</sup> /mL

the resistance is not linear regarding flow rate [14]. This is more prominent at lower r/min values as the smaller peak to peak values highlight this offset.

The simulation results can be compared to the test results by determining the Pearson correlation coefficient of the two values. The Pearson correlation coefficient values of 1 indicate a positive correlation, -1 a negative correlation, and 0 indicate no correlation. Fig. 6.19 indicates the Pearson correlation coefficient over the motor speed of the experiments. The coefficient is initially relatively low for both the inlet and outlet pressures as expected (due to the signal-to-noise ratio). The coefficient rises gradually implying a closer correlation of the simulated results and test results and reaches exceptional values of 0.98 at 120 r/min for the inlet pressure and 0.95 at 110 r/min for the outlet pressure. The inlet pressures of Simulation A, B, and C had average correlation coefficients of 0.83, 0.85, and 0.80 respectively. The average correlation coefficients of the outlet pressures are slightly lower than that of the inlet pressures, with values of 0.74, 0.75, and 0.79 respectively. Interestingly the simulation with the approximated roller volume shows a marginally better average correlation to the test data than the simulation with the measured roller volume. This is likely due to the fitting of the measured roller data (in which the initial and end results were discarded) changing the form of the induced flow.

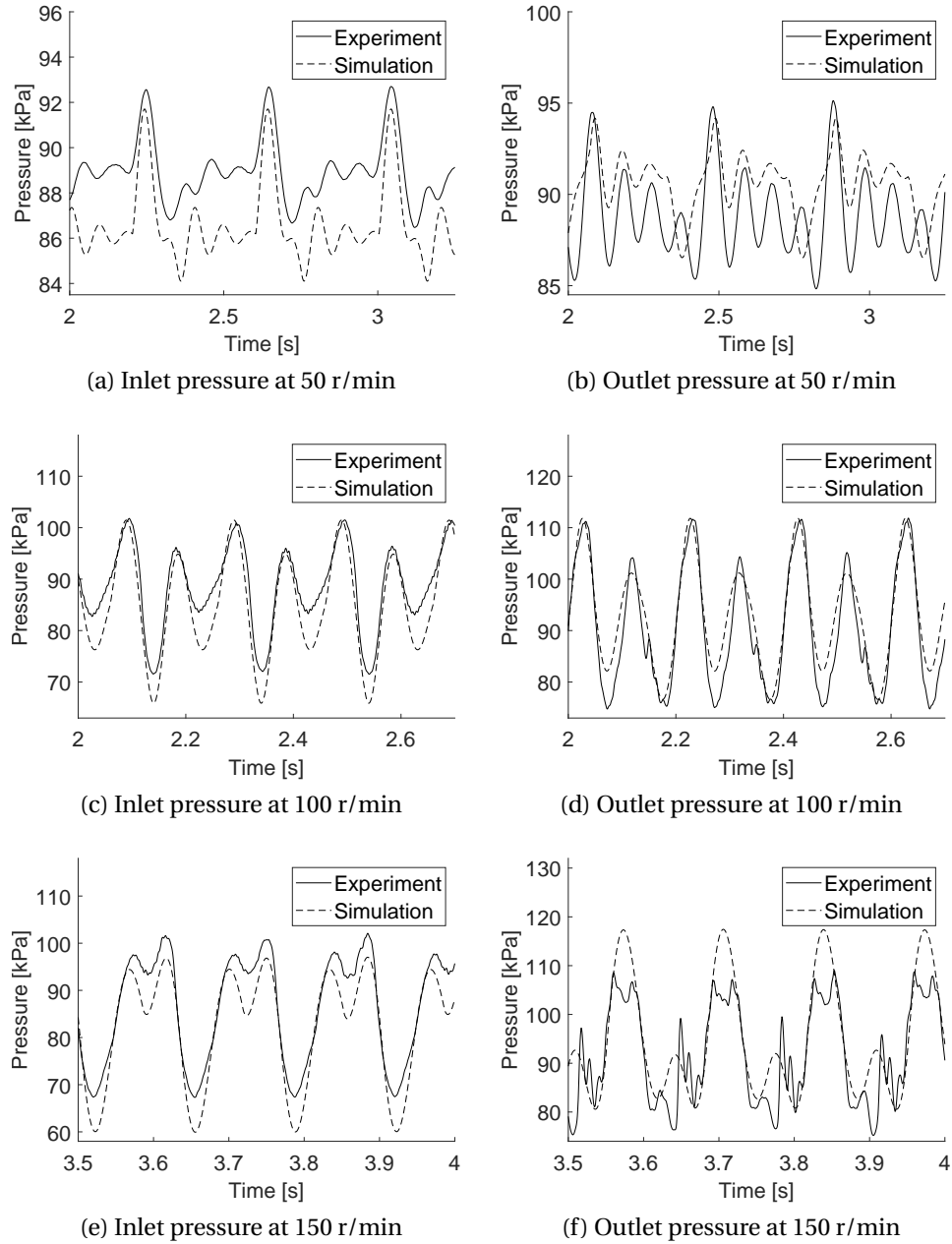


Figure 6.17: Experiment B: Comparison to Simulation A pressure results

The peak average comparison used to compare the height tests can be used with the simulation data to see the simulation response over various motor speeds and as to whether or not it correlates to the experimental data. These peak averages are compared to one another in Fig. 6.20. The simulation data

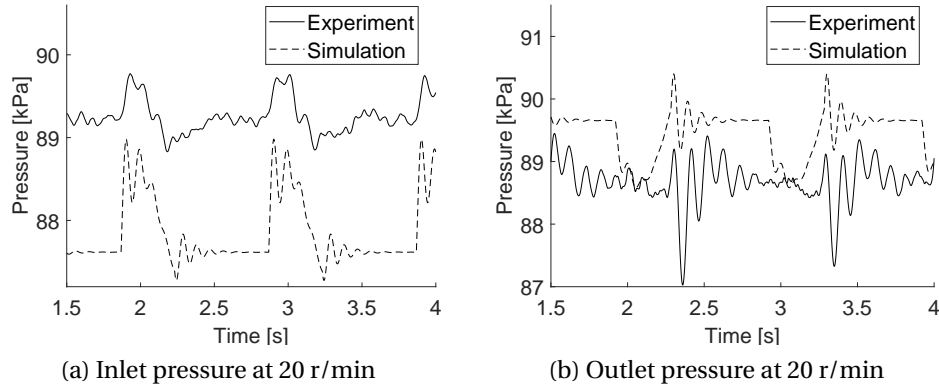


Figure 6.18: Experiment B: Comparison to Simulation A pressure values for a motor speed of 20 r/min

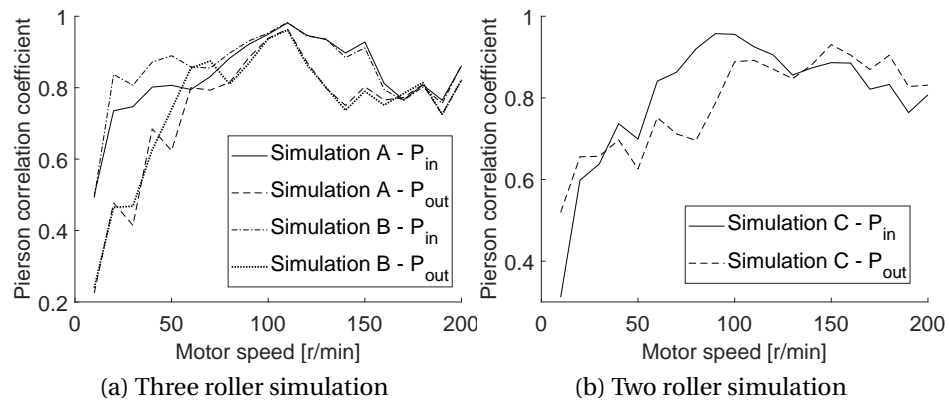


Figure 6.19: Experiment B and D: Pearson correlation coefficient of the simulated inlet and outlet pressures

mimics the response of the system regarding resonant peaks and troughs however there is a large difference between the peak values at larger r/min values. The RMSE can also be used for each r/min test to indicate the error of the simulation in relation to the experimental value and is shown in Fig. 6.21.

The RMSE does not address much information pertaining to the fit of the model, however, it can be indicative of the maximum error value associated with the motor speed. As an example, Fig. 6.17c has a RMSE value of 19.34 kPa located at the local minimum, or secondary trough, of the experimental value. This value is quite large even though the Pearson correlation coefficient for this specific test is 0.973. The approximated volume follows extremely closely to the simulation regarding the measured roller data.



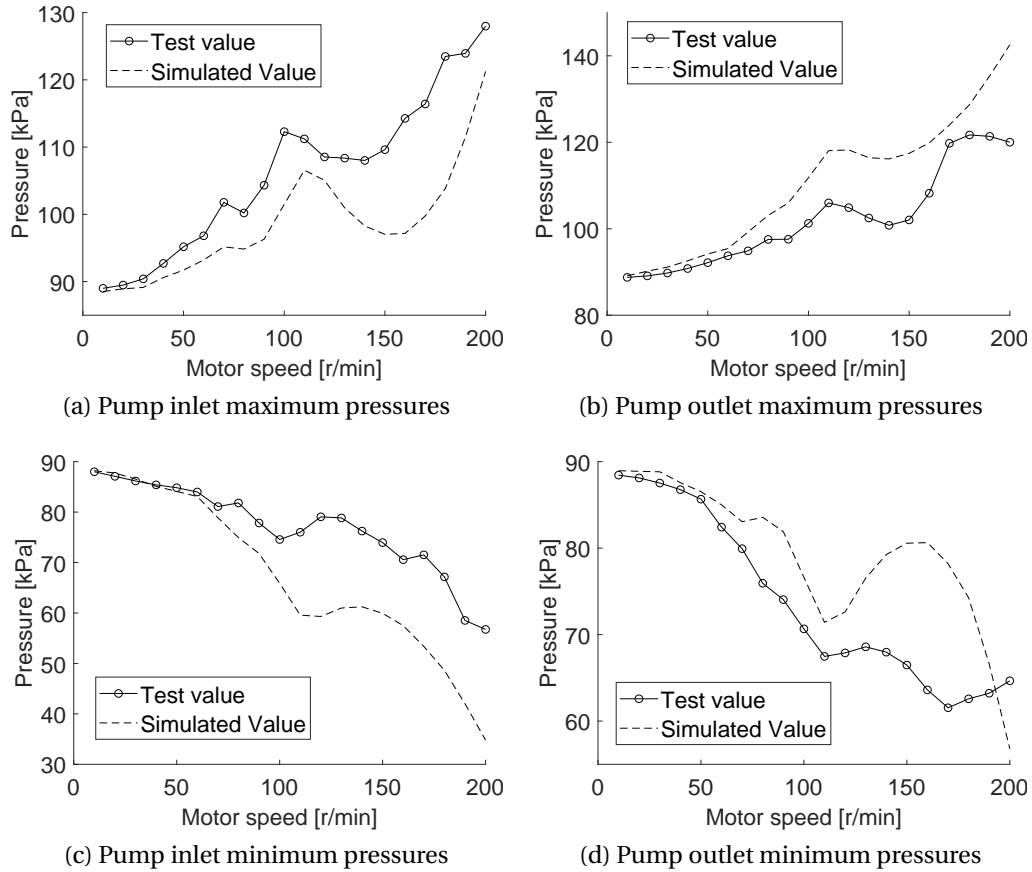


Figure 6.20: Experiment B: Comparison of peak maximum and minimum pressure values of Simulation A

The large RMSE and peak pressure differences are attributed to unmodelled dynamics, as the lumped parameter model is a reduced form of that in [16] for more generalised applications. The average Pearson correlation coefficient of the three-roller pump configuration was noted to be higher than that of the two-roller pump configuration. This can be attributed to the change in the system parameters attributed to the pump design, specifically the length of tube extending into the pump. As the number of rollers decreases, the length of the process tube extending into the pump becomes larger. This can have an impact on the capacitance and inductance values used as parameters of the simulation.

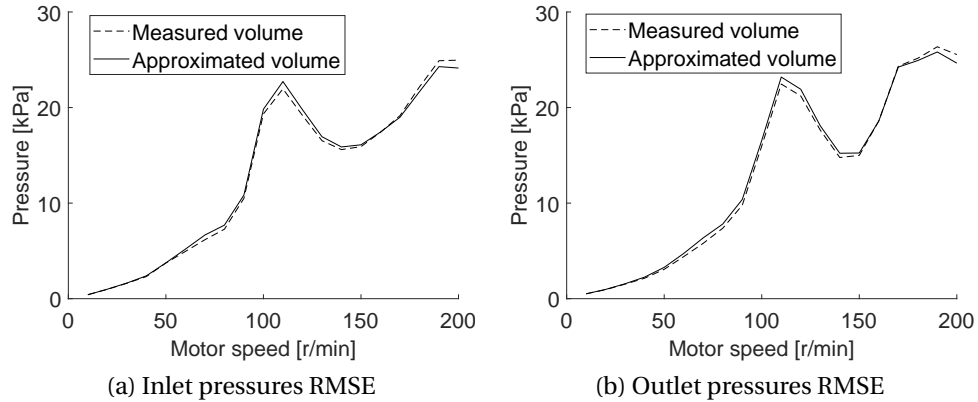


Figure 6.21: RMSE values over varying r/mins for simulations with both the measured roller volume and approximated roller volume

### 6.3 Pump characteristics

The maximum pressure was tested by closing the gate valve on the outlet line and rotating the pump at low motor speeds in the range of 20 r/min to ensure maximum torque. The same was done for the minimum pressure (maximum vacuum) test of the pump. Figs. 6.22 and 6.23 indicate the maximum and minimum working pressure test results for the three-roller pump configuration and two-roller pump configuration respectively. As the pressure increased for the three-roller pump configuration slipping of the motor started to occur. This can be seen in Fig. 6.22a

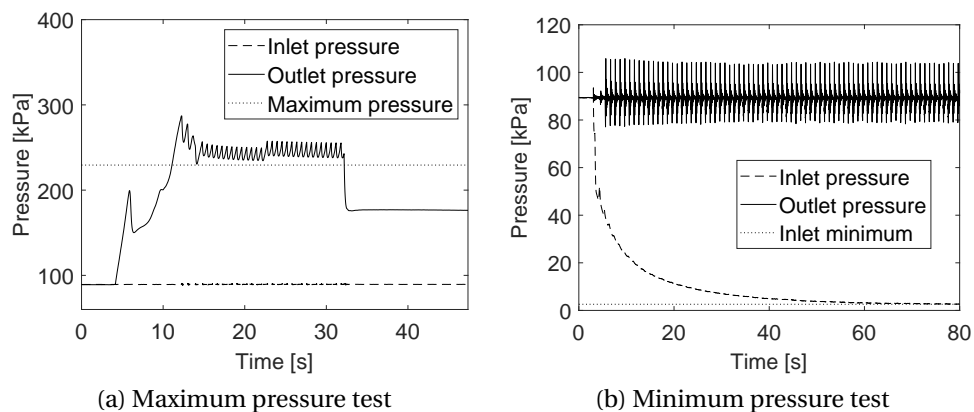


Figure 6.22: Maximum and minimum working pressure test results for the three-roller pump configuration

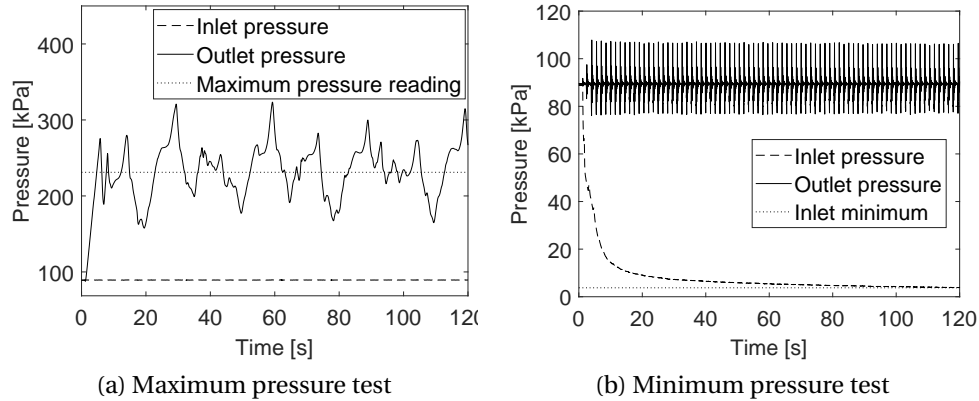


Figure 6.23: Maximum and minimum working pressure test results for the two-roller pump configuration

The maximum speed for the three-roller configuration was in the range of 155 r/min where two-roller configuration achieved a speed of 410 r/min before failing. For this reason the working rotational speed was selected as a rotational speed before the motor started to slip.

Motor slip occurred when testing for the maximum working pressure of the three-roller pump configuration. In order to avoid any damage to the motor the test was stopped prematurely. Motor slip can clearly be seen by the sawtooth-like shapes occurring near the top of the graph in Fig. 6.22a. The pressure value near the lowest point of the outlet pressure during motor slip was taken as the maximum pressure indication of the three-roller pump configuration.

The two-roller pump configuration did not have motor slip during the maximum pressure test and could therefore be run continuously as seen in Fig. 6.23b. The average of the outlet pressure reading was taken as the maximum working pressure for the two-roller pump configuration.

The pump has the ability to dry run and does not form cavitation. It can thus be said that the required net positive suction head (NPSH) to deter cavitation is non existent. The hydrostatic capabilities of both pump configurations were tested in the same fashion as the maximum and minimum pressure tests. However, instead of shutting down the pump, the motor was stopped with the enable signal high. This allowed the stepper motor to maintain a torque on the pump without moving. The moment the motor was stopped is referred to as the motor cut-off point.

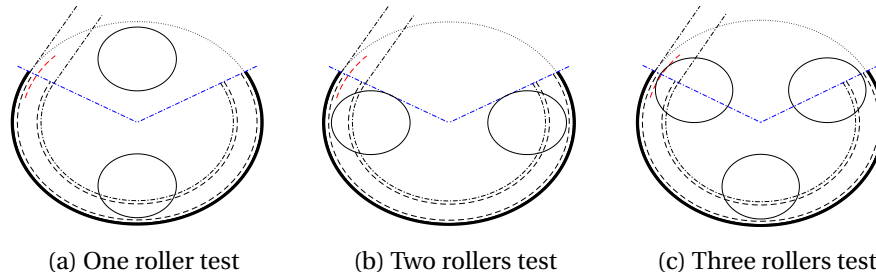


Figure 6.24: Hydrostatic test: Roller positions for the positive and negative pressure gradients

The hydrostatic test was completed with one single roller in full contact, two rollers in full contact, and the full three-roller configuration, where there is always at least two rollers in contact. The single and dual roller hydrostatic tests were completed on the two-roller configuration and were timed to stop with the roller in a desired position. It should be noted that the three-roller hydrostatic test had a higher positional uncertainty than that of the two-roller test. This is due to a very specific position required for testing the hydrostatic pressure capabilities of the pump with all three rollers engaged. These testing positions are indicated in Fig. 6.24. The hydrostatic capability is measured based on the rate of change of the pressure difference between the two pressure sensors over time.

The high pressure hydrostatic test results seen in Fig. 6.25 indicate that the three-roller configuration has a better hydrostatic stability for high pressures. The two-roller has the second best stability but has the steepest rate of decline when only one roller is occluding the tube. The one roller test only becomes stable after approximately halving its initial pressure gradient.

The low pressure hydrostatic stability test results, indicated in Fig. 6.26, reveal that the two-roller is ideal for a pump with a hydrostatic vacuum requirement. The three-roller configuration is close to the two-roller test and is second best for the low pressure hydrostatic test due to its steep rate of decline in pressure gradient. The one roller is unfavourable in the low pressure hydrostatic test, similar to the high pressure test, but not to the same degree.

The hydrostatic tests indicate that having more rollers on the pump increases the hydrostatic capability holds merit. The positioning of the three rollers around the central axis might be the reason for the poorer performance in the low pressure hydrostatic test, as the angles between the rollers can push the central roller housing off center. This is due to the normal forces exerted on

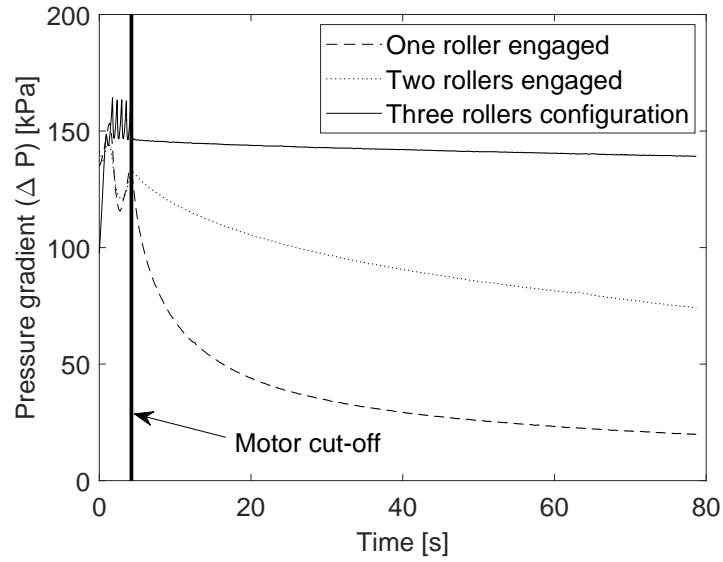


Figure 6.25: Hydrostatic test: Positive pressure gradient results

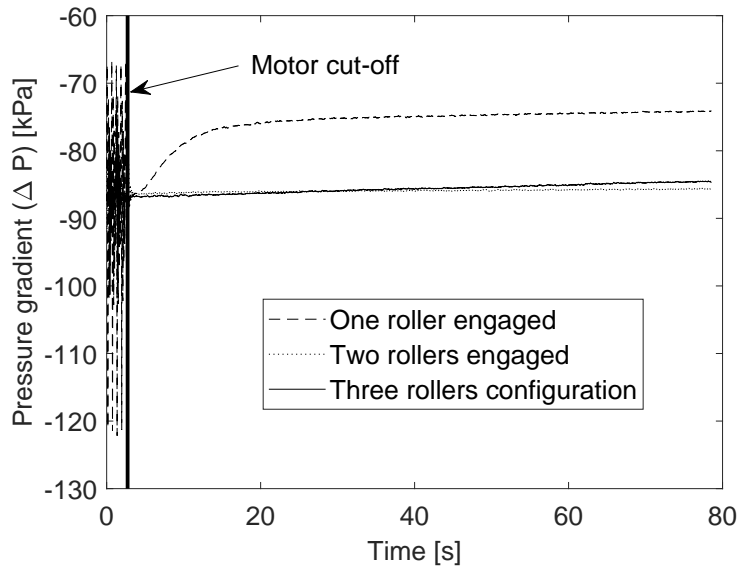


Figure 6.26: Hydrostatic test: Negative pressure gradient results

the rollers creating a moment on the axis of rotation, on which the housing sits.

It is speculated that this can be attributed to the symmetrical 180 ° design of the two-roller housing. This can balance the moment applied to the axis of rotation of the pump more evenly while both rollers are engaged. The moment around the axis of rotation would be unbalanced for the three-roller roller housing design, as one roller is almost always not in contact with the tube or outer casing. Aligning all three rollers on the three-roller pump configuration to achieve full occlusion on each roller is extremely difficult to do. It can be reasoned then that the two-roller pump configuration only displayed better hydrostatic stability for negative pressure gradients due to improper roller positioning of the three-roller pump configuration.

The pump characteristics can be summed up for both the two-roller and three-roller configuration of the pump in Table 6.6. The hydraulic force is determined with reference to the specified hydraulic cylinder in Chapter 4 with a bore size of 25 mm.

Table 6.6: Pump characteristics for three-roller and two-roller configuration

	<b>Three-roller configuration</b>	<b>Two-roller configuration</b>
Working rotational speed:	0 - 150 r/min	0 - 400 r/min
Maximum theoretical flow rate:	3.28 L/min	9.35 L/min
Pressure range (absolute):	2.58 - 229.39 kPa	3.76 - 231.09 kPa
Ambient pressure:	89.36 kPa	89.31 kPa
Hydraulic force (positive head):	69.32 N	70.25 N
Hydraulic force (negative head):	42.01 N	41.35 N

## 6.4 Conclusion

The main aspects of the model described in Chapter 3 are experimentally validated and presented in this chapter. This was done using the model-based peristaltic pump design of Chapter 4 and test benches discussed in Chapter 5.

The roller volume displacement approximation closely resembled the volume displaced over the angle of rotation of the motor and has a RMSE of 0.1218 mL (5.86 %). The form of the curve is emphasised as the most important aspect of

the approximation for simulation purposes, as the time derivative of this volume (roller induced flow) is used as an input variable. The maximum volume that the roller displaces is the most important aspect in modelling the flow rate of the pump, as it effectively reduces the volume displaced by the pump per rotation.

The volume that the pump displaces per rotation was modelled with both the approximated roller volume and the measured roller volume to give additional insight into the accuracy of the approximation. The volume that the pump displaced for one rotation was measured at 2 r/min and 20 r/min to avoid any non-linear flow characteristics of the pump, such as harmonic gains and losses. The modelled value of the three-roller pump configuration using the measured roller volume had an error of 1.28 %, while the modelled value using the approximated roller volume had an error of 4.03 %. The same errors for the two-roller pump configuration were determined to be 2.32 % and 4.02 % respectively. The inconsistency of the errors is attributed to the tube not being perfectly aligned to the backplate.

The modelled flow rates using the measured roller volume were on average within 2.37 % and 1.97 % for the three-roller and two-roller configurations respectively. The modelled flow rates using the approximated roller volume were on average within 3.64 % and 3.10 % for the three-roller and two-roller configurations respectively. Larger deviations of the flow can mostly be attributed to the non-linear dynamics of the flow rate noticed in the experimental results. The non-linear flow rate is most likely caused by harmonic gains/losses resulting from operating conditions near resonant frequencies of either the pump or system. This becomes evident by the high correlation between the non-linear flow characteristics and the non-linear peak pressure responses of the system over varying operating speeds.

The pressure responses of the simulations show a very strong correlation to the experimental results, however, tend to have large RMSE values. Large deviations of the peak pressures between the simulation and experimental results are also noted. The strong correlation coefficients indicated that the model is capable of accurately describing the shape, or waveform, of the pressure response for both the two-roller and three-roller pump configurations. Even so, the large deviation in pressure, indicated by the large RMSE values, suggests that the amplitude of the model is unreliable.

The three dimensional (3D) printed peristaltic pump is able to generate pressures above 140 kPa (14.28 m head), and create a vacuum under 5 kPa absolute for both the two-roller and three-roller configuration. The hydrostatic stability

for a positive pressure differential across the pump was better for the three-roller pump configuration, as expected. The additional roller of the three-roller pump configuration is also noted to reduce the maximum operating speed in comparison to the two-roller configuration. The maximum operating speed of the three-roller pump configuration is equal to 150 r/min, whereas the two-roller configuration had a maximum operating speed of 400 r/min. This can be attributed to a friction caused by the additional roller on the three-roller pump configuration.



## CHAPTER 7

---

### Conclusion

---

#### 7.1 Introduction

This chapter discusses the findings of the study with respect to the objectives and methodology outlined in Chapter 1 and concludes the study.

The chapter begins with a brief reflection of the objectives to ensure that they were met. The findings of the model-assisted design approach for a three dimensional (3D) printed peristaltic pump, outlined in Chapters 3 and 4, are then discussed with reference to the model validation results in Chapter 6.

Recommendations are then provided where improvements can be made on this study with reference to problems found, or areas not covered by the scope of this study. Suggestions for further research topics that align with the aim of this study are then given. This chapter is then concluded with the final remarks on the study.

## 7.2 Reflection on research objectives

The problem statement of this study indicates that the goal is to derive a model-assisted design approach for 3D printed peristaltic pumps. The objectives outlined in Chapter 1 were identified as critical success factors in attempting to derive a model-assisted design approach for 3D printed peristaltic pumps. This section describes how these objectives were achieved in this study.

**Modelling the dynamics of a roller-type peristaltic pump:** The roller-type peristaltic pump was modelled using a first principles approach. The flow characteristics were obtained from the geometric relations commonly associated with roller-type peristaltic pumps. A generalised lumped parameter model (a reduced form of the model provided in [16]) was created to model the pressure response of the system that the pump is integrated with. The pump was simulated in the Simulink/Simscape simulation environment in conjunction with MATLAB.

**Designing and manufacturing a peristaltic pump with desired characteristics with the use of the model, capable of being 3D printed:** Polyethylene terephthalate (PETG) was selected as the material used for manufacturing the pump parts on a Prusa MK2.5 and Prusa MK3 printers. Design specifications of the pump were produced with reference to a hypothetical application as an electro-hydrostatic actuator (EHA). The design was required to achieve a desired flow rate at a given operational speed in order to actuate a specified hydraulic piston at a certain speed. The roller and roller offset radius sizes of the pump required to obtain the specified flow rate were obtained by using the model provided in Chapter 3. A three-roller pump, capable of being modified to a two-roller pump, was designed using Solidworks. The pump was manufactured and assembled for testing using a triangular infill (40 % infill) on the printed parts, with a 2 mm wall thickness.

**Designing and constructing a test bench for characterising the performance of the peristaltic pump and for model validation purposes:** Four test benches were constructed in order to validate the model provided in this study. The first test bench was created in order to validate the roller volume displacement approximation. Two other test benches were catered towards obtaining the resistance and compliance parameters of the fourth test bench (peristaltic pump test bench) used to validate the pump model. Data acquisition and control of the system was conducted via a dSPACE 1104 R & D board for the peristaltic pump tests.

**Testing the pump for model validation and further recommendations:** A number of experiments were conducted in order to validate the peristaltic pump model. The roller volume displacement tests pertain to the experiments conducted on the pump in order to obtain the volume that a roller displaces as the roller engages the process tube. The flow tests measured the fluid displaced by the pump over a defined number of rotations of the motor with varying motor speeds. Multiple tests were conducted with regards to the flow of the pump in an attempt to account for as many variables as possible. The pressure tests measured the pressure at the inlet and outlet of the pump in order to validate the modelled pressure response of the simulation over varying motor speeds.

### 7.3 Research findings

A model-based design approach for roller-type peristaltic pumps was created and applied to design a three-roller peristaltic pump within this study. Additionally, a two-roller configuration of the same pump was designed by altering the roller housing of the pump.

The model utilises methods of approximating the roller volume, which is the volume that the roller displaces within the process tube during occlusion. This was not only done to acquire the volume that the roller displaces, but also for deriving the roller induced flow. The discrete approximation method was used in the validated model of the study and achieved a root-mean square error (RMSE) of 0.1218 mL (5.86 %) compared to the measured roller volume. This amounted to a 3.95 % error in the calculated roller induced flow.

The volume displacement test results, pertaining to the volume that the pump displaces for one rotation, indicated an error associated with imperfect testing conditions, specifically regarding the process tube. Using the measured roller volume, this error was calculated and found to behave predictably (within 0.07 %) with regards to the approximated roller volume error. The testing error is most likely caused by the tube not being perfectly aligned to the backplate of the pump. This can cause the tube to bend, reducing the total volume within the tube. With higher rotational speeds of the motor (such as those of the flow rate tests) this error diminished. This is thought to be due to the tube not having enough time to move away from the backplate between rollers forcing the tube shut.

With a known roller volume displacement, the model was accurate in cal-

culating the volume displaced per rotation of the three-roller and two-roller pump configurations at a low motor speed to within 1.28 % and 2.32 % of the measured values respectively. Without a known roller volume displacement, the model, using the roller volume approximation, achieved accuracies within 4.03 % and 4.02 % of the measured values for the three-roller and two-roller pump configurations respectively.

Similarly, with a known roller volume displacement, the model was accurate in calculating the volume flow rate of the pump for the three-roller and two-roller configurations to within an average of 2.37 % and 1.97 % of the measured values respectively. Using the roller volume approximation, these values increase to 3.64 % and 3.10 % respectively.

Large deviations between the modelled flow rate and measured flow rate were noted at certain motor speeds, with a maximum deviation of 9.02 % and 4.03 % for the three-roller and two-roller pump configurations respectively. This was found to be caused by a non-linear flow rate of the pump over varying motor speeds. The strong correlation between the flow rate and the inlet pressure of the pump suggests that the non-linear flow of the pump is caused by the pressure response of the system. It is theorised that at certain rotational speeds of the pump, the rollers isolate the tube segment between two rollers with a pressure similar to that of the system response. This implies that if a low pressure peak occurs right before the roller fully occludes the tube, the volume within the tube segment is reduced. Similarly, if the pressures are larger, the tube may expand and cause the pump to transport larger quantities of fluid during a rotation. The larger deviations were also noted to occur at larger motor speeds.

The simulations showed strong correlations for the pressure values of both the three-roller and two-roller pump configurations. As with the verification results, the outlet pressures correlated weaker to the measured pressure values in comparison to the inlet pressures. This is expected to be a result of the reduced form of the generalised lumped parameter model, where the compliance of the tube between rollers is not taken into account.

Although the simulated response of the model correlated strongly to the measured values, the simulation showed large deviations from the measured values. This implies that the lumped parameter model is good for modelling the pressure's waveform, but unreliable in terms of the amplitudes of the pressure response. The model can be useful in determining resonant or harmonic operating speeds of the pump, which in turn may prove useful in optimising the flow rate of the pump. This can be said, as the flow rate correlates strongly

to the inlet pressures. Further refinement of the lumped parameter model is, however, necessary for it to be used to accurately determine the amplitudes of the pressure responses.

The pump managed to achieve pressures of 140 kPa above ambient pressure (gauge pressure), and vacuums of below 5 kPa absolute. For the specified hydraulic cylinder that the pump was designed for, these pressures would translate to roughly 70 N of force from the outlet of the pump, and 41 N from the inlet. It is not realistic to assume that the pump is capable of achieving both of these values simultaneously (resulting in a net force of  $\sim 111$  N). However, the values do show promise for the application of the pump as an EHA.

The peristaltic pump showed favourable hydrostatic characteristics for the three roller pump, as a minimum of one roller occluding the tube (found on the two-roller configuration) was associated to unstable pressure gradients over the pump. The three-roller pump configuration could not achieve the same speeds as the two-roller pump configuration due to resistances associated with the rollers. The effect of the additional resistance of the roller was, admittedly, not taken into consideration when designing the pump. This, however, only had an adverse effect on the flow experiments of the pump, as the pump was able to reach the desired 200 r/min motor speed with the pressure tests. For this reason, the specified flow rate of 73.63 mL/s at a rotational speed of 200 r/min could not be validated, as the motor started slipping near 160 r/min. This does not negatively affect the validation of the values obtained in this study, as the accuracy of the modelled flow rate can be deduced from the various motor speeds. It rather provides an important design consideration for future studies to be taken into account.

## 7.4 Recommendations

The accuracy of the integration approximation method can be improved by making a more realistic assumption of how the tube wall bends around the roller. The method described in this study assumes that the tube wall perfectly fits around the roller's surface, and does not bend further outwards. Better assumptions of the tube deflection (or bend) would allow the approximation model to more closely resemble that of the experimental data.

The lumped parameter model can possibly be improved upon by adding an additional channel between the inlet and outlet to include the elasticity of the

process tube (capacitance) between rollers. The channel should theoretically allow the inlet peak pressures developed to be transferred across the pump to the outlet in an attempt to model the harmonic gains and losses of the peak pressure values. The simulation can also be improved by testing the resistance of the inlet and outlet lines separately, as the flow direction might have different characteristics pertaining to orifices and bends. The resistance values can further be improved by testing the resistance values at the simulated flow speeds of the pump.

Wear was noted on the bottom of the tubes used for the experiments, indicating a design flaw. This design flaw seems to be related to gravitational effects, as it only occurs on the bottom side of the tube. It is theorised that the tube is dragged across the bottom of the roller raceway during operation. This can be seen with distinct scratches rather than a uniform wear. It is therefore recommended to improve this aspect of the pump design for further research into this design.

The 3 Nm Nema 23 stepper motor (model number 57BYGH115-003) was not sufficient in achieving motor speeds of 200 r/min for the three-roller configuration flow tests. This was due to motor slip occurring at motor speeds near and above 160 r/min. It can be recommended to re-evaluate the selected motor in order to achieve larger motor speeds and thus extend the range of the tests.

## 7.5 Further research

This section provides information regarding suggestions for future research. These suggestions are based on the aim and objectives of this study, as well as observed inconsistencies, discrepancies, and recommendations.

**Modelling the roller volume displacement:** The volume that the roller displaces is approximated in this study using assumptions that may prove to be inaccurate regarding tubes with larger moduli of elasticity ( $E > 0.05$  GPa). The accuracy of the approximation provided in this study could thus vary greatly depending on material of the selected process tube. It would be beneficial to model the bend of the tube around the roller during occlusion, and the effects material strength has on this.

**Using a peristaltic pump as an EHA:** A secondary objective of this study is to provide alternative actuation methods to 3D printed robotics. A study in the effectiveness of using a 3D printed pump for actuation, and the comparison of

its effectiveness to that of current actuation methods could be beneficial for 3D printed robotics.

**Modelling the dynamic flow of the peristaltic pump:** The modelled flow rate in this study was determined with regards to the geometry of the pump. This provided a linear flow rate with respect to the operating speed of the motor. The experimental results suggest that the flow rate is non-linear and may correlate to the inlet pressures, and thus the harmonic frequencies of the pump or system.

**Modelling and analysis of the friction on the roller:** The friction that the process tube imparts on the roller of the pump is complex and dynamic with regards to motor speeds. The effects are noted, as the two-roller configuration achieved significantly higher operational speeds than that of the three-roller configuration. The friction imparted on the rollers can affect the maximum pressures generated and operating speeds achieved by the pump. An in depth analysis on what causes the friction and how it affects performance may help to select appropriate motors for the pump based on torque requirements.

**Extended tests with re-evaluated motor:** As the stepper motor could not achieve the desired operating speeds for the flow tests, further studies with a re-evaluation of the motor is suggested. Extended testing (implying tests at larger motor speeds) may give more data on the water hammering phenomena that is hypothesised to cause the non-linear flow of the pump.

## 7.6 Final remarks

A model-assisted design approach for 3D printed peristaltic pumps is described, utilised, and validated in this study. The model-assisted design approach is useful in obtaining the required pump geometries in order to achieve a desired flow rate with specified parameters. There is still room for improvement on both the modelling and testing of the pump.

The model can be improved upon by evaluating assumptions made pertaining to the process tube. Additionally the lumped parameter model can also be improved upon, as the model is simplistic in order to allow for a more general application. The modelled values can be better validated by fixing the process tube to the backplate when testing the pump.

The model described in this study was found to be accurate for modelling

both the flow rates and pressure waveforms of both a two-roller and a three-roller peristaltic pump. This validates that the model is somewhat generally applicable to roller-type pumps with varying numbers of rollers, with exception of a single-roller pump. This should yield true provided that the process tube is compliant (has a low modulus of elasticity) and has a low roller to backplate radius ratio.

The peristaltic pump presented in this study showed favourable characteristics pertaining to its use as an EHA. The three-roller configuration was also noted to exhibit better performance as an EHA based on the hydrostatic stability of the pump than the two-roller configuration. Additionally, the study can conclude that roller-type peristaltic pumps can be manufactured using cost-effective manufacturing techniques and materials, such as additive manufacturing and thermoplastics with a relatively high degree of accuracy regarding desired flow rates.



---

## Bibliography

---

- [1] T. W. Latham, "Fluid motions in a peristaltic pump." Ph.D. dissertation, Massachusetts Institute of Technology, 1966.
- [2] N. G. Kling, "Roller type pump," U.S. Patent US3 172 367A, March 9, 1965. [Online]. Available: <https://patents.google.com/patent/US3172367A/en>
- [3] E. N. Aitavade, S. D. Patil, A. N. Kadam, and T. S. Mulla, "An overview of peristaltic pump suitable for handling of various slurries and liquids," in *IOSR Journal of Mechanical and Civil Engineering (IOSR-JMCE)*, 2009, pp. 19–24.
- [4] V. Rybin, T. Karimov, M. Sigaeva, E. Solomevich, G. Kolev, and E. Kopets, "Design of a smart bartender with peristaltic pumps," *Inventions*, vol. 4, no. 2, 2019. [Online]. Available: <https://www.mdpi.com/2411-5134/4/2/26>
- [5] Verder International B.V. (2020) Verderflex product range. [Online]. Available: <https://www.verderflex.com/en/peristaltic-pump-product-range/>
- [6] Watson Marlow - Fluid technology group. (2020) Watson-marlow - product range. [Online]. Available: <https://www.watson-marlow.com/za-en/range/>
- [7] R. Kang, J. Charles, and Z. Jiao, "Nonlinear modeling and control design of electro-hydrostatic actuator," in *Proceedings of the JFPS International Symposium on Fluid Power*, vol. 2008, no. 7-3. The Japan Fluid Power System Society, 2008, pp. 665–670.
- [8] S. J. Ezell, "A policymaker's guide to smart manufacturing," *Information technology & innovation foundation*, 2016.
- [9] M. Quigley, A. Asbeck, and A. Ng, "A low-cost compliant 7-dof robotic manipulator," in *2011 IEEE International Conference on Robotics and Automation*. IEEE, 2011, pp. 6051–6058.

- [10] M. Volk, *Pump characteristics and applications*. CRC Press, 2013.
- [11] J. Klespitz and L. Kovács, “Peristaltic pumps - a review on working and control possibilities,” in *IEEE 12th International Symposium on Applied Machine Intelligence and Informatics*. Budapest University of Technology and Economics, 1 2014, pp. 191–194.
- [12] A. Loth and R. Förster, “Disposable high pressure peristaltic micro pump for standalone and on-chip applications,” in *Proceedings of the 11th IEEE Annual International Conference on Nano/Micro Engineered and Molecular Systems (NEMS)*, 2013.
- [13] D. C. Karnopp, D. L. Margolis, and R. C. Rosenberg, *System Dynamics: Modeling, Simulation, and Control of Mechatronic Systems*. John Wiley & Sons, 2006.
- [14] E. Doebelin, *System Dynamics: modelling, analysis, simulation, design*. Marcel Dekker, Inc., 1998.
- [15] G. Wright, “Mechanical simulation of cardiac function by means of pulsatile blood pumps,” *Journal of cardiothoracic and vascular anesthesia*, vol. 11, no. 3, pp. 299–309, 1997.
- [16] F. Moscato, F. M. Colacino, M. Arabia, and G. A. Danieli, “Pressure pulsation in roller pumps: A validated lumped parameter model,” *Medical Engineering & Physics*, vol. 30, pp. 1149–1158, 2008.
- [17] B. Redwood, F. Schöffner, and B. Garret, *The 3D Printing Handbook: Technologies, Design and Applications*. 3D Hubs B.V., 2017. [Online]. Available: <https://books.google.co.za/books?id=R3OvswEACAAJ>
- [18] H. Bikas, P. Stavropoulos, and G. Chryssolouris, “Additive manufacturing methods and modelling approaches: a critical review,” *The International Journal of Advanced Manufacturing Technology*, vol. 83, no. 1-4, pp. 389–405, 2016.
- [19] H. Lipson and M. Kurman, *Fabricated: The new world of 3D printing*. John Wiley & Sons, 2013.
- [20] P. Kobryn, N. Ontko, L. Perkins, and J. Tiley, “Additive manufacturing of aerospace alloys for aircraft structures,” Air Force Research Lab Wright-Patterson AFB OH Materials and Manufacturing . . . , Tech. Rep., 2006.

- [21] U. Berger, "Aspects of accuracy and precision in the additive manufacturing of plastic gears," *Virtual and Physical Prototyping*, vol. 10, no. 2, pp. 49–57, 2015. [Online]. Available: <https://doi.org/10.1080/17452759.2015.1026127>
- [22] W. Brostow and H. Hagg Lobland, "Predicting wear from mechanical properties of thermoplastic polymers," *Polymer Engineering & Science*, vol. 48, pp. 1982–1985, 10 2008.
- [23] D. Klitou, J. Conrads, M. Rasmussen, L. Probst, and B. Pedersen, "Germany: Industrie 4.0," CARSA & PwC, Digital Transformation Monitor technical report, 2017.
- [24] M. Rüßmann, M. Lorenz, P. Gerbert, M. Waldner, J. justus, P. Engel, and M. Harnisch, "Industry 4.0: The future of productivity and growth in manufacturing industries," The Boston Consulting Group, Working paper, 2015.
- [25] PricewaterhouseCoopers, "Industry 4.0: Building the digital enterprise," PricewaterhouseCoopers, Industry survey, 2016.
- [26] M. Brettel, N. Friederichsen, M. Keller, and M. Rosenberg, "How virtualization, decentralization and network building change the manufacturing landscape: An industry 4.0 perspective," *International journal of mechanical, industrial science and engineering*, vol. 8, no. 1, pp. 37–44, 2014.
- [27] Deloitte, "Industry 4.0: Challenges and solutions for the digital transformation and use of exponential technologies," 2015.
- [28] H. Kagermann, W. Wahlster, and J. Helbig, "Recommendations for implementing the strategic initiative industrie 4.0," Forschungsunion and Acatech, Working paper, 2013.
- [29] S. Vaidya, P. Ambad, and S. Bhosle, "Industry 4.0 - a glimpse," *Procedia manufacturing*, 2018.
- [30] M. Hermann, T. Pentek, and B. Otto, "Design principles for industry 4.0 scenarios: a literature review," 2015.
- [31] R. Porter and J. Bradley, "Elastic-tube pump," U.S. Patent US12 753A, April 17, 1855. [Online]. Available: <https://patents.google.com/patent/US12753A/en>
- [32] G. P. Gravlee, *Cardiopulmonary bypass: principles and practice*. Lippincott Williams & Wilkins, 2008.

- [33] A. Passaroni, M. Silva, and W. Yoshida, "Cardiopulmonary bypass: Development of John Gibbon's heart-lung machine," *Revista Brasileira de Cirurgia Cardiovascular*, vol. 30, 03 2015.
- [34] B. L. Mejak, A. Stammers, E. Rauch, S. Vang, and T. Viessman, "A retrospective study on perfusion incidents and safety devices," *Perfusion*, vol. 15, no. 1, pp. 51–61, 2000, PMID: 10676868. [Online]. Available: <https://doi.org/10.1177/026765910001500108>
- [35] I. Phallen and D. Vogt, "Linear peristaltic pump," U.S. Patent US6 213 739B1, April 10, 2001. [Online]. Available: <https://patents.google.com/patent/US6213739B1/en>
- [36] B. Huber, "Flow injection apparatus for carrying out chemical analyses," U.S. Patent US4 952 372A, August 28, 1990. [Online]. Available: <https://patents.google.com/patent/US4952372A/en>
- [37] R. P. Davis, "Surgical irrigation and aspiration system with dampening device," U.S. Patent US4 921 477A, May 1, 1990. [Online]. Available: <https://patents.google.com/patent/US4921477A/en>
- [38] J. L. Orth, "Extra corporeal support system," U.S. Patent US5 188 604A, February 23, 1993. [Online]. Available: <https://patents.google.com/patent/US5188604A/en>
- [39] S. Roslon, T. Surber, and F. Zanger, "Reduced pulsation tapered ramp pump head," U.S. Patent US5 230 614A, July 27, 1993. [Online]. Available: <https://patents.google.com/patent/US5230614A/en>
- [40] A. Geipel, "Novel two-stage peristaltic micropump optimized for automated drug delivery and integration into polymer microfluidic systems," Ph.D. dissertation, Albert-Ludwigs-Universität, 2008.
- [41] F. Thoma, F. Goldschmidtböing, and P. Woias, "A new concept of a drug delivery system with improved precision and patient safety features," *Micromachines*, 2015.
- [42] G. Beckers and B. Dehez, "Design and modeling of a quasi-static peristaltic piezoelectric micropump," in *2013 International Conference on Electrical Machines and Systems*, 2013.
- [43] Q. Lin, B. Yang, J. Xie, and Y.-C. Tai, "Dynamic simulation of a peristaltic micropump considering coupled fluid flow and structural motion," *Journal of Micromechanics and Microengineering*, 2007.

- [44] K. Tatsumi, Y. Matsunaga, Y. Miwa, and K. Nakabe, "Numerical study on fluid-flow characteristics of peristaltic pump," *Progress in Computational Fluid Dynamics*, vol. 9, no. 3, p. 176, 2009.
- [45] P. Czop, G. Kost, D. Sławik, and G. Wszolek, "Formulation and identification of first-principle data-driven models," *Journal of Achievements in materials and manufacturing Engineering*, vol. 44, no. 2, pp. 179–186, 2011.
- [46] S. L. Weinberg, E. C. Eckstein, and A. H. Shapiro, "An experimental study of peristaltic pumping," *Journal of Fluid Mechanics*, vol. 49, no. 3, pp. 461–479, 1971.
- [47] E. Menon, *Piping Calculations Manual*, 1st ed. McGraw-Hill, 2015.
- [48] G. Formato, R. Romano, A. Formato, J. Sorvari, T. Koiranen, A. Pellegrino, and F. Villecco, "Fluid–structure interaction modeling applied to peristaltic pump flow simulations," *Machines*, vol. 7, no. 3, p. 50, 2019.
- [49] C.-C. Yeh and Y.-F. Chen, "Critical success factors for adoption of 3d printing," *Technological Forecasting and Social Change*, vol. 132, pp. 209–216, 2018. [Online]. Available: <http://www.sciencedirect.com/science/article/pii/S0040162517308466>
- [50] uFactory. (2020) uarm. [Online]. Available: <https://store.ufactory.cc/products/uarm>
- [51] L. Ángel, D. Royer, and D. van den Heuvel. (2020) Thor. [Online]. Available: <https://hackaday.io/project/12989-thor>
- [52] C. Franciscone. (2018) Eezybotarm mk2 - 3dprintable robotic arm. [Online]. Available: [http://www.eezyrobots.it/eba\\_mk2.html](http://www.eezyrobots.it/eba_mk2.html)
- [53] Slant Concepts. (2020) Slant concepts. [Online]. Available: <https://hackaday.io/SlantConcepts>
- [54] Roboteurs. (2020) Rbx1 remix 3d printed 6-axis robot arm kit. [Online]. Available: <https://roboteurs.com/products/rbx1-remix-3d-printed-6-axis-robot-arm-kit>
- [55] A. Hoelldorfer and D. Royer. (2020) 3d printable robot arm. [Online]. Available: <https://hackaday.io/project/3800-3d-printable-robot-arm>
- [56] Zortax. (2020) Zortax robotic arm. [Online]. Available: <https://library.zortrax.com/project/zortrax-robotic-arm/>

- [57] BCN3D Technologies, Inc. (2020) Bcn3d moveo – a fully open source 3d printed robot arm. [Online]. Available: <https://www.bcn3d.com/bcn3d-moveo-the-future-of-learning/>
- [58] J. Oh, B. Drincic, and D. S. Bernstein, “Nonlinear feedback models of hysteresis,” in *IEEE Control Systems Magazine*. IEEE, 2 2009, pp. 100–119.
- [59] D. R. Askeland, P. P. Fulay, and W. J. Wright, *The Science and Engineering of Materials, SI Edition*, 6th ed. CL-Engineering, 2011.
- [60] I. Karassik, J. Messina, P. Cooper, and C. Heald, *Pump Handbook*, ser. Harvard Business Review Book Series. Mcgraw-hill, 2000. [Online]. Available: <https://books.google.co.za/books?id=yU5TyJrOMF8C>
- [61] C. B. Pedersen, T. Buhl, and O. Sigmund, “Topology synthesis of large-displacement compliant mechanisms,” *International Journal for numerical methods in engineering*, vol. 50, no. 12, pp. 2683–2705, 2001.
- [62] X. Yang, Y. Xie, and G. Steven, “Evolutionary methods for topology optimisation of continuous structures with design dependent loads,” *Computers & Structures*, vol. 83, no. 12, pp. 956 – 963, 2005. [Online]. Available: <http://www.sciencedirect.com/science/article/pii/S0045794904004122>
- [63] J. Alexandersen, N. Aage, C. S. Andreasen, and O. Sigmund, “Topology optimisation for natural convection problems,” *International Journal for Numerical Methods in Fluids*, vol. 76, no. 10, pp. 699–721, 2014. [Online]. Available: <https://onlinelibrary.wiley.com/doi/abs/10.1002/flid.3954>
- [64] J. Alexandersen, O. Sigmund, and N. Aage, “Large scale three-dimensional topology optimisation of heat sinks cooled by natural convection,” *International Journal of Heat and Mass Transfer*, vol. 100, pp. 876 – 891, 2016. [Online]. Available: <http://www.sciencedirect.com/science/article/pii/S0017931015307365>
- [65] C & C Hydraulcis Ltd. (2020) Micro cylinders. [Online]. Available: <https://www.cchdraulcis.co.uk/standard-cylinders/double-acting-cylinders/micro-cylinders/>
- [66] Bansbach. (2020) Micro hydraulcis. [Online]. Available: <https://www.bansbach.com/index.php/en/products/micro-hydraulcis>
- [67] Hydrokit. (2019) Mini cylinders. [Online]. Available: <https://www.hydrokit.com/en/produit/hydraulic-cylinders/mini-cylinders/double-acting-micro-cylinder-16x25-xrp6536-xpr21435.html>

- [68] P. Schober, C. Boer, and L. A. Schwarte, "Correlation coefficients: appropriate use and interpretation," *Anesthesia & Analgesia*, vol. 126, no. 5, pp. 1763–1768, 2018.
- [69] R. W. Schafer, "What is a savitzky-golay filter? [lecture notes]," *IEEE Signal Processing Magazine*, vol. 28, no. 4, pp. 111–117, 2011.
- [70] D. Chen, Y. Chen, and D. Xue, "Digital fractional order savitzky-golay differentiator," *IEEE Transactions on Circuits and Systems II: Express Briefs*, vol. 58, no. 11, pp. 758–762, 2011.
- [71] L. V. Sorg and J. C. Lamkin, "Linear peristaltic pump," U.S. Patent US2 877 714A, March 17, 1959. [Online]. Available: <https://patents.google.com/patent/US2877714A/en>
- [72] O. M. King, "Peristaltic pumps," U.S. Patent US4 496 295A, January 29, 1985. [Online]. Available: <https://patents.google.com/patent/US4496295A/en>
- [73] J. Bradley, "Linear peristaltic pump," U.S. Patent US4 561 830A, December 31, 1985. [Online]. Available: <https://patents.google.com/patent/US4561830A/en>
- [74] M. G. Gordon, B. Rubalcaba, and J. L. Jackman, "Continuous peristaltic pump," U.S. Patent 4 869 646, September 26, 1989. [Online]. Available: <https://patents.google.com/patent/US4869646>
- [75] J. F. Heminway and E. P. Freischlag, U.S. Patent US4 893 991A, January 16, 1990. [Online]. Available: <https://patents.google.com/patent/US4893991A/en>
- [76] F handling method, system, and fluid interface apparatus usable therewith, "Charles e. beuchat and harold j. walbrink," U.S. Patent US5 041 096A, August 20, 1991. [Online]. Available: <https://patents.google.com/patent/US5041096A/en>
- [77] R. D. Robinson, "Implantable peristaltic pump techniques," U.S. Patent US5 840 069A, November 24, 1998. [Online]. Available: <https://patents.google.com/patent/US5840069A/en>
- [78] K. Armstrong and K. Kemp, "Peristaltic pump with flow control," U.S. Patent US6 099 272A, August 8, 2000. [Online]. Available: <https://patents.google.com/patent/US6099272A/en>

- [79] H. Kanda, H. Tashiro, and H. Kato, "Irrigation-aspiration apparatus," Japan Patent US6 527 745B1, March 04, 2003. [Online]. Available: <https://patents.google.com/patent/US6527745B1/en>
- [80] S. G. Davis, R. Gordon, V. P. Injev, K. D. Leukanech, M. D. Morgan, M. M. Oliveira, and G. P. S. J. Wilson, "Surgical cassette having an aspiration pressure sensor," U.S. Patent US6 962 488B2, November 8, 2005. [Online]. Available: <https://patents.google.com/patent/US6962488B2/en>
- [81] L. J. Cull, J. T. Perkins, and R. Fries, "Peristaltic pump with air venting via the movement of a pump head or a backing plate during surgery," U.S. Patent US7 168 930B2, January 30, 2007. [Online]. Available: <https://patents.google.com/patent/US7168930B2/en>
- [82] D. D. Blight, E. N. Stubkjaer, and J. A. Fritz, "Peristaltic irrigation pump system," U.S. Patent US20 050 095 155A1, May 5, 2005. [Online]. Available: <https://patents.google.com/patent/US20050095155A1/en>
- [83] A.-M. Moubayed, "Rotary axial peristaltic pumps and related methods," U.S. Patent US7 556 481B2, July 07, 2009. [Online]. Available: <https://patents.google.com/patent/US7556481B2/en>
- [84] S. X. Gao and D. L. Williams, "Method of operating a peristaltic pump," U.S. Patent US20 070 207 041A1, September 06, 2007. [Online]. Available: <https://patents.google.com/patent/US20070207041A1/en>
- [85] R. Gordon, K. D. Leukanech, M. D. Morgan, and G. P. Sorensen, "Peristaltic pump," U.S. Patent US20 070 217 919A1, September 20, 2007. [Online]. Available: <https://patents.google.com/patent/US20070217919>
- [86] G. P. Sorensen, "Multiple segmented peristaltic pump and cassette," U.S. Patent US8 790 096B2, July 29, 2014. [Online]. Available: <https://patents.google.com/patent/US8790096B2/en>
- [87] B. Greener, "Negative pressure device," London Patent US10 188 776B2, January 29, 2019. [Online]. Available: <https://patents.google.com/patent/US10188776B2/en>



# **Appendices**

## **APPENDIX A**

---

### **Peristaltic pump patents**

---

Table A.1: Various patents filed for peristaltic pump designs and operations from 1957 to 2011

<b>Patent no:</b>	<b>Description:</b>	<b>Initial filing date:</b>	<b>Inventor(s):</b>	<b>Initial assignee (company):</b>	<b>Pump design:</b>
US2877714A [71]	Variable displacement tubing pump	1957/10/30	L.V. Sorg et al.	Standard Oil Company	Linear
US3172367A [2]	Roller type pump	1963/01/08	N.G. Kling	Technicon Instruments Corporation	Rotary
US4496295A [72]	Peristaltic pumps	1984/03/20	O.M. King	Private	Rotary
US4561830A [73]	Linear peristaltic pump	1984/10/01	J. Bradley	IVAC Corporation	Linear
US4869646A [74]	Continuous peristaltic pump	1984/10/15	M.G. Gordon et al.	American Hospital Supply corp	Linear
US4952372A [36]	Flow injection apparatus for carrying out chemical analyses	1988/07/14	B. Huber	The Perkin Elmer Corporation	Rotary
US4893991A [75]	Method and means for improving efficiency of peristaltic pumps	1988/10/19	J.F. Heminway et al.	Private	Linear

US4921477A [37]	Surgical irrigation and aspiration system with dampening device	1989/06/21	R.P. Davis	The Cooper Companies, Inc.	Rotary
US5041096A [76]	Fluid handling method and system and fluid interface apparatus usable therewith	1989/10/27	C.E. Beuchat et al.	Nestle, S.A.(Texas)	Rotary
US5188604A [38]	Extra corporeal support system	1990/05/02	J.L. Orth	Rockey mountain Research, Inc.	Rotary
US5230614A [39]	Reduced pulsation tapered ramp pump head	1992/06/03	F. Zanger et al.	Allergan, Inc.	Rotary
US5840069A [77]	Implantable peristaltic pump techniques	1996/04/04	R.D. Robinson et al.	Medtronic, Inc.	Rotary
US6099272A [78]	Peristaltic pump with flow control	1997/09/18	K. Armstrong et al.	FSI International	Rotary
US6213739B1 [35]	Linear peristaltic pump	1998/01/16	I.J. Phallen et al.	Niagara Pump Corperation	Linear
US6527745B1 [79]	Irrigation-aspiration apparatus	2000/10/06	H. Kanda et al.	Nidek Co., Ltd.	Rotary
US6962488B2 [80]	Surgical cassette having an aspiration pressure sensor	2003/04/04	S.G. Davis et al.	Alcon, Inc.	Rotary

US7168930B2 [81]	Peristaltic pump with air venting via the movement of a pump head or a backing plate during surgery	2003/09/29	L.J. Cull et al.	Bausch & Lomb Incorporated	Rotary
US20050095155A1 [82]	Peristaltic irrigation pump system	2003/11/05	D.D. Blight et al.	Private	Rotary
US7556481B2 [83]	Rotary axial peristaltic pumps and related methods	2005/08/26	A.-M. Moubayed	Baxter International Inc.	Rotary
US20070207041A1 [84]	Method of operating a peristaltic pump	2006/03/01	S.X. Gao et al.	Alcon, Inc.	Rotary
US20070217919A1 [85]	Peristaltic pump	2006/03/14	R. Gordon et al.	Alcon, Inc.	Rotary
US8790096B2 [86]	Multiple segmented peristaltic pump and cassette	2010/04/07	G.P. Sorensen	Alcon Research, Ltd.	Rotary
US10188776B2 [87]	Negative pressure device	2011/09/16	B. Greener	Smith & Nephew PLC	Linear

## APPENDIX B

---

### Simulink model and MATLAB code

---

The Simulink model and MATLAB code used for the simulation is available [here](#) or by following the links:

- 1) <https://nextcloud.nwu.ac.za/index.php/s/BCoZcHoFBL9aZBx>
- 2) <https://doi.org/10.25388/nwu.12911582>

Fig. B.1 indicates the files used with a brief description of their purpose.

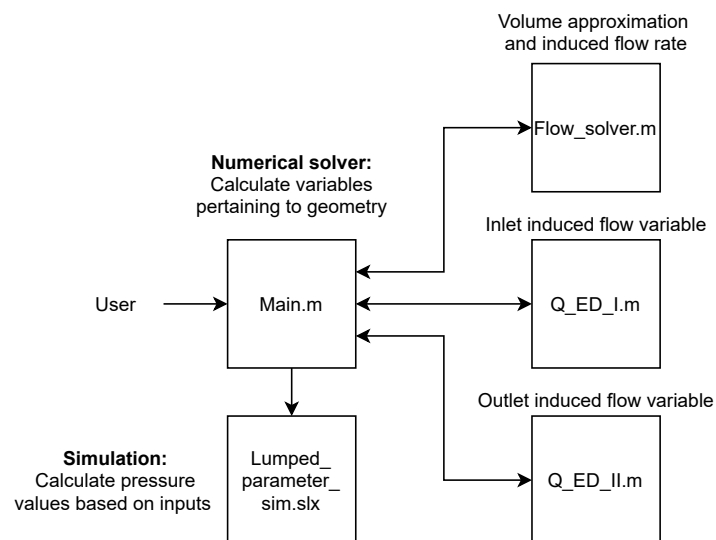


Figure B.1: Modelling and simulation block diagram

## APPENDIX C

---

### Design drawings

---

This appendix indicates the design drawings of the peristaltic pump and its parts. The geometry of the parts are often complex and thus multiple drawings are used to accommodate the large amount of information. It should be noted that the designs are symmetrical around the y-axis as stated in the design section. Item number 6 listed in both bill of material tables is not present in the drawings as it is a reference part that does not contain vital information.

The Solidworks parts, drawings, bills of materials, renderings, and STL (commonly associated with 3D printing) can be located [here](#) or by following the links:

- 1) <https://nextcloud.nwu.ac.za/index.php/s/tzij6MkmLQxFtPf>
- 2) <https://doi.org/10.25388/nwu.12911639>

Table C.1 indicates the drawing numbers and their descriptions. Table C.2 indicates the bill of materials table for the three-roller pump. Table C.3 indicates the bill of materials for the two-roller pump. Note that the only difference is shown in the last parts listed.

Table C.1: Table indicating design drawing numbers and their descriptions

<b>Drawing no.</b>	<b>Description</b>
1A	— Peristaltic pump component analysis - trimetric view
1B	— Peristaltic pump component analysis - exploded trimetric view
1C	— Peristaltic pump component analysis - exploded trimetric view
2A	— Three roller housing component analysis
2B	— Two-roller housing component analysis
3A	— Inlet and outlet intermediate section hole positions and part dimensions
3B	— Inlet and outlet intermediate section hole and radius sizes
3C	— Inlet and outlet intermediate section hole positions and dimensions - side view
4A	— Intermediate section between the top and bottom plate containing the majority of the backplate
5A	— Top plate hole locations
5B	— Top plate hole and radius sizes
5C	— Top plate part dimensions
5D	— Top plate part dimensions - bottom view
6A	— Bottom plate hole locations
6B	— Bottom plate hole and radius sizes
6C	— Bottom plate part dimensions
6D	— Bottom plate part dimensions - bottom view
7A	— 3 NM Nema 23 stepper motor dimensions
8A	— Three-roller housing top part dimensions
9A	— Three-roller housing bottom part dimensions
10A	— Two-roller housing top part dimensions
11A	— Two-roller housing bottom part dimensions
12A	— Roller part dimensions
13A	— Simplistic representation of the roller bearing dimensions
14A	— Simplistic representation of shaft bearing dimensions
15A	— Simplistic representation of the 8x8 coupler - spider type dimensions
16A	— Shaft dimensions

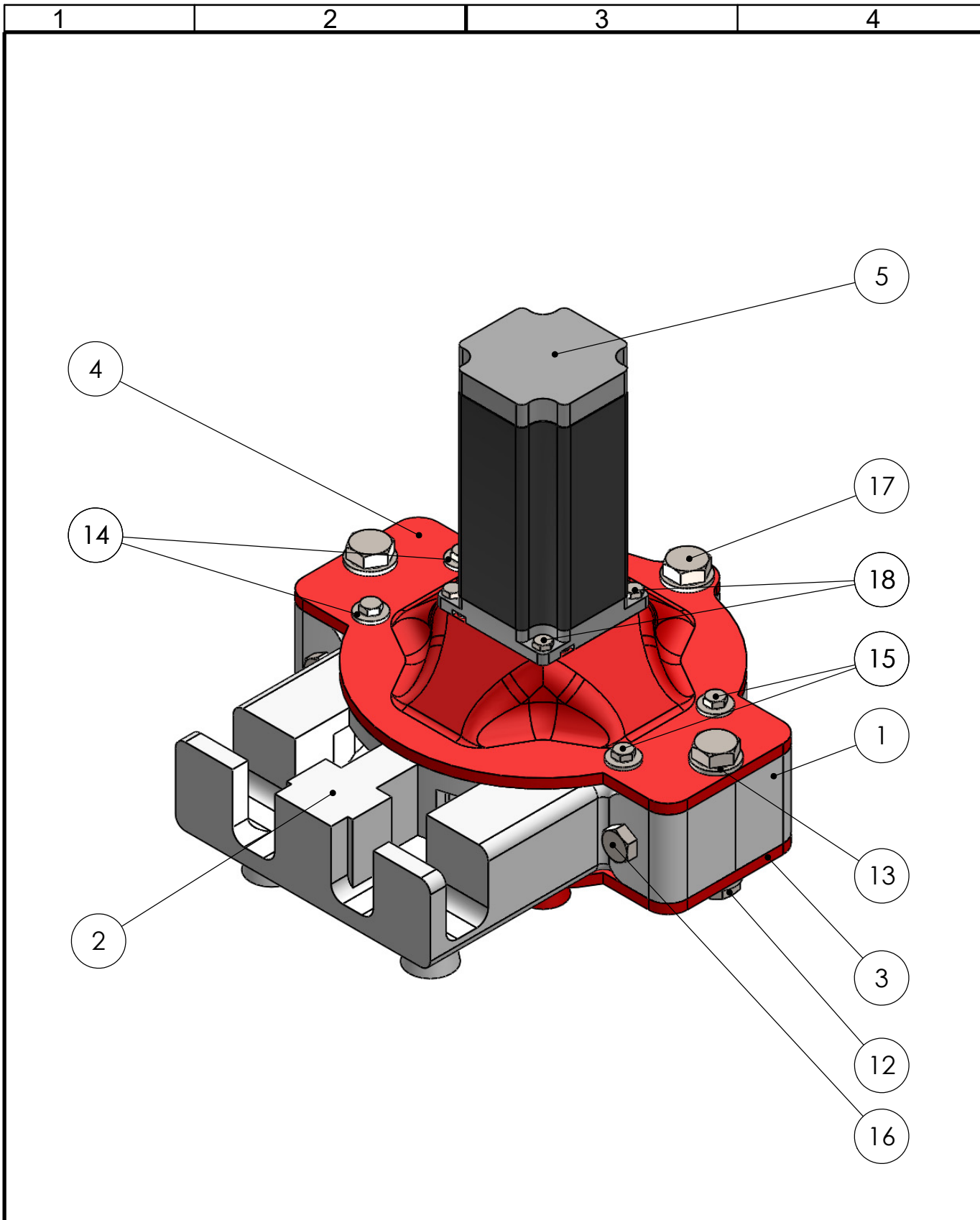



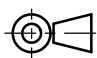
Table C.2: Peristaltic pump bill of materials: three-roller configuration

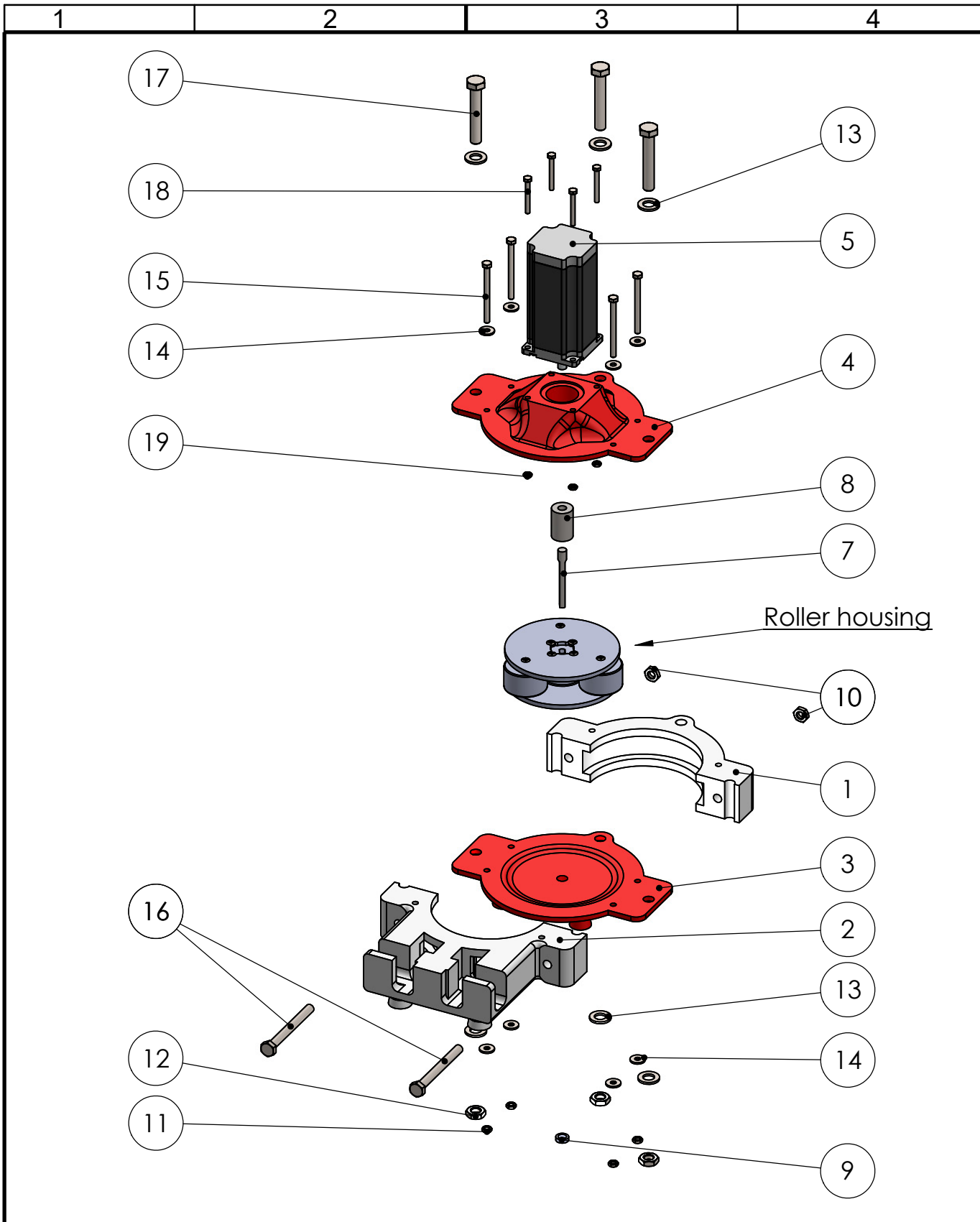
Item no.	Drawing no.	Part no.	Description	Qty.
1	4	Mid_section-backplate	Printed part (body)	1
2	3	Mid_section-Inlet_x_outlet	Printed part (body)	1
3	6	Bottom_plate	Printed part (body)	1
4	5	Top_plate	Printed part (body)	1
5	7	Nema23HS8	Reference part (motor)	1
6		<i>Tee_6mm_ID_30mm_length</i>	<i>Not included</i>	2
7	16	Shaft	Manufactured part (shaft)	1
8	15	8mm-8mm_shaft_Coupler	Reference part (coupler)	1
9	14	MR128.2ZR_shaft_bearing	Reference part (bearing)	1
10		M8_thin_nut	Reference part (fastener)	2
11		M5_thin_nut	Reference part (fastener)	4
12		M10_thin_nut	Reference part (fastener)	3
13		M10_plain_washer	Reference part (washer)	6
14		M5_plain_washer	Reference part (washer)	8
15		M5x60_Hex_bolt	Reference part (fastener)	4
16		M8x80_Hex_bolt	Reference part (fastener)	2
17		M10x60_Hex_bolt	Reference part (fastener)	3
18		M4x35_Hex_bolt	Reference part (fastener)	4
19		M4_thin_nut	Reference part (fastener)	11
20	9	Three_roller_housing_bottom	Printed part (roller housing)	1
21	8	Three_roller_housing_top	Printed part (roller housing)	1
22	12	Roller	Printed part (roller housing)	3
23		M4x30_Pan_head_screw	Reference part (fastener)	7
24	13	MR104.2ZR_roller_bearing	Reference part (bearing)	6


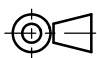
Table C.3: Peristaltic pump bill of materials: two-roller configuration

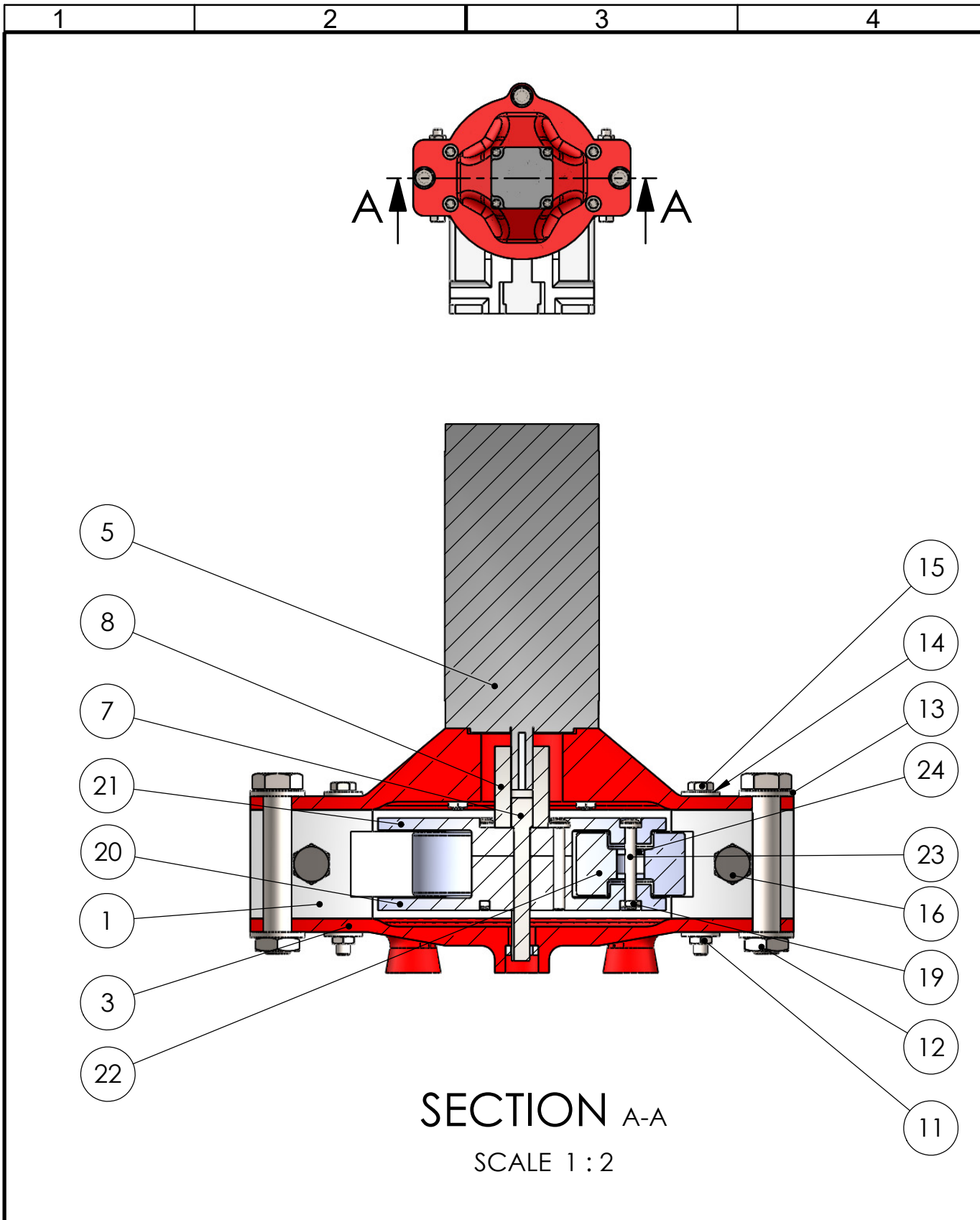
Item no.	Drawing no.	Part no.	Description	Qty.
1	4	Mid_section-backplate	Printed part (body)	1
2	3	Mid_section-Inlet_x_outlet	Printed part (body)	1
3	6	Bottom_plate	Printed part (body)	1
4	5	Top_plate	Printed part (body)	1
5	7	Nema23HS8	Reference part (motor)	1
6		<i>Tee_6mm_ID_30mm_length</i>	<i>Not included</i>	2
7	16	Shaft	Manufactured part (shaft)	1
8	15	8mm-8mm_shaft_Coupler	Reference part (coupler)	1
9	14	MR128.2ZR_shaft_bearing	Reference part (bearing)	1
10		M8_thin_nut	Reference part (fastener)	2
11		M5_thin_nut	Reference part (fastener)	4
12		M10_thin_nut	Reference part (fastener)	3
13		M10_plain_washer	Reference part (washer)	6
14		M5_plain_washer	Reference part (washer)	8
15		M5x60_Hex_bolt	Reference part (fastener)	4
16		M8x80_Hex_bolt	Reference part (fastener)	2
17		M10x60_Hex_bolt	Reference part (fastener)	3
18		M4x35_Hex_bolt	Reference part (fastener)	4
19		M4_thin_nut	Reference part (fastener)	10
20	11	Two_roller_housing_bottom	Printed part (roller housing)	1
21	10	Two_roller_housing_top	Printed part (roller housing)	1
22	12	Roller	Printed part (roller housing)	2
23		M4x30_Pan_head_screw	Reference part (fastener)	6
24	13	MR104.2ZR_roller_bearing	Reference part (bearing)	4




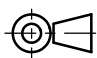
Material:		This drawing and any information or descriptive material set out on it are the confidential and copyright property of the <b>North-West University</b> . © and MUST NOT BE DISCLOSED, COPIED, LOANED in whole or part or used for any purpose without the written permission of the <b>North-West University</b> .	Description: <b>Peristaltic pump component analysis - trimetric view</b>		
Finish:			Drawn by: <b>Mr. M. McIntyre</b>	Drawn Date: <b>17/03/2020</b>	
Unless Otherwise Stated: Linear Tol.: ±0.2, Angular Tol.: 0°15' Surface Finish: 0.8µm All Dimensions: mm		Document Type: <b>Masters dissertation</b>	Checked/Approved by: <b>Mr. CP Kloppers</b>		
Drawing Scale: <b>1:2</b>		<b>Company Confidential</b>	Checked/Approved Date: <b>31/03/2020</b>		
Approx Weight: ~ Kg	Drawing Produced In Accordance With: <b>BS8888</b>	Legal Owner:	Part Number: <b>PERISTALTIC_PUMP_ASSEMBLY</b>		
Projection Method: <b>THIRD ANGLE</b>	Sheet Size: <b>A4</b>	 The North-West University, 11 Hofman street, Potchefstroom, 2531	Drawing Number: <b>1A</b>	Sheet: <b>1 of 3</b>	Revision: <b>1</b>
					

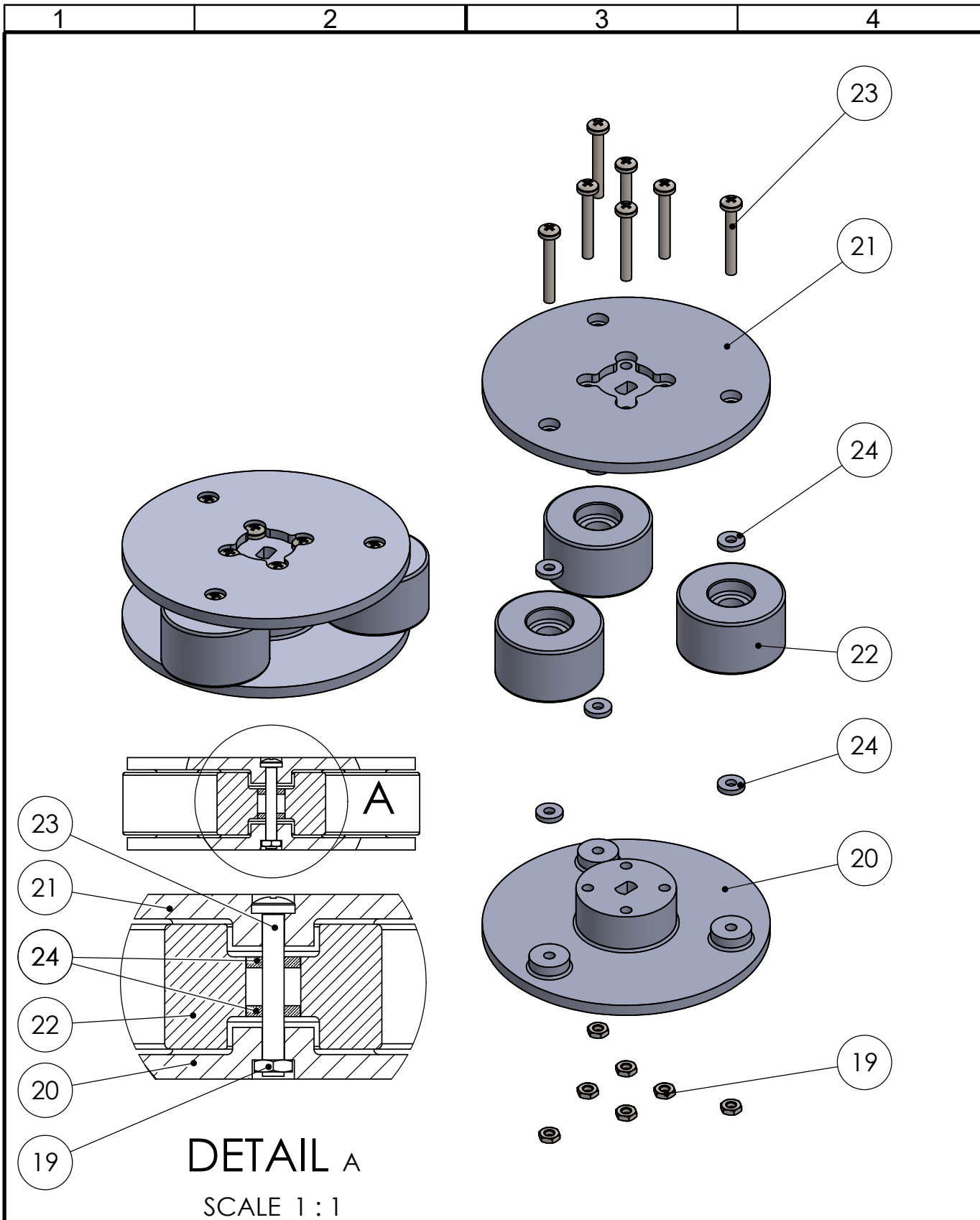


Material:		This drawing and any information or descriptive material set out on it are the confidential and copyright property of the <b>North-West University</b> . © and MUST NOT BE DISCLOSED, COPIED, LOANED in whole or part or used for any purpose without the written permission of the <b>North-West University</b> .	Description: <b>Peristaltic pump component analysis - exploded trimetric view</b>		
Finish:			Drawn by: <b>Mr. M. McIntyre</b>	Drawn Date: <b>17/03/2020</b>	
Unless Otherwise Stated: Linear Tol.: ±0.2, Angular Tol.: 0°15' Surface Finish: 0.8µm All Dimensions: mm		Document Type: <b>Masters dissertation</b>	Checked/Approved by: <b>Mr. CP Kloppers</b>		
Drawing Scale: <b>1:5</b>		<b>Company Confidential</b>	Checked/Approved Date: <b>31/03/2020</b>		
Approx Weight: ~ Kg	Drawing Produced In Accordance With: <b>BS8888</b>	Legal Owner:  The North-West University, 11 Hofman street, Potchefstroom, 2531	Part Number: <b>PERISTALTIC_PUMP_ASSEMBLY</b>		
Projection Method: <b>THIRD ANGLE</b> 	Sheet Size: <b>A4</b>		Drawing Number: <b>1B</b>	Sheet: <b>2 of 3</b>	Revision: <b>1</b>




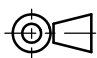
SECTION A-A  
SCALE 1 : 2

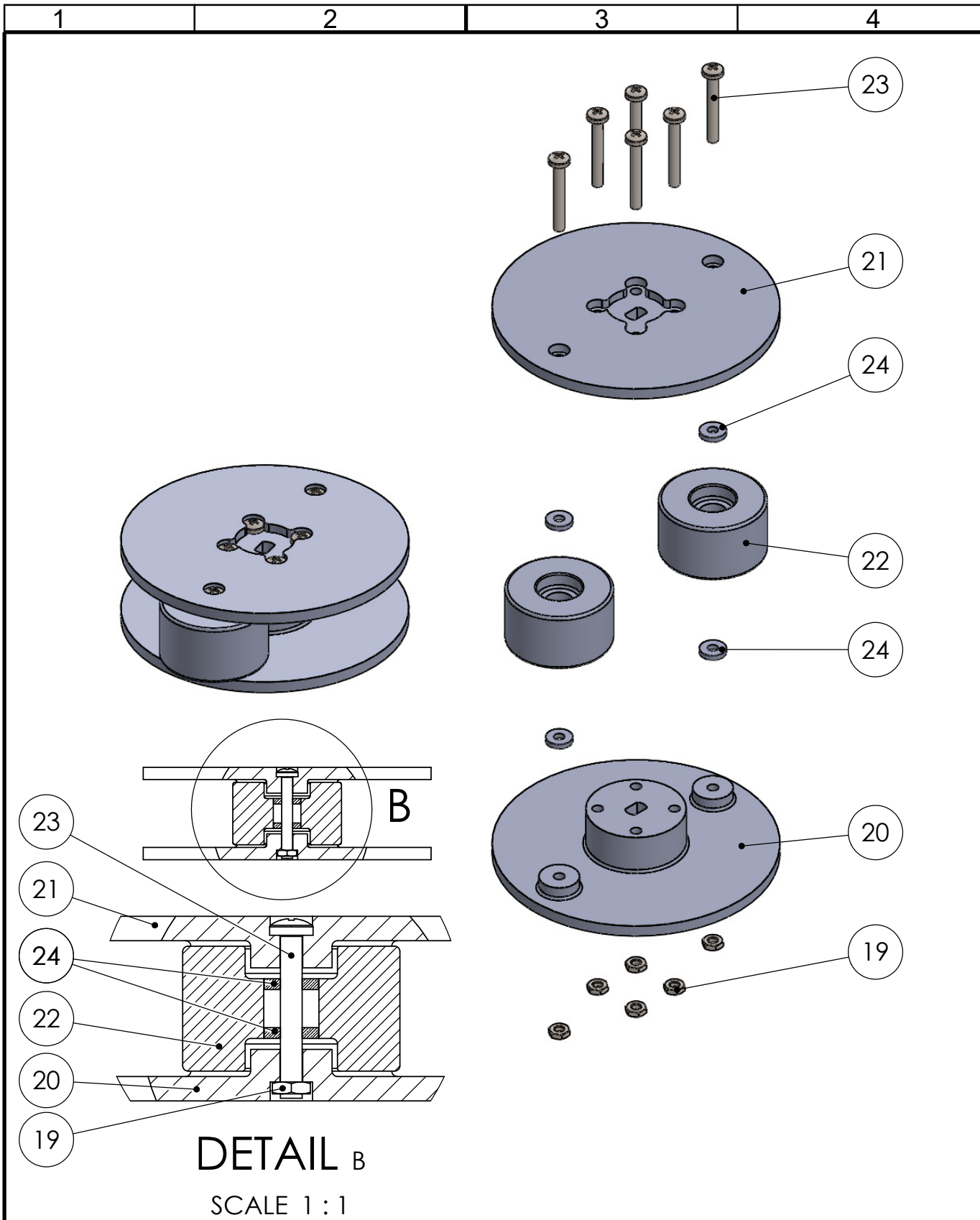
Material:		This drawing and any information or descriptive material set out on it are the confidential and copyright property of the <b>North-West University</b> . © and MUST NOT BE DISCLOSED, COPIED, LOANED in whole or part or used for any purpose without the written permission of the <b>North-West University</b> .	Description: <b>Peristaltic pump component analysis - sectional cut</b>		
Finish:			Drawn by: <b>Mr. M. McIntyre</b>	Drawn Date: <b>17/03/2020</b>	
Unless Otherwise Stated: Linear Tol.: ±0.2, Angular Tol.: 0°15' Surface Finish: 0.8µm All Dimensions: mm		Document Type: <b>Masters dissertation</b>	Checked/Approved by: <b>Mr. CP Kloppers</b>		
Drawing Scale: <b>1:5</b>		<b>Company Confidential</b>	Checked/Approved Date: <b>31/03/2020</b>		
Approx Weight: ~ Kg	Drawing Produced In Accordance With: <b>BS8888</b>	Legal Owner:  The North-West University, 11 Hofman street, Potchefstroom, 2531	Part Number: <b>PERISTALTIC_PUMP_ASSEMBLY</b>		
Projection Method: <b>THIRD ANGLE</b> 	Sheet Size: <b>A4</b>		Drawing Number: <b>1C</b>	Sheet: <b>3 of 3</b>	Revision: <b>1</b>




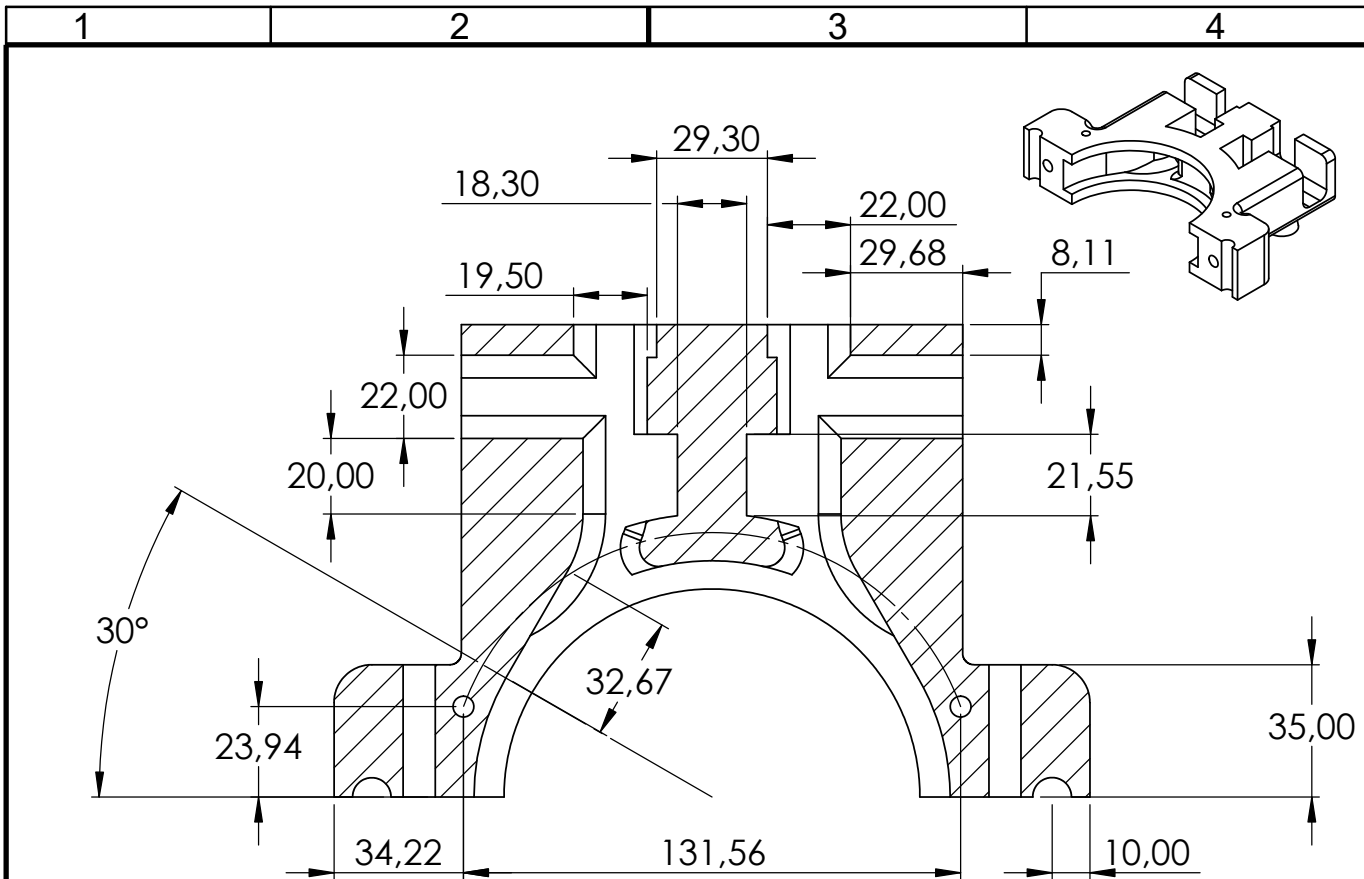
**DETAIL A**

SCALE 1 : 1

Material: <b>PETG</b>		This drawing and any information or descriptive material set out on it are the confidential and copyright property of the <b>North-West University</b> . © and <b>MUST NOT BE DISCLOSED, COPIED, LOANED</b> in whole or part or used for any purpose without the written permission of the <b>North-West University</b> .	Description: <b>Three roller housing component analysis</b>		
Finish: <b>Rough/None</b>			Drawn by: <b>Mr. M. McIntyre</b>	Drawn Date: <b>17/03/2020</b>	
Unless Otherwise Stated: Linear Tol.: <b>±0.2</b> , Angular Tol.: <b>0°15'</b> Surface Finish: <b>0.8µm</b> All Dimensions: <b>mm</b>		Document Type: <b>Masters dissertation</b>	Checked/Approved by: <b>Mr. CP Kloppers</b>		
Drawing Scale: <b>1:2</b>		<b>Company Confidential</b>	Checked/Approved Date: <b>31/03/2020</b>		
Approx Weight: ~ Kg	Drawing Produced In Accordance With: <b>BS8888</b>	Legal Owner:  <b>NWU</b> The North-West University, 11 Hofman street, Potchefstroom, 2531	Part Number: <b>THREE_ROLLER_HOUSING_ASSEMBLY</b>		
Projection Method: <b>THIRD ANGLE</b> 	Sheet Size: <b>A4</b>		Drawing Number: <b>2A</b>	Sheet: <b>1 of 1</b>	Revision: <b>1</b>

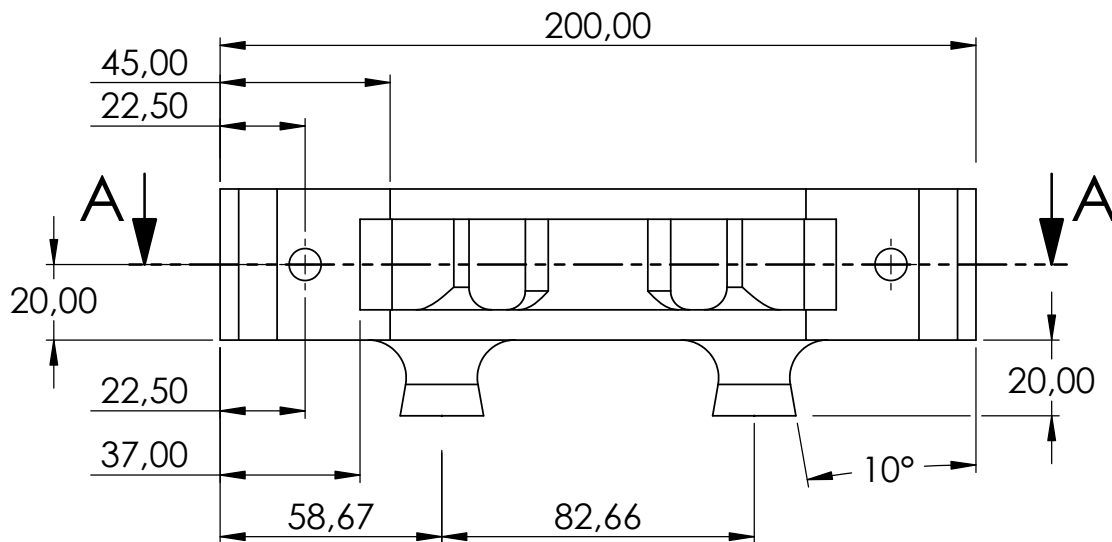




Material: <b>PETG</b>		This drawing and any information or descriptive material set out on it are the confidential and copyright property of the <b>North-West University</b> . © and <b>MUST NOT BE DISCLOSED, COPIED, LOANED</b> in whole or part or used for any purpose without the written permission of the <b>North-West University</b> .	Description: <b>Two roller housing component analysis</b>		
Finish: <b>Rough/None</b>			Drawn by: <b>Mr. M. McIntyre</b>	Drawn Date: <b>17/03/2020</b>	
Unless Otherwise Stated: Linear Tol.: $\pm 0.2$ , Angular Tol.: $0^{\circ}15'$ Surface Finish: $0.8\mu\text{m}$ All Dimensions: <b>mm</b>			Checked/Approved by: <b>Mr. CP Kloppers</b>		
Drawing Scale: <b>1:2</b>			Checked/Approved Date: <b>31/03/2020</b>		
Approx Weight: ~ Kg	Drawing Produced In Accordance With: <b>BS8888</b>	Document Type: <b>Masters dissertation</b>	Part Number: <b>TWO_ROLLER_HOUSING_ASSEMBLY</b>		
Projection Method: <b>THIRD ANGLE</b>	Sheet Size: <b>A4</b>	Legal Owner:  The North-West University, 11 Hofman street, Potchefstroom, 2531	Drawing Number: <b>2B</b>	Sheet: <b>1 of 1</b>	Revision: <b>1</b>



SECTION A-A

SCALE 1 : 2



Material: <b>PETG</b>		This drawing and any information or descriptive material set out on it are the confidential and copyright property of the <b>North-West University</b> . © and MUST NOT BE DISCLOSED, COPIED, LOANED in whole or part or used for any purpose without the written permission of the <b>North-West University</b> .	Description: <b>Inlet and outlet intermediate section hole positions and part dimensions</b>		
Finish: <b>Rough/None</b>			Drawn by: <b>Mr. M. McIntyre</b>	Drawn Date: <b>17/03/2020</b>	
Unless Otherwise Stated: Linear Tol.: ±0.2, Angular Tol.: 0°15' Surface Finish: 0.8µm All Dimensions: mm		Document Type: <b>Masters dissertation</b>	Checked/Approved by: <b>Mr. CP Kloppers</b>		
Drawing Scale: <b>1:2</b>		<b>Company Confidential</b>	Checked/Approved Date: <b>31/03/2020</b>		
Approx Weight: ~ Kg	Drawing Produced In Accordance With: <b>BS8888</b>	Legal Owner:  The North-West University, 11 Hofman street, Potchefstroom, 2531	Part Number: <b>MID_SECTION--INLET_X_OUTLET</b>		
Projection Method: <b>THIRD ANGLE</b> 	Sheet Size: <b>A4</b>		Drawing Number: <b>3A</b>	Sheet: <b>1 of 3</b>	Revision: <b>1</b>

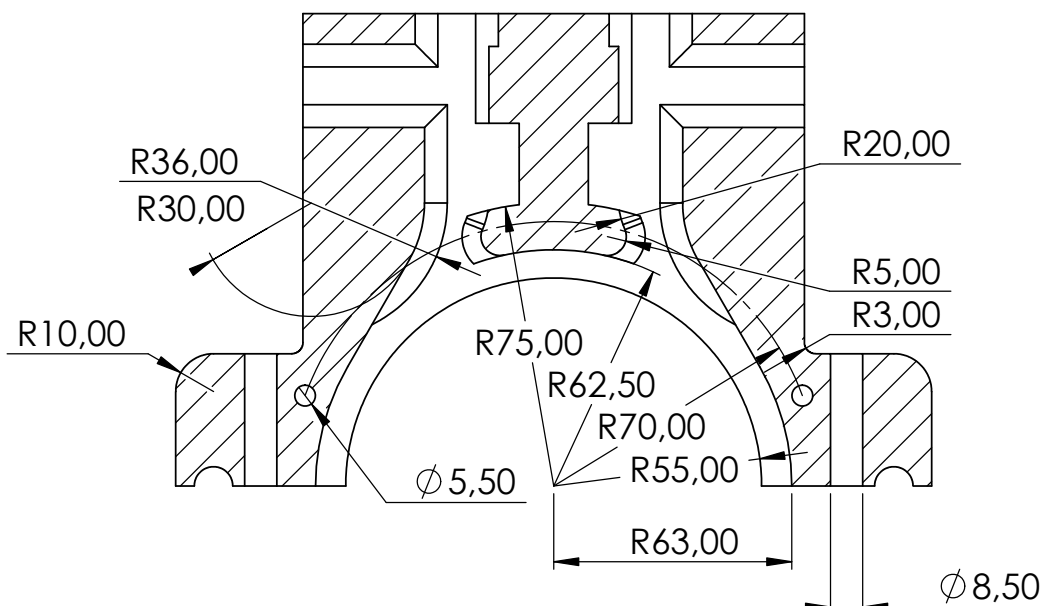
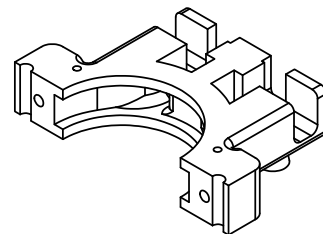


1

2

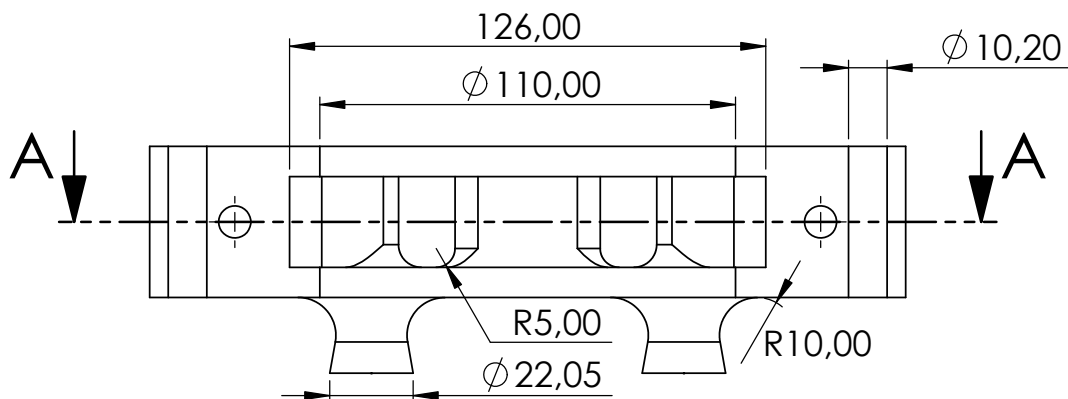
3


4

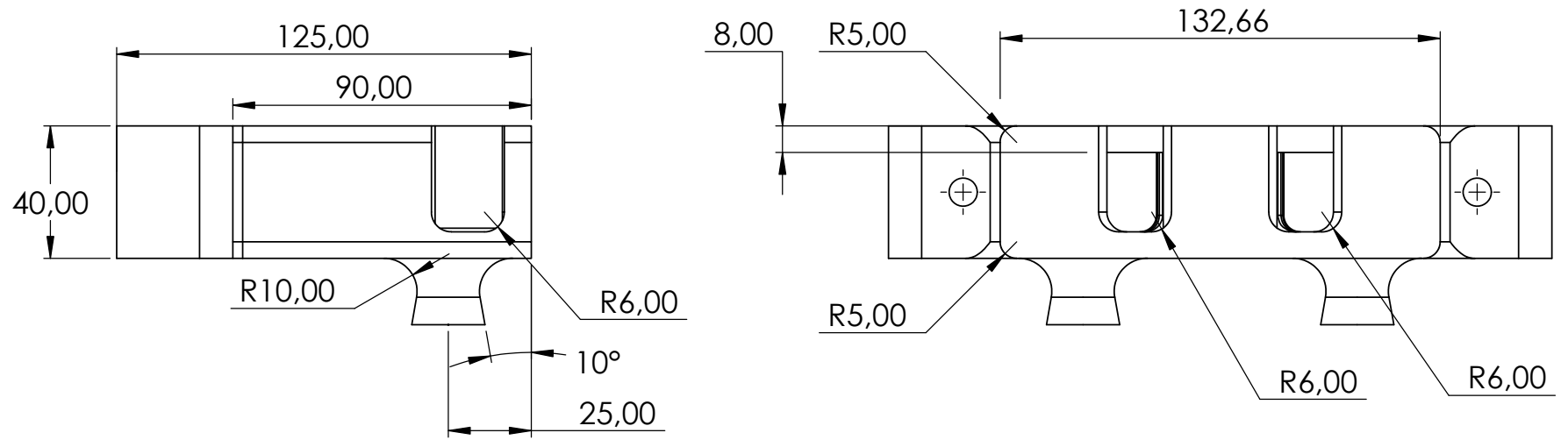
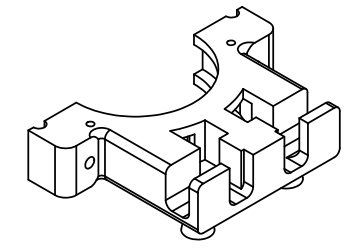



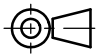
SECTION A-A

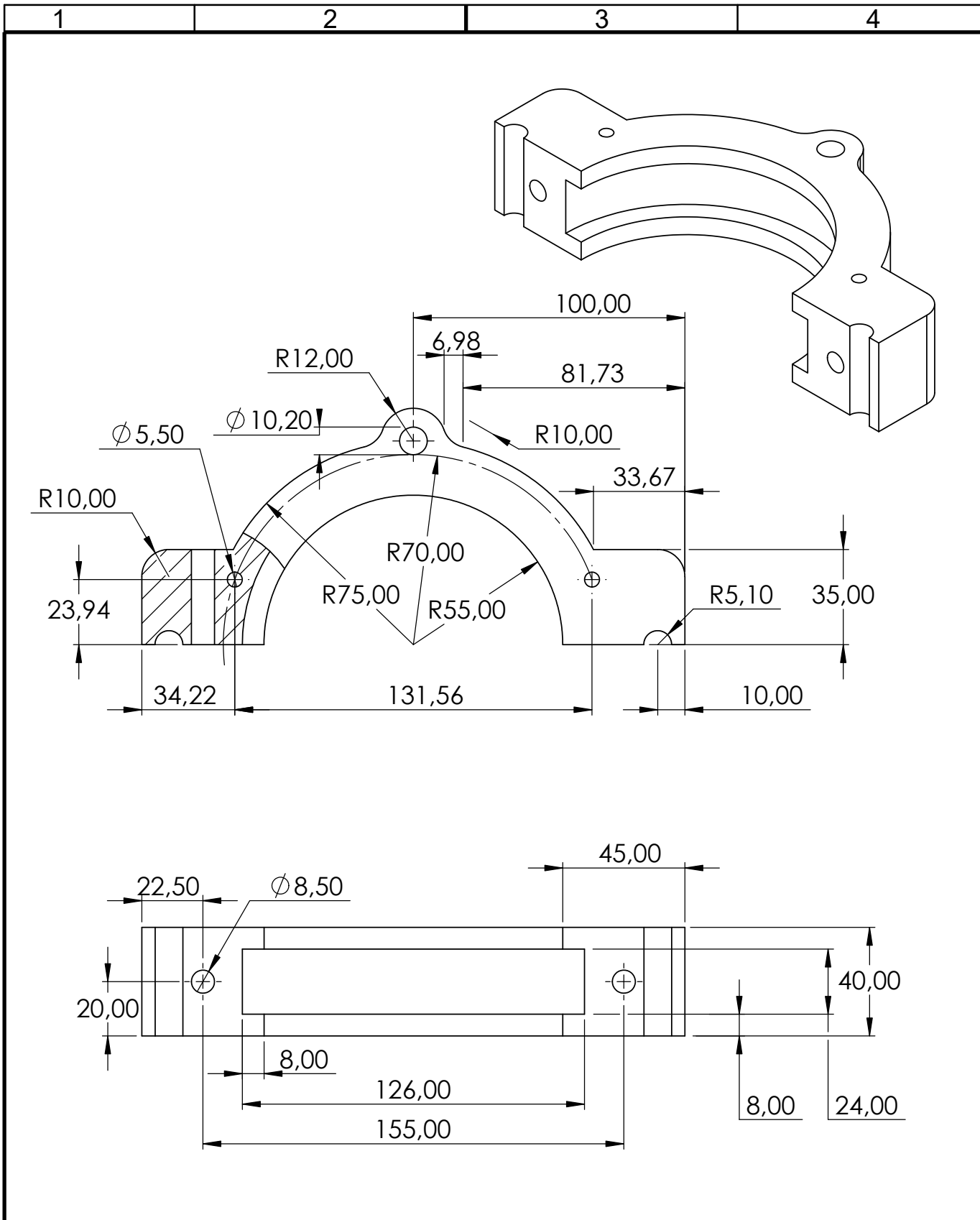
SCALE 1 : 2




Material: <b>PETG</b>		This drawing and any information or descriptive material set out on it are the confidential and copyright property of the <b>North-West University</b> . © and <b>MUST NOT BE DISCLOSED, COPIED, LOANED</b> in whole or part or used for any purpose without the written permission of the <b>North-West University</b> .	Description: <b>Inlet and outlet intermediate section hole and radius sizes</b>		
Finish: <b>Rough/None</b>			Drawn by: <b>Mr. M. McIntyre</b>	Drawn Date: <b>17/03/2020</b>	
Unless Otherwise Stated: Linear Tol.: $\pm 0.2$ , Angular Tol.: $0^{\circ}15'$ Surface Finish: $0.8\mu\text{m}$ All Dimensions: <b>mm</b>			Checked/Approved by: <b>Mr. CP Kloppers</b>		
Drawing Scale: <b>1:2</b>			Checked/Approved Date: <b>31/03/2020</b>		
Approx Weight: ~ Kg	Drawing Produced In Accordance With: <b>BS8888</b>	Document Type: <b>Masters dissertation</b>	Part Number: <b>MID_SECTION--INLET_X_OUTLET</b>		
Projection Method: <b>THIRD ANGLE</b>	Sheet Size: <b>A4</b>	Legal Owner:  The North-West University, 11 Hofman street, Potchefstroom, 2531	Drawing Number: <b>3B</b>	Sheet: <b>2 of 3</b>	Revision: <b>1</b>



Material: <b>PETG</b>		This drawing and any information or descriptive material set out on it are the confidential and copyright property of <b>Company Name</b> . © and MUST NOT BE DISCLOSED, COPIED, LOANED in whole or part or used for any purpose without the written permission of <b>Company Name</b> .	Description: <b>Inlet and outlet intermediate section hole positions and dimensions - side view</b>		
Finish: <b>Rough/None</b>			Document Type: <b>Masters dissertation</b>	Drawn by: <b>Mr. M. McIntyre</b>	Drawn Date: <b>17/03/2020</b>
Unless Otherwise Stated: Linear Tol.: ±0.2, Angular Tol.: 0°15' Surface Finish: 0.8µm All Dimensions: mm		Legal Owner:  <b>NWU</b> The North-West University, 11 Hofman street, Potchefstroom, 2531	Checked/Approved by: <b>Mr. CP Kloppers</b>	Checked/Approved Date: <b>31/03/2020</b>	
Drawing Scale: <b>1:2</b>			Part Number: <b>MID_SECTION--INLET_X_OUTLET</b>		
Approx Weight: ~ Kg	Drawing Produced In Accordance With: <b>BS8888</b>	Drawing Number: <b>3C</b>		Sheet: <b>3 of 3</b>	Revision: <b>1</b>
Projection Method: <b>THIRD ANGLE</b> 		Sheet Size: <b>A4</b>			



Material: <b>PETG</b>		This drawing and any information or descriptive material set out on it are the confidential and copyright property of the <b>North-West University</b> . © and <b>MUST NOT BE DISCLOSED, COPIED, LOANED</b> in whole or part or used for any purpose without the written permission of the <b>North-West University</b> .	Description: <b>Intermediate section between the top and bottom plate containing the majority of the backplate</b>		
Finish: <b>Rough/None</b>			Drawn by: <b>Mr. M. McIntyre</b>	Drawn Date: <b>17/03/2020</b>	
Unless Otherwise Stated: Linear Tol.: ±0.2, Angular Tol.: 0°15' Surface Finish: 0.8µm All Dimensions: mm			Checked/Approved by: <b>Mr. CP Kloppers</b>		
Drawing Scale: <b>1:2</b>			Checked/Approved Date: <b>31/03/2020</b>		
Approx Weight: ~ Kg	Drawing Produced In Accordance With: <b>BS8888</b>	Document Type: <b>Masters dissertation</b>	Part Number: <b>MID_SECTION--BACKPLATE</b>		
Projection Method: <b>THIRD ANGLE</b>		Legal Owner:  The North-West University, 11 Hofman street, Potchefstroom, 2531	Drawing Number: <b>4A</b>	Sheet: <b>1 of 1</b>	Revision: <b>1</b>
Sheet Size: <b>A4</b>					

1

2

3

4

A

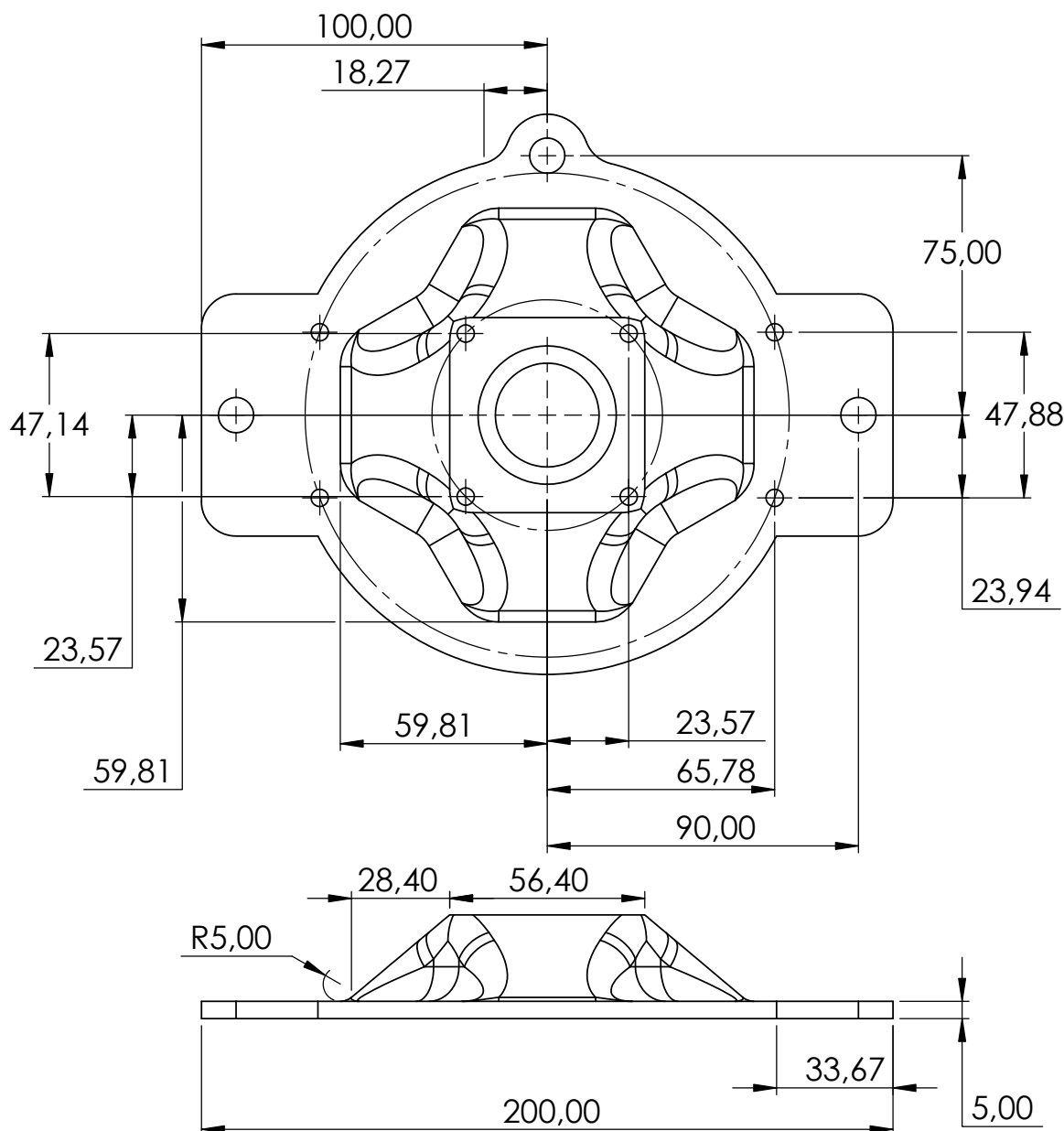
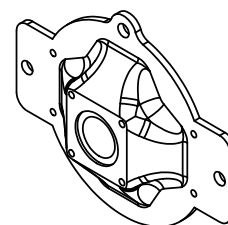
B



C

D

E

F



Material: <b>PETG</b>		This drawing and any information or descriptive material set out on it are the confidential and copyright property of the <b>North-West University</b> . © and MUST NOT BE DISCLOSED, COPIED, LOANED in whole or part or used for any purpose without the written permission of the <b>North-West University</b> .	Description: <b>Top plate hole locations</b>		
Finish: <b>Rough/None</b>			Drawn by: <b>Mr. M. McIntyre</b>	Drawn Date: <b>17/03/2020</b>	
Unless Otherwise Stated: Linear Tol.: $\pm 0.2$ , Angular Tol.: $0^{\circ}15'$ Surface Finish: $0.8\mu\text{m}$ All Dimensions: <b>mm</b>		Document Type: <b>Masters dissertation</b>	Checked/Approved by: <b>Mr. CP Kloppers</b>		
Drawing Scale: <b>1:2</b>		<b>Company Confidential</b>	Checked/Approved Date: <b>31/03/2020</b>		
Approx Weight: ~ Kg	Drawing Produced In Accordance With: <b>BS8888</b>	Legal Owner:  <b>NWU</b> The North-West University, 11 Hofman street, Potchefstroom, 2531	Part Number: <b>TOP_PLATE</b>		
Projection Method: <b>THIRD ANGLE</b> 	Sheet Size: <b>A4</b>		Drawing Number: <b>5A</b>	Sheet: <b>1 of 4</b>	Revision: <b>1</b>

1 2 3 4

A

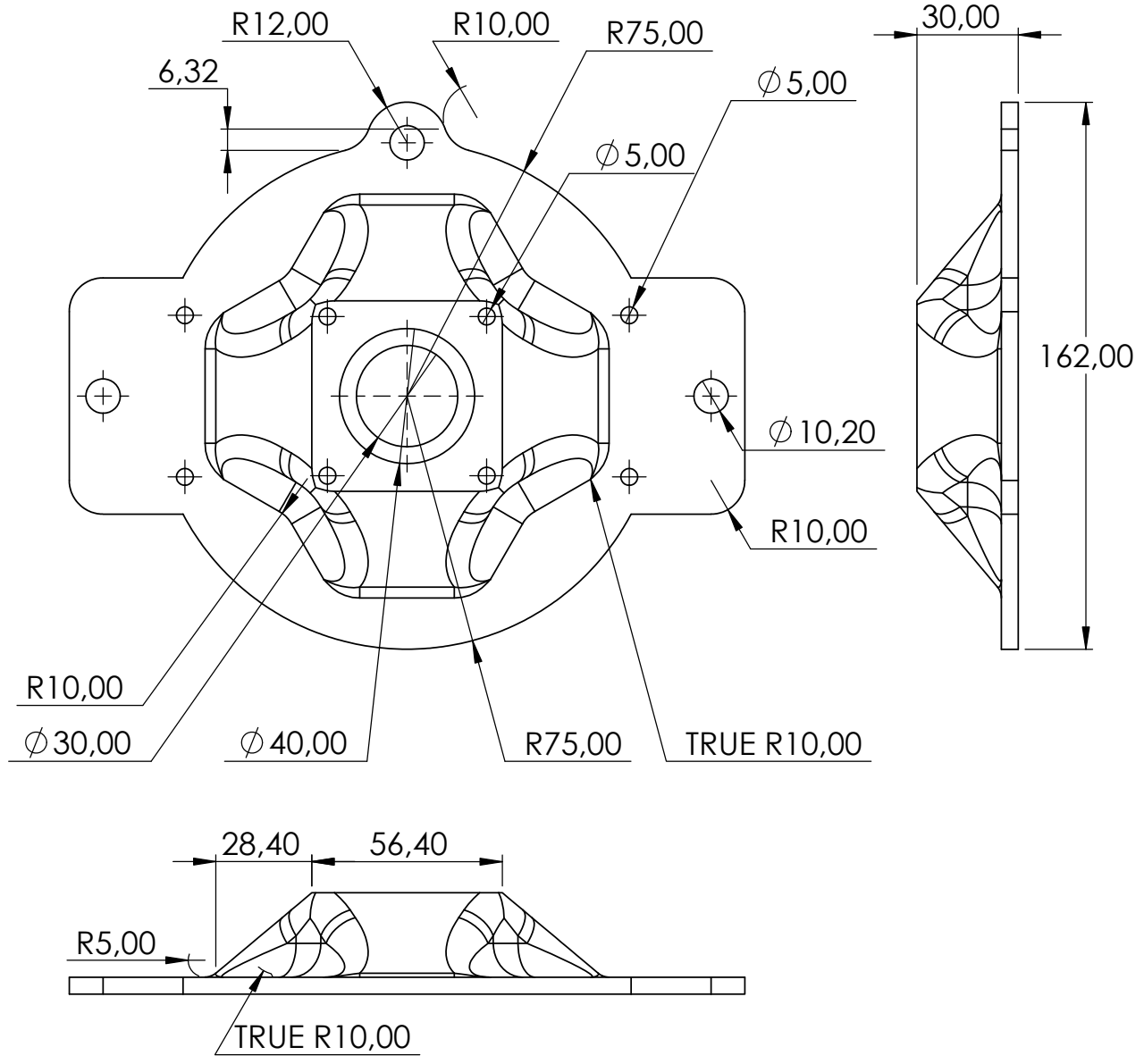
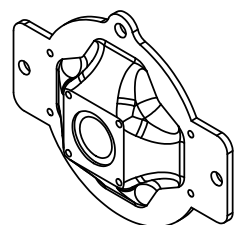
B


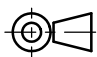
C

D

E

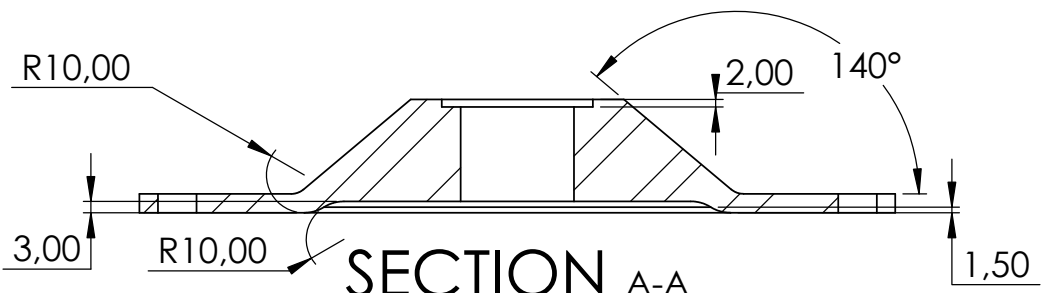
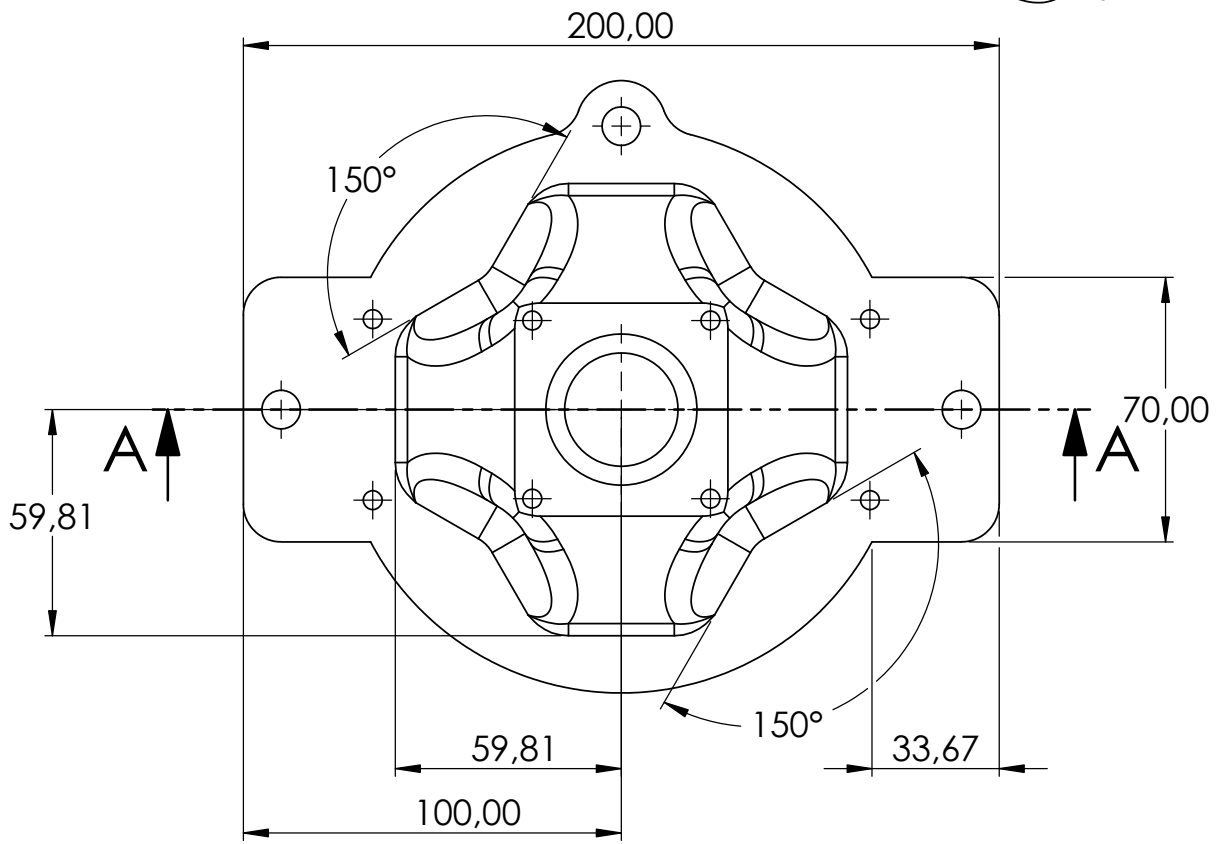
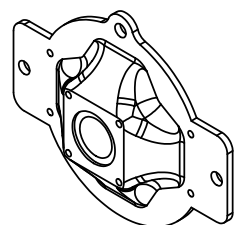
F



Material: <b>PETG</b>		This drawing and any information or descriptive material set out on it are the confidential and copyright property of the <b>North-West University</b> . © and MUST NOT BE DISCLOSED, COPIED, LOANED in whole or part or used for any purpose without the written permission of the <b>North-West University</b> .	Description: <b>Top plate hole and radius sizes</b>		
Finish: <b>Rough/None</b>			Drawn by: <b>Mr. M. McIntyre</b>	Drawn Date: <b>17/03/2020</b>	
Unless Otherwise Stated: Linear Tol.: ±0.2, Angular Tol.: 0°15' Surface Finish: 0.8µm All Dimensions: mm			Checked/Approved by: <b>Mr. CP Kloppers</b>	Checked/Approved Date: <b>31/03/2020</b>	
Drawing Scale: <b>1:2</b>		Document Type: <b>Masters dissertation</b>	Part Number: <b>TOP_PLATE</b>		
Approx Weight: ~ Kg	Drawing Produced In Accordance With: <b>BS8888</b>	Legal Owner:  The North-West University, 11 Hofman street, Potchefstroom, 2531	Drawing Number: <b>5B</b>	Sheet: <b>2 of 4</b>	Revision: <b>1</b>
Projection Method: <b>THIRD ANGLE</b> 	Sheet Size: <b>A4</b>				


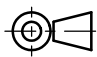
1 2 3 4

A  
B  
C  
D  
E  
F



**SECTION A-A**

SCALE 1 : 2

Material: <b>PETG</b>		This drawing and any information or descriptive material set out on it are the confidential and copyright property of the <b>North-West University</b> . © and <b>MUST NOT BE DISCLOSED, COPIED, LOANED</b> in whole or part or used for any purpose without the written permission of the <b>North-West University</b> .	Description: <b>Top plate part dimensions</b>		
Finish: <b>Rough/None</b>			Drawn by: <b>Mr. M. McIntyre</b>	Drawn Date: <b>17/03/2020</b>	
Unless Otherwise Stated: Linear Tol.: ±0.2, Angular Tol.: 0°15' Surface Finish: 0.8µm All Dimensions: mm			Checked/Approved by: <b>Mr. CP Kloppers</b>	Checked/Approved Date: <b>31/03/2020</b>	
Drawing Scale: <b>1:2</b>			Part Number: <b>TOP_PLATE</b>		
Approx Weight: ~ Kg	Drawing Produced In Accordance With: <b>BS8888</b>	Legal Owner:  The North-West University, 11 Hofman street, Potchefstroom, 2531	Drawing Number: <b>5C</b>	Sheet: <b>3 of 4</b>	Revision: <b>1</b>
Projection Method: <b>THIRD ANGLE</b> 	Sheet Size: <b>A4</b>				

1

2

3

4

A

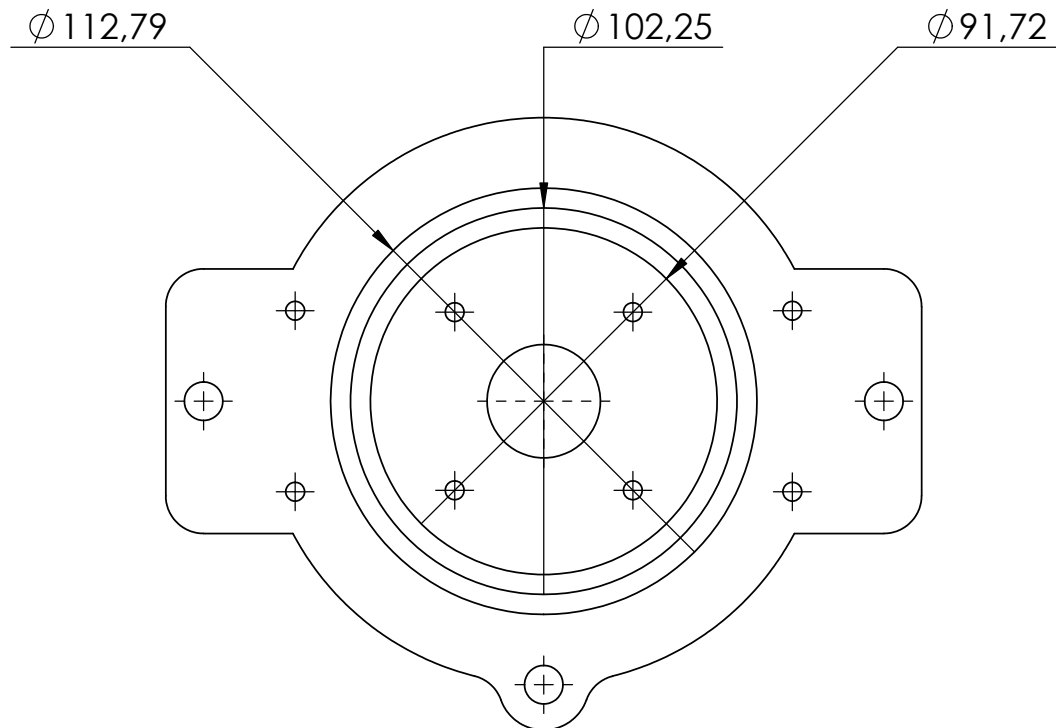
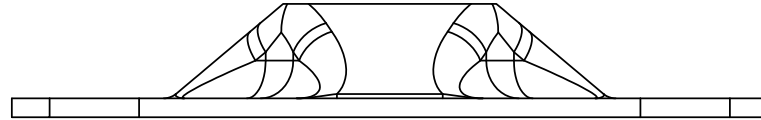
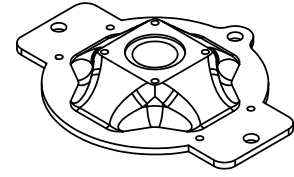
B


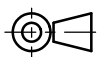
C

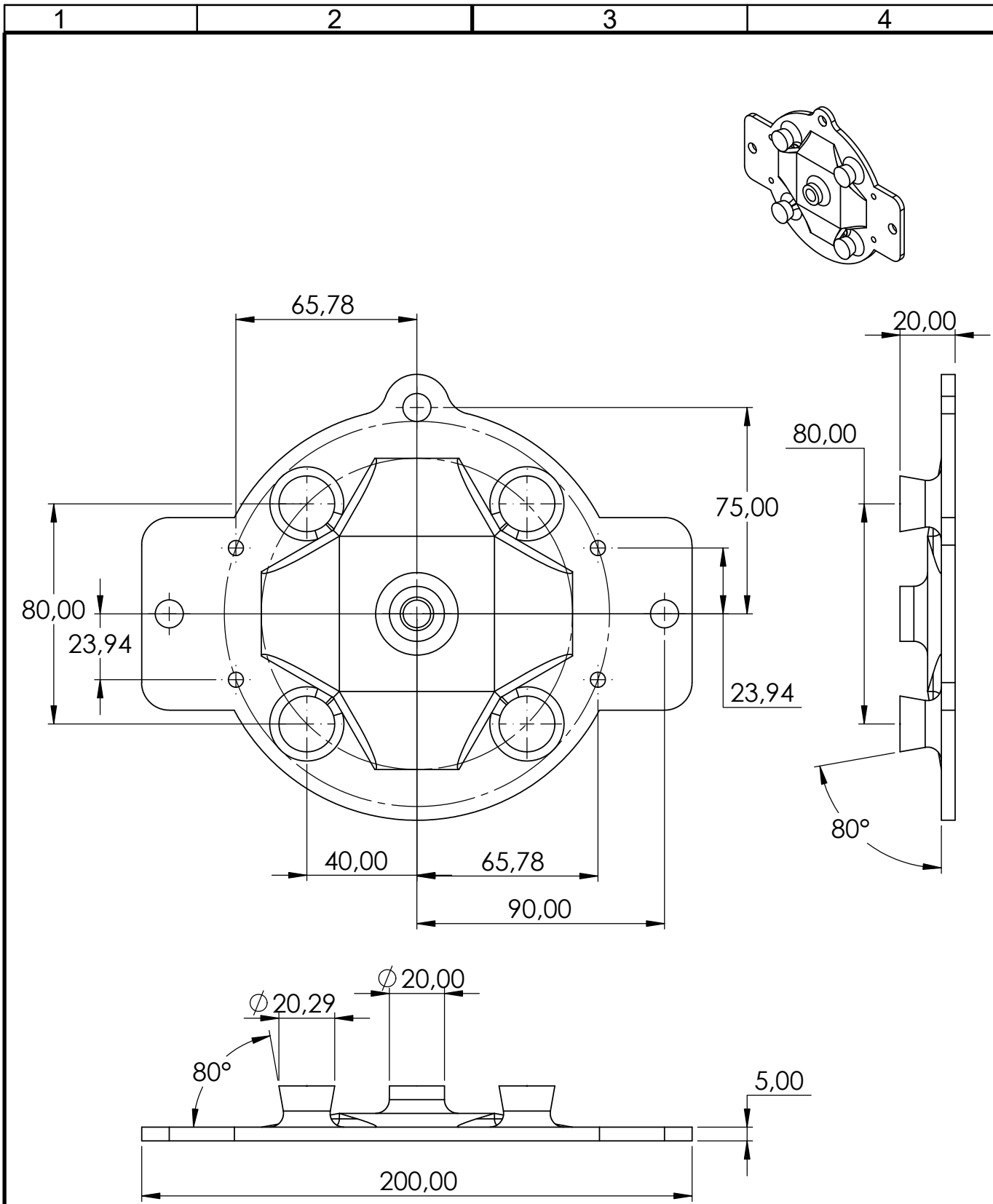
D


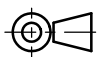
E

F

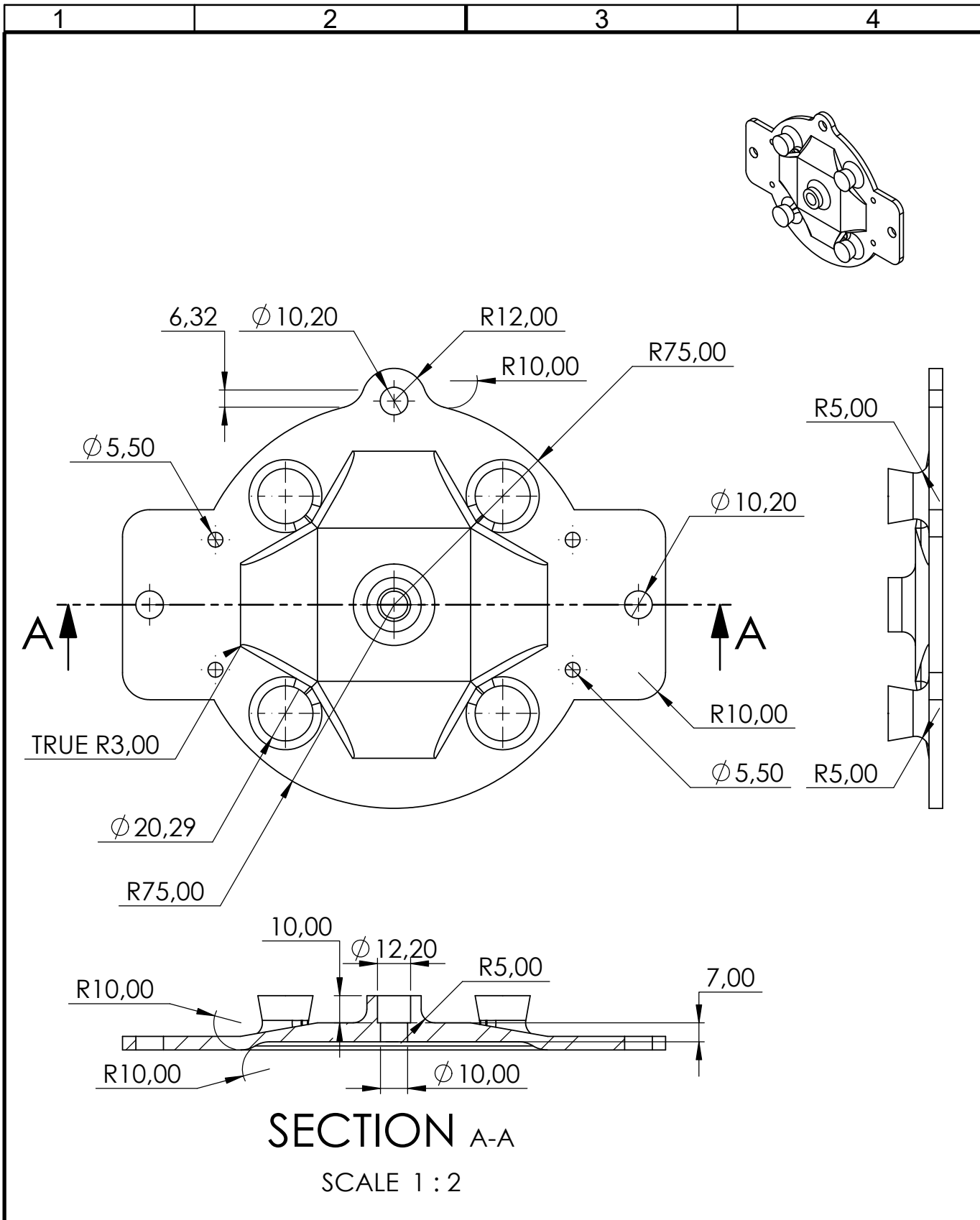


Material: <b>PETG</b>		This drawing and any information or descriptive material set out on it are the confidential and copyright property of the <b>North-West University</b> . © and <b>MUST NOT BE DISCLOSED, COPIED, LOANED</b> in whole or part or used for any purpose without the written permission of the <b>North-West University</b> .	Description: <b>Top plate part dimensions - bottom view</b>		
Finish: <b>Rough/None</b>			Drawn by: <b>Mr. M. McIntyre</b>	Drawn Date: <b>17/03/2020</b>	
Unless Otherwise Stated: Linear Tol.: $\pm 0.2$ , Angular Tol.: $0^{\circ}15'$ Surface Finish: $0.8\mu\text{m}$ All Dimensions: <b>mm</b>			Checked/Approved by: <b>Mr. CP Kloppers</b>	Checked/Approved Date: <b>31/03/2020</b>	
Drawing Scale: <b>1:2</b>		Document Type: <b>Masters dissertation</b>	Part Number: <b>TOP_PLATE</b>		
Approx Weight: ~ Kg	Drawing Produced In Accordance With: <b>BS8888</b>	Legal Owner:  <b>NWU</b> The North-West University, 11 Hofman street, Potchefstroom, 2531	Drawing Number: <b>5D</b>		Revision: <b>1</b>
Projection Method: <b>THIRD ANGLE</b> 	Sheet Size: <b>A4</b>		Sheet: <b>4 of 4</b>		




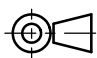
Material: <b>PETG</b>		This drawing and any information or descriptive material set out on it are the confidential and copyright property of the <b>North-West University</b> . © and <b>MUST NOT BE DISCLOSED, COPIED, LOANED</b> in whole or part or used for any purpose without the written permission of the <b>North-West University</b> .	Description: <b>Bottom plate hole locations</b>		
Finish: <b>Rough/None</b>			Drawn by: <b>Mr. M. McIntyre</b>	Drawn Date: <b>17/03/2020</b>	
Unless Otherwise Stated: Linear Tol.: ±0.2, Angular Tol.: 0°15' Surface Finish: 0.8µm All Dimensions: mm			Checked/Approved by: <b>Mr. CP Kloppers</b>	Checked/Approved Date: <b>31/03/2020</b>	
Drawing Scale: <b>1:2</b>		Document Type: <b>Masters dissertation</b>	Part Number: <b>BOTTOM_PLATE</b>		
Approx Weight: ~ Kg	Drawing Produced In Accordance With: <b>BS8888</b>	Legal Owner:  The North-West University, 11 Hofman street, Potchefstroom, 2531	Drawing Number: <b>6A</b>	Sheet: <b>1 of 4</b>	Revision: <b>1</b>
Projection Method: <b>THIRD ANGLE</b> 	Sheet Size: <b>A4</b>				

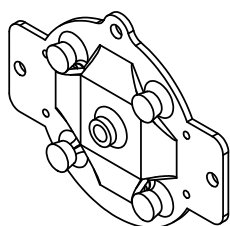
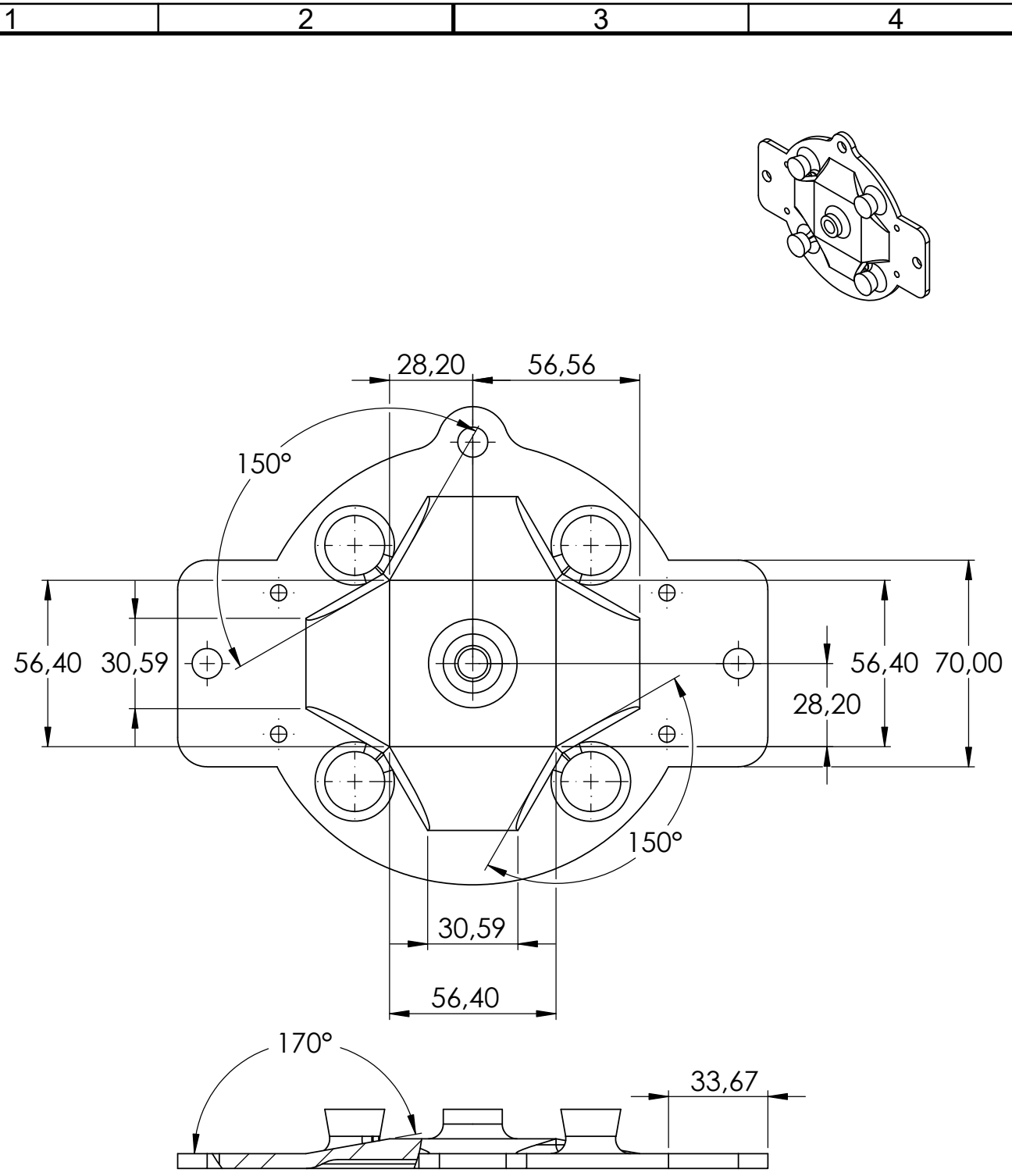





**SECTION A-A**

SCALE 1 : 2

Material: <b>PETG</b>		This drawing and any information or descriptive material set out on it are the confidential and copyright property of the <b>North-West University</b> . © and <b>MUST NOT BE DISCLOSED, COPIED, LOANED</b> in whole or part or used for any purpose without the written permission of the <b>North-West University</b> .	Description: <b>Bottom plate hole and radius sizes</b>		
Finish: <b>Rough/None</b>			Drawn by: <b>Mr. M. McIntyre</b>	Drawn Date: <b>17/03/2020</b>	
Unless Otherwise Stated: Linear Tol.: ±0.2, Angular Tol.: 0°15' Surface Finish: 0.8µm All Dimensions: mm			Checked/Approved by: <b>Mr. CP Kloppers</b>	Checked/Approved Date: <b>31/03/2020</b>	
Drawing Scale: <b>1:2</b>		Document Type: <b>Masters dissertation</b>	Part Number: <b>BOTTOM_PLATE</b>		
Approx Weight: ~ Kg	Drawing Produced In Accordance With: <b>BS8888</b>	Legal Owner:  The North-West University, 11 Hofman street, Potchefstroom, 2531	Drawing Number: <b>6B</b>	Sheet: <b>2 of 4</b>	Revision: <b>1</b>
Projection Method: <b>THIRD ANGLE</b> 	Sheet Size: <b>A4</b>				



Material: <b>PETG</b>		This drawing and any information or descriptive material set out on it are the confidential and copyright property of the <b>North-West University</b> . © and <b>MUST NOT BE DISCLOSED, COPIED, LOANED</b> in whole or part or used for any purpose without the written permission of the <b>North-West University</b> .	Description: <b>Bottom plate part dimensions</b>		
Finish: <b>Rough/None</b>			Drawn by: <b>Mr. M. McIntyre</b>	Drawn Date: <b>17/03/2020</b>	
Unless Otherwise Stated: Linear Tol.: $\pm 0.2$ , Angular Tol.: $0^{\circ}15'$ Surface Finish: $0.8\mu\text{m}$ All Dimensions: <b>mm</b>			Checked/Approved by: <b>Mr. CP Kloppers</b>		
Drawing Scale: <b>1:2</b>			Checked/Approved Date: <b>31/03/2020</b>		
Approx Weight: ~ <b>Kg</b>	Drawing Produced In Accordance With: <b>BS8888</b>	Document Type: <b>Masters dissertation</b>	Part Number: <b>BOTTOM_PLATE</b>		
Projection Method: <b>THIRD ANGLE</b>		Legal Owner:  The North-West University, 11 Hofman street, Potchefstroom, 2531	Drawing Number: <b>6C</b>	Sheet: <b>3 of 4</b>	Revision: <b>1</b>
Sheet Size: <b>A4</b>					

1

2

3

4

A

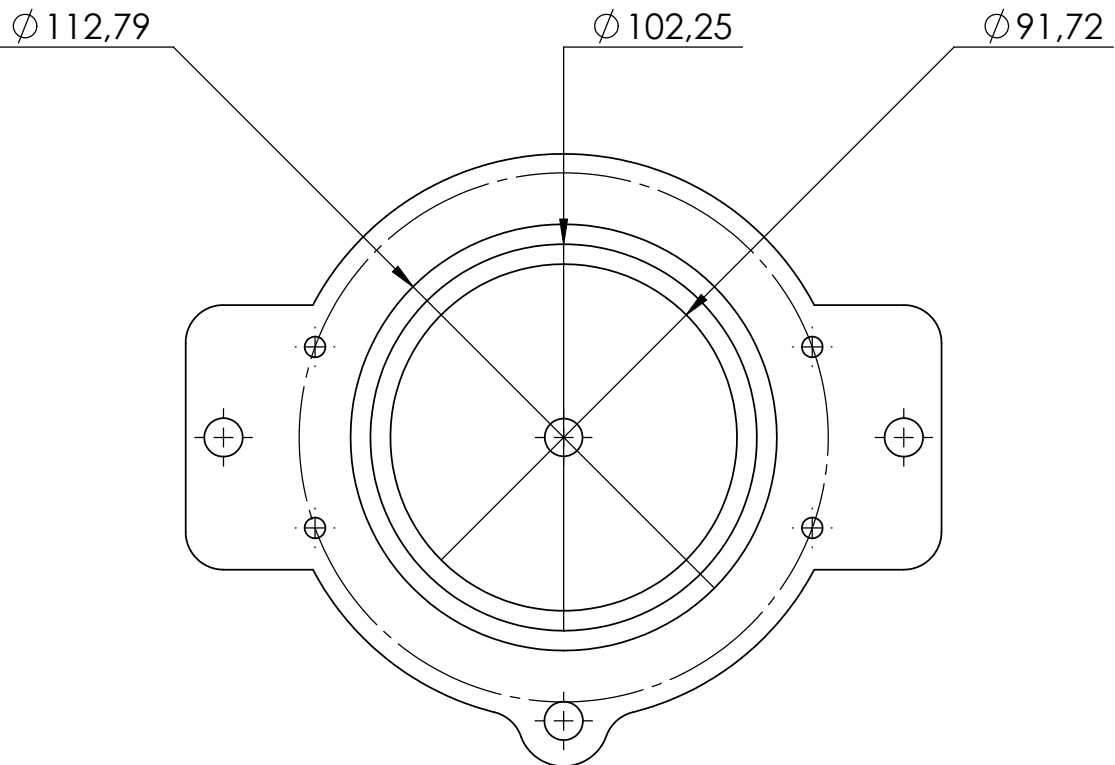
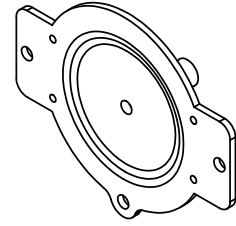
B


C

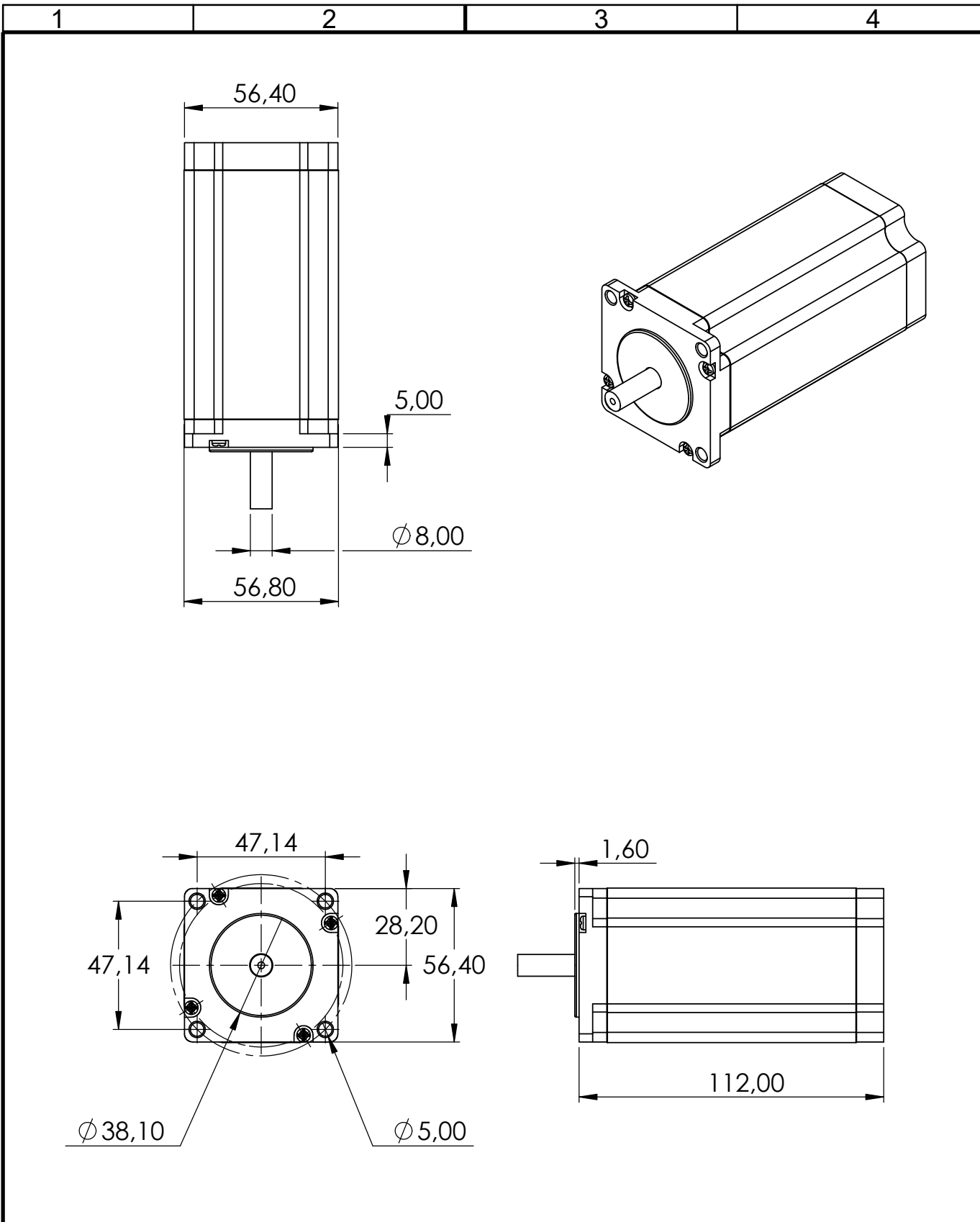
D


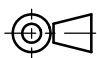
E

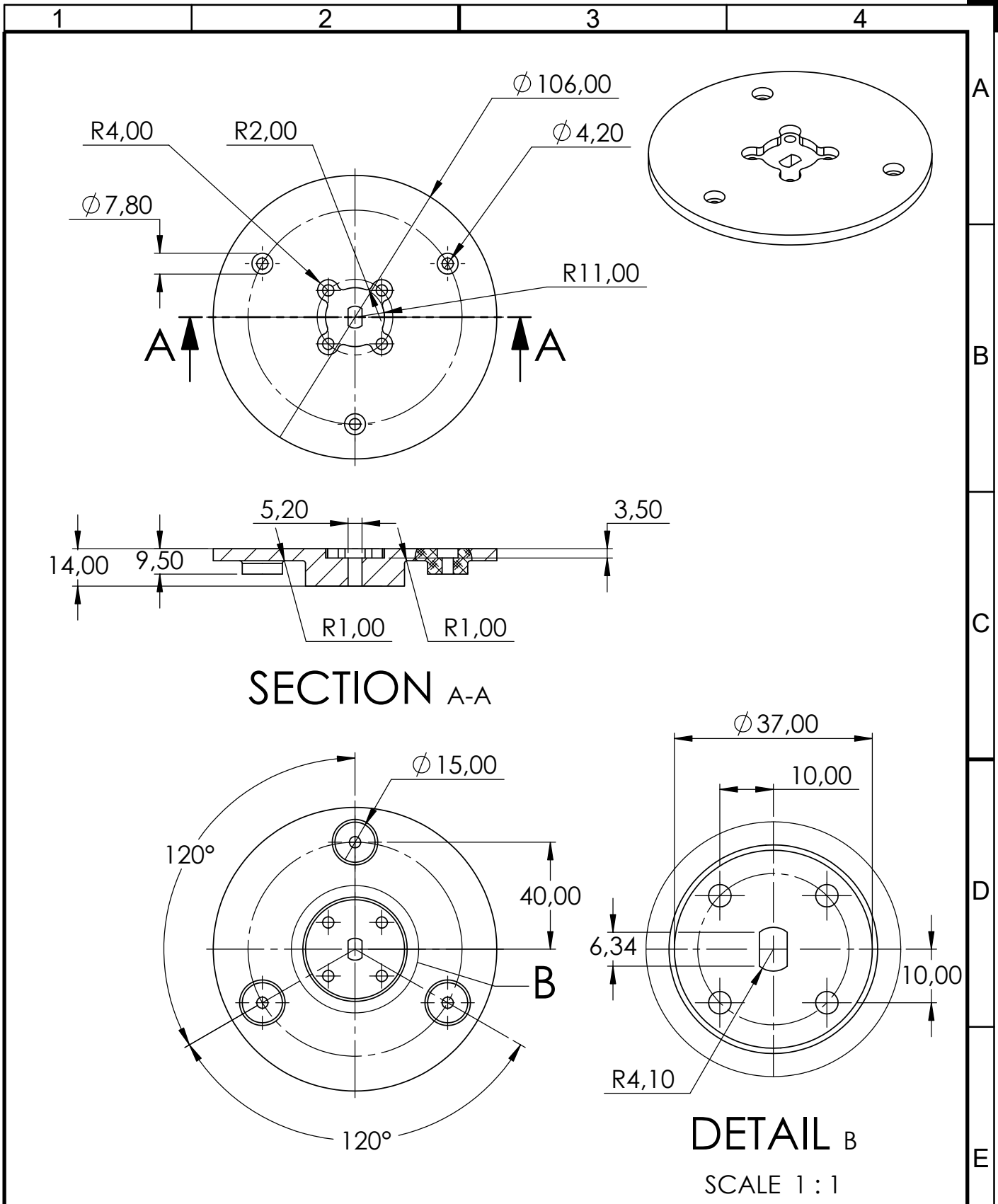
F



Material: <b>PETG</b>		This drawing and any information or descriptive material set out on it are the confidential and copyright property of the <b>North-West University</b> . © and MUST NOT BE DISCLOSED, COPIED, LOANED in whole or part or used for any purpose without the written permission of the <b>North-West University</b> .	Description: <b>Bottom plate part dimensions - bottom view</b>		
Finish: <b>Rough/None</b>			Drawn by: <b>Mr. M. McIntyre</b>	Drawn Date: <b>17/03/2020</b>	
Unless Otherwise Stated: Linear Tol.: $\pm 0.2$ , Angular Tol.: $0^{\circ}15'$ Surface Finish: $0.8\mu\text{m}$ All Dimensions: <b>mm</b>			Checked/Approved by: <b>Mr. CP Kloppers</b>		
Drawing Scale: <b>1:2</b>			Checked/Approved Date: <b>31/03/2020</b>		
Approx Weight: ~ Kg	Drawing Produced In Accordance With: <b>BS8888</b>	Document Type: <b>Masters dissertation</b>	Part Number: <b>BOTTOM_PLATE</b>		
Projection Method: <b>THIRD ANGLE</b>		Legal Owner:  The North-West University, 11 Hofman street, Potchefstroom, 2531	Drawing Number: <b>6D</b>	Sheet: <b>4 of 4</b>	Revision: <b>1</b>
Sheet Size: <b>A4</b>					




Material: <b>PETG</b>		This drawing and any information or descriptive material set out on it are the confidential and copyright property of the <b>North-West University</b> . © and MUST NOT BE DISCLOSED, COPIED, LOANED in whole or part or used for any purpose without the written permission of the <b>North-West University</b> .	Description: <b>3 NM Nema 23 stepper motor dimensions</b>		
Finish: <b>Rough/None</b>			Drawn by: <b>Mr. M. McIntyre</b>	Drawn Date: <b>17/03/2020</b>	
Unless Otherwise Stated: Linear Tol.: $\pm 0,2$ , Angular Tol.: $0^{\circ}15'$ Surface Finish: $0,8\mu\text{m}$ All Dimensions: <b>mm</b>		Document Type: <b>Masters dissertation</b>	Checked/Approved by: <b>Mr. CP Kloppers</b>		
Drawing Scale: <b>1:2</b>		<b>Company Confidential</b>	Checked/Approved Date: <b>31/03/2020</b>		
Approx Weight: ~ Kg	Drawing Produced In Accordance With: <b>BS8888</b>	Legal Owner:  <b>NWU</b> The North-West University, 11 Hofman street, Potchefstroom, 2531	Part Number: <b>NEMA23HS8</b>		
Projection Method: <b>THIRD ANGLE</b> 	Sheet Size: <b>A4</b>		Drawing Number: <b>7A</b>	Sheet: <b>1 of 1</b>	Revision: <b>1</b>



**SECTION A-A**

**DETAIL B**  
SCALE 1 : 1

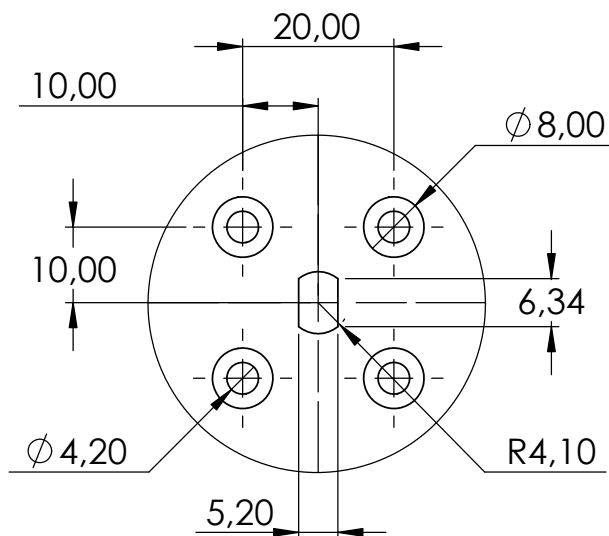
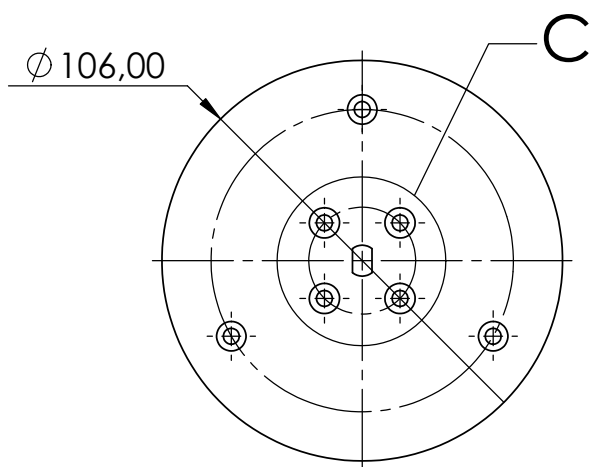
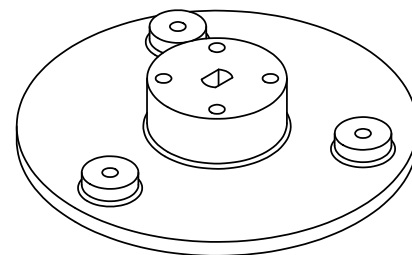
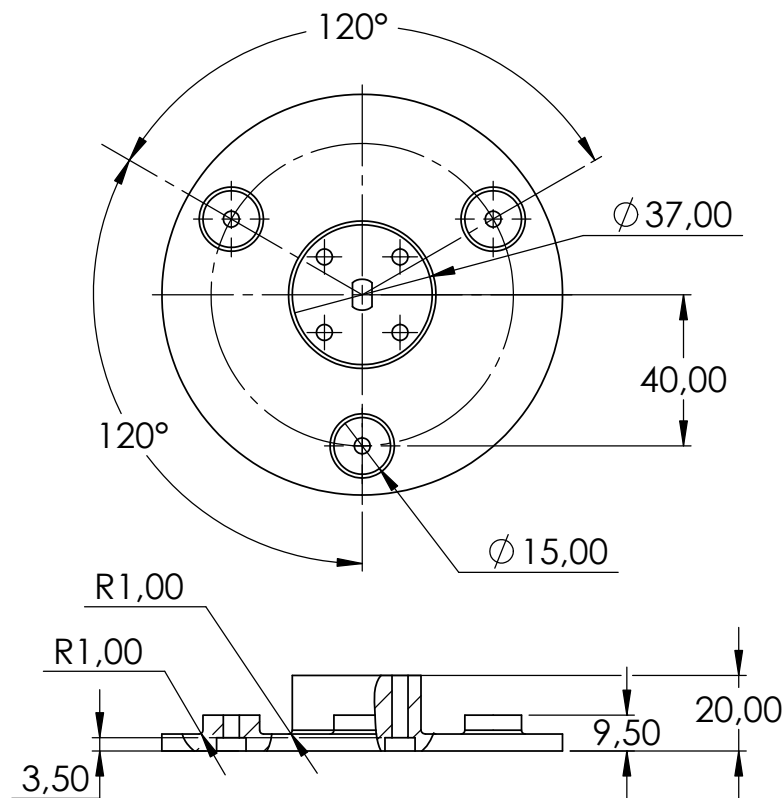
Material: <b>PETG</b>		This drawing and any information or descriptive material set out on it are the confidential and copyright property of the <b>North-West University</b> . © and <b>MUST NOT BE DISCLOSED, COPIED, LOANED</b> in whole or part or used for any purpose without the written permission of the <b>North-West University</b> .	Description: <b>Three roller housing top part dimensions</b>		
Finish: <b>Rough/None</b>			Drawn by: <b>Mr. M. McIntyre</b>	Drawn Date: <b>17/03/2020</b>	
Unless Otherwise Stated: Linear Tol.: $\pm 0.2$ , Angular Tol.: $0^{\circ}15'$ Surface Finish: $0.8\mu\text{m}$ All Dimensions: <b>mm</b>			Checked/Approved by: <b>Mr. CP Kloppers</b>	Checked/Approved Date: <b>31/03/2020</b>	
Drawing Scale: <b>1:2</b>		Document Type: <b>Masters dissertation</b> <b>Company Confidential</b>	Part Number: <b>THREE_ROLLER_HOUSING_TOP</b>		
Approx Weight: ~ <b>Kg</b>	Drawing Produced In Accordance With: <b>BS8888</b>		Legal Owner:  The North-West University, 11 Hofman street, Potchefstroom, 2531		
Projection Method: <b>THIRD ANGLE</b> 	Sheet Size: <b>A4</b>		Drawing Number: <b>8A</b>	Sheet: <b>1 of 1</b>	Revision: <b>1</b>

1

2



3

4



**DETAIL C**

SCALE 1 : 1

Material: <b>PETG</b>		This drawing and any information or descriptive material set out on it are the confidential and copyright property of the <b>North-West University</b> . © and <b>MUST NOT BE DISCLOSED, COPIED, LOANED</b> in whole or part or used for any purpose without the written permission of the <b>North-West University</b> .	Description: <b>Three roller housing bottom part dimensions</b>		
Finish: <b>Rough/None</b>			Drawn by: <b>Mr. M. McIntyre</b>	Drawn Date: <b>17/03/2020</b>	
Unless Otherwise Stated: Linear Tol.: $\pm 0.2$ , Angular Tol.: $0^{\circ}15'$ Surface Finish: $0.8\mu\text{m}$ All Dimensions: <b>mm</b>			Checked/Approved by: <b>Mr. CP Kloppers</b>	Checked/Approved Date: <b>31/03/2020</b>	
Drawing Scale: <b>1:2</b>		Document Type: <b>Masters dissertation</b>	Part Number: <b>THREE_ROLLER_HOUSING_BOTTOM</b>		
Approx Weight: ~ Kg	Drawing Produced In Accordance With: <b>BS8888</b>	Legal Owner:  <b>NWU</b> The North-West University, 11 Hofman street, Potchefstroom, 2531	Drawing Number: <b>9A</b>	Sheet: <b>1 of 1</b>	Revision: <b>1</b>
Projection Method: <b>THIRD ANGLE</b> 	Sheet Size: <b>A4</b>				

A

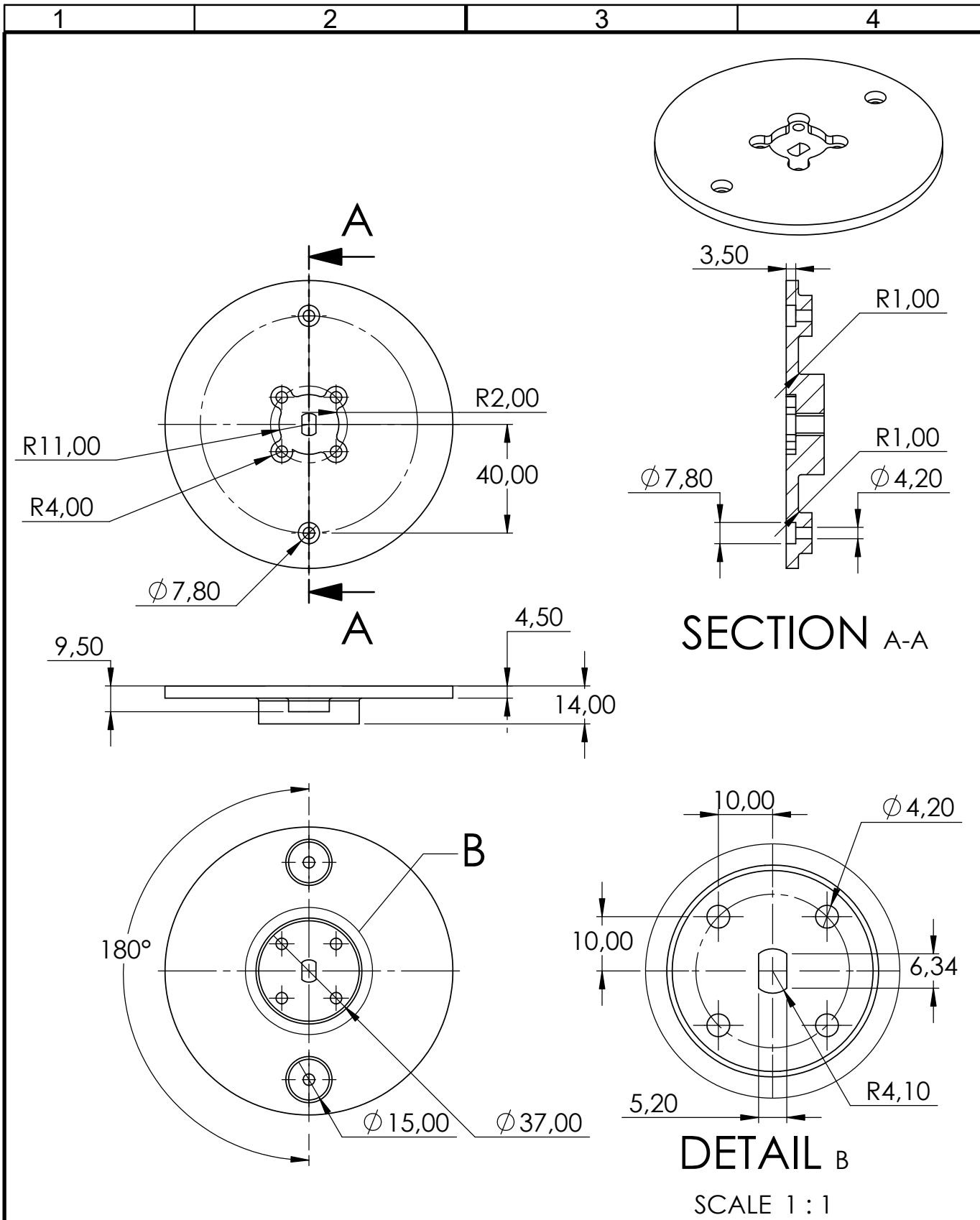
B


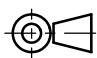
C

D

E

F



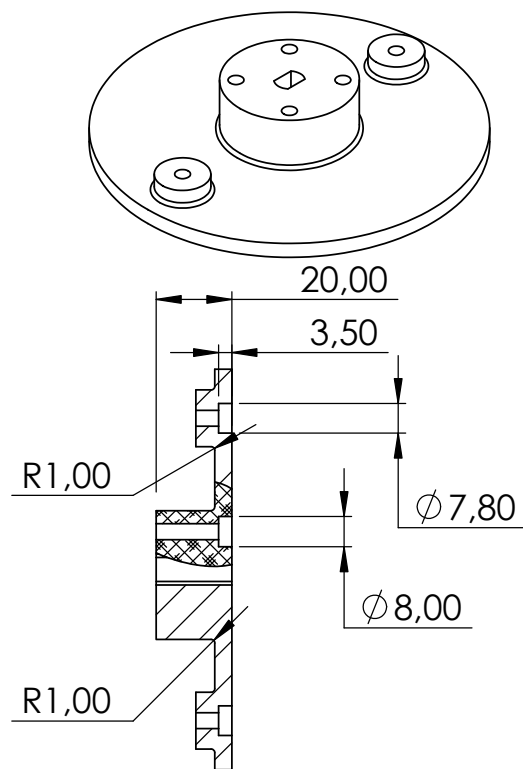
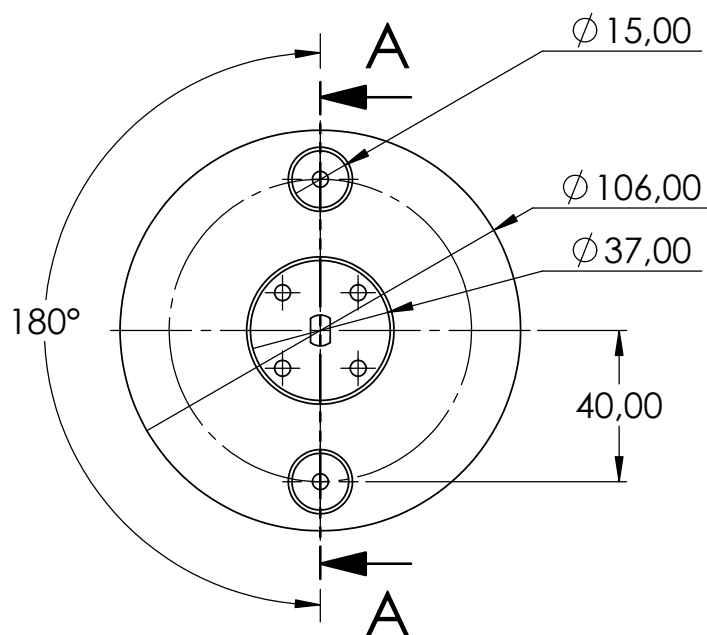
Material: <b>PETG</b>		This drawing and any information or descriptive material set out on it are the confidential and copyright property of the <b>North-West University</b> . © and <b>MUST NOT BE DISCLOSED, COPIED, LOANED</b> in whole or part or used for any purpose without the written permission of the <b>North-West University</b> .	Description: <b>Two roller housing top part dimensions</b>		
Finish: <b>Rough/None</b>			Drawn by: <b>Mr. M. McIntyre</b>	Drawn Date: <b>17/03/2020</b>	
Unless Otherwise Stated: Linear Tol.: ±0.2, Angular Tol.: 0°15' Surface Finish: 0.8µm All Dimensions: mm			Checked/Approved by: <b>Mr. CP Kloppers</b>	Checked/Approved Date: <b>31/03/2020</b>	
Drawing Scale: <b>1:2</b>		Document Type: <b>Masters dissertation</b>	Part Number: <b>TWO_ROLLER_HOUSING_TOP</b>		
Approx Weight: ~ Kg	Drawing Produced In Accordance With: <b>BS8888</b>	Legal Owner:  The North-West University, 11 Hofman street, Potchefstroom, 2531	Drawing Number: <b>10A</b>	Sheet: <b>1 of 1</b>	Revision: <b>1</b>
Projection Method: <b>THIRD ANGLE</b> 	Sheet Size: <b>A4</b>				

1

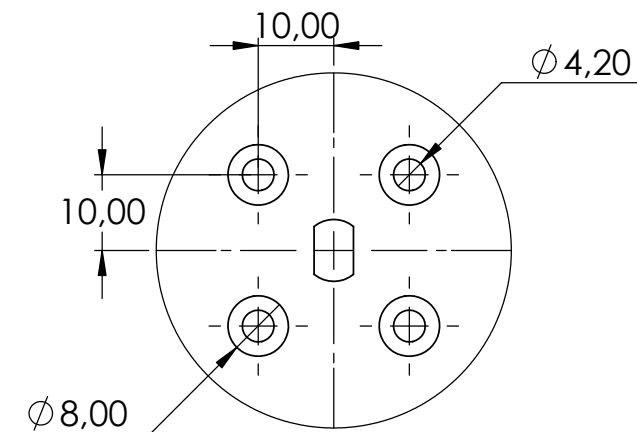
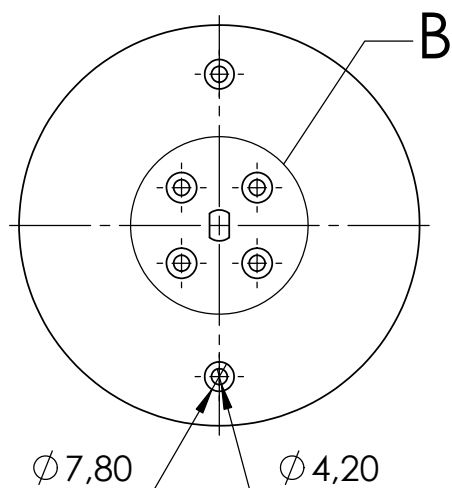
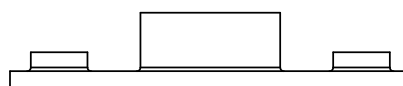
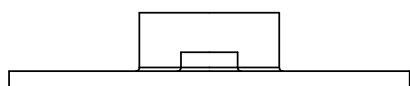
2

3

4





SECTION A-A



DETAIL B

SCALE 1 : 1

Material: <b>PETG</b>		This drawing and any information or descriptive material set out on it are the confidential and copyright property of the <b>North-West University</b> . © and <b>MUST NOT BE DISCLOSED, COPIED, LOANED</b> in whole or part or used for any purpose without the written permission of the <b>North-West University</b> .	Description: <b>Two roller housing bottom part dimensions</b>		
Finish: <b>Rough/None</b>			Drawn by: <b>Mr. M. McIntyre</b>	Drawn Date: <b>17/03/2020</b>	
Unless Otherwise Stated: Linear Tol.: $\pm 0.2$ , Angular Tol.: $0^{\circ}15'$ Surface Finish: $0.8\mu\text{m}$ All Dimensions: <b>mm</b>			Checked/Approved by: <b>Mr. CP Kloppers</b>	Checked/Approved Date: <b>31/03/2020</b>	
Drawing Scale: <b>1:2</b>		Document Type: <b>Masters dissertation</b>	Part Number: <b>TWO_ROLLER_HOUSING_BOTTOM</b>		
Approx Weight: ~ Kg	Drawing Produced In Accordance With: <b>BS8888</b>	Legal Owner:  <b>NWU</b> The North-West University, 11 Hofman street, Potchefstroom, 2531	Drawing Number: <b>11A</b>	Sheet: <b>1 of 1</b>	Revision: <b>1</b>
Projection Method: <b>THIRD ANGLE</b> 	Sheet Size: <b>A4</b>				

A

B

C

D

E

F



1

2

3

4

A

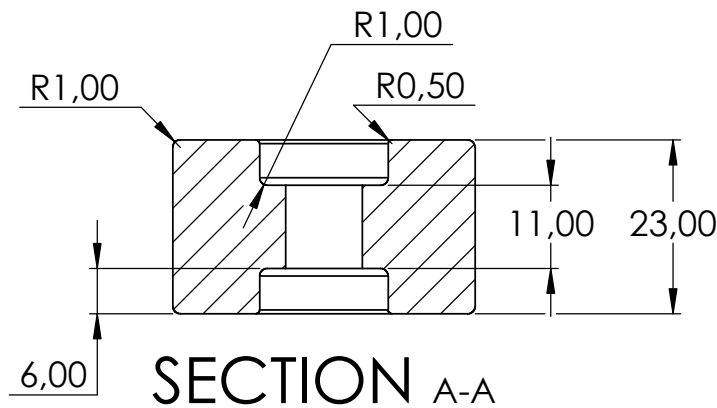
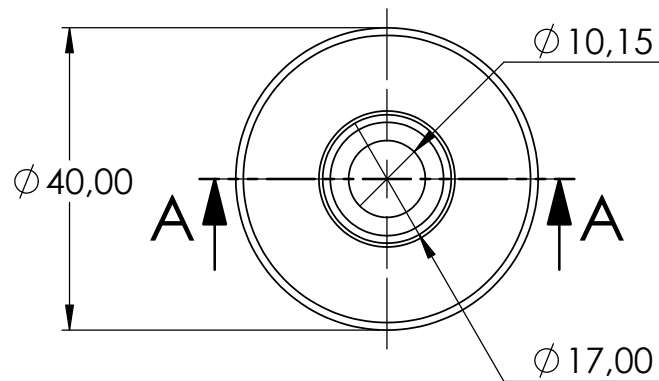
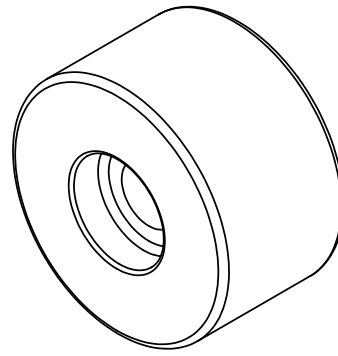
B


C

D

E

F



Material: <b>PETG</b>		This drawing and any information or descriptive material set out on it are the confidential and copyright property of the <b>North-West University</b> . © and <b>MUST NOT BE DISCLOSED, COPIED, LOANED</b> in whole or part or used for any purpose without the written permission of the <b>North-West University</b> .	Description: <b>Roller part dimensions</b>		
Finish: <b>Rough/None</b>			Drawn by: <b>Mr. M. McIntyre</b>	Drawn Date: <b>17/03/2020</b>	
Unless Otherwise Stated: Linear Tol.: $\pm 0.2$ , Angular Tol.: $0^{\circ}15'$ Surface Finish: $0.8\mu\text{m}$ All Dimensions: <b>mm</b>			Checked/Approved by: <b>Mr. CP Kloppers</b>		
Drawing Scale: <b>1:1</b>			Checked/Approved Date: <b>31/03/2020</b>		
Approx Weight: ~ Kg	Drawing Produced In Accordance With: <b>BS8888</b>	Document Type: <b>Masters dissertation</b>	Part Number: <b>ROLLER</b>		
Projection Method: <b>THIRD ANGLE</b>		Legal Owner:  The North-West University, 11 Hofman street, Potchefstroom, 2531	Drawing Number: <b>12A</b>	Sheet: <b>1 of 1</b>	Revision: <b>1</b>
Sheet Size: <b>A4</b>					

1

2

3

4

A

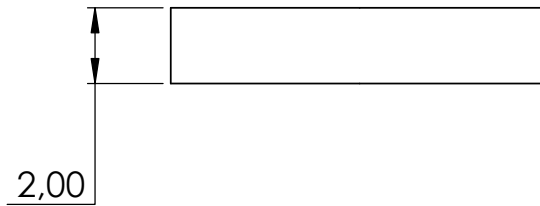
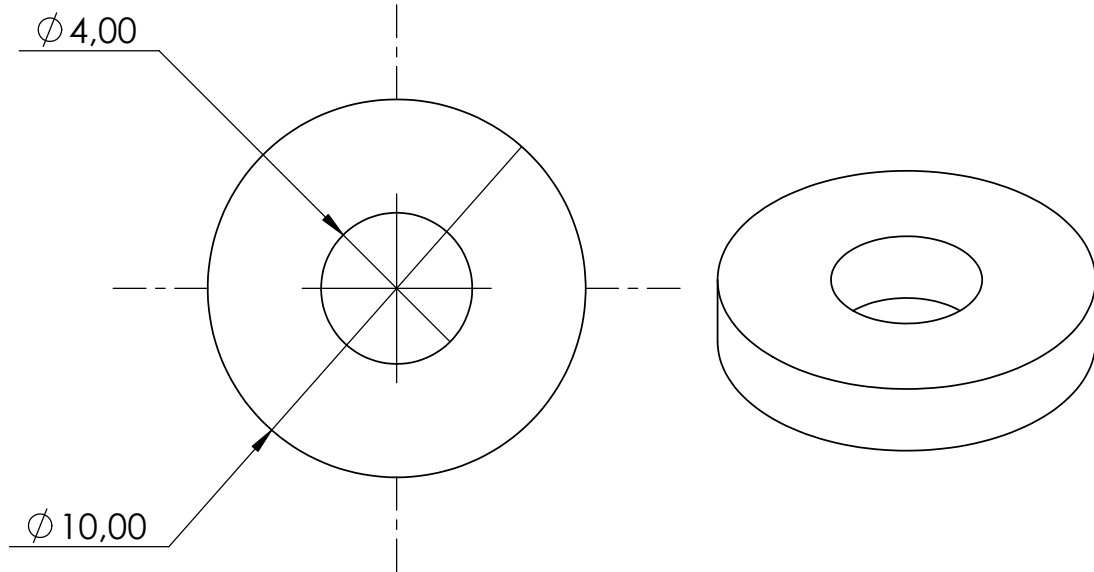
B


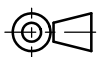
C

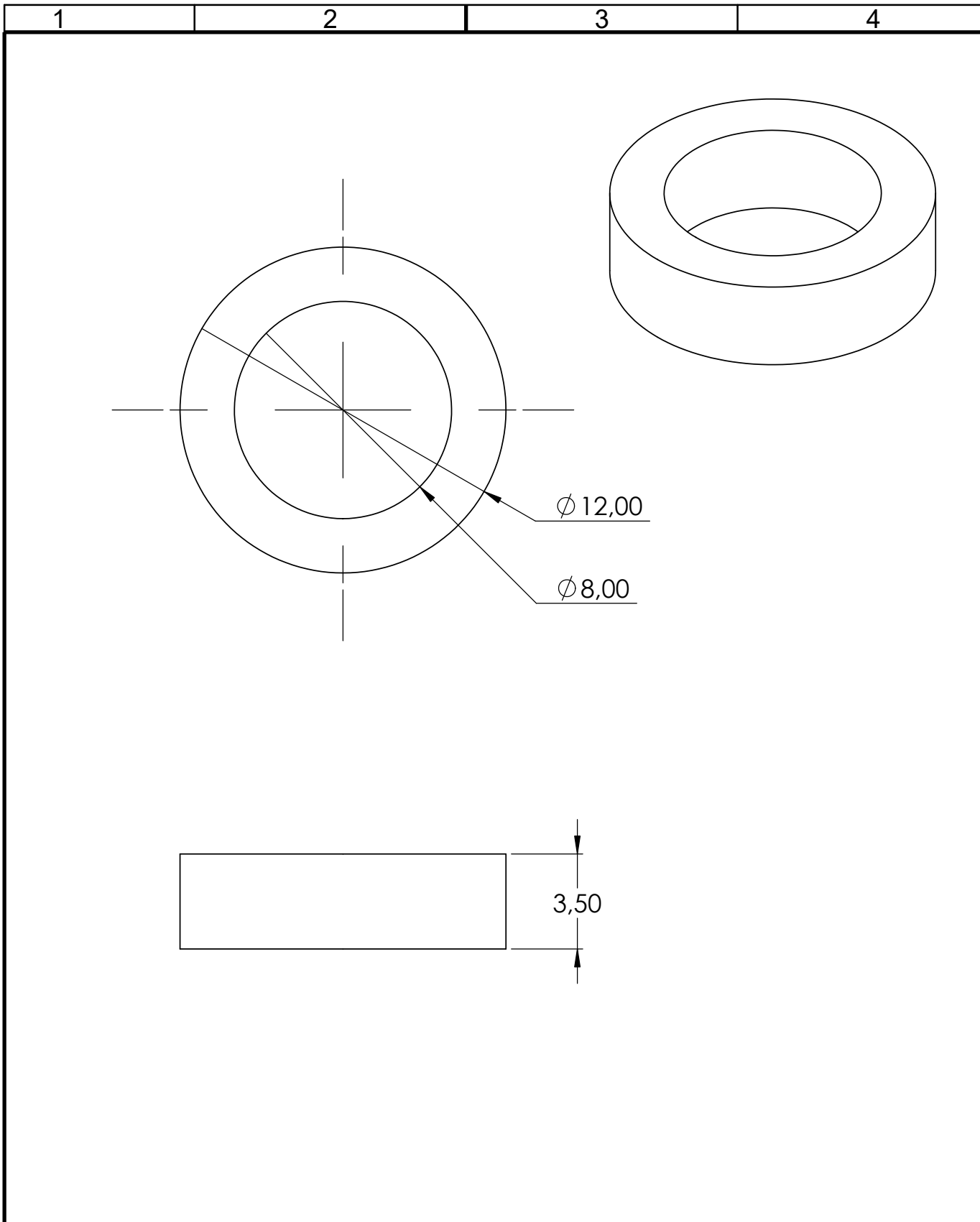
D


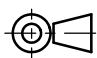
E

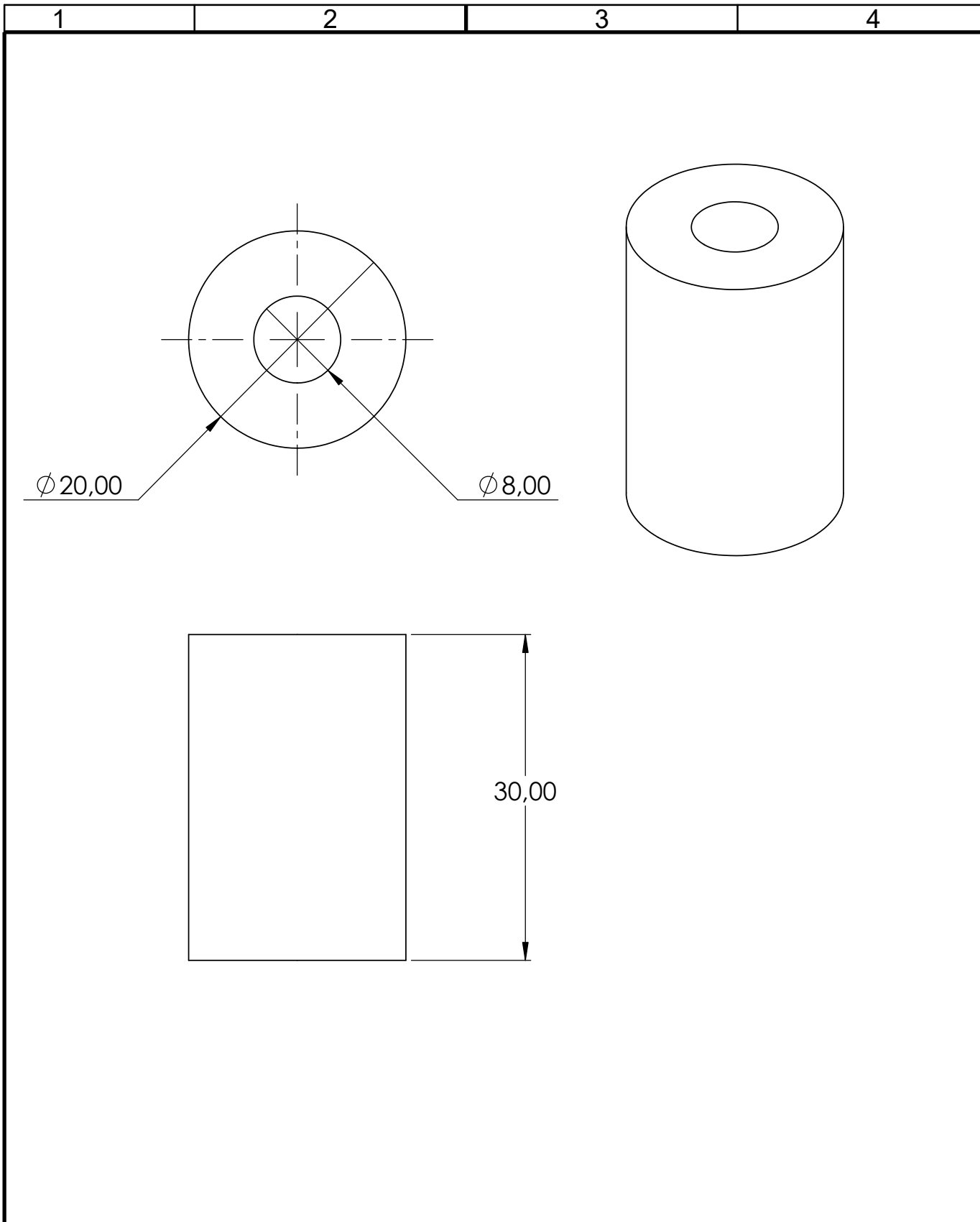
F


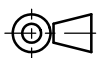


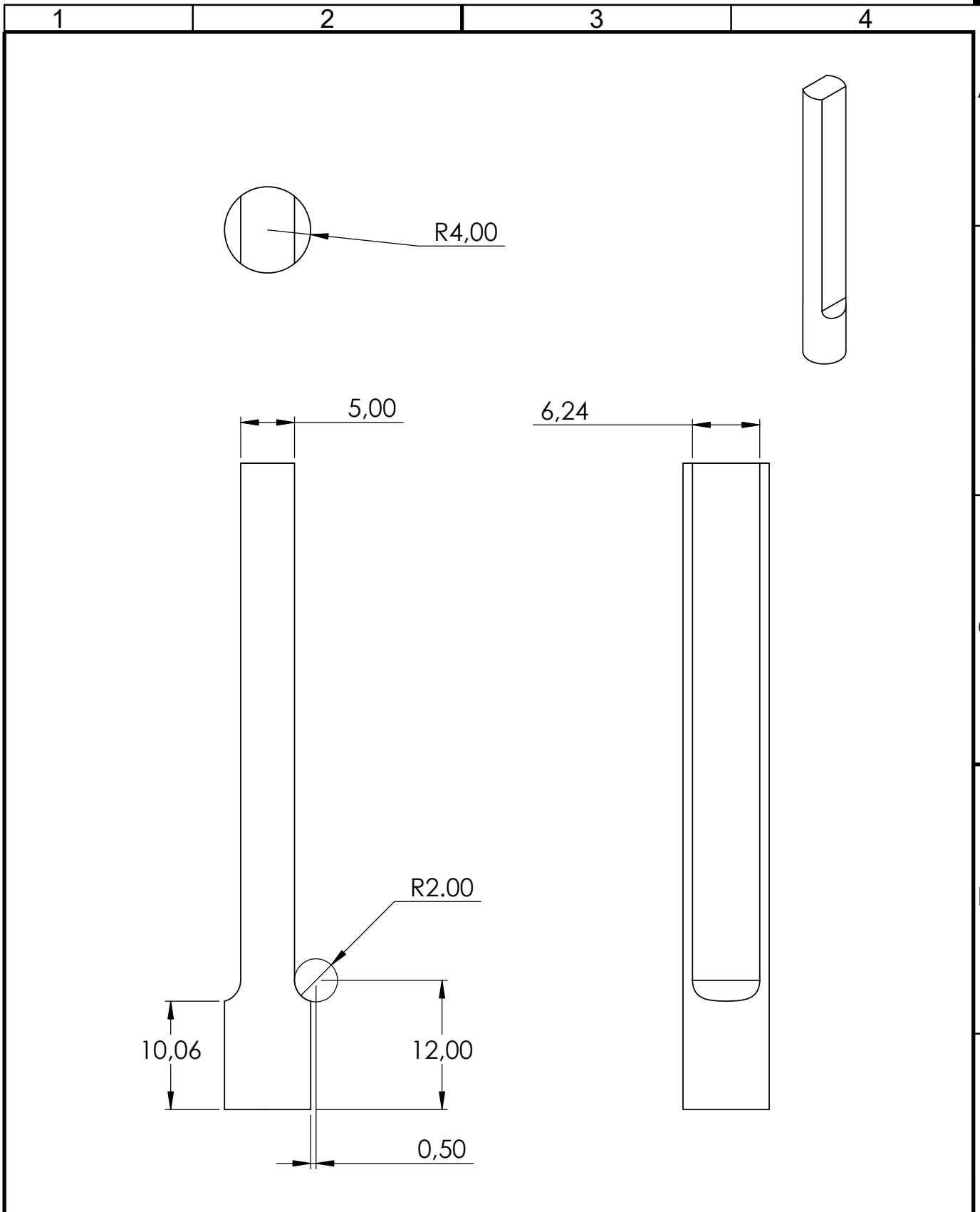
Material: <b>Stainless steel</b>		This drawing and any information or descriptive material set out on it are the confidential and copyright property of the <b>North-West University</b> . © and MUST NOT BE DISCLOSED, COPIED, LOANED in whole or part or used for any purpose without the written permission of the <b>North-West University</b> .	Description: <b>Simplistic representation of the roller bearing dimensions</b>		
Finish: <b>Smooth</b>			Drawn by: <b>Mr. M. McIntyre</b>	Drawn Date: <b>17/03/2020</b>	
Unless Otherwise Stated: Linear Tol.: $\pm 0.2$ , Angular Tol.: $0^{\circ}15'$ Surface Finish: $0.8\mu\text{m}$ All Dimensions: <b>mm</b>			Checked/Approved by: <b>Mr. CP Kloppers</b>	Checked/Approved Date: <b>31/03/2020</b>	
Drawing Scale: <b>5:1</b>		Document Type: <b>Masters dissertation</b>	Part Number: <b>MR104.2ZR_ROLLER_BEARING</b>		
Approx Weight: ~ Kg	Drawing Produced In Accordance With: <b>BS8888</b>	Legal Owner:  The North-West University, 11 Hofman street, Potchefstroom, 2531	Drawing Number: <b>13A</b>	Sheet: <b>1 of 1</b>	Revision: <b>1</b>
Projection Method: <b>THIRD ANGLE</b> 	Sheet Size: <b>A4</b>				




Material: <b>Stainless steel</b>		This drawing and any information or descriptive material set out on it are the confidential and copyright property of the <b>North-West University</b> . © and MUST NOT BE DISCLOSED, COPIED, LOANED in whole or part or used for any purpose without the written permission of the <b>North-West University</b> .	Description: <b>Simplistic representation of shaft bearing dimensions</b>		
Finish: <b>Smooth</b>			Drawn by: <b>Mr. M. McIntyre</b>	Drawn Date: <b>17/03/2020</b>	
Unless Otherwise Stated: Linear Tol.: $\pm 0.2$ , Angular Tol.: $0^{\circ}15'$ Surface Finish: $0.8\mu\text{m}$ All Dimensions: <b>mm</b>			Checked/Approved by: <b>Mr. CP Kloppers</b>	Checked/Approved Date: <b>31/03/2020</b>	
Drawing Scale: <b>5:1</b>		Document Type: <b>Masters dissertation</b>	Part Number: <b>MR128.2ZR_SHAFT_BEARING</b>		
Approx Weight: ~ Kg	Drawing Produced In Accordance With: <b>BS8888</b>	Legal Owner:  The North-West University, 11 Hofman street, Potchefstroom, 2531	Drawing Number: <b>14A</b>	Sheet: <b>1 of 1</b>	Revision: <b>1</b>
Projection Method: <b>THIRD ANGLE</b> 	Sheet Size: <b>A4</b>				



Material: <b>Aluminium</b>		This drawing and any information or descriptive material set out on it are the confidential and copyright property of the <b>North-West University</b> . © and MUST NOT BE DISCLOSED, COPIED, LOANED in whole or part or used for any purpose without the written permission of the <b>North-West University</b> .	Description: <b>Simplistic representation of the 8x8 coupler - spider type dimensions</b>		
Finish: <b>Rough/None</b>			Drawn by: <b>Mr. M. McIntyre</b>	Drawn Date: <b>17/03/2020</b>	
Unless Otherwise Stated: Linear Tol.: $\pm 0.2$ , Angular Tol.: $0^{\circ}15'$ Surface Finish: $0.8\mu\text{m}$ All Dimensions: <b>mm</b>			Checked/Approved by: <b>Mr. CP Kloppers</b>	Checked/Approved Date: <b>31/03/2020</b>	
Drawing Scale: <b>2:1</b>		Document Type: <b>Masters dissertation</b>	Part Number: <b>8MM-8MM_SHAFT_COUPLER</b>		
Approx Weight: ~ Kg	Drawing Produced In Accordance With: <b>BS8888</b>	Legal Owner:  The North-West University, 11 Hofman street, Potchefstroom, 2531	Drawing Number: <b>15A</b>	Sheet: <b>1 of 1</b>	Revision: <b>1</b>
Projection Method: <b>THIRD ANGLE</b> 	Sheet Size: <b>A4</b>				



Material: <b>Stainless steel</b>		This drawing and any information or descriptive material set out on it are the confidential and copyright property of the <b>North-West University</b> . © and MUST NOT BE DISCLOSED, COPIED, LOANED in whole or part or used for any purpose without the written permission of the <b>North-West University</b> .	Description: <b>Shaft dimensions</b>		
Finish: <b>Smooth</b>			Drawn by: <b>Mr. M. McIntyre</b>	Drawn Date: <b>17/03/2020</b>	
Unless Otherwise Stated: Linear Tol.: $\pm 0.2$ , Angular Tol.: $0^{\circ}15'$ Surface Finish: $0.8\mu\text{m}$ All Dimensions: <b>mm</b>			Checked/Approved by: <b>Mr. CP Kloppers</b>		
Drawing Scale: <b>2:1</b>			Checked/Approved Date: <b>31/03/2020</b>		
Approx Weight: ~ Kg	Drawing Produced In Accordance With: <b>BS8888</b>	Document Type: <b>Masters dissertation</b>	Part Number: <b>SHAFT</b>		
Projection Method: <b>THIRD ANGLE</b>		Legal Owner:  The North-West University, 11 Hofman street, Potchefstroom, 2531	Drawing Number: <b>16A</b>	Sheet: <b>1 of 1</b>	Revision: <b>1</b>
Sheet Size: <b>A4</b>					

## APPENDIX D

---

### Additional test bench information

---

The collection of datasheets of the components can be located [here](#), or alternatively, the individual datasheets can be located with the links below.

MAX 6675 Cold-Junction-Compensated K-Thermocouple-to-Digital Converter (0°C to +1024°C):

<https://nextcloud.nwu.ac.za/index.php/s/afP6x86doMjGGCf>

Wantai DQ542MA stepper motor driver:

<https://nextcloud.nwu.ac.za/index.php/s/7SqiLzRQT4pHikm>

57BYGH115-003 Stepper motor:

<https://nextcloud.nwu.ac.za/index.php/s/fXG7LScjwstMTwA>

Honeywell PX2EF1XX050PAAAX pressure sensors:

<https://nextcloud.nwu.ac.za/index.php/s/bn3TPXNybptzzLD>

ATmel ATmega 2560 processor:

<https://nextcloud.nwu.ac.za/index.php/s/Y7eyzjkX7HCTgoz>

Arduino Mega 2560 PCB:

<https://nextcloud.nwu.ac.za/index.php/s/eZ8sAmGzbzpgZCi>

Pedrolo CP 100 0.25 kW pump:

<https://nextcloud.nwu.ac.za/index.php/s/TkbB7jm2f9zN6bQ>

Fluke 325:

<https://nextcloud.nwu.ac.za/index.php/s/sBEpWafK922GJZC>

DMM VA90A:

<https://nextcloud.nwu.ac.za/index.php/s/mynAMWTYLiA8SHG>

Testo 622 hygrometer (barometer):

<https://nextcloud.nwu.ac.za/index.php/s/q9n4owS7ec8PkXT>

Versilon SPX-60 FB silicon tubing:

<https://nextcloud.nwu.ac.za/index.php/s/bTr9aMyjJ449rGS>

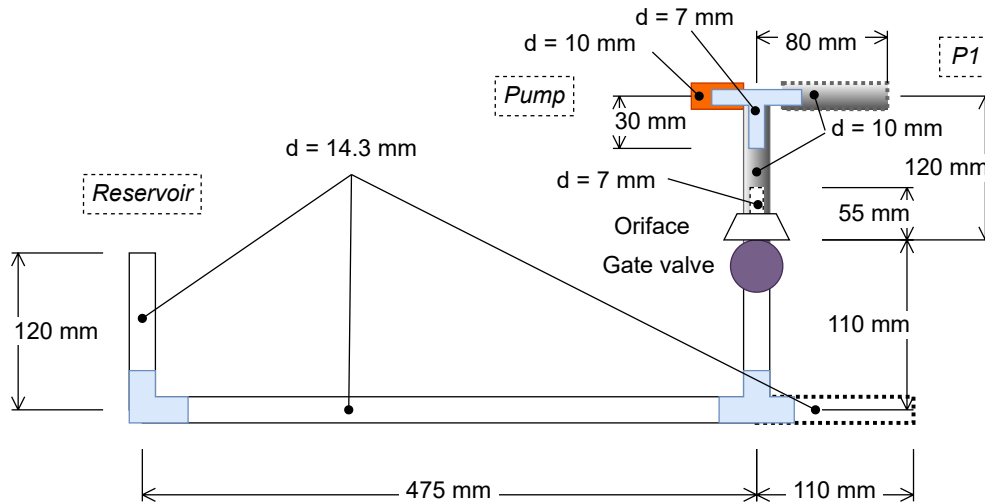


Figure D.1: Peristaltic pump test bench inlet line dimensions

## dSPACE Simulink model

The dSPACE files (including the Simulink model and dSPACE virtual environment build) used for the test can be obtained [here](#) or by following the link:

<https://nextcloud.nwu.ac.za/index.php/s/Fwxcq9XzX7DpKg5>

APPENDIX D. ADDITIONAL TEST BENCH INFORMATION

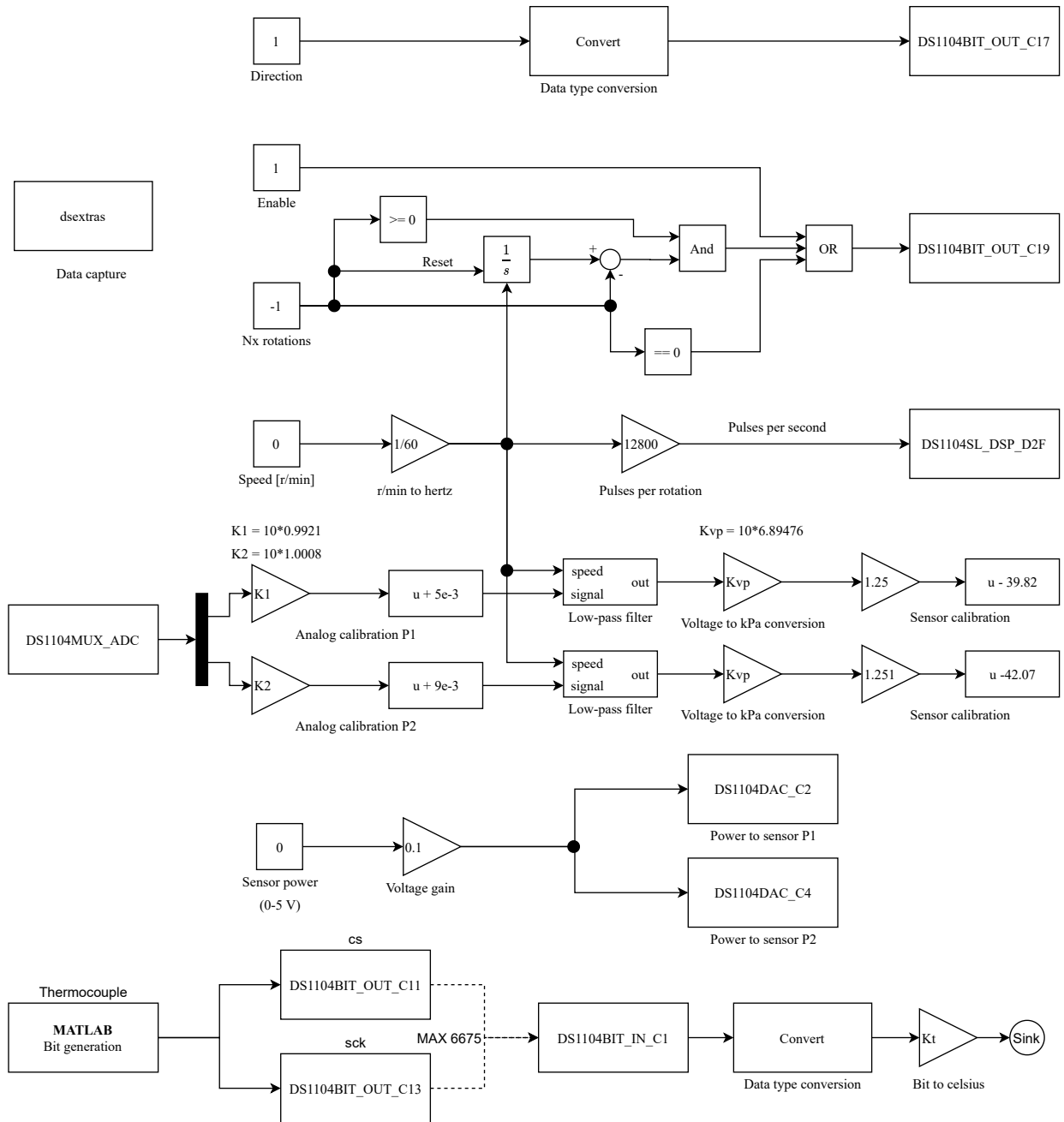


Figure D.2: dSPACE 1104 Simulink block diagram



## APPENDIX E

---

### Additional experiment information

---

The test and simulation data can be found [here](#) or by following the links:

- 1) <https://nextcloud.nwu.ac.za/index.php/s/MpCbBf2t53kWxod>
- 2) <https://doi.org/10.25388/nwu.12911564>

In order to obtain the motor speed values from the experimental data, the peak to peak periods can be measured to calculate the motor speed with (3.48). This is done by sectioning or resizing the pressure data (from a vector) from each sensor to the length of one period in a repeating sequence for the entire test. This forms a matrix where, depending on the restructuring scheme, the width provides data entries for one period length, and the length provides the number of periods within the test. This matrix can be plotted as a surface and is indicated in Fig. E.1. This technique allows for easy recognition of unstable data, which indicates motor slip.

Fig. E.2 indicates the processed pressure sensor data for Experiment B, with the minimum peaks indicated by a white plus (+), and the maximum peaks indicated by a black asterisk (\*). The sample set with the minimum standard deviation, in reference to the average peak time between periods, is circled (O) and used to determine the motor speed of the data set.

Table E.1 provides the calculated motor speed values for Experiments A, B, and C, as well as Simulations A and B. Table E.2 provides the calculated motor speed values for Experiments 1–4. Table E.3 provides the calculated motor speed values pertaining to the two-roller tests and simulations (Experiments D and 5, as well as Simulation C).

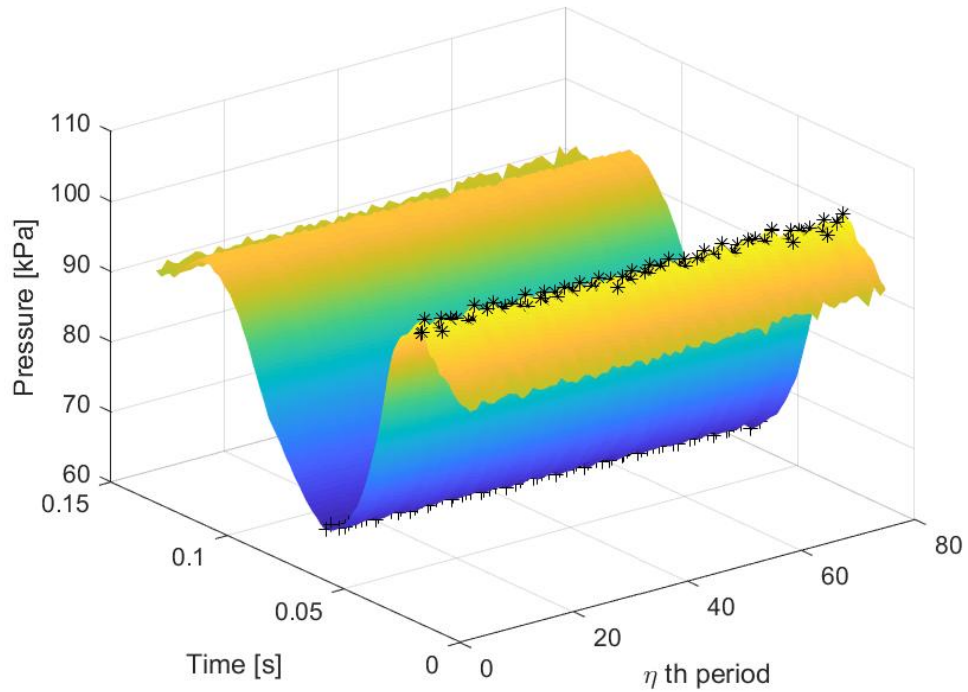


Figure E.1: Experiment B: Surface plot of the inlet pressure sensor (P1) data at 150 r/min

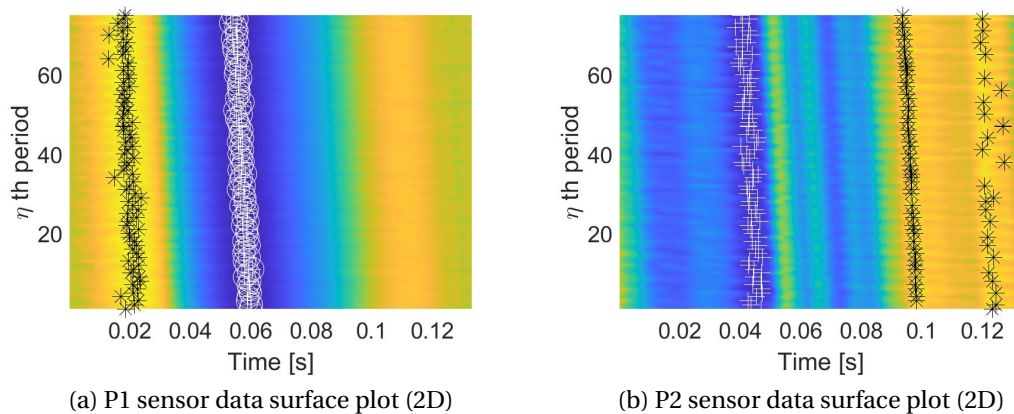


Figure E.2: Experiment B: Surface plot indicating the processed pressure sensor data for 150 r/min

Table E.1: Calculated motor speeds in r/min for the pressure tests and simulations of three-roller pump configuration

<b>Test speed</b>	<b>Experiment A</b>	<b>Experiment B</b>	<b>Experiment C</b>	<b>Simulation A</b>	<b>Simulation B</b>
10	9.93	9.97	9.97	10.00	10.00
20	20.01	19.98	20.00	20.00	20.00
30	29.99	29.98	29.98	30.00	30.00
40	39.96	39.97	39.98	40.00	40.00
50	49.98	49.98	49.99	50.00	50.00
60	59.99	59.96	60.04	60.00	60.00
70	69.94	69.93	69.92	70.00	70.00
80	79.88	79.88	79.92	80.00	80.00
90	89.86	89.86	89.88	90.00	90.00
100	99.84	99.83	99.85	100.00	100.00
110	109.96	109.98	109.99	110.00	110.00
120	119.83	119.81	119.85	120.01	120.01
130	129.82	129.82	129.85	130.00	130.00
140	139.68	139.68	139.71	140.00	140.00
150	149.78	149.76	149.78	150.00	150.00
160	159.48	159.48	159.49	160.00	160.00
170	169.56	169.57	169.60	169.99	169.99
180	179.76	179.70	179.71	180.00	180.00
190	189.48	189.46	189.45	190.00	190.00
200	199.71	199.71	199.71	200.00	200.00

APPENDIX E. ADDITIONAL EXPERIMENT  
INFORMATION

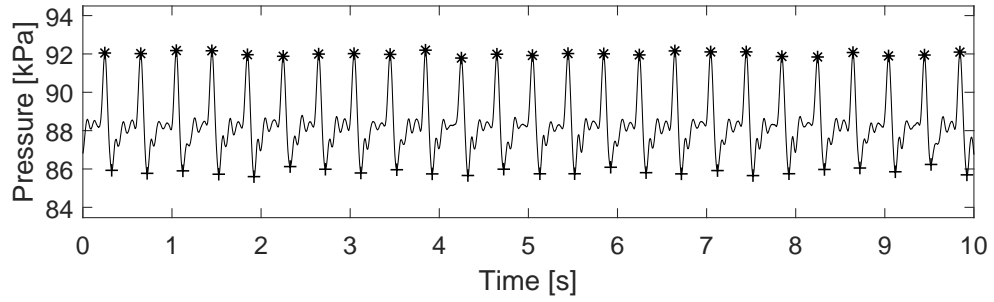
---

Table E.2: Calculated motor speeds in r/min for the flow tests of three-roller pump configuration

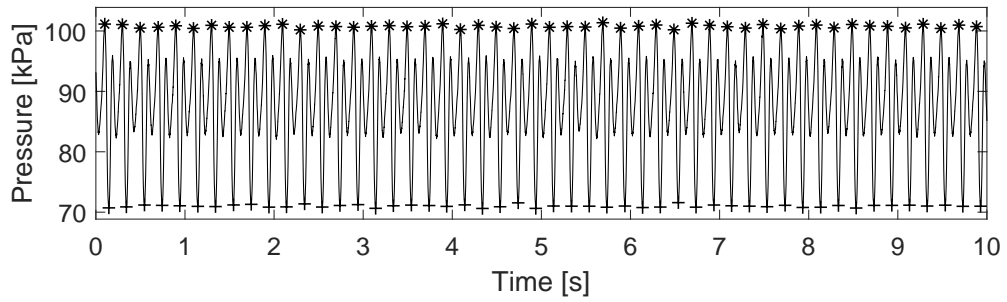
<b>Test speed</b>	<b>Experiment 1</b>	<b>Experiment 3</b>	<b>Experiment 4</b>	<b>Test speed</b>	<b>Experiment 2</b>
10	9.97	9.98	10.33	15	14.99
20	20.01	20.01	19.95	25	25.13
30	29.98	30.06	29.98	35	34.79
40	39.97	39.98	40.01	45	44.89
50	49.97	49.93	50.06	55	54.89
60	60.04	59.94	59.99	65	64.92
70	69.90	-	70.08	75	74.87
80	79.85	79.88	79.84	85	84.95
90	89.95	89.87	89.85	95	95.08
100	99.85	99.97	99.95	105	104.99
110	109.92	109.98	110.00	115	114.85
120	119.84	119.94	119.96	125	124.60
130	129.86	129.85	129.83	135	134.87
140	139.63	139.61	139.65	145	144.85
150	149.81	149.65	149.80	155	152.68
160	159.62	159.51	159.51	165	165.26
170	-	169.93	169.67	175	-

Table E.3: Calculated motor in r/min speeds for the two-roller pump configuration experiments

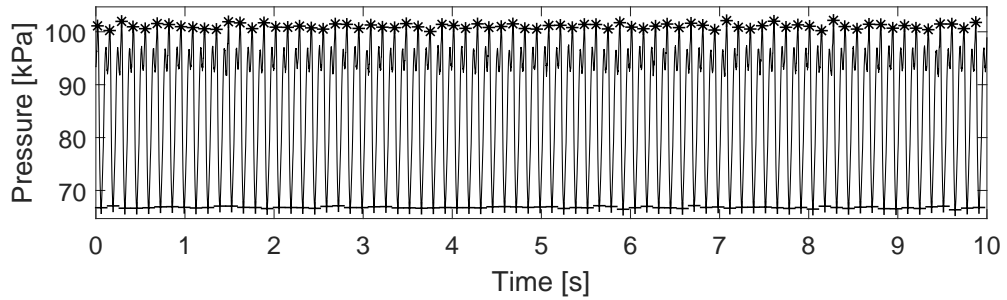
<b>Test speed</b>	<b>Experiment 5</b>	<b>Simulation C</b>	<b>Experiment D</b>
10	9.99	10.00	10.00
20	20.00	20.00	19.96
30	30.00	30.00	29.99
40	39.98	40.00	39.97
50	49.99	50.00	49.99
60	59.99	60.00	59.99
70	69.94	70.00	69.93
80	79.87	80.00	79.88
90	89.87	89.99	89.86
100	100.06	100.00	99.86
110	110.13	110.00	109.99
120	119.88	120.00	119.80
130	129.85	130.00	129.78
140	139.80	140.00	139.73
150	149.85	150.00	149.78
160	159.52	160.01	159.50
170	169.49	169.99	169.53
180	179.74	180.01	179.80
190	189.51	190.00	189.47
200	199.86	200.00	199.75
210	210.11	210.00	-
220	219.95	220.01	-
230	229.06	230.02	-
240	239.74	240.00	-
250	249.34	250.00	-
260	259.78	260.01	-
270	268.82	270.00	-
280	279.30	280.00	-
290	288.74	290.01	-
300	299.66	300.00	-



(a) P1 sensor data at 50 r/min



(b) P1 sensor data at 100 r/min



(c) P1 sensor data at 150 r/min

Figure E.3: Experiment B: Processed pressure waveforms of P1 sensor data

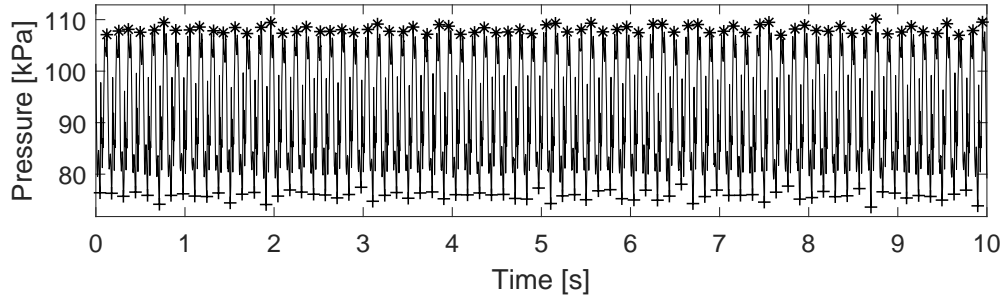
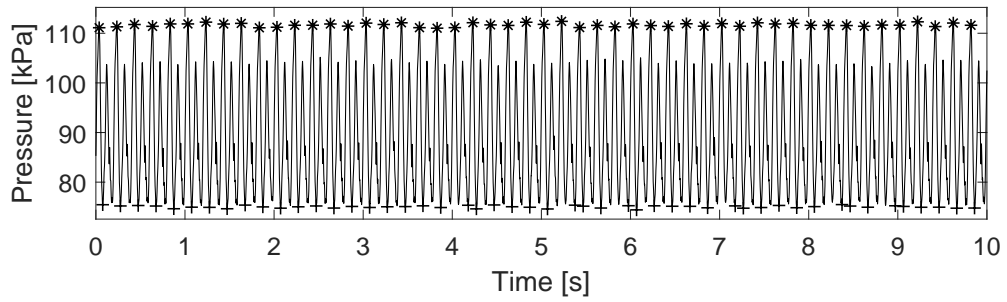
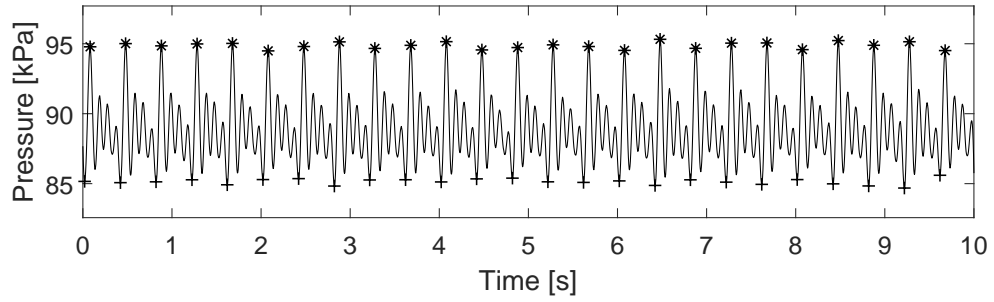
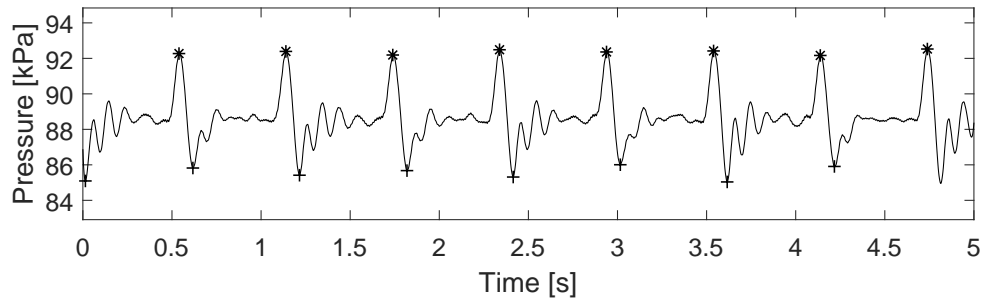
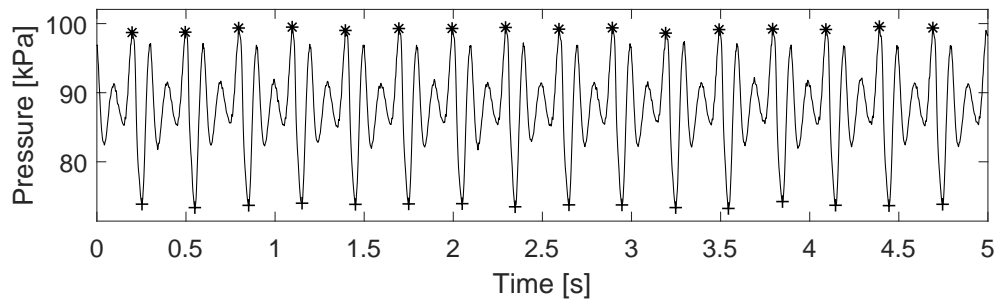


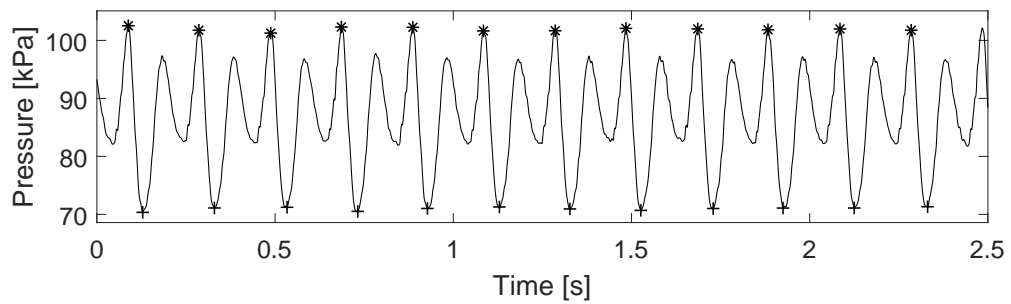
Figure E.4: Experiment B: Processed pressure waveforms of P2 sensor data



(a) P1 sensor data at 50 r/min



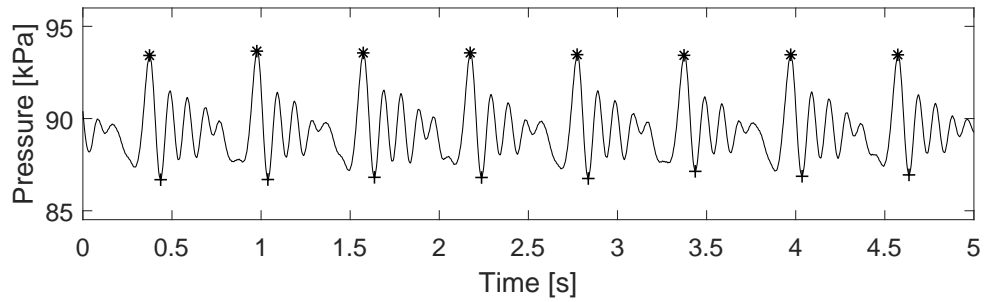
(b) P1 sensor data at 100 r/min



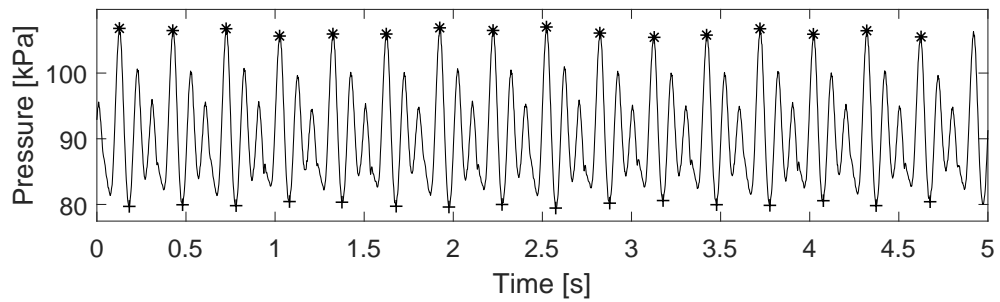
(c) P1 sensor data at 150 r/min

Figure E.5: Experiment D: Processed pressure waveforms of P1 sensor data

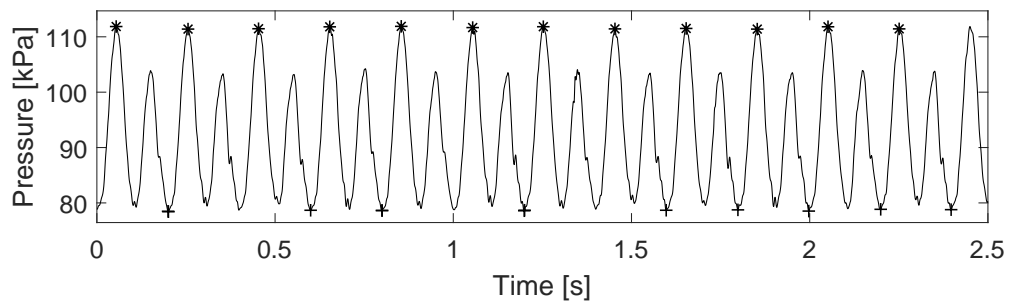




(a) P2 sensor data at 50 r/min



(b) P2 sensor data at 100 r/min



(c) P2 sensor data at 150 r/min

Figure E.6: Experiment D: Processed pressure waveforms of P2 sensor data